UC Riverside

UC Riverside Electronic Theses and Dissertations

Title

Gas-Phase Silylation as a Way to Passivate Silicon Oxide Surfaces for Area-Selective Atomic Layer Deposition

Permalink

https://escholarship.org/uc/item/28p2p4br

Author

Alam, Mohammed Sadman

Publication Date

2024

Peer reviewed|Thesis/dissertation

eScholarship.org Powered by the California Digital Library
University of California

UNIVERSITY OF CALIFORNIA
RIVERSIDE

Gas-Phase Silylation as a Way to Passivate Silicon Oxide Surfaces for Area-Selective Atomic Layer Deposition

A Dissertation submitted in partial satisfaction
of the requirements for the degree of

Doctor of Philosophy

in

Chemistry

by

Mohammed Sadman Alam

September 2024

Dissertation Committee:
Dr. Francisco Zaera, Chairperson
Dr. Gregory Beran
Dr. Yadong Yin

Copyright by
Mohammed Sadman Alam
2024

The Dissertation of Mohammed Sadman Alam is approved:

_____

_____

_____

Committee Chairperson

University of California, Riverside

ACKNOWLEDGEMENTS

I extend my sincerest gratitude to my Ph.D. advisor Professor Francisco Zaera who gave me the unique opportunity to join his research group and pursue my graduate studies. His firm support and extensive knowledge have been instrumental in shaping me to be the scientist I am today. Professor Zaera's intense passion for scientific inquiry continues to inspire me, educating me on the importance of meticulously scrutinizing and continuously questioning all pieces of work in the pursuit of accurate science. His exceptional patience allowed me to fail (many times), but learn from my mistakes each time, cultivating my growth as an independent problem solver. I will never forget the mentorship, guidance, and wisdom he bestowed me with not only in academic research, but also in various aspects of my personal life.

I thank Professor Beran for his role on my advancement and doctoral committee as well as always providing helpful advice and guidance to the graduate students, and Professor Yin for his role on my doctoral committee.

I express my heartfelt appreciation to Prisciliano Saavedra for his dedicated assistance with locating items, ensuring timely deliveries, and most importantly, for displaying genuine benevolence to others. Special thanks go to Dr. Andreas Hupfer from SPECS (in Germany) who provided prompt and detailed troubleshooting advice even across a 9-hour time zone difference, and to the cleanroom manager Dr. Dong Yan for his role in maintaining the nanofabrication facility after COVID-19 even with limited support and resources. Their help was instrumental for completing the work in this dissertation.

I am also thankful for the lifetime friendships I made in the Zaera group. Dr. Mindika Tilan Nayakasinghe stands out as not only a brilliant scientist whom I learned much from through our research discussions, but also a dependable friend. Fixing the XPS computer would have been impossible without technical support from Ameer Ahmed Siddique; I have tremendous respect for his positive attitude and vast patience. The stressful onset of COVID-19 would have been unmanageable without Leticia Rasteiro, who helped make that period more enjoyable through our conversations in the lab. Zihao Wang made the lab a fun environment especially with his delicious homemade pastries, and Philipp Haugg brought a newfound sense of joy with him during his short visit here; I will always treasure the jokes we shared and memories we made together. It is difficult to comprehend how different my life would be without the mentorship and guidance of Dr. Md Abdul Motin. His amiable sense of humor and tenacious work ethic created a supportive and welcoming atmosphere that made me eager to come to the lab. I will always cherish the hard laughs we shared and challenging struggles we overcame together that helped develop an unbreakable camaraderie between us over the years. I am unable to express the depth of my gratitude to Hyeonkyeong Lee, whose altruistic and kind-hearted nature helped me get through some of my bleakest moments. I will be forever indebted for your steadfast support through this journey (especially when I was not the most pleasant person to be around) and for having you in my life. Finally, I also express my thanks to the remaining colleagues in our group.

My deepest appreciation goes to my family for their constant love and support throughout my endeavors, without which none of this would have been made possible.

DEDICATION

This dissertation is dedicated to all my family, alive or deceased, whose unconditional love and support throughout my entire life were instrumental in the completion of my arduous academic journey. This accomplishment is not solely mine; it is equally theirs.

To my parents

Mohammed Jahangir Alam and **Saiyedatun Nessa**

Your unwavering encouragement and immeasurable sacrifice have been the foundation upon which I have been able to succeed thus far. You gave up pursuing your own dreams in life so that I had the opportunity to achieve mine. Words cannot describe how blessed I am to have such a supportive and loving family. In dedicating this work to you, I express my profound gratitude for being the pillars of strength that inspired me to reach for something I thought was beyond my grasp. I hope I have made you proud.

To my future family

This achievement is a testament to my commitment and love for you. I hope that you are able to have a future that shines even brighter than the one I was given.

ABSTRACT OF THE DISSERTATION

Gas-Phase Silylation as a Way to Passivate Silicon Oxide Surfaces for Area-Selective Atomic Layer Deposition

by

Mohammed Sadman Alam

Doctor of Philosophy, Graduate Program in Chemistry
University of California, Riverside, September 2024
Dr. Francisco Zaera, Chairperson

The ability to grow thin films on solid substrates through chemical deposition, such as atomic layer deposition (ALD), in an area-selective (AS) fashion is a hallmark of manufacturing processes within the semiconductor industry. One promising method to achieve this is through silylation – a method to passivate surfaces against chemical reactions using inhibitor molecules possessing substituted silyl moieties. These surface modifiers have traditionally been used ex-situ in the liquid-phase, creating limitations for their integration into existing semiconductor process design due to their long reaction times and high costs involved at an industrial scale. Additionally, solvent effects present in the liquid phase may be detrimental to the quality of the organosilane monolayer. This research addresses these issues by employing an all gas-phase silylation process, affording the unique advantage of in-situ analysis combined with the ability to be integrated with other

gas-phase microelectronics processing steps. Finally, this passivation scheme was evaluated in the context of AS-ALD of metal oxides.

The nucleation delay and subsequent growth associated with the ALD of titania and hafnia thin films on silica surfaces silylated with *N*-(trimethylsilyl)dimethylamine (TMSDMA) in both the liquid and gas phase was characterized using X-ray photoelectron spectroscopy. Both silylation methods resulted in comparable passivation efficacies regardless of the starting surface or the ALD reactions used, demonstrating an intrinsic limitation to the extent of inhibition achievable. Moreover, a lower degree of carbon content was observed when using the gas-phase silylation approach suggestive of the formation of a higher quality monolayer.

The interaction of TMSDMA with copper substrates was investigated, in which it was determined that trimethylsilyl moieties did not chemisorb on copper under conditions that otherwise passivate silica. A simple AS-ALD scheme was developed to control the selective deposition of titania where the role of the growth and non-growth surface between copper and silica could be interchanged using TMSDMA.

This modification scheme also shows promise in the field of heterogenous catalysis as it affords the ability to control the extent of silylation should partial blocking of surface hydroxyl nucleation sites be desired, which may be beneficial for the growth of immobilized nanoparticles in the future.

Table of Contents

ONE – Introduction and Overview 1
1.1 Device Miniaturization in Semiconductor Manufacturing 1
1.2 Atomic Layer Deposition 2
1.3 Area-Selective (AS) Deposition 5
1.3.1 Inherent Selectivity 6
1.3.2 Self-Assembled Monolayers 6
1.3.3 Small-molecule Inhibitors 7
1.4 Reaction Phase 9
1.5 Dissertation Objectives 9
TWO – Experimental 12
2.1 Introduction 12
2.2 Ultra-High Vacuum System 12
2.2.1 X-ray Photoelectron Spectroscopy 14
2.2.2 Preparation of Flat Substrates 17
2.2.3 Silylation Reaction 21
2.2.4 ALD Film Growth 22
2.3 Surface Modification of SBA-15 23
2.3.1 Silanol Density Reduction 24
2.3.2 Silanol Density Enhancement 25
2.3.3 Analysis of Silanol Density 26
THREE – Initial Studies on Gas-phase Silylation using TMSDMA 27
3.1 Introduction 27
3.2 Initial Studies 30
3.2.1 Initial Silylation of SiO_2/Si(100) (1 nm Native Oxide) 31
3.2.2 High-temperature Cleaning Pretreatment 33
3.2.3 Addition of Alternating H_2O Exposures 35
3.3 Ex-Situ Cleaning Pretreatment and Inhibitor Flux Enhancement 37
3.4 Conclusion 38

FOUR – Metal Oxide ALD on Silylated PE-CVD-grown vs. RCA-cleaned SiO_2/Si(100) – Gas- vs. Liquid-phase Silylation 39
4.1 Introduction 39
4.2 Experimental 41
4.3 Estimation of PE-CVD Grown SiO_2 Film Thickness 41
4.4 Silylation Efficacy Against TiO_2 ALD – Gas vs. Liquid Phase 43
4.4.1 PE-CVD-Grown SiO_2/Si(100) 43
4.4.2 RCA-cleaned SiO_2/Si(100) 60
4.6 Silylation Efficacy Against HfO_2 ALD on PE-CVD-Grown SiO_2/Si(100) – Gas vs. Liquid Phase 66
4.7 Discussion 79
4.8 Conclusion 86
FIVE – TMSDMA Treatment of Copper Surfaces as a Way to Control Metal Oxide ALD 88
5.1 Introduction 88
5.2 Experimental 89
5.3 Initial Studies on Cu Substrates 91
5.3.1 Surface Cleaning and WCA Measurements 92
5.3.2 OFHC Cu vs. Sputter-deposited Cu/PE-CVD SiO_2 93
5.3.3 Interaction of TMSDMA with Ar^+-Sputtered OFHC Cu (CuO_x/Cu) 96
5.4 TiO_2 ALD 98
5.4.1 CuO_x/Cu – With (W/) vs. Without (W/o) TMSDMA 98
5.4.2 TMSDMA-treated: PE-CVD SiO_2 vs. CuO_x/Cu 102
5.4.3 Unmodified: PE-CVD SiO_2 vs. CuO_x/Cu 104
5.5 HfO_2 ALD 106
5.5.1 CuO_x/Cu – With (W/) vs. Without (W/o) TMSDMA 106
5.5.2 TMSDMA-treated: PE-CVD SiO_2 vs. CuO_x/Cu 108
5.5.3 Unmodified: PE-CVD SiO_2 vs. CuO_x/Cu 110
5.5.4 TMSDMA-treated CuO_x/Cu: Cleaning method 1 vs. 2 115
5.6 TMSDMA Inhibitor Reapplications: PE-CVD SiO_2 vs. CuO_x/Cu 120
5.6.1 TiO_2 ALD 121
5.6.2 HfO_2 ALD 127
5.7 Discussion 136

5.8 Conclusion 150
SIX – Controlling ALD Nucleation Site (Silanol) Density in Mesoporous Silica (SBA-15) via Chemical Treatments 151
6.1 Introduction 151
6.2 Experimental 155
6.3 Partial Silylation to Reduce the Silanol Density 158
6.4 NaOH Etching to Enhance the Silanol Density 162
6.5 Discussion 171
6.6 Conclusion 174
SEVEN – Conclusions and Future Directions 177
7.1 Overall Conclusions 177
7.2 Prospective Work 180
7.2.1 Studies on Cu(0) Surfaces 180
7.2.2 Expanding Supercycle Process to Include an Etch-back Step 182
7.2.3 Studies on Other Potential Growth Surfaces 182
7.2.4 Metal Oxide ALD on Surface-modified SBA-15 183
References 185

List of Figures

Figure 1.1 Schematic depicting the process of a typical ALD cycle that is comprised of two half-cycles using precursors A and B.[18] 3

Figure 1.2 Graph depicting the "ALD window" mapping the process temperature where linear film growth occurs.[18] Non-ideal growth occurs beyond the lower and upper temperature limits. 4

Figure 1.3 Schematic depicting an example of AS-ALD employing surface modifiers as inhibitors to passivate the NGS prior to ALD, resulting in film deposition on the GS.[23] .. 6

Figure 1.4 Structure of the N-(trimethylsilyl)dimethylamine (TMSDMA) inhibitor (ChemDraw) used for the silylation reactions in this dissertation. The green box highlights the trimethylsilyl moiety that covalently bonds to surface nucleation sites on SiO_2 to generate an organosilane passivating monolayer. 8

Figure 2.1 Photo of the UHV chamber (UC System) used to conduct the experiments discussed in this dissertation. 13

Figure 2.2 Schematic of the XPS chamber depicting the process of the photoelectric effect. 14

Figure 2.3 O 1s XPS data displaying the standard 20 min. Ar^+ sputtering treatment used in this work, in addition to the other surface treatments explored to attempt to further remove the residual oxygen that persisted on the OFHC Cu substrates following sputtering. 20

Figure 2.4 Photos of the nanofabrication cleanroom ALD batch reactor with a silica substrate inside (left), and the arrangement of precursors available to be delivered through the manifold (right) allowing for the deposition TiO_2, HfO_2, and Al_2O_3 films. 23

Figure 2.5 Picture of the reactor used for the partial silylation of SBA-15 (left), the sample holder connected to the feedthrough used for resistive-heating of the sample (center), and set of precision and Swagelok valves (right) used for controlling the dosing pressure and pumping throughput. 25

Figure 3.1 Schematic depicting the surface reaction between TMSDMA and SiO_2. The chemisorption of trimethylsilyl groups occurs on surface hydroxyl nucleation sites resulting in the formation of $(CH_3)_2NH$ as a byproduct. 28

Figure 3.2 Macrographs of a few selected samples used to acquire some of the WCA measurements shown in Table 3.2. From left to right: SiO_2/Si(100) (native oxide, as is), after cleaning with acetone and DI H_2O, and after gas-phase silylation for 24 hours using the procedures described above and experimental conditions listed in Table 3.2. The corresponding WCA measurements for each surface are provided in Table 3.1..... 32

Figure 3.3 Macrograph of SiO_2/Si(100), pretreated by annealing to 1000 K for 15 min., after silylation with TMSDMA using the procedures described above and experimental conditions listed in Table 3.3. The corresponding WCA measurement is provided in Table 3.1..... 34

Figure 3.4 Macrograph of SiO_2/Si(100) after exposure to 8 alternate TMSDMA/H_2O cycles. The corresponding WCA measurement is provided in Table 3.1..... 36

Figure 3.5 Macrographs of a few selected samples used to acquire WCA measurements shown in Table 3.1. From left to right, SiO_2/Si(100) after: RCA cleaning, SiO_2 PE-CVD, and gas-phase silylation with TMSDMA for 15 min..... 37

Figure 4.1 Chemical structures of tetrakis(dimethylamino)titanium (IV) (TDMATi) and tetrakis(dimethylamino)hafnium (IV) (TDMAHf) metalorganic precursors used to conduct TiO_2 and HfO_2 ALD, respectively. These structures were re-drawn using ChemDraw... 41

Figure 4.2 (a) Ta 4f, (b) O 1s, and (c) Si 2p XPS data before and after SiO_2 film growth on Ta foil using PE-CVD, carried out at 473 K for 10 s with SiH_4 and N_2O..... 42

Figure 4.3 Ti 2p (a), O 1s (b), and Si 2p (c) XPS data for the gas-phase TMSDMA-silylated (TMSDMA-G/PE-CVD SiO_2/Si(100), denoted as S) and non-silylated (PE-CVD SiO_2/Si(100), denoted as NS) PE-CVD-grown SiO_2/Si(100) substrates as a function of increasing number of TiO_2 ALD cycles. The raw data are shown as dots and the fitted peaks as lines..... 44

Figure 4.4 Peak areas of the TiO_2 component of the O 1s XPS signal (TiO_2-O 1s XPS) measured for gas- and liquid-phase silylated PE-CVD-grown SiO_2/Si(100) (denoted as TiO_2 ALD/TMSDMA-G/PE-CVD SiO_2/Si(100) and TiO_2 ALD/TMSDMA-L/PE-CVD SiO_2/Si(100), respectively) after depositing TiO_2 films via ALD. The TiO_2-O 1s data are compared to that of a non-silylated substrate (TiO_2 ALD/PE-CVD SiO_2/Si(100)) and are plotted as a percentage of the total O 1s XPS signal (obtained from Figures 4.3 and 4.6) versus the number of TiO_2 ALD cycles conducted. 47

Figure 4.5 Peak areas of the SiO_2-2p and Ti 2p XPS data reported in Figures 4.3 and 4.6 for both gas- and liquid-phase silylated PE-CVD grown SiO_2/Si(100) compared to that of a non-silylated substrate, as a function of the increasing number of TiO_2 ALD cycles conducted. 48

Figure 4.6 Ti 2p (a), O 1s (b), and Si 2p (c) XPS data for the liquid-phase TMSDMA-silylated (TMSDMA-L/PE-CVD SiO_2/Si(100), denoted as S) and non-silylated (PE-CVD SiO_2/Si(100), denoted as NS) PE-CVD-grown SiO_2/Si(100) substrates as a function of increasing number of TiO_2 ALD cycles. The raw data are shown as dots and the fitted peaks as lines..... 49

Figure 4.7 (a) Si and Ti surface atomic-percent composition profiles for both gas- and liquid-phase silylated PE-CVD SiO_2 substrates (TMSDMA-G and -L/PE-CVD SiO_2/Si(100) as a function of increasing number of ALD cycles used to grow TiO_2 films on those surfaces, estimated using the SiO_2-Si 2p and SiO_2-O 1s XPS peak areas in combination with corresponding ASFs. These are contrasted with the results obtained for a non-silylated surface. (b) Average TiO_2 film thickness calculated from the data in panel (a) by assuming layer-by-layer type growth. 50

Figure 4.8 C 1s XPS data for the gas- (a) and liquid- (b) phase TMSDMA-silylated (TMSDMA-G or – L/PE-CVD SiO_2/Si(100); S) and non-silylated (PE-CVD SiO_2/Si(100); NS) substrates as a function of increasing number of TiO_2 ALD cycles. The raw data, shown as dots, were fitted to four peaks (from high to low BE: O-C=O, C=O, C-O-C/C-O-H, and C-C/C-H bonding environments), shown as lines..... 56

Figure 4.9 (a) C 1s XPS peak area and (b) C surface atomic-percent composition profiles for both gas- and liquid-phase silylated TMSDMA-G or -L/PE-CVD SiO_2/Si(100) surfaces as a function of increasing TiO_2 ALD cycles. The data is compared to the results from the non-silylated (PE-CVD SiO_2/Si(100)) substrate..... 57

Figure 4.10 N 1s XPS data for the gas- (a) and liquid- (b) phase TMSDMA silylated (TMSDMA-G or -L/PE-CVD SiO_2/Si(100); S) and non-silylated (PE-CVD SiO_2/Si(100); NS) substrates as a function of increasing TiO_2 ALD cycles. 59

Figure 4.11 Ti 2p (a), O 1s (b), and Si 2p (c) XPS data for the gas-phase TMSDMA-silylated (TMSDMA-G/RCA SiO_2/Si(100), denoted in this figure as S), and non-silylated (RCA SiO_2/Si(100), denoted as NS) RCA-cleaned SiO_2/Si(100) substrates as a function of increasing number of TiO_2 ALD cycles. The raw data are shown as dots and the fitted peaks as lines..... 61

Figure 4.12 Ti 2p (a), O 1s (b), and Si 2p (c) XPS data for the liquid-phase TMSDMA-silylated (TMSDMA-L/RCA SiO_2/Si(100), denoted in this figure as S), and non-silylated (RCA SiO_2/Si(100)), denoted as NS) RCA-cleaned SiO_2/Si(100) substrates as a function of increasing number of TiO_2 ALD cycles. The raw data are shown as dots and the fitted peaks as lines..... 62

Figure 4.13 Si and Ti (a) and C (b) surface atomic-percent composition profiles for both TMSDMA-G and -L/RCA SiO_2/Si(100) surfaces as a function of increasing number TiO_2 ALD cycles conducted. They are compared to the results from the non-silylated (RCA SiO_2/Si(100)) substrate. 63

Figure 4.14 Average TiO_2 film thickness for TMSDMA-G and -L/RCA SiO_2/Si(100) compared to the non-silylated (RCA SiO_2/Si(100)) substrate, estimated using the SiO_2-Si 2p and SiO_2-O 1s XPS peak areas in combination with corresponding ASFs. 65

Figure 4.15 Hf 4f XPS data for the gas- (a) and liquid- (b) phase TMSDMA-silylated (TMSDMA-G or -L/PE-CVD SiO_2/Si(100); S) and non-silylated (PE-CVD SiO_2/Si(100); NS) substrates as a function of increasing number of HfO_2 ALD cycles. The raw data are shown as dots and the fitted peaks as lines. 67

Figure 4.16 Hf 4f (a), O 1s (b), and Si 2p (c) XPS data for the gas-phase TMSDMA-silylated (TMSDMA-G/PE-CVD SiO_2/Si(100); S), and non-silylated (PE-CVD SiO_2/Si(100); NS) PE-CVD-grown SiO_2/Si(100) substrates as a function of increasing number of HfO_2 ALD cycles. The raw data are shown as dots and the fitted peaks as lines. The Hf 4f XPS data in Figure 4.16a is the same as that displayed in Figure 4.15a..... 68

Figure 4.17 Hf 4f (a), O 1s (b), and Si 2p (c) XPS data for the liquid-phase TMSDMA-silylated (TMSDMA-L/PE-CVD SiO_2/Si(100); S), and non-silylated (PE-CVD SiO_2/Si(100); NS) PE-CVD-grown SiO_2/Si(100) substrates as a function of increasing number of HfO_2 ALD cycles. The raw data are shown as dots and the fitted peaks as lines. The Hf 4f XPS data in Figure 4.17a is the same as that displayed in Figure 4.15b. 69

Figure 4.18 (a) Areas of the SiO_2-Si 2p and Hf 4f peaks derived from the XPS data presented in Figures 4.16 and 4.17 for both gas- and liquid-phase silylated PE-CVD-grown SiO_2/Si(100) compared to that of a non-silylated substrate as a function of increasing number of HfO_2 ALD cycles. (b) Si and Ti surface atomic-percent composition profiles calculated from the data in panel (a) in combination with corresponding ASFs..... 71

Figure 4.19 Peak areas of the HfO_2 component of the O 1s XPS signal (HfO_2-O 1s XPS) measured for gas- and liquid-phase silylated PE-CVD-grown SiO_2/Si(100) (denoted as HfO_2 ALD/TMSDMA-G/PE-CVD SiO_2/Si(100) and TiO_2 ALD/TMSDMA-L/PE-CVD SiO_2/Si(100), respectively) after depositing HfO_2 films via ALD. The HfO_2-O 1s data are compared to that of a non-silylated substrate (HfO_2 ALD/PE-CVD SiO_2/Si(100)) and are plotted as a percentage of the total O 1s XPS signal (obtained from Figures 4.16 and 4.17) versus the number of HfO_2 ALD cycles conducted..... 72

Figure 4.20 Average HfO_2 film thickness for TMSDMA-G and -L/PE-CVD SiO_2/Si(100) compared to the non-silylated (PE-CVD SiO_2/Si(100)) substrate, estimated using the SiO_2-Si 2p and SiO_2-O 1s XPS peak areas in combination with corresponding ASFs..... 73

Figure 4.21 C 1s XPS data for the gas- (a) and liquid- (b) phase TMSDMA-silylated (TMSDMA-G or – L/PE-CVD SiO_2/Si(100); S) and non-silylated (PE-CVD SiO_2/Si(100); NS) substrates as a function of increasing number of HfO_2 ALD cycles. The raw data, shown as dots, were fitted to four peaks (from high to low BE: O-C=O, C=O, C-O-C/C-O-H, and C-C/C-H bonding environments), shown as lines. 75

Figure 4.22 (a) C 1s XPS peak area and (b) C surface atomic-percent composition profiles for both gas- and liquid-phase silylated TMSDMA-G or -L/PE-CVD SiO_2/Si(100) surfaces as a function of increasing HfO_2 ALD cycles. The data is compared to the results from the non-silylated (PE-CVD SiO_2/Si(100)) substrate. 76

Figure 4.23 N 1s XPS data for the gas- (a) and liquid- (b) phase TMSDMA silylated (TMSDMA-G or -L/PE-CVD SiO_2/Si(100); S) and non-silylated (PE-CVD SiO_2/Si(100); NS) substrates as a function of increasing HfO_2 ALD cycles. 78

Figure 4.24 Schematic depicting possible chemisorption pathways that may exist between TDMATi and TDMAHf based on differences in the affinity to react with hydroxyl nucleation centers. The byproduct formed in either of these reactions is dimethylamine. 84

Figure 5.1 O 1s (a), C 1s (b), Cu 2p (c) XPS, and Cu LMM AES (d) for OFHC bulk Cu compared to sputter-deposited PVD Cu/PE-CVD-grown SiO_2/Si(100) surfaces (purple). OFHC Cu (CuO_x/Cu) treated with cleaning method 1 (Ar^+ sputtering only, green) is also compared to OFHC Cu (cleaner CuO_x/Cu) cleaned using method 2 (Ar^+ sputtering while rastering, blue). The information for the preparation of the OFHC bulk Cu and PVD Cu/PE-CVD-grown SiO_2/Si(100) samples are located in tables 5.1 and 5.2, respectively. 94

Figure 5.2 O 1s (a), Cu 2p (b), Si 2p (c), and N 1s (d) XPS data for an OFHC Cu (CuO_x/Cu) substrate after a 20 min. Ar^+ sputtering treatment followed by treatment with TMSDMA. 96

Figure 5.3 Ti 2p (a), O 1s (b), and Cu 2p (c) XPS data for OFHC Cu (CuO_x/Cu) substrates treated with (W/) and without (W/o) TMSDMA as a function of increasing number of TiO_2 ALD cycles. 99

Figure 5.4 (a) Cu 2p, O 1s, C 1s, and Ti 2p XPS peak areas for OFHC Cu (CuO_x/Cu) substrates treated with (W/) and without (W/o) TMSDMA as a function the number of ALD cycles used to grow TiO_2 films. (b) Atomic-percent composition profiles estimated from the data in panel (a) in combination with corresponding ASFs. 101

Figure 5.5 Ti 2p (a) and O 1s (b) XPS data for TMSDMA-silylated PE-CVD-grown SiO_2/Si(100) and TMSDMA-treated OFHC Cu (CuO_x/Cu) substrates as a function of increasing number of TiO_2 ALD cycles. 103

Figure 5.6 Ti 2p (a) and O 1s (b) XPS data for unmodified PE-CVD-grown SiO_2/Si(100) and untreated OFHC Cu (CuO_x/Cu) substrates as a function of increasing number of TiO_2 ALD cycles. 105

Figure 5.7 Hf 4f (a), O 1s (b), and Cu 2p (c) XPS data for OFHC Cu (CuO_x/Cu) substrates treated with (W/) and without (W/o) TMSDMA as a function of increasing number of HfO_2 ALD cycles. 107

Figure 5.8 Hf 4f (a) and O 1s (b) XPS data for TMSDMA-silylated PE-CVD-grown SiO_2/Si(100) and TMSDMA-treated OFHC Cu (CuO_x/Cu) substrates as a function of increasing number of HfO_2 ALD cycles. 109

Figure 5.9 Hf 4f (a) and O 1s (b) XPS data for unmodified PE-CVD-grown SiO_2/Si(100) and untreated OFHC Cu (CuO_x/Cu) substrates as a function of increasing number of HfO_2 ALD cycles. 111

Figure 5.10 Ti 2p (a) and Hf 4f (b) XPS peak area profiles on PE-CVD-grown SiO_2 and OFHC Cu (CuO_x/Cu) substrates treated with and without TMSDMA as a function of the increasing number of ALD cycles used to deposit the respective TiO_2 or HfO_2 films. . 112

Figure 5.11 Hf 4f (a) and O 1s (b) XPS data for TMSDMA-treated OFHC Cu comparing cleaning method 1 vs. 2 as a function of increasing number of HfO_2 ALD cycles. 115

Figure 5.12 Hf 4f XPS peak area profiles for TMSDMA-silylated PE-CVD-grown SiO_2/Si(100) and TMSDMA-treated OFHC Cu (CuO_x/Cu) substrates, comparing those that were treated with cleaning methods 1 and 2, as a function of increasing number of HfO_2 ALD cycles. The data presented here was derived from Figure 5.11. 117

Figure 5.13 Cu 2p XPS (a) and Cu LMM AES (b) for the TMSDMA-treated cleaner OFHC Cu (cleaner CuO_x/Cu, method 2) substrate used in the data in Figure 5.11**.** 119

Figure 5.14 Ti 2p (a) and O 1s (b) XPS for TMSDMA-silylated PE-CVD-grown SiO_2/Si(100) and TMSDMA-treated OFHC Cu (CuO_x/Cu) substrates as a function of increasing number of TiO_2 ALD cycles. TMSDMA was reapplied on each surface after every 5 TiO_2 ALD cycles until after the 10^{th} cycle. 121

Figure 5.15 Cu 2p XPS (a) and Si 2p XPS (b) for the TMSDMA-treated OFHC Cu (CuO_x/Cu) substrate, and Si 2p XPS (c) for the TMSDMA-silylated PE-CVD-grown SiO_2/Si(100) substrate used for the data displayed in Figure 5.10, as a function of increasing number of TiO_2 ALD cycles. TMSDMA was reapplied on each surface after every 5 TiO_2 ALD cycles until after the 10^{th} cycle. 123

Figure 5.16 (a) Cu(0)/Cu(I)-Cu 2p, Cu(II)-Cu 2p, CuO_x-O 1s, TiO_2-O 1s, C 1s, and Ti 2p XPS peak areas derived from the XPS data for TMSDMA-treated OFHC Cu (CuO_x/Cu) substrate displayed in Figure 5.14 and 5.15a, as a function of increasing TiO_2 ALD cycles and TMSDMA inhibitor exposures. TMSDMA was reapplied on each surface after every 5 TiO_2 ALD cycles until after the 10th cycle, where "5R1" and "10R2" denote the first and second inhibitor reapplication after the 5th and 10th ALD cycle, respectively. (b) Atomic-percent composition profiles estimated from the data in panel (a) in combination with corresponding ASFs. 125

Figure 5.17 Hf 4f (a) and O 1s (b) XPS for TMSDMA-silylated PE-CVD-grown SiO_2/Si(100) and TMSDMA-treated OFHC Cu (CuO_x/Cu) substrates as a function of increasing number of HfO_2 ALD cycles. TMSDMA was reapplied on each surface after every 2 HfO_2 ALD cycles until after the 8thth cycle. 127

Figure 5.18 Cu 2p XPS (a) and Si 2p XPS (b) for the TMSDMA-treated OFHC Cu (CuO_x/Cu) substrate, and Si 2p XPS (c) for the TMSDMA-silylated PE-CVD-grown SiO_2/Si(100) substrate used for the data displayed in Figure 5.13, as a function of increasing number of HfO_2 ALD cycles. TMSDMA was reapplied on each surface after every 2 HfO_2 ALD cycles until after the 8thth cycle. 129

Figure 5.19 (a) Cu(0)/Cu(I)-Cu 2p, Cu(II)-Cu 2p, CuO_x-O 1s, HfO_2-O 1s, C 1s, and Hf 4f XPS peak areas derived from the XPS data for the TMSDMA-treated OFHC Cu (CuO_x/Cu) substrate, displayed in Figure 5.17 and 5.18a, as a function of increasing HfO_2 ALD cycles. TMSDMA was reapplied on each surface after every 2 HfO_2 ALD cycles until after the 8th cycle, where "2R1", "4R2", "6R3", and "8R4" denote the first, second, third, and fourth inhibitor reapplication after the 2nd, 4th, 6th, and 8th ALD cycle, respectively. (b) Atomic-percent composition profiles estimated from the data in panel (a) in combination with corresponding ASFs. 131

Figure 5.20 (a) SiO_2-Si 2p, Si(0)-Si 2p, SiO_2-O 1s, TiO_2-O 1s, C 1s, and Ti 2p XPS peak areas for the TMSDMA-silylated PE-CVD-grown SiO_2/Si(100) substrate (from Figure 5.15c), as a function of increasing TiO_2 ALD cycles. (b) SiO_2-Si 2p, Si(0)-Si 2p, SiO_2-O 1s, HfO_2-O 1s, C 1s, and Hf 4f XPS peak areas for the TMSDMA-silylated PE-CVD-grown SiO_2/Si(100) substrate (from Figure 5.18c), as a function of increasing HfO_2 ALD cycles. In both cases, the TMSDMA reapplication label, "R", denotes the same information as previously described. 133

Figure 5.21 (a) Hf 4f, (b) O 1s, and (c) Si 2p XPS for TMSDMA-silylated PE-CVD-grown SiO_2/Si(100) after each HfO_2 ALD cycle up to the first two cycles. TMSDMA was reapplied between each ALD cycle. 135

Figure 5.22 Schematic depicting an ideal TiO_2 ALD "supercycle" where an etch-back corrective measure can be utilized to remove defect nuclei from the GS. The amount of material removed should be less than the amount to be deposited during the ALD sequence. In the case of film deposition on the dielectric surface, the defective organosilane monolayer should also be removed so that new trimethylsilyl moieties can adsorb in the following supercycle prior to ALD. 148

Figure 6.1 Schematic depicting two different surface modification steps to alter the density of silanol nucleation centers present on the silica surface. Partial silylation may be employed to reduce the number of Si-OH sites while NaOH etching may be used to enhance them. 154

Figure 6.2 Chemical structures corresponding to each of the labels used to assign peak components in the ^{29}Si and ^{13}C CP/MAS ssNMR data. 157

Figure 6.3 ^{29}Si (a) and ^{13}C (b) CP/MAS ssNMR spectra for gas-phase TMSDMA-silylated SBA-15 as a function of increasing inhibitor exposure time. The raw data are shown as dots and the fitted peaks as lines. 159

Figure 6.4 Relative peak area fractions for the main components of the ^{29}Si CP/MAS ssNMR spectra displayed in Figure 6.4a. Features from two types of Si chemical environments exist, with those associated with hydroxyl groups labeled as Q and those associated with trimethylsilyl groups labeled as M. The former are designated as Q^2 (green, -91.5 ppm), Q^3 (blue, -100.4 ppm), and Q^4 (dark red, -110.0) corresponding to geminal silanol groups, isolated silanol groups, and Si atoms from the SiO_2 bulk, respectively. The latter are designated as M^1 (light red, 15.0 ppm) and M^* (purple, 20.0 ppm) corresponding to Si atoms from trimethylsilyl groups after reacting with isolated silanol sites and those after reacting with geminal sites, respectively. 161

Figure 6.5 ATR-IR spectra for SBA-15 before and after etching with NaOH for 5 min. as a function of increasing [NaOH]. The O-H vibration region between 3750-1400 cm^{-1} is displayed in (a) while that of the Si-O-Si and Si-OH between 1400-550 cm^{-1} is displayed in (b). It should be noted that the scale in panel (a) is approximately 25x smaller than that shown in panel (b). The data was acquired after drying the samples overnight at 423 K. 165

Figure 6.6 (a) Isotherm trend, (b) BET pore size distribution, and (c) various parameters for SBA-15 before and after etching with NaOH for 5 min. as a function of increasing [NaOH]. 167

Figure 6.7 (a) ^{29}Si CP/MAS ssNMR spectra for SBA-15 before and after etching with NaOH for 5 min. as a function of increasing [NaOH]. The raw data are shown as dots and the fitted peaks as lines. (b) Absolute peak areas integrated from the main components of the ^{29}Si CP/MAS ssNMR spectra displayed in panel (a), labeled as Q^2 (green, -89.9 ppm), Q^3 (blue, -98.1 ppm), and Q^4 (red, -108.6) corresponding to geminal silanol groups, isolated silanol groups, and Si atoms from the SiO_2 bulk, respectively..... 168

Figure 6.8 (a) Relative peak area fractions for the main components of the ^{29}Si CP/MAS ssNMR spectra displayed in Figure 6.8b, labeled as Q^2 (green, -89.9 ppm), Q^3 (blue, -98.1 ppm), and Q^4 (red, -108.6) corresponding to geminal silanol groups, isolated silanol groups, and Si atoms from the SiO_2 bulk, respectively. To better understand how the density of specific silanol groups changes as a function of increasing [NaOH], a plot focusing on Q^2 vs. Q^4 is displayed in (b)..... 170

List of Tables

Table 2.1 IMFP values, taken from the QUASES-IMFP-TPP2M software, used to calculate the thickness of SiO_2, TiO_2, or HfO_2 films grown on the various surfaces listed below. 17

Table 3.1 WCA measurements for different Si(100) surfaces after various cleaning treatments. TMSDMA-G and -L denote silylation in the gas and liquid phase using TMSDMA, respectively. 31

Table 3.2 Experimental conditions used for the initial silylation of SiO_2/Si(100) with TMSDMA. 32

Table 3.3 Experimental conditions used for the silylation of SiO_2/Si(100) with TMSDMA following a high temperature cleaning pretreatment at 1000 K for 15 min. 34

Table 4.1 BE, peak area, and FWHM values for the C-C/C-H, C-O-C/C-O-H, C=O, and O-C=O fitted components (of the C 1s XPS data shown in Figure 4.8) provided for the gas-phase TMSDMA-silylated (TMSDMA-G/PE-CVD SiO_2/Si(100)) substrate as the number of ALD cycles used to deposit TiO_2 was increased. 53

Table 4.2 BE, peak area, and FWHM values for the C-C/C-H, C-O-C/C-O-H, C=O, and O-C=O fitted components (of the C 1s XPS data shown in Figure 4.8) provided for the liquid-phase TMSDMA-silylated (TMSDMA-L/PE-CVD SiO_2/Si(100)) substrate as the number of ALD cycles used to deposit TiO_2 was increased. 54

Table 4.3 BE, peak area, and FWHM values for the C-C/C-H, C-O-C/C-O-H, C=O, and O-C=O fitted components (of the C 1s XPS data shown in Figure 4.8) provided for the non-silylated (PE-CVD SiO_2/Si(100)) substrate as the number of ALD cycles used to deposit TiO_2 was increased. 55

Table 5.1 Description of the two cleaning methods applied to the OFHC Cu surfaces used. 90

Table 5.2 Parameters used for the sputter-deposition of Cu films on PE-CVD-grown SiO_2. The average thickness of the sputter-deposited Cu film was approximately 157 nm and the sputtering rate derived from this measurement was 0.05 Å/s. The average was calculated by measuring the thickness at 3 separate points on the substrate surface. 91

Table 5.3 WCA measurements for various Cu substrates after ex-situ cleaning with acetic acid to etch the native oxide layer. 92

Table 6.1 Evolution of SBA-15 mass loss after 5 min. of etching with increasing [NaOH]. 163

Table 6.2 Assignment of the vibrational modes that appear in the ATR-IR data in Figure 6.5 for SBA-15 after treatment with increasing [NaOH]. The relative intensity of each peak is provided next to its wavenumber. 164

ONE

Introduction and Overview

1.1 Device Miniaturization in Semiconductor Manufacturing

The field of microelectronics has undergone remarkable growth in recent decades, driven by a proliferation of scientific discoveries that has profoundly shaped the global technological landscape. Milestones ranging from the inception of the integrated circuit and metal-oxide-semiconductor field-effect-transistor (MOSFET) to more recent breakthroughs in extreme ultraviolet lithography and FinFET technology have all significantly contributed to the advancement of modern device fabrication. As the demand for enhanced device performance continues to grow, so does the need to downscale these devices to enhance their transistor density in accordance with Moore's Law: an empirical observation that states that the number of transistors on an integrated circuit will double approximately every two years.[1] However, as process nodes continue to decrease with each subsequent die shrink and aspect ratios of surface structures become larger, microfabrication has evolved to require a more stringent means of surface patterning requiring film deposition with nanoscale control. Current methods for the deposition of thin films include physical vapor deposition (PVD) techniques such as sputtering and thermal evaporation, as well as chemical approaches such as chemical vapor deposition (CVD) and its subset, atomic layer deposition (ALD).

1.2 Atomic Layer Deposition

The deposition of thin films on solid surfaces plays a crucial role in a myriad of applications, particularly in microelectronics manufacturing but also in the fields of energy storage, nanomaterials, display technologies, and catalysis, to name a few.[2–13] In the former, semiconductor processing steps have developed to demand isotropic deposition on topographically complex surfaces in order to resolve modern challenges of enhancing device performance while consistently shrinking surface patterning dimensions.[14–16] As technology nodes continue to scale down below the 2-nm process, conventional patterning techniques may not be able to keep up with some of the strict guidelines over critical dimensions. One of the most promising approaches to obtain such stringent means of surface patterning with nanoscale precision is by using ALD (invented by Tuomo Suntola in 1974)[17]: a thin-film growth technique that splits the overall chemical reaction involved into two alternating and self-limiting half-cycles, affording a number of advantages such as conformality, uniformity, and thickness control at the Angstrom level.[18]

The reactants in ALD, also referred to as precursors, are never present simultaneously (like they are in CVD) and are instead pulsed individually into the reaction chamber, separated by inert-gas purging steps. These chemical precursors must be carefully selected based on their reactivity and stability such that each half-reaction prepares the surface for the following complementary half-reaction to deposit only the desired material and avoid unwanted side reactions. A schematic of a typical ALD cycle following a pulse/purge sequence of precursor A and B is shown in Figure 1.1 (adapted from ref. 18).

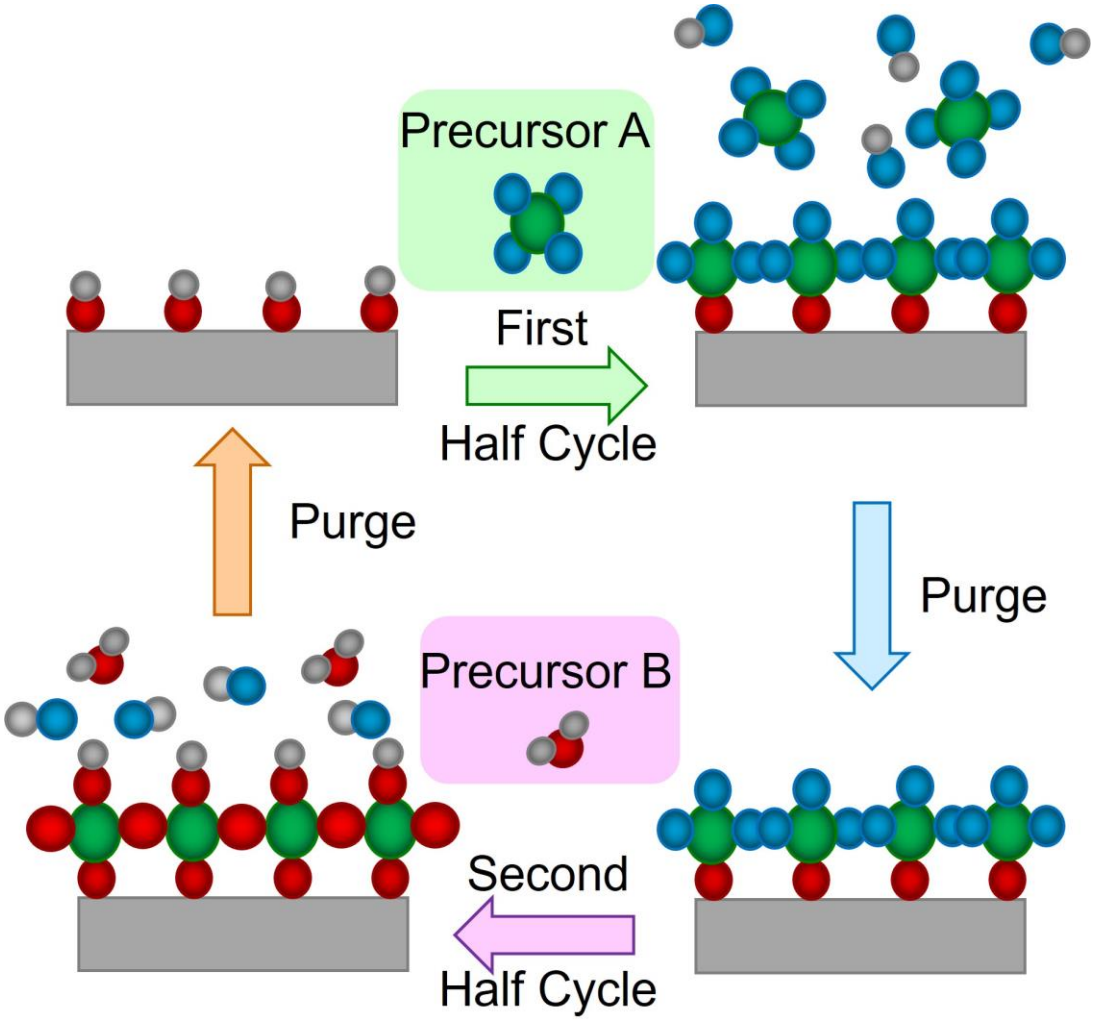


Figure 1.1 Schematic depicting the process of a typical ALD cycle that is comprised of two half-cycles using precursors A and B.[18]

One of the hallmark advantages of ALD lies in its ability to produce thin solid films on flat surfaces using repeating "AB" cycles. A high level of control is achieved by separating the full chemical reaction into two half-cycles this way, resulting in extremely linear film growth dependent only on the number of ALD cycles used rather than the exposure time (as is the case in CVD). An inert purging gas is used between each half-

cycle to remove undesirable excess precursor molecules, which may still remain physisorbed on the surface, and reaction by-products thereby preventing undesirable CVD-type growth that may occur in the following cycle. The process temperature regime for these reactions must fall within the "ALD window" where ideal linear growth-per-cycle (GPC) may be achieved that is reflective of the layer-by-layer nature of ALD (Figure 1.2).[18]

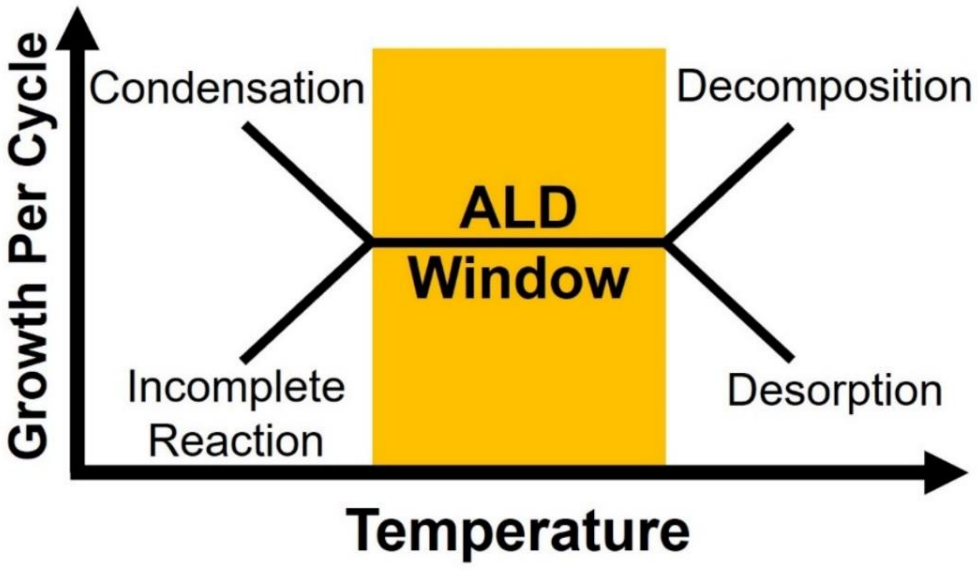


Figure 1.2 Graph depicting the "ALD window" mapping the process temperature where linear film growth occurs.[18] Non-ideal growth occurs beyond the lower and upper temperature limits.

A quintessential example highlighting the capabilities of ALD is the growth of Al_2O_3 films using trimethylaluminum (TMA) and H_2O. The surface chemistry of this model system is quite reactive, with the formation of a strong stable Al-O bond (512 kJ/mol) driving the exothermic reaction.[19] The overall reaction mechanism can be broken down as follows (with asterisks denoting the surface species)[19]:

$$Al\text{-}OH^* + Al(CH_3)_3 \rightarrow Al\text{-}O\text{-}Al(CH_3)_2^* + CH_4 \quad (1)$$

$$Al\text{-}CH_3^* + H_2O \rightarrow Al\text{-}OH^* + CH_4 \quad (2)$$

The resulting Al_2O_3 ALD films deposited with repeated ALD cycles of TMA and H_2O shown in (1) and (2) have been reported to be smooth and conformal to the underlying surface, with typical growth rates falling between 1.1-1.2 Å.[20] These exquisite properties of Al_2O_3 grown this way have allowed it to be used in many technologically relevant applications such as for the gate dielectric in MOSFETs[21] due to low leakage currents and thermo-optical protective coatings in spacecraft due to its insulation properties.[22]

1.3 Area-Selective (AS) Deposition

Another common requirement for device fabrication is area-selectivity, in which films can be selectively grown on specific regions on a substrate, defined as the growth surface (GS), while avoiding deposition on other non-growth surfaces (NGS).[23,24] While this is currently accomplished using top-down photolithography-based surface patterning methods, these are often time-consuming and expensive, require the use of harsh etching agents, and can lead to undesirable effects such as edge placement error resulting in misalignment of stacked layers.[23,25,26] Comparatively, ALD may provide an alternative way to resolve these issues by exploiting differences in the local surface chemistry between two different substrates.

1.3.1 Inherent Selectivity

One method in achieving such area-selectivity arises from the inherent selectivity that may exist between two substrates based on differences in the nature of the surfaces and reactant adsorption energetics.[27–29] While this can be useful as no further processing steps are needed, inherently selective processes not only pose strict limitations in reaction design, but also typically suffer from shorter selectivity windows. Thus, some form of surface modification is usually necessary to achieve spatial control over the lateral arrangement of atoms when considering the AS-ALD of a broader range of materials.

1.3.2 Self-Assembled Monolayers

A more direct approach to AS-ALD involves chemically removing the surface nucleation sites where ALD reactions are initiated on by pretreating the surface prior to ALD through the use of surface modifiers (Figure 1.3). This way, precursor nucleation is inhibited on the NGS while film growth occurs only on the GS.[23]



Figure 1.3 Schematic depicting an example of AS-ALD employing surface modifiers as inhibitors to passivate the NGS prior to ALD, resulting in film deposition on the GS.[23]

One of the most common examples of these modifiers are self-assembled monolayers (SAMs), which have been extensively employed to spatially direct film deposition during ALD processes in an area-controlled manner.[30–32] These organic molecules can spontaneously form a well-organized and densely-packed network of amphiphilic chains due to the high degree of Van der Waals intermolecular interactions that exist between the non-polar carbon backbones of these molecules.[33] However, one major drawback with using SAMs is their low volatility, which may prevent them from being easily integrated into vapor-phase manufacturing processes such as those used for microelectronics fabrication. In addition, due to their bulky nature the efficacy of SAMs in surface patterning processes is diminished around high-aspect ratio features as they may block film growth on not only the NGS but also the GS as well, likely by physically preventing the chemisorption of the precursor onto the nucleation sites of the GS. While the spontaneous and self-assembly nature of SAMs can be useful, it has become more imperative in recent years to find another approach due to the drawbacks described above.

1.3.3 Small-molecule Inhibitors

Small-molecule inhibitors (SMIs) are alternative surface modifiers that have recently garnered interest due to the ease with which these molecules can be vaporized and delivered in the gas phase.[34–36] Unlike SAMs, SMIs typically possess high vapor pressure and less steric hinderance compared to their longer-chained counterparts, making them excellent for controllable vapor dosing to passivate substrates with small pitch sizes and high-aspect ratio features. Moreover, SMIs afford chemical selectivity through the

formation of strong covalent bonds directly with surface nucleation centers, rendering them unavailable for further chemical reactions. One way of implementing SMIs is via silylation, a method to passivate a surface by functionalizing it with substituted silyl moieties. The SMI *N*-(trimethylsilyl)dimethylamine (TMSDMA; also referred to as (dimethylamino)trimethylsilane, DMATMS, or *N*,*N*-dimethyltrimethylsilylamine) was employed as a surface modifier for the experiments conducted in this work (Figure 1.4). The chemistry of SiO_2 surface passivation using this silylation agent involves the attachment of trimethylsilyl functional groups ($-Si(CH_3)_3$) to chemically occupy silanol (Si-OH) nucleation centers, the same hydroxyl nucleation sites that are consumed in ALD reactions.

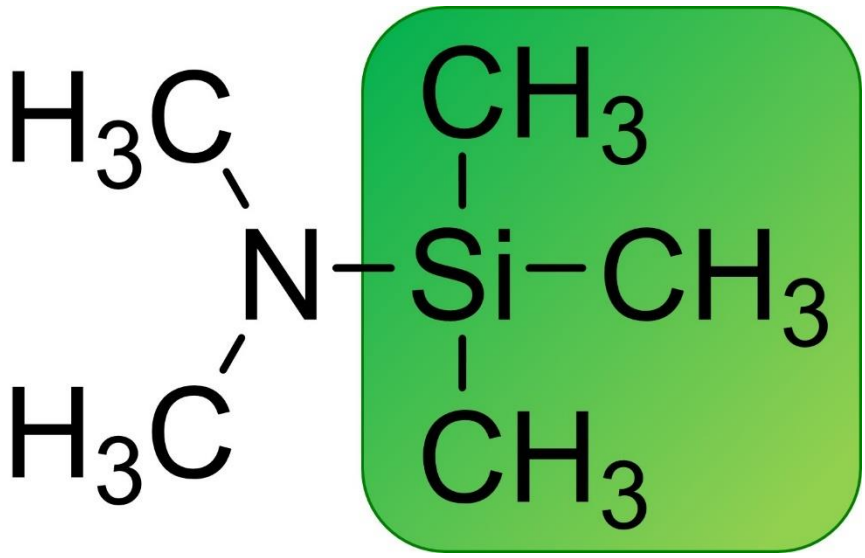


Figure 1.4 Structure of the *N*-(trimethylsilyl)dimethylamine (TMSDMA) inhibitor (ChemDraw) used for the silylation reactions in this dissertation. The green box highlights the trimethylsilyl moiety that covalently bonds to surface nucleation sites on SiO_2 to generate an organosilane passivating monolayer.

1.4 Reaction Phase

The media that the passivation reaction is carried out is vital to achieve control over the surface modification step. Solution-phase methods can suffer from a number of disadvantages such as long processing times up to 24-48 hrs., potentially undesirable solvent effects, and deterioration in the quality of the passivating layer due to precursor aggregation prior to adsorption.[37,38] Additionally, a liquid-phase environment provides little control over the reaction and can result in the formation of defects in the organosilane monolayer.[39–41] Besides this, liquid-phase silylation is not compatible with in-situ manufacturing steps used in the microelectronics industry. These drawbacks may be removed altogether by conducting the silylation step in the gas phase under a controlled contaminant-free environment, which may form a passivating layer with a lower degree of defects and impurities.

1.5 Dissertation Objectives

The primary goal of this dissertation was to prove that in-situ gas phase silylation was advantageous over traditional liquid-phase methods by evaluating the passivation efficacies achieved using both methods. The first comprehensive X-ray photoelectron spectroscopy (XPS)-oriented study directly comparing the impact of phase on the silylation efficacy of silica surfaces using TMSDMA is presented in this dissertation. The results herein demonstrate that the degree of passivation achieved in the gas phase is similar to that of the liquid phase while still affording the unique advantage of the ability to be integrated in microelectronics processing. A lower carbon content in the monolayers

formed in the gas phase was also observed, indicative of higher controllability over its formation with fewer undesirable impurities that get incorporated within. The higher controllability over the silylation reaction in the gas-phase also possesses significant implications in other fields such as heterogeneous catalysis. Finally, the gas-phase silylation scheme was evaluated in the context of AS-ALD of metal oxides using copper and silica surfaces. To the best of our knowledge, this work is the first to directly investigate the interaction between TMSDMA and copper substrates using XPS.

The research presented in this dissertation is divided into 7 chapters. Chapter 1 introduced relevant background information and provided an outlook as to how the scope of this work fits in the context of AS-ALD. Chapter 2 describes the vacuum systems and experimental procedures used in these studies. Chapter 3 introduces the results of the initial gas-phase silylation trials performed, which assisted with elucidating the correct passivation scheme that would be finally employed. Chapter 4 focuses on evaluating the passivation efficacy for gas- vs. liquid-phase silylated silica surfaces against titania or hafnia ALD using two different sample cleaning procedures. Chapter 5 assesses the application of the gas-phase silylation process for AS-ALD on copper vs. silica blanket substrates using titania or hafnia ALD, as well as evaluating the impact of multiple TMSDMA reapplications between ALD cycles on both surfaces. Chapter 6 explores surface modification of mesoporous silica powers to control the nucleation site (silanol) density by using gas-phase silylation and ex-situ chemical etching processes. Chapter 7 provides an overall summary of this work as well as a discussion on prospective directions. These include continuing the research discussed in Chapter 5 to implement ALD

"supercycles" using etch-back corrective measures in the form of Ar^+ sputtering to mitigate and remove undesirable defect nuclei from the GS, evaluating next-generation interconnect materials such as cobalt and ruthenium as potential GS metals for AS-ALD applications, and applying the surface modification steps carried out on the mesoporous silica powders discussed in Chapter 6 to flat silica substrates.

TWO

Experimental

2.1 Introduction

The research carried out in this dissertation can be categorized into two types. The majority of the work done in this dissertation was focused on flat substrates characterized inside an ultra-high vacuum (UHV) system, detailed in section 2.2. Secondary experiments were performed on mesoporous Santa Barbara Amorphous-15 (SBA-15, ACS Material) powders using surface modification procedures described in section 2.3, some of which were carried out inside an ALD batch reactor.

2.2 Ultra-High Vacuum System

The studies on flat substrates reported in this work were conducted in a stainless-steel UHV dual-chamber system (named Union Carbide (UC)) equipped with an X-ray photoelectron spectrometer (XPS) and PHI rare-gas ion gun for Ar^+ sputtering (Figure 2.1), described elsewhere.[42,43] The base pressures for the primary and auxiliary chambers were 4×10^{-9} Torr and 1×10^{-8} Torr, respectively, established by evacuating the chambers using two separate turbomolecular pumps (backed with individual mechanical pumps capable of pumping down to approximately 10 mTorr). A manipulator rod was used to transfer the sample between the two chambers. This allowed for vapor dosing of the silylation agent in the auxiliary chamber and XPS analysis in the clean primary chamber without needing to

expose the sample to atmospheric conditions during the entire preparation and characterization process. The sample temperature was monitored using a K-type thermocouple secured between the sample and metallic clips that fastened the sample onto the tantalum heating mount underneath it. The sample was capable of resistive heating up to approximately 1000 K when liquid nitrogen (LN_2) was used to prevent overheating the manipulator rod.

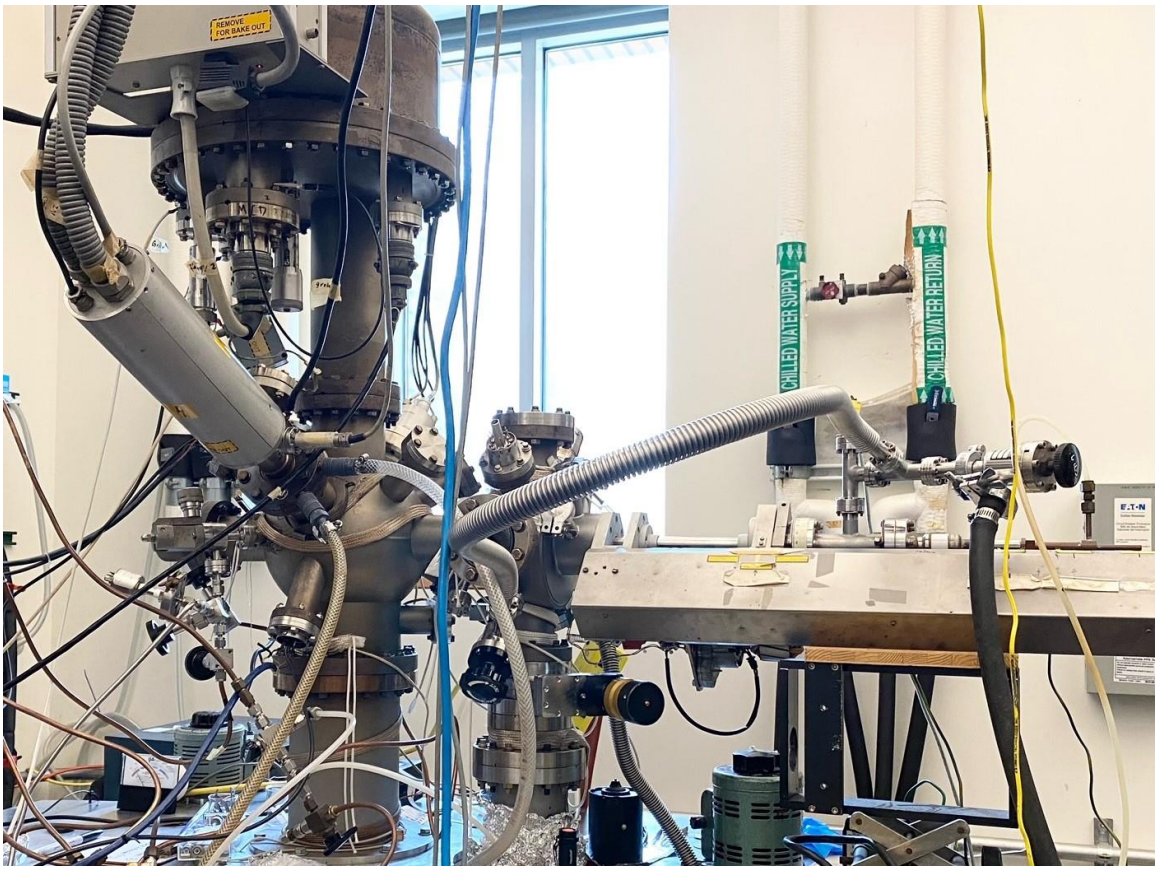


Figure 2.1 Photo of the UHV chamber (UC System) used to conduct the experiments discussed in this dissertation.

2.2.1 X-ray Photoelectron Spectroscopy

XPS is a surface sensitive technique that provides information on surface elemental composition, oxidation state, and speciation within approximately the first 10 nm.[44] The process of XPS (sometimes referred to as electron spectroscopy for chemical analysis, ESCA) is based on the photoelectric effect, which is defined as the ejection of electrons off a surface due to bombardment with incident electromagnetic radiation (Figure 2.2).[44]

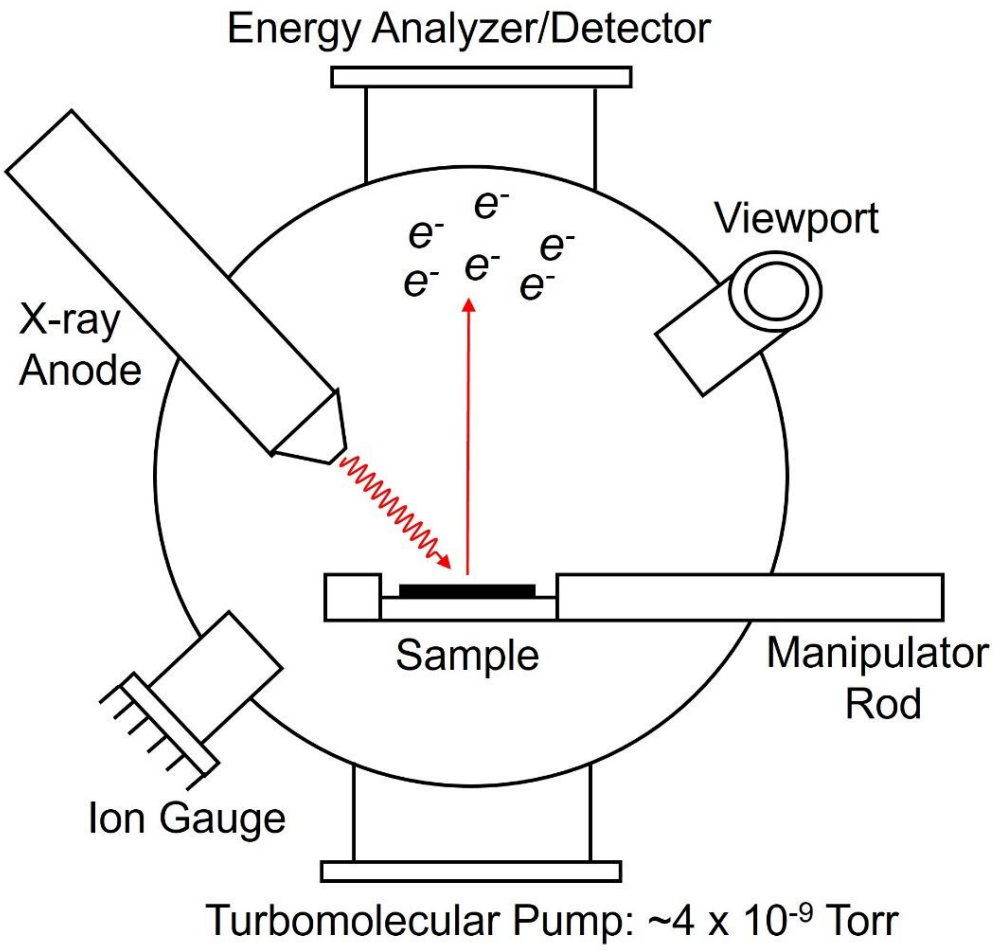


Figure 2.2 Schematic of the XPS chamber depicting the process of the photoelectric effect.

The kinetic energy of the emitted photoelectrons is measured after being collected into the energy analyzer. The binding energy (BE) of the photoelectron, defined as the minimum energy needed to remove an electron it's orbital, can be calculated using the Einstein relationship shown in equation (1) where E_b is the electron binding energy, $h\nu$ is the X-ray photon energy, E_k is the electron kinetic energy, and Φ is the spectrometer work function.[44]

$$E_b = h\nu - (E_k + \phi) \quad (1)$$

As every element exhibits a distinct set of electron BEs, a "fingerprint" of photoelectron lines unique for that particular element is produced. XPS signals can therefore be used to identify unknown elements. The peak intensities are typically proportional to their corresponding surface concentration, while shifts in binding energy provide useful information regarding changes in oxidation state.

The XPS data presented here were acquired using a non-monochromatized Al-Kα excitation source (hv = 1486.6 eV) and a Leybold EA-11 hemi-spherical energy analyzer equipped with a multi-channel detector. A fixed pass energy of 100.8 eV was used for both the survey and high-resolution scans. XPS peak positions could be determined with an accuracy of 0.1 eV and are reported as "BE" in the spectra. A linear fit correction was applied to the XPS data using a plot of experimental vs. theoretical BE values such that the Cu 2p XPS peak position could be fixed to a standard value of 932.4 eV. In the case of the SiO_2/Si(100) samples, an additional calibration step was applied to displace the binding

energies to reported values for either the Si 2p signal of SiO_2 at 103.3 eV or the Si 2p signal of Si(0) at 99.3 eV depending on the surface modification step that was used (plasma or chemical cleaning).[45]

The XPS data were analyzed using the CasaXPS software (version 2.3.23PR1.0) by first applying a Shirley-type background and then peak-fitting each component using a line shape of Gaussian (70%): Lorentzian (30%) (GL:30) composition for the C 1s, Si 2p, Cu 2p, Ti 2p, and Hf 4f XPS; a line shape of GL:50 was used for the O 1s XPS.[46,47] Peak positions and widths were constrained when fitting the data from each set of experiments to minimize the number of adjustable parameters. In the case of elements that exhibit spin-orbit coupling, the peak positions and area ratios between the two states were fixed using the reported electron degeneracy of each state and the spin-orbit splitting energy difference between the two states.[48] Surface atomic-percent compositions were approximated by dividing the integrated XPS peak intensities by their appropriate atomic sensitivity factors (ASFs; C 1s=0.25, O 1s=0.66, Si 2p=0.27, Cu 2p=6.3, Ti 2p=1.8, and Hf 4f=2.05) followed by reporting the corrected area for each element as fractions of the total area comprising the surface.[49] Film thicknesses were estimated by using a layer-by-layer growth model (assumed), a combination of the attenuation of the SiO_2-Si 2p, Si(0)-Si 2p, or SiO_2-O 1s XPS signals (depending on plasma or chemical cleaning), and electron inelastic mean free path (IMFP) values using the QUASES-IMFP-TPP2M program (Ver. 3), based on those reported in the literature.[50] This information is summarized in Table 2.1 below.

Table 2.1 IMFP values, taken from the QUASES-IMFP-TPP2M software, used to calculate the thickness of SiO_2, TiO_2, or HfO_2 films grown on the various surfaces listed below.

Surface	Material	XPS Signal	IMFP / Å
Ta Foil	SiO_2	Ta_2O_5-Ta $4f_{7/2}$	39.10
PE-CVD SiO_2	TiO_2	SiO_2-Si 2p	26.73
		SiO_2-O 1s	20.07
	HfO_2	SiO_2-Si 2p	20.75
		SiO_2-O 1s	15.68
RCA SiO_2	TiO_2	Si(0)-Si 2p	26.79
		SiO_2-O 1s	20.07

These calculations were carried out by applying a modified version of the Beer-Lambert treatment, commonly used to approximate the thickness of an oxide overlayer, to the XPS peak intensities of the substrate as shown in equation (2).[51]

$$\frac{I}{I_0} = e^{\frac{-d}{\lambda}} \quad (2)$$

2.2.2 Preparation of Flat Substrates

In the case of the silica samples, the 1 cm^2 Si(100) (approximately 1 nm native oxide) used in most studies were cut from commercial silicon wafers (Si-Tech) and sonicated in acetone for 15 min. prior to any experiment. After a 1 min. DI water and acetone rinse, the samples were treated with one of two ways to further clean the surface.

The first method consisted of cleaning the wafers using a Radio Corporation of America (RCA) cleaning protocol described elsewhere.[52,53] Briefly, samples were

sequentially submerged in nanostripping, dilute HF etching, and standard clean (SC)-1 and SC-2 solutions. For the nanostripping treatment, a 3:1 H_2SO_4:H_2O_2 room-temperature mixture was used as a preliminary step to remove organic residues from the surface. This was followed by a 1:20 HF:Milli-Q H_2O room-temperature treatment to etch the native oxide layer resulting in a hydrogen-terminated surface. Afterwards, a 1:1:4 NaOH:H_2O_2:Milli-Q H_2O treatment at 353 K (SC-1) was applied to grow a fresh native oxide layer that possessed fewer impurities and was highly hydroxylated. Finally, a 1:1:4 HCl:H_2O_2:Milli-Q H_2O treatment at 353 K (SC-2) was used to remove any remaining ionic contaminants that may have been introduced in the previous step. The wafers were submerged in a Milli-Q H_2O bath for 10 min. between each treatment and were given a final rinse with a Milli-Q H_2O stream for 1-2 min. before being dried under an N_2 flow. Ultimately, the parameters most critical to generating a clean hydroxylated silica surface were the nanostripping and SC-1 steps. It is noted here that treatment in piranha solution (heated nanostripping solution) is also known to generate a clean hydroxylated surface;[54] however, the additional dilute HF etching and SC-2 procedures in the RCA protocol were believed to be sufficient to assist with further sample cleaning, providing a more stringent means to remove surface impurities.

In the second surface preparation process, plasma enhanced (PE)-CVD with SiH_4 (400 mTorr) and N_2O (900 mTorr) was used to deposit fresh SiO_2 films at a sample temperature of 473 K. The plasma was generated using a remote radio-frequency (15.6 MHz) helical resonator source, allowing for SiO_2 films (4.5 nm thick) to be grown in 10 s when using a power setting of 10 W.

Similarly for the copper samples, the 1 cm^2 Cu used in these studies were cut from commercial oxygen-free high-conductivity (OFHC) Cu (McMaster-Carr, 99.99% Cu content) and initially sonicated in acetone and ultrapure (200 proof) ethanol for 15 min. The samples were immersed in pure glacial acetic acid (Sigma Aldrich, 99.7+% purity) for at least 5 min. to etch the native oxide layer, followed by a 1-2 min. ultrapure ethanol rinse. Afterwards, they were transferred into the load-lock (rough vacuum) of the UHV apparatus within 2 min., the preparation chamber (1×10^{-8} Torr) within 3 min., and to the XPS chamber (4×10^{-9} Torr) within 8 min.; the short transfer times for this operation were critical to minimize re-oxidation of the metal. The OFHC Cu substrates were then Ar^+ sputtered in-situ for 20 min. at 3×10^{-6} Torr to further remove oxygen, which was the final cleaning treatment applied to the samples.

It is also noted here that in addition to the 20 min. Ar^+ sputtering treatment, alternative methods for cleaning the OFHC Cu substrates were also explored in order to attempt to fully remove the residual surface oxygen. These included Ar^+ sputtering after adjusting the focus to collimate the ion beam on the sample, sputtering at a higher pressure, and attempting to chemically remove oxygen through CO exposures to reduce the surface. The O 1s XPS results for both the standard 20 min. Ar^+ sputtering (used in this work), along with these alternative treatments are shown in Figure 2.3. It should be clarified that no further experiments involving TMSDMA or ALD were ever conducted using the alternative surface cleaning procedures described here, as most of these other options were explored during the later stages of this project. Future work will be needed to optimize and implement these cleaning procedures to the OFHC Cu substrates used here.

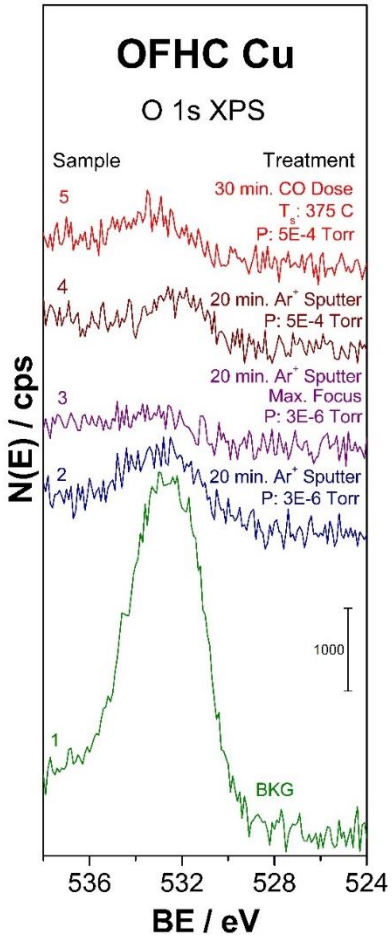


Figure 2.3 O 1s XPS data displaying the standard 20 min. Ar^+ sputtering treatment used in this work, in addition to the other surface treatments explored to attempt to further remove the residual oxygen that persisted on the OFHC Cu substrates following sputtering.

Figure 2.3 demonstrates that attenuation of the O 1s XPS signal occurs after a 20 min Ar^+ sputtering treatment; however, some surface oxygen still remained present. Some of the alternative cleaning methods described above displayed lower O 1s XPS signals and may be useful to apply to OFHC Cu substrates in the future. The 20 min. Ar^+ sputtering procedure (blue trace) was used as the final cleaning step for the OFHC Cu substrates

(discussed in Chapter 5). It is also noted here that while the residual O 1s signal is likely due to CuO_x, it is also possible that it arises from atomic oxygen adsorbed on the surface. The surface cleanliness of sputter-deposited Cu/PE-CVD SiO_2 samples was also assessed (shown later in Chapter 5) but ALD was not conducted on these surfaces.

Finally, surface hydrophilicity/hydrophobicity measurements were used to qualitatively assess the sample cleanliness ex-situ after surface modification, by carrying out water contact angle (WCA) measurements using the software ImageJ. 4-6 measurements were made on different locations on the substrate surface using approximately 100 uL droplets to achieve an overall measurement error of ± 2°.

2.2.3 Silylation Reaction

Clean silica surfaces were functionalized in either the gas or liquid phase using TMSDMA (Sigma Aldrich, 98% purity). For the gas phase studies, TMSDMA was purified in-situ using multiple freeze-pump-thaw cycles prior to being dosed into the UHV chamber via a leak valve. The liquid (room temperature) could be easily dosed directly into the chamber without heating due to its high vapor pressure. To enhance the silylation processing, the gate valve to the turbomolecular pump was first closed and the butterfly valve to the roughing pump then opened to establish a new base pressure of approximately 150 mTorr. This way, both the PE-CVD-grown and RCA-cleaned silica substrates could be silylated in only 15 min. while holding the chamber pressure at 300 mTorr, as opposed to a 24-hr. reflux process used for liquid-phase silylation method. The leak and roughing pump valves were then closed off for an additional 15 min. to trap the inhibitor molecules

inside the chamber and ensure surface saturation. The sample temperature was kept at 423 K and the chamber was heated to 373 K to minimize condensation on its walls. Afterwards, the chamber was pumped down using the roughing pump for 15 min. and the gate valve to the turbomolecular pump opened to re-establish the original base pressure. Applying the same TMSDMA treatment on Cu substrates did not result in surface passivation, indicative that silylation was ineffective on those surfaces (discussed in Chapter 5).

For the liquid-phase functionalization process, the treated silica wafers were placed in clean, dry round-bottom flasks containing 5 mL of TMSDMA and refluxed at 360 K for 24 hours in an inert N_2 environment. Silylation of Cu substrates was not tested this way.

2.2.4 ALD Film Growth

Metal oxide ALD was conducted in a class-100 nanofabrication cleanroom facility using a commercial Savannah Ultratech/Cambridge Nanotech batch reactor connected to a manifold for gas delivery (Figure 2.4). An alternating precursor sequence using tetrakis(dimethylamino) titanium(IV) (TDMATi; Strem Chemicals, 99% total purity) or tetrakis(dimethylamino) hafnium(IV) (TDMAHf; Strem Chemicals, 98+% total purity and 99.99+% Hf purity) and deionized (DI) H_2O with dry N_2 purging in-between was used to deposit titanium dioxide (TiO_2) or hafnium dioxide (HfO_2) films. The time sequences used for these processes were as follows: 0.10 s/20 s/0.010 s/20 s for TDMATi or TDMAHf/N_2/H_2O/N_2. The metalorganic precursor was maintained at a temperature of 338 K and delivered using a bubbler and a N_2 carrier gas flow rate of 20 sscm. The sample and chamber temperatures were kept at 373 K and the manifold at 388 K during ALD.

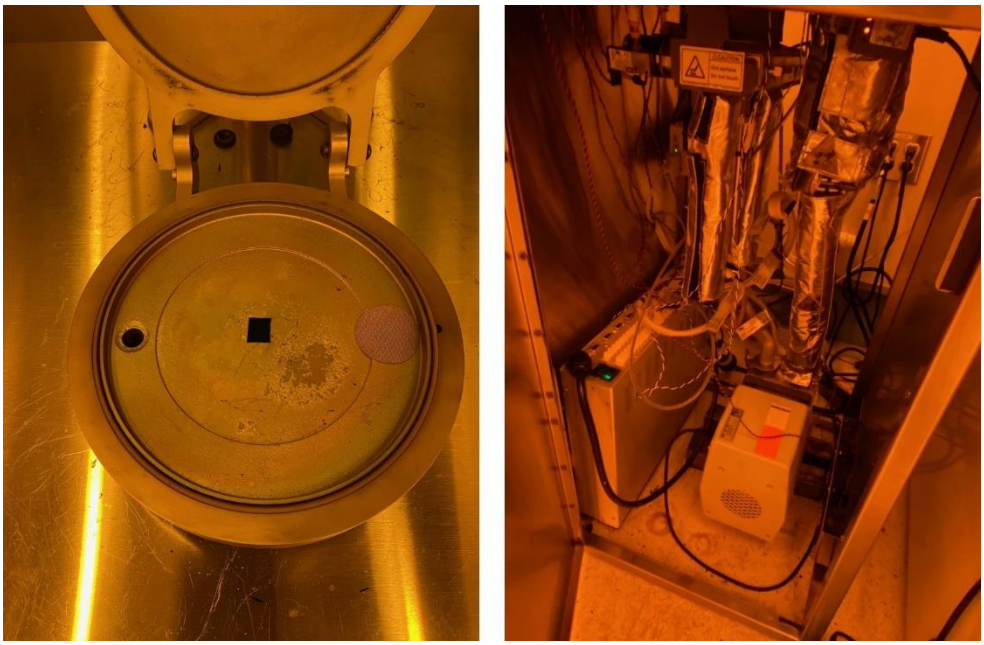


Figure 2.4 Photos of the nanofabrication cleanroom ALD batch reactor with a silica substrate inside (left), and the arrangement of precursors available to be delivered through the manifold (right) allowing for the deposition TiO_2, HfO_2, and Al_2O_3 films.

2.3 Surface Modification of SBA-15

Surface modification of commercial mesoporous SBA-15 was carried out using two distinct methods in order to control the density of silanol nucleation centers. In the first treatment, in-situ partial silylation using TMSDMA in the gas phase was used to reduce the density of silanol nucleation sites, described in section 2.3.1. For the second type of modification, SBA-15 was etched ex-situ using sodium hydroxide (NaOH) to enhance the density of surface hydroxyl groups as detailed in section 2.3.2.

2.3.1 Silanol Density Reduction

The silylation of SBA-15 was conducted in a home-built customizable reactor designed using a 2.75 inch 5-way CF flange as the body (Figure 2.5, left). The reactor was evacuated using a mechanical pump to establish a base pressure of approximately 45 mTorr. About 50 mg of the powder sample was uniformly spread in a sample holder tray designed from Ni foil, which was attached to a feedthrough using Ta wires. The sample was resistively heated using a transformer to channel current through a pair of Cu wires to the Ni tray (Figure 2.5, center). A stainless-steel mesh cover was spot-welded to the sample tray prior to attaching the feedthrough to the reactor in order to prevent the powder from escaping when pumping and purging. The sample and chamber were heated to 473 K and 373 K, respectively, for 2 hrs. prior to the start of any experiment. The sample temperature was monitored using a K-type thermocouple spot-welded to the bottom of the Ni tray near the center. A pair of precision valves were used to control the extent of the silylation reaction (Figure 2.5, right). The first valve, connected to the silylation agent, was capable of reducing the amount of inhibitor introduced into the reactor. The second valve, attached to the pump-end, enabled control over the pumping throughput. This dual-valve system facilitated controllable dosing of the volatile inhibitor, conducted at a fixed pressure of approximately 50 mTorr using TMSDMA (room temperature) with dosing times varying from 1 min. up to 2 hrs. After a 2-hr. heating pretreatment to remove adventitious carbon, approximately 50 mg of SBA-15 could be silylated at a sample temperature of 423 K using this setup.



Figure 2.5 Picture of the reactor used for the partial silylation of SBA-15 (left), the sample holder connected to the feedthrough used for resistive-heating of the sample (center), and set of precision and Swagelok valves (right) used for controlling the dosing pressure and pumping throughput.

2.3.2 Silanol Density Enhancement

NaOH etching of SBA-15 was conducted ex-situ by first dispersing 200 mg of SBA-15 in 15 mL of DI H_2O. 15 mL of NaOH solutions of increasing concentration were slowly added to obtain a final 30 mL solution of a desired etching concentration (0.1, 1, 2, 3, or 4 M). The etching reaction proceeded for 5 min. after mixing the solutions. The samples were then centrifuged for 7 min. at 9000 revolutions per minute (rpm) to remove the solvent, after which they were then washed with DI H_2O three times and EtOH twice (centrifuged in between each washing step). It should be noted that the samples were continuously etched for approximately 7 additional min. during the first centrifugation step since they still remained in the etching solution for that initial process. While the actual total etching time is approximated to be 12 min., some minor variations (less than 30 s) in etching time may exist as a result of the time required to transfer the sample to the centrifuge. For the sake of simplicity, the NaOH etching time will be referred to as 5 min. in later chapters. Finally, the powders were dried overnight at approximately 423 K to remove residual water prior to any analysis.

2.3.3 Analysis of Silanol Density

Characterization of the modified SBA-15 surfaces was primarily conducted using ^{29}Si and ^{13}C solid-state nuclear magnetic resonance (ssNMR) spectroscopy. Cross-polarization (CP) magic-angle-spinning (MAS) ssNMR experiments were conducted at 14.1 T (^{1}H frequency 600 MHz) on a Bruker Avance NEO 600 spectrometer, which was equipped with a 4-mm MAS probe that spun at 10 kHz. 4096 data points with a dwell time of 10 μs (spectral width 50 kHz, total acquisition time 41.01 ms) were collected for each spectrum. 20480 transients were coadded resulting in a total experiment time of 17 hrs. and 18 min. The ^{29}Si and ^{13}C CP/MAS data were calibrated to sodium trimethylsilylpropanesulfonate (1.46 ppm) and adamantane (38.48 ppm) references, respectively. The ssNMR data was processed and fitted using OriginPro 9 software. Peak positions and widths were constrained to minimize the number of adjustable parameters during fitting.

Secondary analysis using attenuated total reflection-infrared (ATR-IR) spectroscopy was performed using a Nicolet iS50 advanced KBr gold spectrometer equipped with both diamond ATR and transmission modes. The spectral range for data acquisition spanned between 4000-400 cm^{-1} and a total instrument resolution of 0.09 cm^{-1} was possible. The acquisition resolution was set to 4 cm^{-1} and a total of 256 scans were collected for each spectrum during the analysis of the powder samples. Brunauer-Emmett-Teller (BET) analysis was also used to examine changes in the SBA-15 pore size distribution as a function of the applied etching treatment.

THREE

Initial Studies on Gas-phase Silylation using TMSDMA

3.1 Introduction

Small-molecule inhibitors (SMIs) encompass a broad set of molecules that interact with surfaces through the formation of strong covalent bonds with surface nucleation sites, unlike the dynamic self-assembly nature of self-assembled monolayers (SAMs) typically used in liquid-phase reactions. Furthermore, as technology nodes continue to shrink towards the 2-nm process and beyond, the bulky nature and low thermal stability of SAMs make them incompatible with vapor phase processes due to their geometric steric hindrance around high-curvature edges of 3-D nanostructures.[55] The high volatility and ease of vaporization of SMIs on the other hand make them excellent choices for high-volume semiconductor manufacturing. One such promising SMI is the aminosilane inhibitor TMSDMA, which has been demonstrated to achieve faster surface saturation, lower lateral swelling, and a denser trimethylsilyl monolayer compared to other molecules with similar structures, such as hexamethyldisilazane.[56,57]

It is well understood that organosilane molecules can chemisorb on and consume surface hydroxyl groups of silica to passivate the surface, making those nucleation sites unavailable for subsequent chemical reactions to occur on.[58] Silylation is a process to attach $-Si(CH_3)_3$ functionalities to the surface (Figure 3.1), which has previously been well-established for glass and other silicon oxide substrates in the liquid-phase.[59]

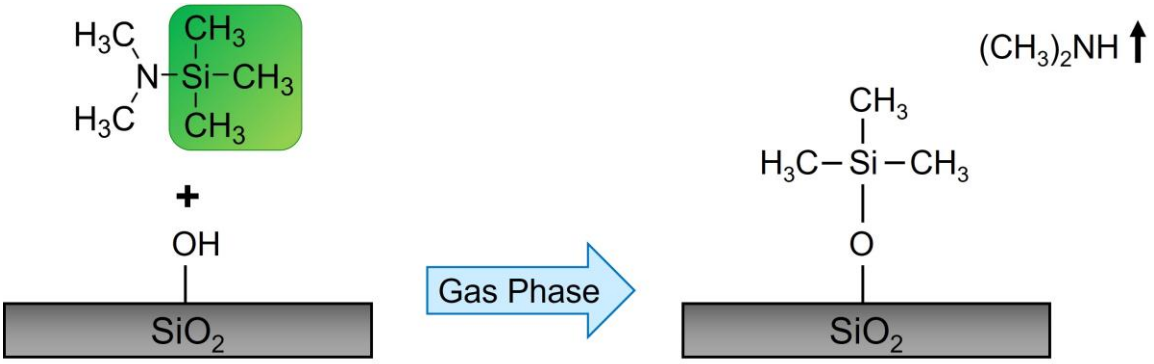


Figure 3.1 Schematic depicting the surface reaction between TMSDMA and SiO_2. The chemisorption of trimethylsilyl groups occurs on surface hydroxyl nucleation sites resulting in the formation of $(CH_3)_2NH$ as a byproduct.

The silylation reaction of TMSDMA on SiO_2 has been reported to initiate through the physisorption of the aminosilane molecule onto the silica surface, likely facilitated through intermolecular forces of attraction. These include hydrogen bonding between the acidic hydrogen atoms of surface hydroxyl nucleation centers to nitrogen atoms within the dimethylamine moiety of the inhibitor, and dipole-dipole interactions between the partial positively charged methyl carbons attached to the amine to surface oxygen in SiO_2. Following this is the chemisorption of the $Si(CH_3)_3$ group onto Si-OH sites in an acid/base-type fashion through the heterolytic cleavage of the Si-N bond (350 kJ/mol); the reaction on silanol sites rather than siloxane sites is more favorable based on the lower bond dissociation energy for O-H (460 kJ/mol) compared to O-Si (799 kJ/mol), leading to the loss of dimethylamine as a reaction byproduct.[60,61] This process is depicted in Equation 1 below, where the asterisks denotes the surface species that are involved.

$$Si\text{-}OH^* + (CH_3)_2NSi(CH_3)_3 \rightarrow SiO\text{-}Si(CH_3)_3^* + (CH_3)_2NH \quad (1)$$

In fact, TMSDMA has been demonstrated to effectively passivate all types of hydroxyl nucleation centers (isolated, geminal, and vicinal groups) that exist on SiO_2 against ALD reactions regardless of their specific arrangement, resulting in the formation of organosilane passivating monolayers with high trimethylsilyl densities.[56,61] Previous studies from our group have also already reported the design of a simple process for AS-ALD using liquid-phase silylation to first render all nucleation sites unavailable for chemisorption, followed by selectively removing part of those organosilane functionalities using an ultra-violet/ozonolysis treatment to reinstate reactivity for subsequent ALD film growth.[52,62,63] As aforementioned, the use of SMIs to perform silylation steps in the gas phase affords the key advantage of the ability to be directly incorporated with other gas-phase microelectronics processing steps. Therefore, TSMDMA was selected as an ideal surface modifier for passivating silica via silylation in the gas phase.

The effectiveness of the cleaning treatments and subsequent silylation of silicon oxide surfaces was assessed using water contact angle (WCA) measurements, a qualitative proxy to assess the hydrophilicity/hydrophobicity after subsequent chemical reactions thus providing insight into the hydroxyl group density. This was particularly useful in obtaining preliminary and quick insight into the silica passivation efficacy as opposed to XPS; the latter provided limited information as no new elements were added to the surface, making it challenging to differentiate those from the underlying surface. After applying the cleaning treatments, the newly acquired surfaces become hydrophilic in nature resulting in

a higher degree of hydrogen bonding interactions that occurs between the hydrogen atoms of the water molecules in the droplet and the hydroxyl groups on the surface. As the surface transitions to becoming more hydrophobic in nature after silylation, water molecules are repelled due to a lower degree of hydrogen bonding with the surface. These molecules are repelled by the non-polar organic ligands of the trimethylsilyl groups and instead have a higher tendency to hydrogen bond with each other, resulting in an increase in surface tension and minimization of the overall surface free energy.[52]

3.2 Initial Studies

Various preliminary studies were performed for the gas-phase silylation process prior to identifying the optimal approach for achieving complete surface passivation. The following section highlights a select few of those studies. While these experiments did not result in the successful formation of a densely packed organosilane monolayer, they provided useful insight in determining the correct procedure that would be used later on.

Preliminary insight into the silylation efficacy was quantified using WCA measurements. Subsequent XPS studies involving ALD were conducted only after confirming that complete surface passivation was achieved based on WCA values.

A comprehensive table summarizing the WCA results described in this chapter is presented in Table 3.1. The experimental procedures for each study are also individually detailed in their respective sections below.

Table 3.1 WCA measurements for different Si(100) surfaces after various cleaning treatments. TMSDMA-G and -L denote silylation in the gas and liquid phase using TMSDMA, respectively.

Figure	Surface	Contact Angle /°
3.2	(a) SiO_2/Si(100) (as is)	37±2
	(b) After acetone/DI treatment	26±2
	(c) TMSDMA-G + clean SiO_2/Si(100)	~85
3.3	1. High-temperature cleaning (1000 K) 2. TMSDMA-G/SiO_2/Si(100)	~80
3.4	TMSDMA-G + H_2O/SiO_2/Si(100) (alternate exposures)	~85
3.5	(a) RCA-cleaned SiO_2/Si(100)	9±2
	(b) PE-CVD grown SiO_2/Si(100)	13±2
	(c) TMSDMA-G/PE-CVD SiO_2/Si(100)	91±1
N/A	TMSDMA-G/RCA-cleaned SiO_2/Si(100)	89±2
N/A	TMSDMA-L/PE-CVD SiO_2/Si(100)	91±2
N/A	TMSDMA-L/RCA-cleaned SiO_2/Si(100)	90±2

3.2.1 Initial Silylation of SiO_2/Si(100) (1 nm Native Oxide)

The experiment for the initial silylation of SiO_2/Si(100) was carried out as follows:

1. Sonicate sample in acetone bath for 20 min.
2. Clean sample with acetone and Milli-Q water stream each for 2 min.
3. Dry under a N_2 flow and transfer into XPS chamber to pump down.
4. Anneal SiO_2/Si(100) substrate to 623 K in the analysis chamber for 30 min. to remove adventitious carbon.
5. Dose TMSDMA inside the preparation chamber using the parameters in Table 3.2.

Note: Steps 1-3 are the same for all SiO_2/Si(100) surfaces presented in this work and will be omitted from further experimental procedures/discussions.

Table 3.2 Experimental conditions used for the initial silylation of SiO_2/Si(100) with TMSDMA.

Parameter	Sub-parameter	Condition
Temperature	Sample	423 K
	Inhibitor	323 K
	Leak Valve	353 K
Pressure	Base	2E-8 Torr
	Dose	5E-5 Torr
Reaction Time	N/A	24 Hrs.

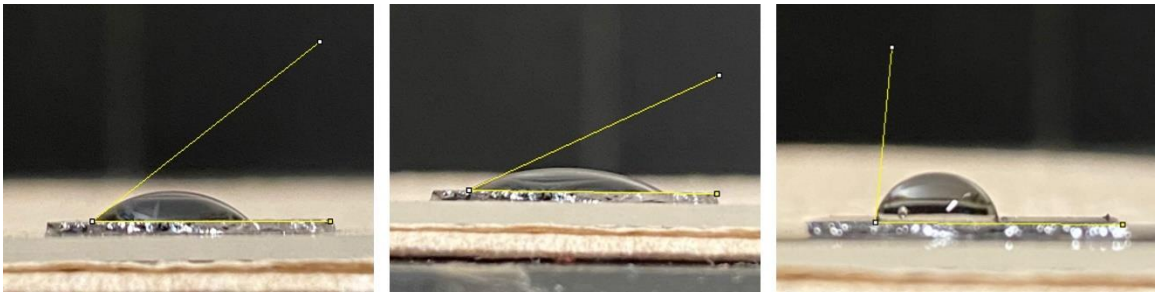


Figure 3.2 Macrographs of a few selected samples used to acquire some of the WCA measurements shown in Table 3.2. From left to right: SiO_2/Si(100) (native oxide, as is), after cleaning with acetone and DI H_2O, and after gas-phase silylation for 24 hours using the procedures described above and experimental conditions listed in Table 3.2. The corresponding WCA measurements for each surface are provided in Table 3.1.

A slight decrease in the WCA for the original untreated SiO_2/Si(100) substrate (Figure 3.2, left) from approximately 37° to 26° was observed after the acetone/DI H_2O cleaning step (Figure 3.2, center). This indicated the removal of some adventitious carbon resulting in a slightly more hydrophilic oxide surface, possibly through liberating obstructed hydroxyl groups. An increase in the WCA to approximately 85° was observed following the in-situ silylation reaction with TMSDMA (Figure 3.2, right). This increase in hydrophobicity indicated the functionalization of the oxide surface with $Si(CH_3)_3$ groups that are expected to nucleate on and consume Si-OH sites. As a result, the newly acquired

surface demonstrated a reduced capacity to hydrogen bond with water molecules, reflected by the higher droplet contact angle.

However, this value was not in good agreement with those reported in the literature for a trimethylsilyl-terminated silica surface.[52,64] While this deviation may seem to be initially minor, it was in fact significant as the lower value indicated that the monolayer was not densely packed. At this stage, the low WCA value was believed to be due to adventitious carbon that remained on the surface even after cleaning, which would block some silanol nucleation sites preventing their reaction with trimethylsilyl groups during silylation. Based on this, additional in-situ cleaning steps were explored to reduce the degree of carbon contaminants on the initial substrate to try and enhance the overall silylation efficacy.

3.2.2 High-temperature Cleaning Pretreatment

Next, a high temperature cleaning pretreatment was applied to the starting sample to further explore the impact of the removal of adventitious carbon. The procedures for this experiment followed the same sequence as listed in chapter 3.2.1, except that steps 4 and 5 are replaced with the following:

1. Anneal SiO_2/Si(100) sample to 1000 K in the analysis chamber for 15 min. to clean the surface. Use LN_2 to cool the manipulator rod during this process to prevent fluorine degasification from the Teflon seal.
2. Double the TMSDMA dosing time from 24 to 48 hrs. Dose TMSDMA inside the preparation chamber using the parameters in Table 3.3.

Table 3.3 Experimental conditions used for the silylation of SiO_2/Si(100) with TMSDMA following a high temperature cleaning pretreatment at 1000 K for 15 min.

Parameter	Sub-parameter	Condition
Temperature	Sample	423 K
	Inhibitor	308 K
	Leak Valve	338 K
Pressure	Base	2E-8 Torr
	Dose	5E-5 Torr
Reaction Time	N/A	48 Hrs.

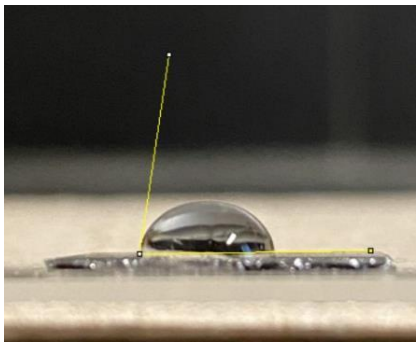


Figure 3.3 Macrograph of SiO_2/Si(100), pretreated by annealing to 1000 K for 15 min., after silylation with TMSDMA using the procedures described above and experimental conditions listed in Table 3.3. The corresponding WCA measurement is provided in Table 3.1.

XPS was used in this case to monitor the changes in the carbon coverage after this annealing treatment. Attenuation in the C 1s XPS signal (not shown) was observed after annealing the sample to 1000 K for 15 min. attributed to the removal of adventitious carbon from the surface; however, some carbon still remained. This procedure did not result in an improvement in the observed WCA measurement following treatment with TMSDMA; rather, a lower value of 80° (Figure 3.3) was obtained representative of a deterioration in monolayer quality from the previous measurement.

These unexpected results were rationalized by the removal of not only adventitious carbon but also some hydroxyl nucleation sites during the annealing process. Previous studies have reported the removal of hydroxyl groups upon sample annealing.[65–67] Vicinal hydroxyls hydrogen bonded to each other desorb as H_2O upon heating the sample to temperatures between 723-873 K, while isolated and geminal groups persist for higher temperatures and do not begin to desorb until 873-1173 K. Based on this information, it is likely that the annealing step led to a reduction of the total number of silanol nucleation centers available for the adsorption of trimethylsilyl groups, ultimately leading to the formation of a poorly packed organosilane monolayer. Furthermore, doubling the reaction time had no impact in improving the silylation efficacy. In light of these findings, it was understood that the original surface may possess an insufficient number of hydroxyl nucleation sites to facilitate the formation of a complete passivating monolayer. As such, it was evident that alternative steps were required to generate more Si-OH groups.

3.2.3 Addition of Alternating H_2O Exposures

It has been reported that using alternating H_2O exposures between inhibitor doses may result in the formation of a more robust passivating monolayer.[68] A similar process was adapted here for the following experiment. The silylation procedure here was similar to that of the previous section, except for the integration of alternating H_2O exposures as described below:

1. Throttle the gate valve to reduce the base pressure to 1.0 x 10^{-5} Torr prior to any H_2O exposures, which would be conducted in the preparation chamber.
2. Conduct a 2-hr. initial H_2O exposure at 2.0 x 10^{-4} Torr while annealing the sample to 523 K.
3. Conduct alternating 1-hr. exposures of TMSDMA (T_s: 423 K) and H_2O (T_s: 523 K) at 2.0 x 10^{-4} Torr until a total of 8 cycles have been completed.
4. Continue dosing TMSDMA until a 24-hr. total reaction time has been completed.

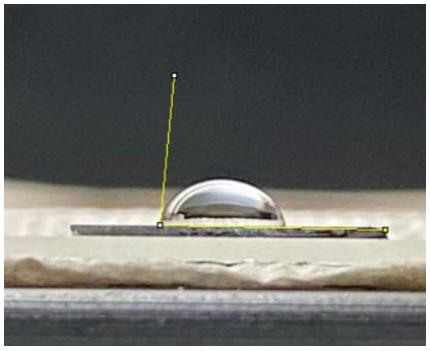


Figure 3.4 Macrograph of SiO_2/Si(100) after exposure to 8 alternate TMSDMA/H_2O cycles. The corresponding WCA measurement is provided in Table 3.1.

A WCA measurement of approximately 85° was obtained as depicted in Figure 3.4, similar to the measurement obtained for the sample depicted in Figure 3.2 that did not undergo the alternating H_2O exposures. No improvement in the density of the passivating layer was discerned based on the constant contact angle. These experiments underscored the difficulty in identifying an appropriate in-situ cleaning condition. It was therefore desirable to consider ex-situ treatments as well.

3.3 Ex-Situ Cleaning Pretreatment and Inhibitor Flux Enhancement

Ex-situ cleaning methods were investigated to enhance the hydrophilicity of the surface before silylation. The two cleaning techniques employed were RCA cleaning and SiO_2 PE-CVD, as discussed in chapter 2.2.2.

Moreover, the gate valve was completely sealed during the silylation process to increase the inhibitor flux and reduce the total vapor dosing time to 15 min., as previously elaborated in section 2.2.3.

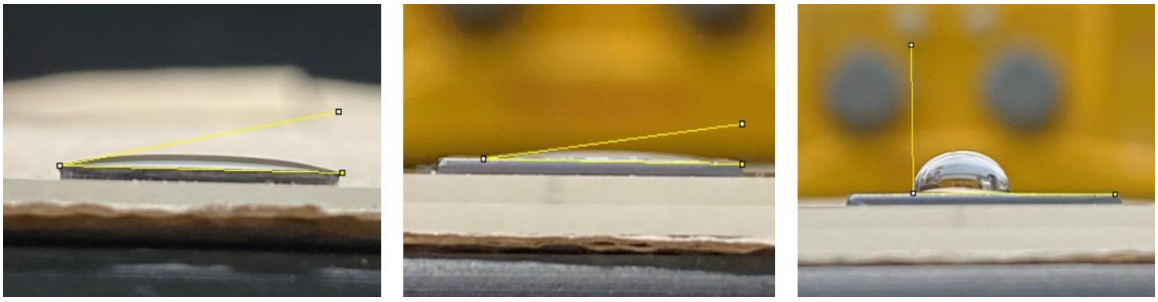


Figure 3.5 Macrographs of a few selected samples used to acquire WCA measurements shown in Table 3.1. From left to right, SiO_2/Si(100) after: RCA cleaning, SiO_2 PE-CVD, and gas-phase silylation with TMSDMA for 15 min.

A reduction in the WCA measurement from 37° for the original SiO_2/Si(100) (1 nm native oxide) surface to values of approximately 13° and 9° were obtained after RCA cleaning (Figure 3.5, left) and SiO_2 PE-CVD (Figure 3.5, center), respectively. This value then increased to 90° on the PE-CVD grown SiO_2 surface after silylation with TMSDMA (Figure 3.5, right), finally in good agreement with those that were reported in the literature (similar value of 89° was obtained on the RCA-cleaned SiO_2 surface, not shown). These measurements indicate that the SiO_2 surfaces prepared through PE-CVD or RCA cleaning

were highly hydrophilic, suggestive of a high density of silanol groups on the surface after the cleaning treatment. The following reaction with TMSMDA demonstrated that the silylation treatment was efficient at capping those -OH groups, rendering the surface highly hydrophobic due to the presence of a densely packed organosilane passivating monolayer. After elucidating the appropriate gas-phase silylation process to block silanol nucleation centers on SiO_2 surfaces, the next steps would involve assessing the passivation efficacy of these surfaces using ALD.

3.4 Conclusion

This chapter summarized the preliminary silylation studies conducted on silica substrates that qualitatively assessed the impact of different surface treatments on passivation efficacy using WCA measurements. It was found that the formation of a densely-packed organosilane monolayer was initially unfavorable on the unmodified blank silica surface. Other treatments such as high-temperature annealing prior to silylation or the addition of alternate H_2O dosing between TMSDMA exposures did not lead to an improvement in the contact angle. A SiO_2 PE-CVD or RCA cleaning pretreatment was ultimately necessary to initially modify the surface to increase the number of Si-OH nucleation sites, generating a new surface conducive towards silylation. These modification steps allowed for the chemisorption of more trimethylsilyl groups thereby increasing the packing of the monolayer. This was evidenced by the ideal WCA measurement of 90° obtained following the TMSDMA exposures on the clean SiO_2 surfaces.

FOUR

Metal Oxide ALD on Silylated PE-CVD-grown vs. RCA-cleaned SiO_2/Si(100) – Gas- vs. Liquid-phase Silylation

4.1 Introduction

The media that a reaction is conducted can have a significant impact on how it progresses throughout its duration, as the surface chemistry at gas-solid interfaces may greatly differ from those in solution.[69] In the latter, various solvent effects can facilitate the displacement of ligands, charge stabilization within the precursor complex, as well as strong ligand-substrate interactions to enhance reaction probabilities with specific nucleation centers.[70] Conversely, gas-surface reactions lack the potential advantages provided from the use of solvents, as the complex topographies of the solid substrate pose additional challenges for the coordination of molecules to the surface, potentially impeding certain favorable reaction pathways.[38] These single-collision events tend to be irreversible, implying that the reaction must already be the kinetically preferred pathway to avoid undesirable side reactions.[71] However, the use of vacuum conditions (especially UHV) helps to maintain a contaminant free environment that is beneficial for avoiding such side reactions. Additionally, multiple binding sites for a single reaction may also exist in the gas phase, promoting unique types of binding modes that exist separately from that of solution-phase chemistry.[69] Moreover, the order and orientation of inhibitor molecules

adsorbed on a substrate can vastly differ based on the reaction media, leading to variations in packing densities and structure of the monolayer lattice.[72] Due to these possibilities, it was imperative to investigate the fundamental similarities and/or differences that existed in the silylation of silica surfaces (modified with two different cleaning procedures) when conducted in either the gas or liquid phase.

An initial understanding of the efficacy of passivation is required in order to develop an AS-ALD process, which can be determined by evaluating the kinetics of metal oxide ALD on the silylated substrates. TiO_2 and HfO_2 ALD were therefore chosen here to investigate the effectiveness of our surface silylation treatments. TiO_2 is a wide-bandgap material possessing diverse applications, including its use as a white pigment due to its high refractive index, its role in photocatalysis within solar cells, and its ability to catalyze the water splitting reaction.[73–76] Hafnium dioxide (HfO_2) shows promise in the field of microelectronics as a "high-κ" dielectric material capable of replacing SiO_2 as a gate oxide in transistors, potentially alleviating the issue of current leakage from the gate that can occur (based on the lower dielectric constant of SiO_2).[77–79] Due to their significance, these metal oxide ALD systems were selected to evaluate the passivation efficacy of the modified silica substrates described in this work. While $TiCl_4$ and $HfCl_4$ are commonly used as the main precursors to deliver the metal atom to the surface during ALD, the use of chlorides is undesirable not only due to the trace Cl impurities that may become incorporated into the deposited film, but also due to the corrosive nature of the HCl byproduct produced that can damage the reaction chamber. Thus, alternative metal-organic precursors such as TDMATi and TDMAHf have become popular for ALD applications (Figure 4.1).[80]

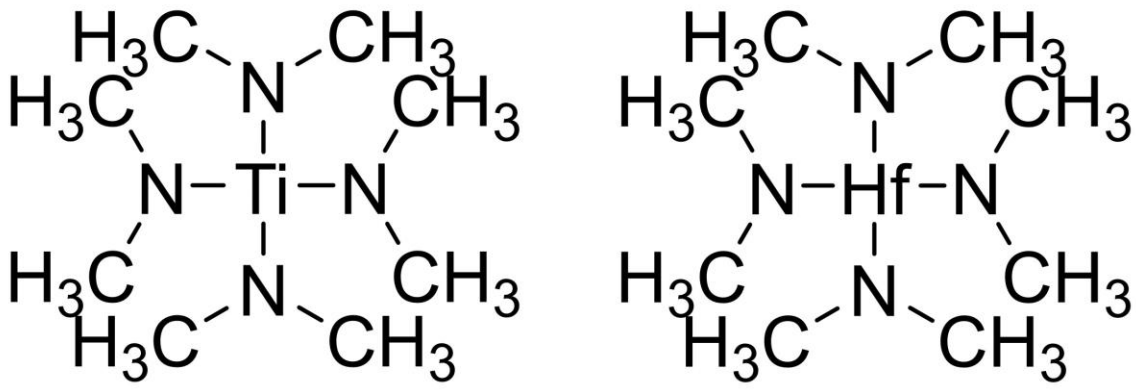


Figure 4.1 Chemical structures of tetrakis(dimethylamino)titanium (IV) (TDMATi) and tetrakis(dimethylamino)hafnium (IV) (TDMAHf) metalorganic precursors used to conduct TiO_2 and HfO_2 ALD, respectively. These structures were re-drawn using ChemDraw.

4.2 Experimental

The experimental details regarding the PE-CVD, RCA, and TMSDMA surface modification procedures as well as the TiO_2 and HfO_2 ALD processes are all described in detail in Chapters 2.2.2 and 2.2.3.

4.3 Estimation of PE-CVD Grown SiO_2 Film Thickness

The thickness of the silica films grown by PE-CVD on the starting SiO_2/Si(100) substrate was initially determined using XPS. A 1 cm^2 piece of tantalum foil (Alfa Aesar, 99.95% purity) was used prior to SiO_2/Si(100) substrates in order to distinguish new elements added to the surface during the deposition process from those of the underlying bulk material using XPS. The film thickness was estimated using the assumptions listed in Chapter 2.2.1, attenuation of the Ta_2O_5-Ta $4f_{7/2}$ XPS signal displayed in Figure 4.2a, corresponding IMFP value listed in Table 2.1, and equation (2).

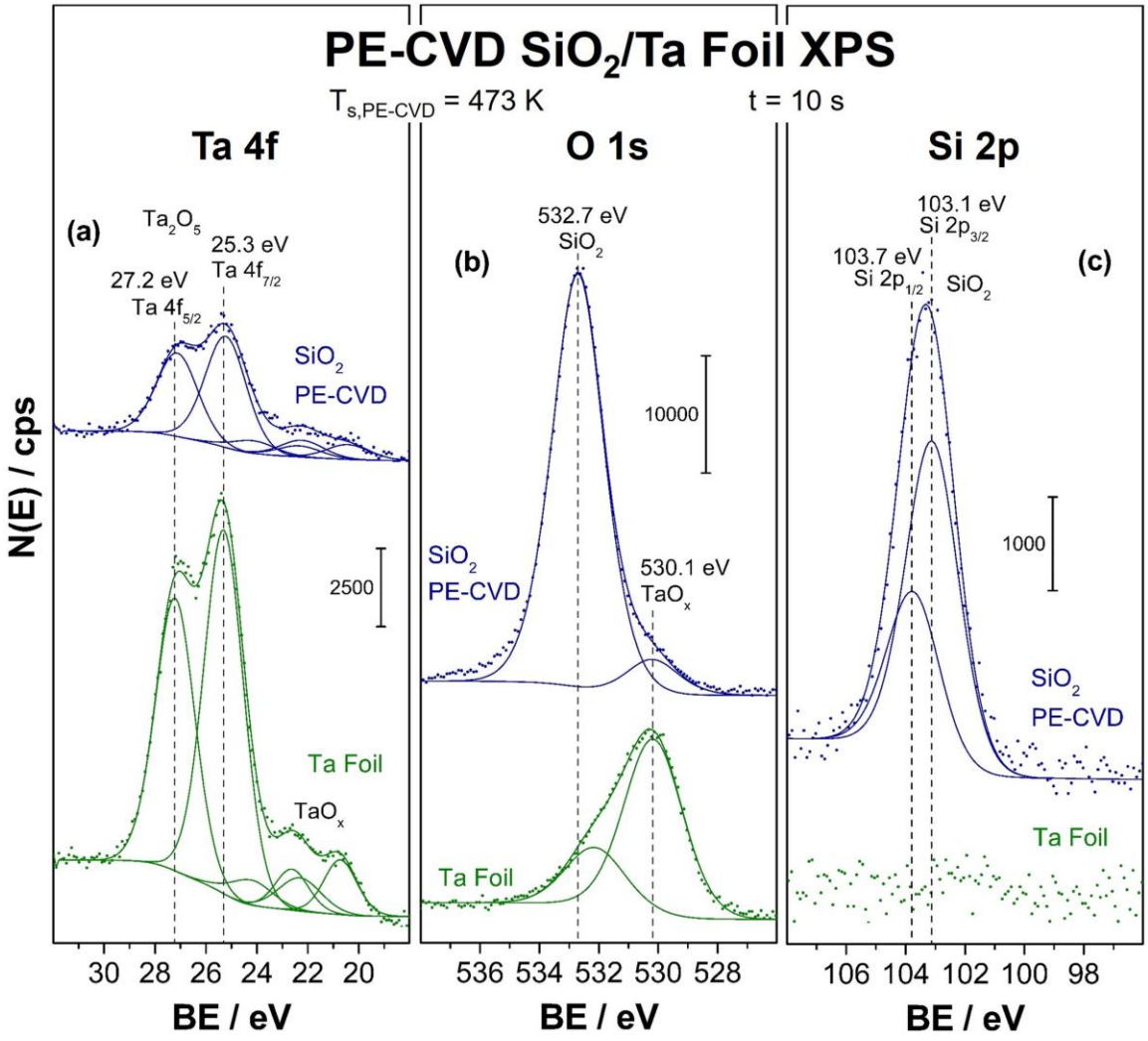


Figure 4.2 (a) Ta 4f, (b) O 1s, and (c) Si 2p XPS data before and after SiO_2 film growth on Ta foil using PE-CVD, carried out at 473 K for 10 s with SiH_4 and N_2O.

Figure 4.2 displays the (a) Ta 4f, (b) O 1s, and (c) Si 2p XPS data obtained after growing a SiO_2 film in 10 s using PE-CVD. The Ta $4f_{5/2}$ and $4f_{7/2}$ XPS peaks observed at 27.2 eV and 25.3 eV, respectively, and the O 1s signal at 530.1 eV are attributed to Ta_2O_5 species on the sample prior to SiO_2 PE-CVD. Silica deposition was confirmed from the

appearance of new characteristic SiO_2 XPS signals at 103.3 eV and 532.7 eV in the Si 2p and O 1s XPS, respectively. Concurrently, attenuation of the Ta 4f XPS signal is observed due to the deposited SiO_2 overlayer while a shift in binding energy is observed in the O 1s XPS signal from 530.1 eV to 532.7 eV, reflective of a change in the surface from Ta_2O_5 to SiO_2. From these measurements, the film thickness of the PE-CVD-grown SiO_2 was determined to be approximately 4.5 nm. Film thicknesses were not calculated for the surfaces cleaned using the RCA protocol as that method etches the native oxide away to generate a fresh hydroxylated native oxide layer. A similar description of the calculations for the film thickness data discussed in this section also applies to those introduced later in this chapter; as such, Table 2.1 should be referred to for the appropriate parameters.

4.4 Silylation Efficacy Against TiO_2 ALD – Gas vs. Liquid Phase

The passivation efficacy was evaluated using TiO_2 ALD after confirming with water contact angle (WCA) measurements that both gas- and liquid-phase silylation were successful in passivating the silica surfaces. The impact of the sample cleaning protocol on the silylation reaction was assessed by employing silicon oxide surfaces prepared using two different modification techniques, namely SiO_2 PE-CVD or RCA cleaning.

4.4.1 PE-CVD-Grown SiO_2/Si(100)

Figure 4.3 displays the (a) Ti 2p, (b) O 1s, and (c) Si 2p XPS data obtained for the gas-phase silylated (S) and non-silylated (NS) PE-CVD-grown SiO_2/Si(100) surfaces as a function of increasing number of TiO_2 ALD cycles conducted.

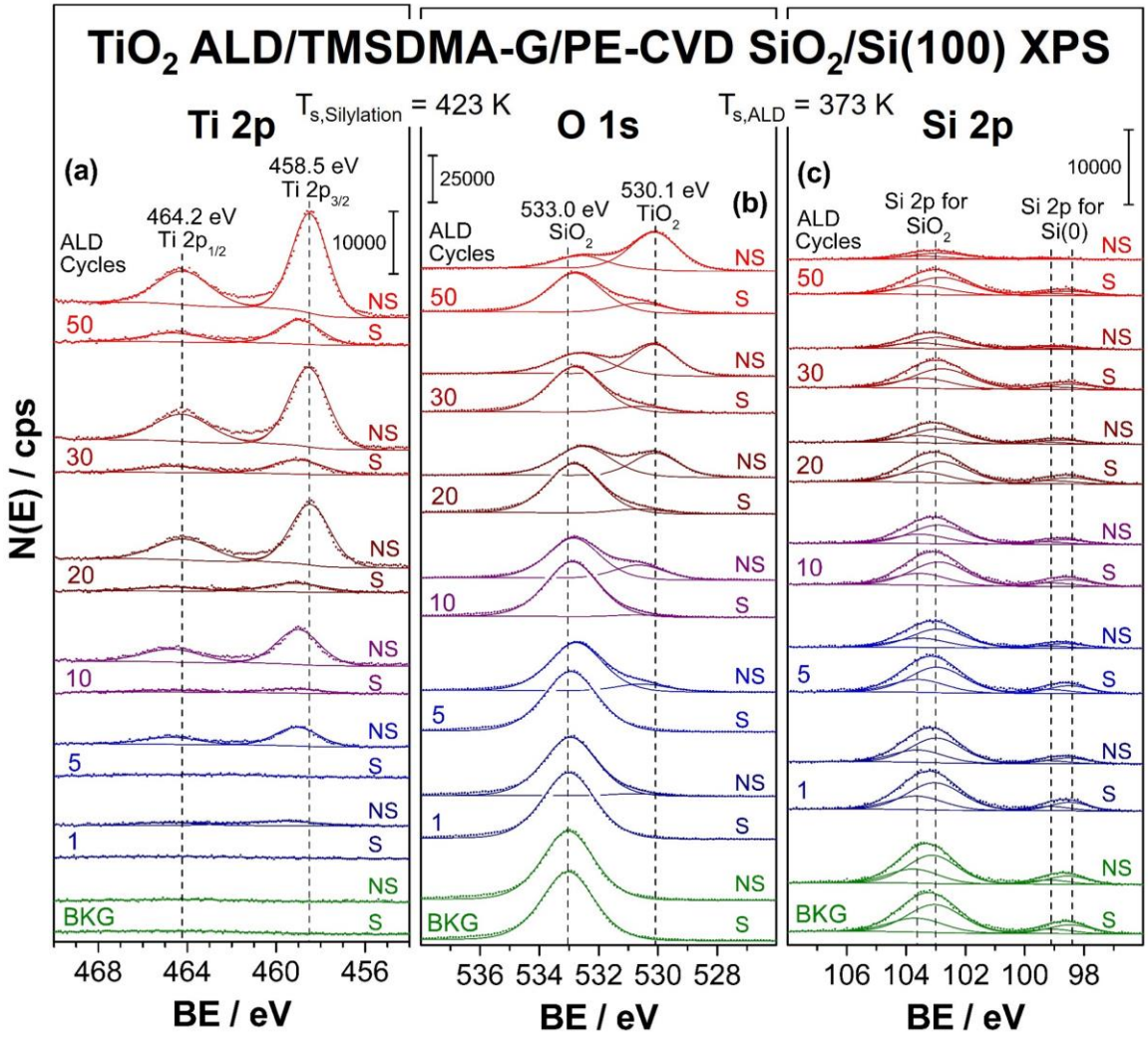


Figure 4.3 Ti 2p (a), O 1s (b), and Si 2p (c) XPS data for the gas-phase TMSDMA-silylated (TMSDMA-G/PE-CVD SiO_2/Si(100), denoted as S) and non-silylated (PE-CVD SiO_2/Si(100), denoted as NS) PE-CVD-grown SiO_2/Si(100) substrates as a function of increasing number of TiO_2 ALD cycles. The raw data are shown as dots and the fitted peaks as lines.

For the unmodified blank sample (PE-CVD SiO_2/Si(100), NS), Ti $2p_{1/2}$ and $2p_{3/2}$ XPS peaks (Figure 4.3a) are observed at 464.2 eV and 458.5 eV, respectively, immediately after the first TiO_2 ALD cycle, indicative of the presence of titanium from the nucleation of the TDMATi precursor on the surface. A rapid evolution of these signals is then

observed up to 50 ALD cycles as the TiO_2 film continues to grow on the blank sample. In contrast, TDMATi is not observed to chemisorb on the gas-phase silylated surface (TMSDMA-G/PE-CVD SiO_2/Si(100), S) until approximately 10 ALD cycles. Only one set of spin-orbit split Ti 2p XPS signals was observed in all cases indicating that only Ti atoms in a 4+ (IV) oxidation state (TiO_2 species) were present on the surface; no other oxidation states for Ti were ever detected in any further experiments.

In the O 1s XPS (Figure 4.3b), a single peak is initially observed at 533.0 eV for both the silylated and non-silylated substrates characteristic of SiO_2 (denoted as SiO_2-O 1s). Immediately after the first TiO_2 ALD cycle however, the appearance of a small new peak is observed at 530.1 eV for the unmodified surface, a feature associated with the Ti-O chemical environment of TiO_2 (TiO_2-O 1s). The appearance of this signal at a lower binding energy from the main SiO_2 peak at 533.0 eV is expected as Ti is less electronegative than Si (EN: 1.54 vs. 1.90), possessing a lower tendency to attract electron density away from oxygen atoms. As such, the electrons from the 1s orbital of O atoms in a TiO_2 chemical environment are ejected with a higher kinetic energy and thus lower binding energy relative to those associated with O atoms bonded to Si in SiO_2. This feature is not observed for the silylated sample until 10 ALD cycles, coinciding with the start of the Ti 2p XPS signal growth. This suggests that TiO_2 film growth is completely inhibited by the silylation process during the first 5 TiO_2 ALD cycles.

Finally, two distinct peaks are observed in the Si 2p XPS (Figure 4.3c) at 103.3 eV and 98.7 eV attributed to the PE-CVD-grown SiO_2 overlayer (SiO_2-Si 2p) and the Si(0) bulk (Si(0)-Si 2p), respectively. Attenuation of both these peaks is observed from the first

cycle on the blank surface but only after the tenth cycle on the silylated sample, as the TiO_2 overlayer that is deposited covers the underlying silica substrate. The TiO_2-O 1s XPS signal continues to evolve after the first 5 ALD cycles on both surfaces up to 50 ALD cycles, but the signal intensities for these peaks on both surfaces are significantly different with those for the non-silylated surface increasing at a faster rate. Furthermore, the attenuation rate for the silylated surface is much lower than that for the non-silylated counterpart, consistent with the diminished rate of TiO_2 deposition observed based on the Ti 2p and O 1s XPS data. The changes in the intensities of these peaks are further quantified in Figures 4.4 and 4.5 as a function of increasing ALD cycles.

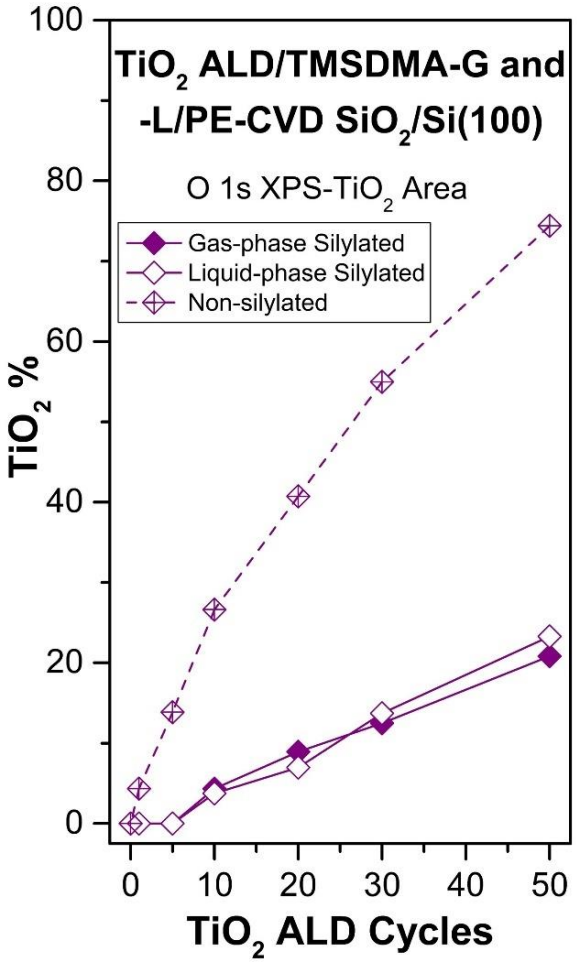


Figure 4.4 Peak areas of the TiO_2 component of the O 1s XPS signal (TiO_2-O 1s XPS) measured for gas- and liquid-phase silylated PE-CVD-grown SiO_2/Si(100) (denoted as TiO_2 ALD/TMSDMA-G/PE-CVD SiO_2/Si(100) and TiO_2 ALD/TMSDMA-L/PE-CVD SiO_2/Si(100), respectively) after depositing TiO_2 films via ALD. The TiO_2-O 1s data are compared to that of a non-silylated substrate (TiO_2 ALD/PE-CVD SiO_2/Si(100)) and are plotted as a percentage of the total O 1s XPS signal (obtained from Figures 4.3 and 4.6) versus the number of TiO_2 ALD cycles conducted.

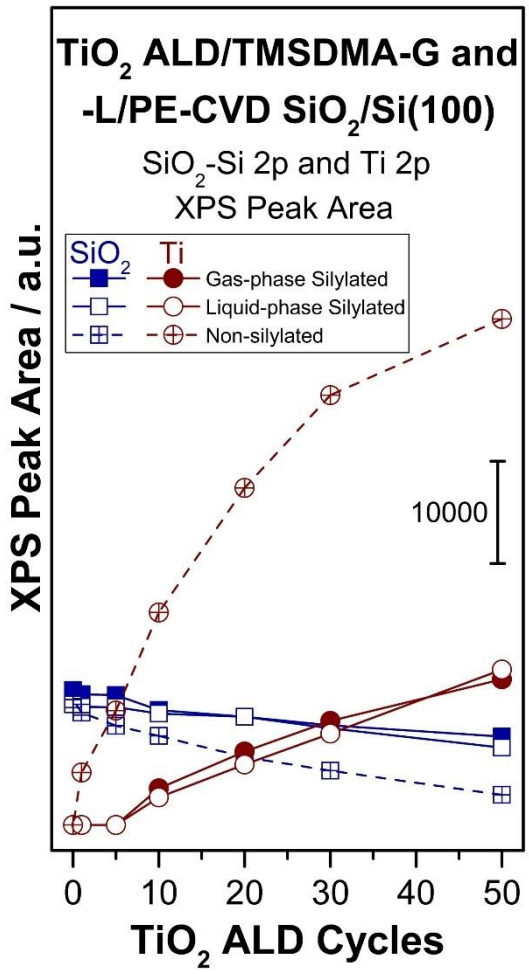


Figure 4.5 Peak areas of the SiO_2-2p and Ti 2p XPS data reported in Figures 4.3 and 4.6 for both gas- and liquid-phase silylated PE-CVD grown SiO_2/Si(100) compared to that of a non-silylated substrate, as a function of the increasing number of TiO_2 ALD cycles conducted.

To better gauge the efficacy of the gas-phase silylation and as a point of comparison, the same series of TiO_2 ALD experiments were repeated on liquid-phase silylated substrates. Surprisingly, the XPS data obtained from these experiments (Figure 4.6) were comparable to those obtained using the gas-phase treatment in terms of the ability to inhibit TiO_2 ALD surface reactions; similar trends in peak shapes and intensities were observed. To highlight this observation, the Si 2p and Ti 2p XPS peak areas, and the TiO_2-

O 1s signal for both the gas- and liquid-phase silylated samples compared to the reference blank surface are plotted in Figures 4.5 and 4.4, respectively, as a function of the increasing number of TiO_2 ALD cycles conducted.

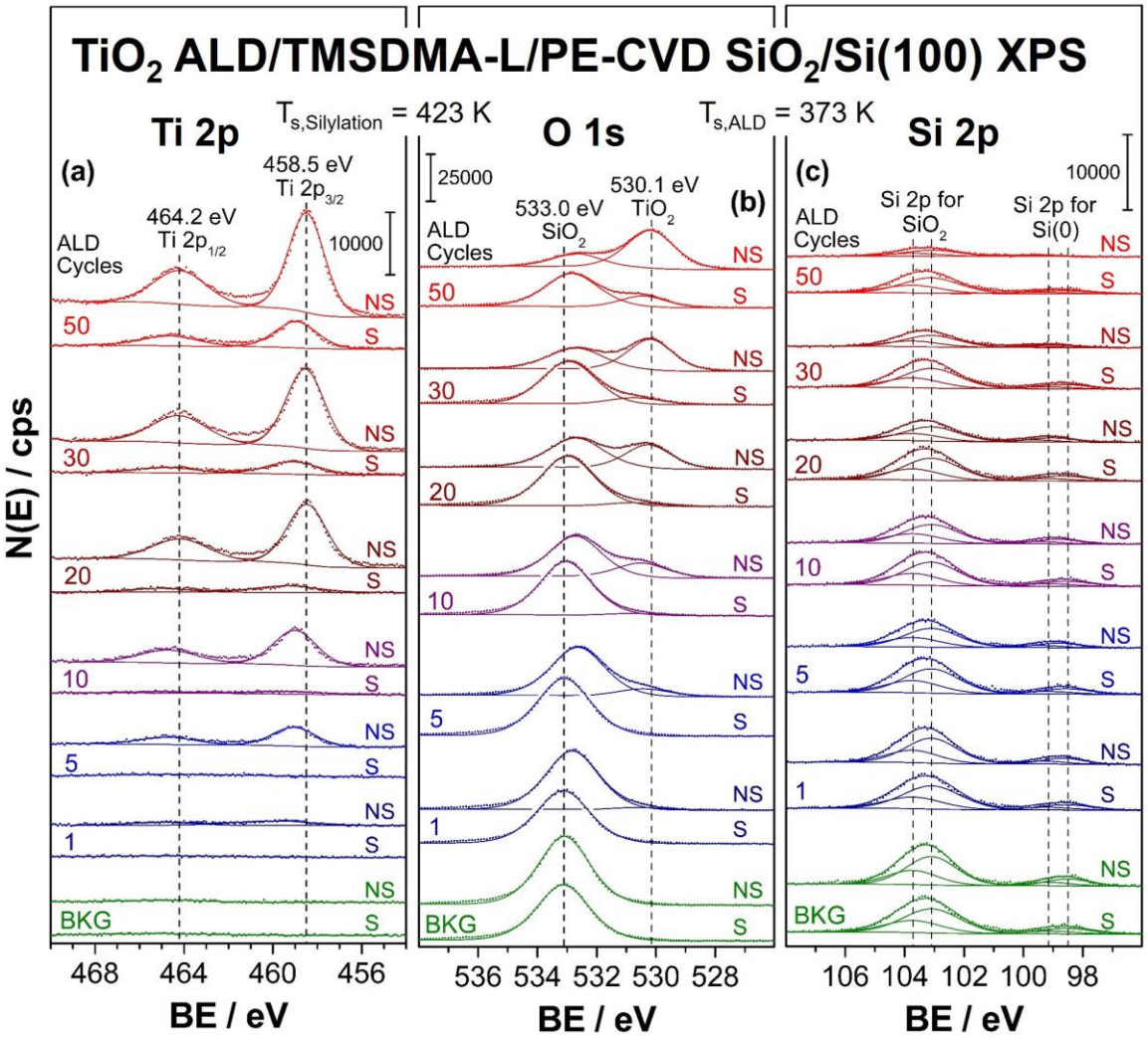


Figure 4.6 Ti 2p (a), O 1s (b), and Si 2p (c) XPS data for the liquid-phase TMSDMA-silylated (TMSDMA-L/PE-CVD SiO_2/Si(100), denoted as S) and non-silylated (PE-CVD SiO_2/Si(100), denoted as NS) PE-CVD-grown SiO_2/Si(100) substrates as a function of increasing number of TiO_2 ALD cycles. The raw data are shown as dots and the fitted peaks as lines.

The XPS data shown here was further processed to quantify how surface species evolved as a function of increasing TiO_2 ALD cycles. The XPS peak intensities of all silica substrates versus the number of ALD cycles used to deposit TiO_2 films on those surfaces are expressed as surface atomic-percent composition profiles displayed in Figure 4.7a; the average film thicknesses using this data are presented in Figure 4.7b.

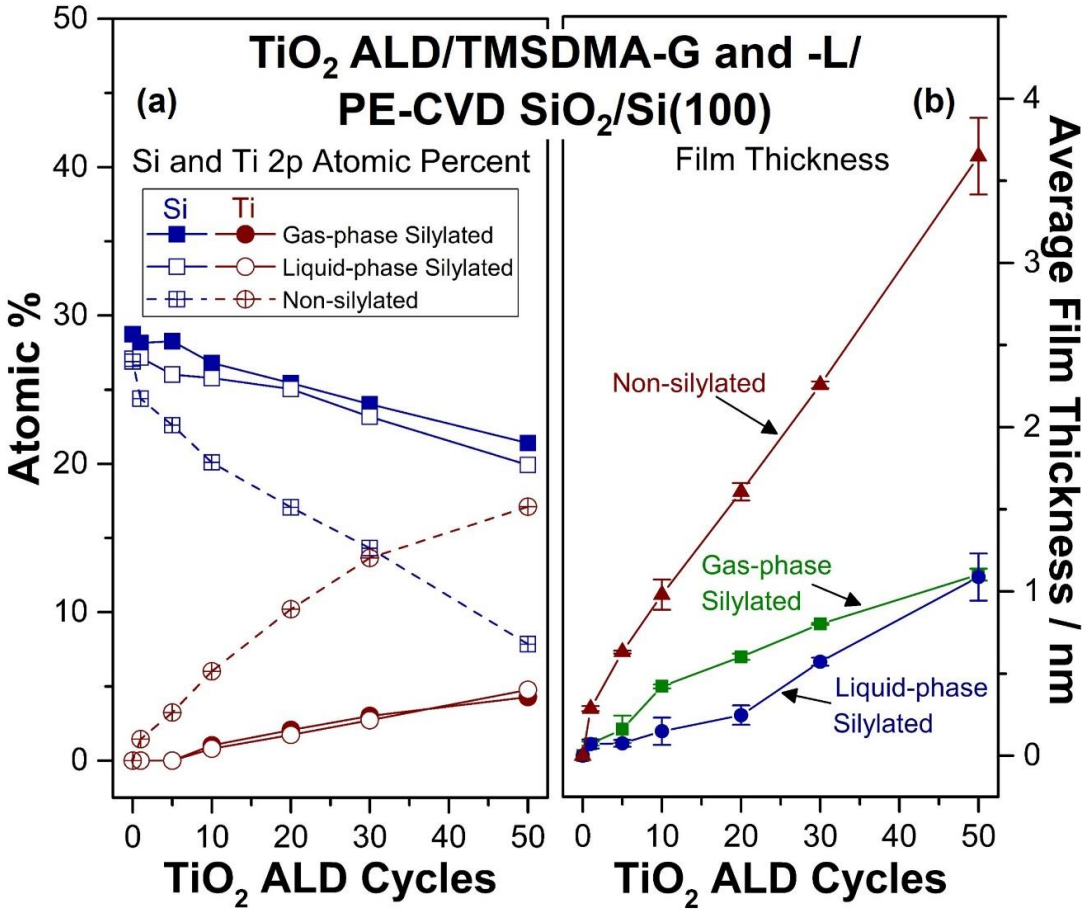


Figure 4.7 (a) Si and Ti surface atomic-percent composition profiles for both gas- and liquid-phase silylated PE-CVD SiO_2 substrates (TMSDMA-G and -L/PE-CVD SiO_2/Si(100) as a function of increasing number of ALD cycles used to grow TiO_2 films on those surfaces, estimated using the SiO_2-Si 2p and SiO_2-O 1s XPS peak areas in combination with corresponding ASFs. These are contrasted with the results obtained for a non-silylated surface. (b) Average TiO_2 film thickness calculated from the data in panel (a) by assuming layer-by-layer type growth.

As aforementioned, film growth does not occur during the first 5 TiO_2 ALD cycles on either of the silylated surfaces; in comparison, a TiO_2 film of approximately 0.3 nm thickness is already deposited on the unmodified substrate after only one cycle. After the 10^{th} cycle, a jump in the film thickness to a higher value is observed in the case of the gas-phase modified surface compared to that for the liquid-phase. TiO_2 film growth is observed at an approximately linear GPC after this 10-cycle threshold, but the deposition rate is still lower than that observed on the unmodified surface: 0.2 vs. 0.8 Å/ALD cycle. The silylation treatment may initially consume all nucleation sites available for TDMATi chemisorption on the silica surface and, once TiO_2 ALD is initiated (likely through defects within the organosilane monolayer, acting as nucleation centers) the density of nucleation sites is lower leading to slower film growth. The case of the liquid-phase silylated surface is more complicated since the initial growth rate is lower between 10 and 20 ALD cycles. However, after 20 cycles the slope of the film thickness versus ALD cycles becomes larger than that of the gas-phase treated sample. Rapid film growth occurs to the point that after 50 ALD cycles, the film thickness on both of the silylated surfaces is approximately the same: 1 nm. The liquid-phase silylated surface may initially exhibit fewer defects that could act as nucleation sites, but after becoming exposed and reacting with TDMATi molecules, those defects may propagate to generate more nucleation sites. The TiO_2 ALD GPC for the liquid-phase silylated surface becomes 0.3 Å/ALD cycle.

In addition to the data demonstrating the comparability of the gas- and liquid-phase silylation procedures in initially blocking and later delaying the chemisorption of precursor

reactants at defect nucleation sites, a noticeable difference between the two methods exists in terms of the amount of carbon deposition observed.

The C 1s XPS data fitted to four peaks (C-C/C-H, C-O-C/C-O-H, C=O, and O-C=O bonding environments from low to high BE) are provided in Tables 4.1, 4.2, and 4.3 for the gas-phase silylated, liquid-phase silylated, and non-silylated PE-CVD-grown SiO_2/Si(100), respectively, after treatment with TiO_2 ALD. The information detailed here serves to not only assist in the reproduction of this analysis, but also as a general example of the type of considerations made when fitting the data in this dissertation. Specifically, the values for parameters such as BE position, peak area, and full-width half-maximum (FWHM) are provided. The BE position for the C-O-C/C-O-H, C=O, and O-C=O components were constrained to that of the C-C/C-H such that they appeared at a BE of 1.5 eV, 3.0 eV, and 4.5 eV higher, respectively. The FWHM was also constrained for these three components such that they were equal to that of the C-C/C-H.

Table 4.1 BE, peak area, and FWHM values for the C-C/C-H, C-O-C/C-O-H, C=O, and O-C=O fitted components (of the C 1s XPS data shown in Figure 4.8) provided for the gas-phase TMSDMA-silylated (TMSDMA-G/PE-CVD SiO_2/Si(100)) substrate as the number of ALD cycles used to deposit TiO_2 was increased.

Gas-phase Silylated TiO_2 ALD Cycles	**Parameter**	**C 1s Peak Component**			
		C-C, C-H	**C-O-C, C-O-H**	**C=O**	**O-C=O**
0	BE / eV	284.5	286.0	287.5	289.0
	Peak Area / a.u.	4029.4	991.7	539.4	259.5
	FWHM		2.019		
1	BE / eV	284.6	286.1	287.6	289.1
	Peak Area / a.u.	4517.0	911.4	143.8	231.3
	FWHM		2.176		
5	BE / eV	284.4	285.9	287.4	288.9
	Peak Area / a.u.	5071.6	1426.3	656.9	139.7
	FWHM		2.068		
10	BE / eV	284.45	285.95	287.45	288.95
	Peak Area / a.u.	6606.0	980.6	575.1	0
	FWHM		2.412		
20	BE / eV	284.4	285.9	287.4	288.9
	Peak Area / a.u.	6870.1	1495.6	587.3	351.2
	FWHM		2.277		
30	BE / eV	284.3	285.8	287.3	288.8
	Peak Area / a.u.	6506.4	1983.2	847.0	470.1
	FWHM		2.070		
50	BE / eV	284.4	285.9	287.4	288.9
	Peak Area / a.u.	6885.0	2359.2	815.1	852.0
	FWHM		2.085		

Table 4.2 BE, peak area, and FWHM values for the C-C/C-H, C-O-C/C-O-H, C=O, and O-C=O fitted components (of the C 1s XPS data shown in Figure 4.8) provided for the liquid-phase TMSDMA-silylated (TMSDMA-L/PE-CVD SiO_2/Si(100)) substrate as the number of ALD cycles used to deposit TiO_2 was increased.

Liquid-phase Silylated TiO_2 ALD Cycles	**Parameter**	**C 1s Peak Component**			
		C-C, C-H	**C-O-C, C-O-H**	**C=O**	**O-C=O**
0	BE / eV	284.7	286.2	287.7	289.2
	Peak Area / a.u.	8570.3	736.5	522.8	0
	FWHM		2.075		
1	BE / eV	284.7	286.2	287.7	289.2
	Peak Area / a.u.	8202.2	790.7	710.6	65.8
	FWHM		2.124		
5	BE / eV	284.6	286.1	287.6	289.1
	Peak Area / a.u.	7164	1021.7	636.4	437.8
	FWHM		2.232		
10	BE / eV	284.5	286.0	287.5	289.0
	Peak Area / a.u.	7010.9	1374.7	585.6	23.2
	FWHM		2.099		
20	BE / eV	284.4	285.9	287.4	288.9
	Peak Area / a.u.	7315.5	1825.6	474.7	0
	FWHM		2.139		
30	BE / eV	284.35	285.85	287.35	288.85
	Peak Area / a.u.	7828.9	2280.1	585.2	332.4
	FWHM		2.044		
50	BE / eV	284.35	285.85	287.35	288.85
	Peak Area / a.u.	9268.4	2507.1	766.0	102.1
	FWHM		2.087		

Table 4.3 BE, peak area, and FWHM values for the C-C/C-H, C-O-C/C-O-H, C=O, and O-C=O fitted components (of the C 1s XPS data shown in Figure 4.8) provided for the non-silylated (PE-CVD SiO_2/Si(100)) substrate as the number of ALD cycles used to deposit TiO_2 was increased.

Non-silylated		C 1s Peak Component			
TiO_2 ALD Cycles	Parameter	C-C, C-H	C-O-C, C-O-H	C=O	O-C=O
0	BE / eV	284.8	286.3	287.8	289.3
	Peak Area / a.u.	5168.5	958.7	388.7	75.0
	FWHM		2.200		
1	BE / eV	284.7	286.2	287.7	289.2
	Peak Area / a.u.	5898.3	1221.4	478.7	219.2
	FWHM		2.228		
5	BE / eV	284.6	286.1	287.6	289.1
	Peak Area / a.u.	5896.9	1815.8	680.4	441.0
	FWHM		2.123		
10	BE / eV	284.55	286.05	287.55	289.05
	Peak Area / a.u.	5386.6	2200.2	617.9	456.5
	FWHM		1.944		
20	BE / eV	284.35	285.85	287.35	288.85
	Peak Area / a.u.	5402.5	1911.8	414.8	492.6
	FWHM		2.053		
30	BE / eV	284.4	285.9	287.4	288.9
	Peak Area / a.u.	5481.1	1827.4	442.1	360.6
	FWHM		2.018		
50	BE / eV	284.45	285.95	287.45	288.95
	Peak Area / a.u.	6226.1	1403.8	596.0	160.5
	FWHM		2.166		

The information described in Tables 4.1-4.3 is displayed in the C 1s XPS data in Figure 4.8, and a plot of the total carbon surface atomic-percent compositions estimated from that data is presented in Figure 4.9.

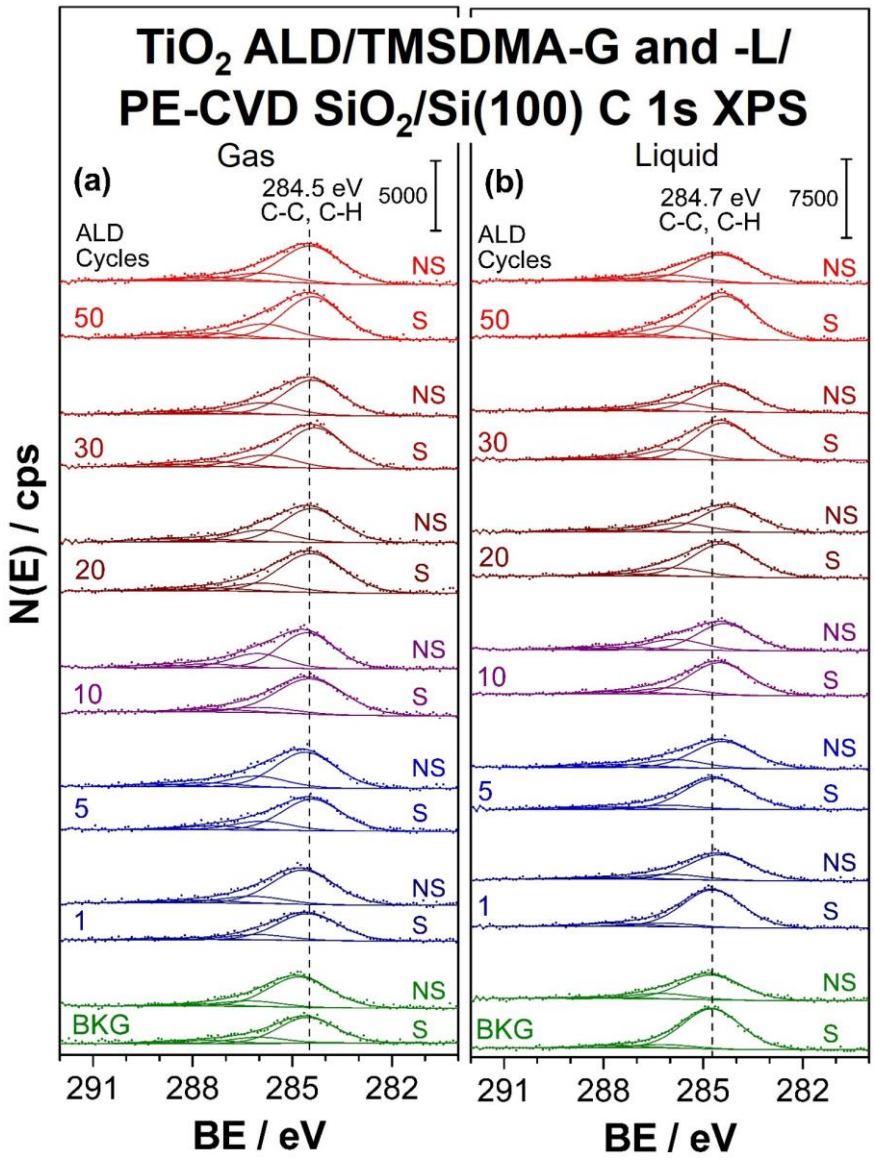


Figure 4.8 C 1s XPS data for the gas- (a) and liquid- (b) phase TMSDMA-silylated (TMSDMA-G or – L/PE-CVD SiO_2/Si(100); S) and non-silylated (PE-CVD SiO_2/Si(100); NS) substrates as a function of increasing number of TiO_2 ALD cycles. The raw data, shown as dots, were fitted to four peaks (from high to low BE: O-C=O, C=O, C-O-C/C-O-H, and C-C/C-H bonding environments), shown as lines.

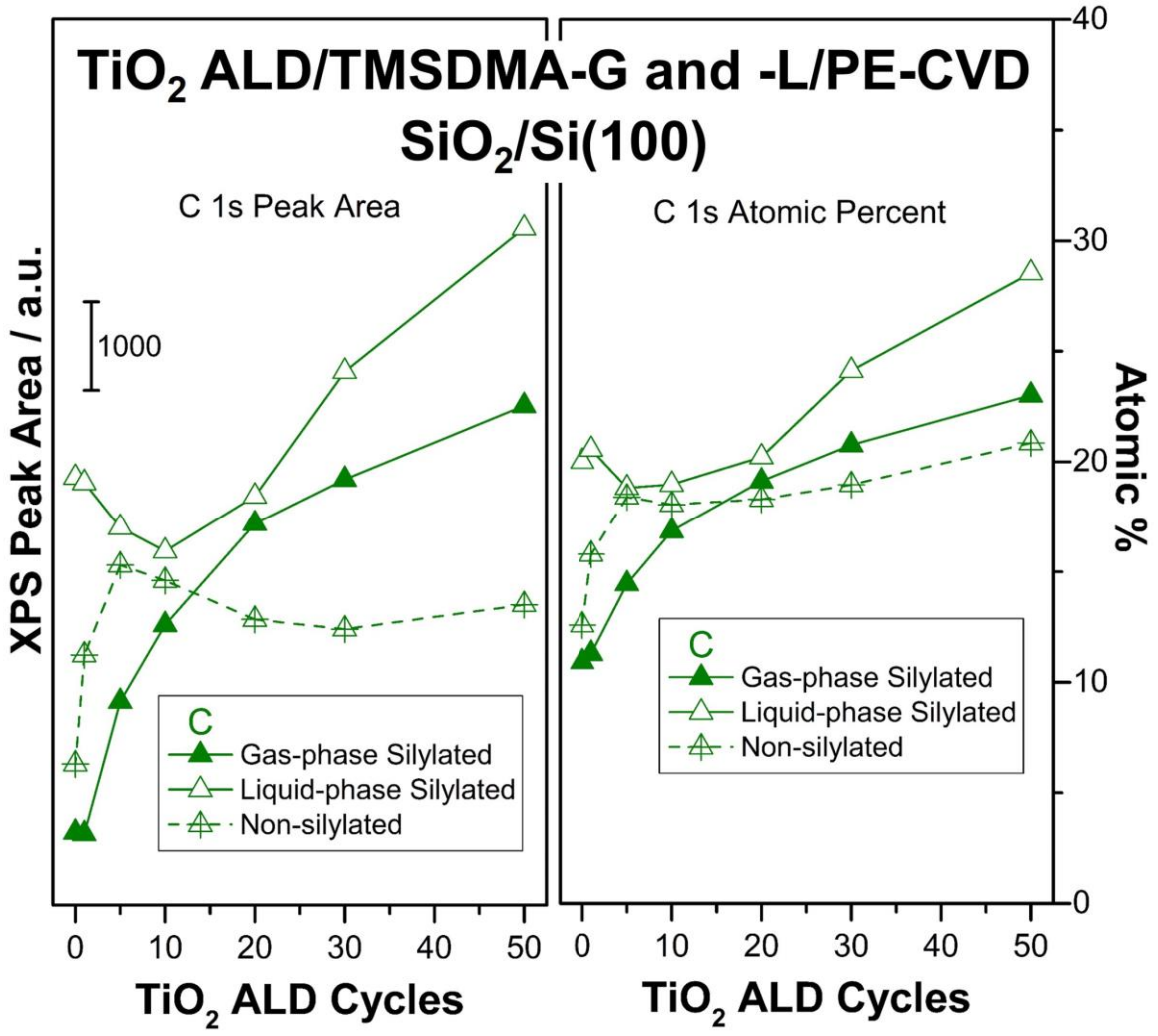


Figure 4.9 (a) C 1s XPS peak area and (b) C surface atomic-percent composition profiles for both gas- and liquid-phase silylated TMSDMA-G or -L/PE-CVD SiO_2/Si(100) surfaces as a function of increasing TiO_2 ALD cycles. The data is compared to the results from the non-silylated (PE-CVD SiO_2/Si(100)) substrate.

As previously mentioned in Chapter 2, all surface composition data presented in this work are reported using atomic percentages as fractions of the total composition (after applying appropriate ASFs) that include not only Ti (replaced by Hf in the case of HfO_2 ALD) and Si but also C and O (the latter is not directly reported here). It is also important

to specify that the analysis of the C 1s XPS data after ex-situ transfer of the solid substrates is partially hindered by the deposition of adventitious carbon that typically accompanies most ex-situ handling procedures. Nevertheless, some conclusions may still be made based on relative trends in carbon content when contrasting the data obtained for various surfaces. For instance, the surface carbon content increased from 13% to 20% immediately after liquid-phase silylation prior to conducting any TiO_2 ALD. In comparison, the surface carbon content using the in-situ gas-phase process surprisingly decreased to 11%. The amount of carbon on both surfaces then evolves with increasing number of ALD cycles but is always lower for the gas-phase silylated surface relative to that of the liquid-phase. The source of this carbon is likely contamination from normal sample handling and not from the decomposition of TDMATi precursor, as the low ALD process temperature of 373 K is not expected to lead to the decomposition of the methyl groups of the dimethylamido ligands on the surface.[81] Furthermore, the absence of any signal in the N 1s XPS data in Figure 4.10 confirms no surface-bound dimethylamido moieties from unreacted or decomposed TDMATi molecules within the growing TiO_2 films. Therefore, the growth of the C atomic-percent over increasing number of TiO_2 cycles is believed to arise from ex-situ exposures.

After assessing the impact of phase on silylation efficacy, we focused our attention on establishing a better understanding of the role of the cleaning process used in these experiments.

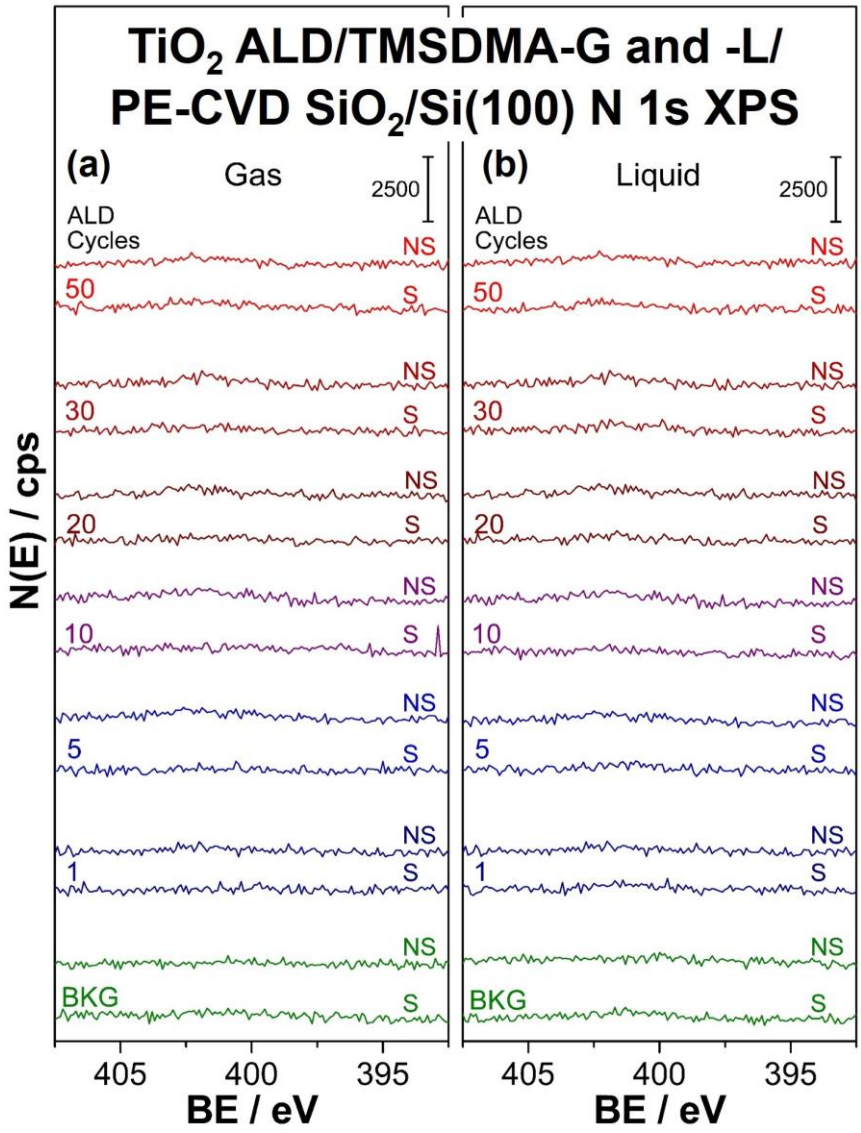


Figure 4.10 N 1s XPS data for the gas- (a) and liquid- (b) phase TMSDMA silylated (TMSDMA-G or -L/PE-CVD SiO_2/Si(100); S) and non-silylated (PE-CVD SiO_2/Si(100); NS) substrates as a function of increasing TiO_2 ALD cycles.

4.4.2 RCA-cleaned SiO_2/Si(100)

To understand the impact of the starting surface on the silylation efficacy to passivate surface nucleation centers against TiO_2 ALD, all prior experiments were repeated using RCA-cleaned SiO_2/Si(100) (RCA SiO_2/Si(100)) substrates. The thickness of the clean hydroxylated oxide layer grown using this protocol is assumed to be similar to that of the original. The XPS data for the experiments involving this new surface for the gas- and liquid-phase silylation processes are provided in Figures 4.11 and 4.12, respectively. The corresponding surface atomic-percent composition as a function of the number of increasing TiO_2 ALD cycles used are plotted in Figure 4.13a.

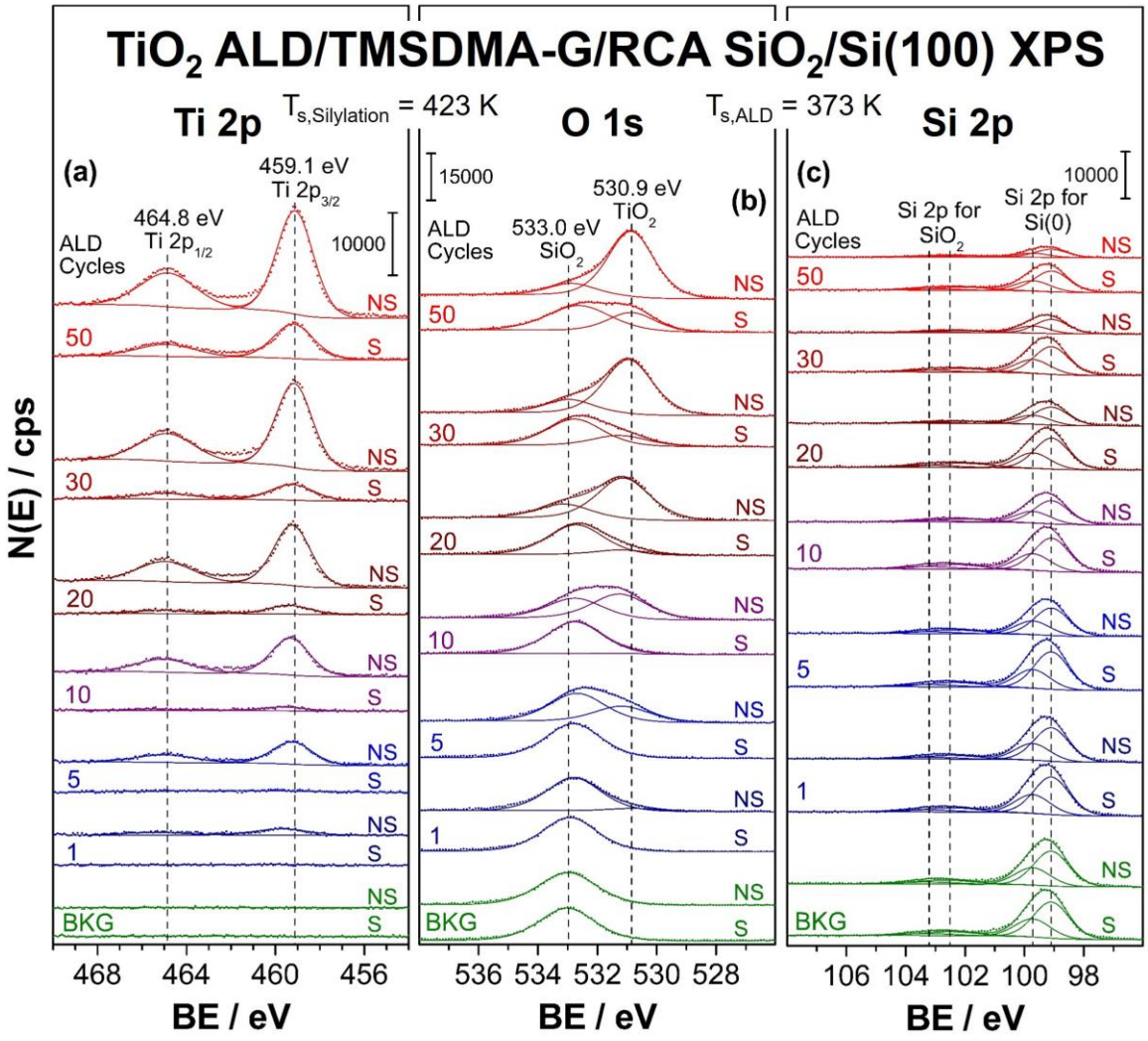


Figure 4.11 Ti 2p (a), O 1s (b), and Si 2p (c) XPS data for the gas-phase TMSDMA-silylated (TMSDMA-G/RCA SiO_2/Si(100), denoted in this figure as S), and non-silylated (RCA SiO_2/Si(100), denoted as NS) RCA-cleaned SiO_2/Si(100) substrates as a function of increasing number of TiO_2 ALD cycles. The raw data are shown as dots and the fitted peaks as lines.

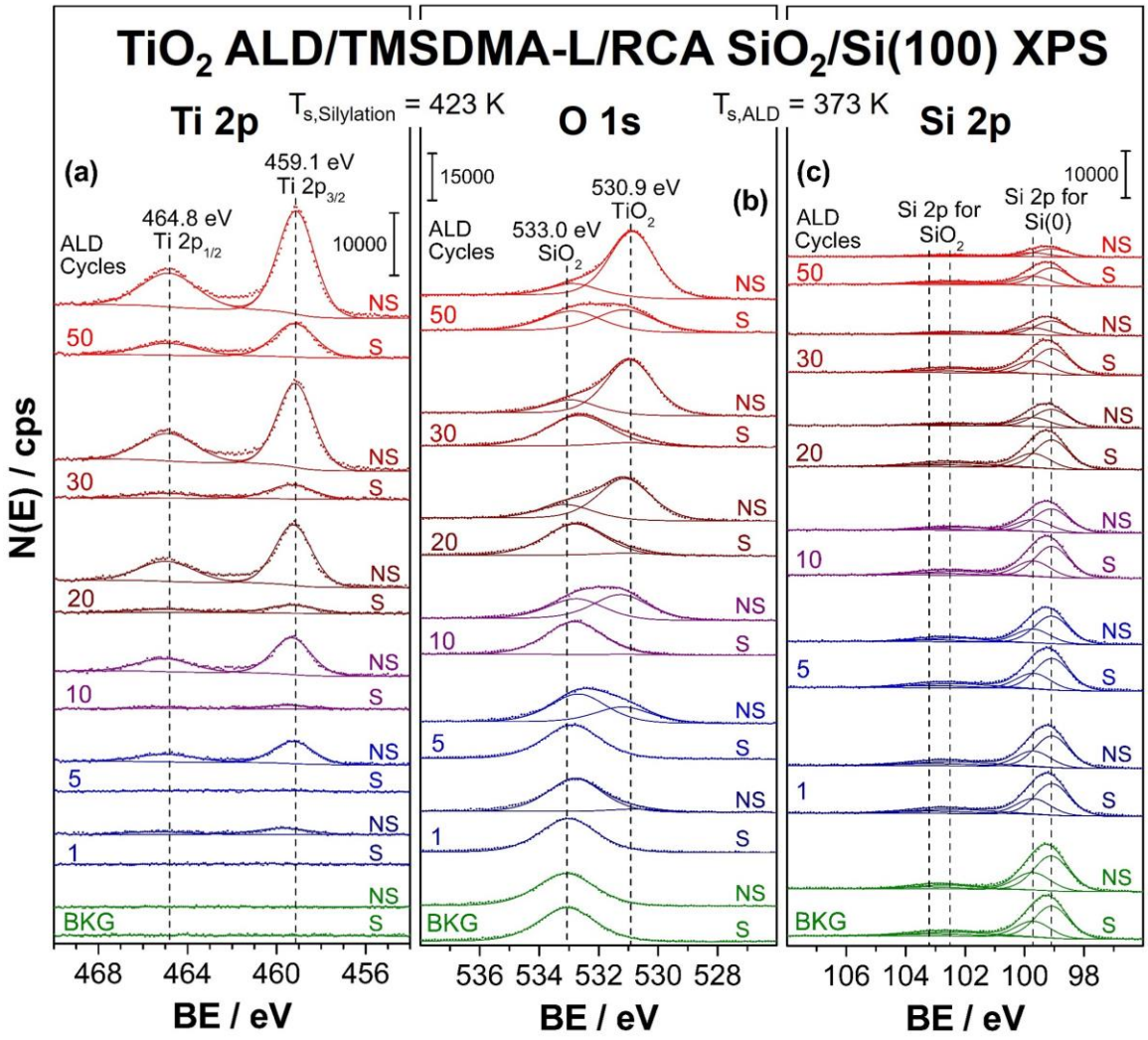


Figure 4.12 Ti 2p (a), O 1s (b), and Si 2p (c) XPS data for the liquid-phase TMSDMA-silylated (TMSDMA-L/RCA SiO_2/Si(100), denoted in this figure as S), and non-silylated (RCA SiO_2/Si(100)), denoted as NS) RCA-cleaned SiO_2/Si(100) substrates as a function of increasing number of TiO_2 ALD cycles. The raw data are shown as dots and the fitted peaks as lines.

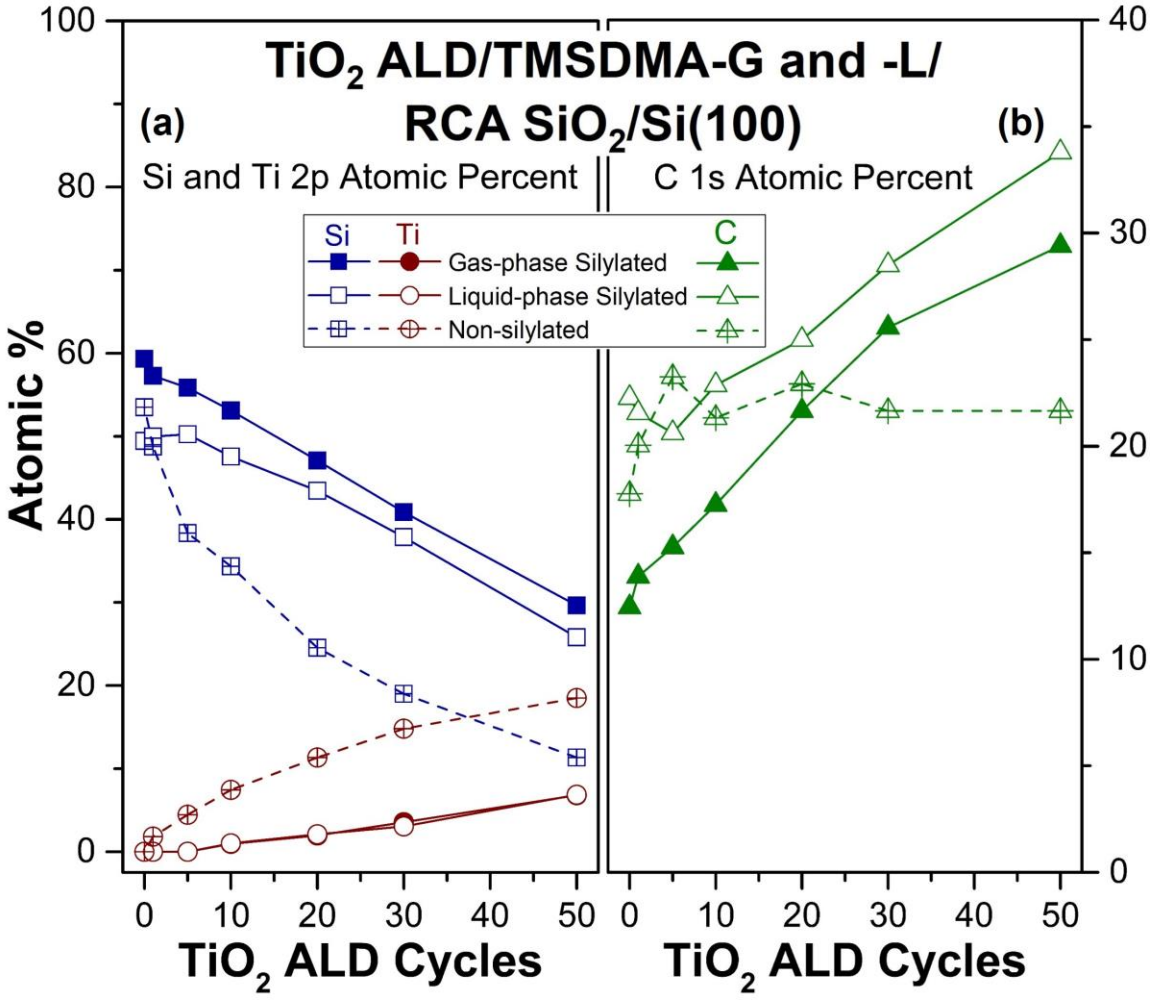


Figure 4.13 Si and Ti (a) and C (b) surface atomic-percent composition profiles for both TMSDMA-G and -L/RCA SiO_2/Si(100) surfaces as a function of increasing number TiO_2 ALD cycles conducted. They are compared to the results from the non-silylated (RCA SiO_2/Si(100)) substrate.

Similar to the previous results using the PE-CVD SiO_2/Si(100) surfaces, the Ti 2p signal is absent for at least the first 5 ALD cycles in the silylated RCA-cleaned samples (TMSDMA-G or -L/RCA SiO_2/Si(100)); the nucleation delay ends following 10 cycles, after which the Ti atomic percent is observed to increase on both of the silylated surfaces. Once again in comparison, a lower degree of carbon is deposited on the sample prepared

using the gas-phase procedure (TMSDMA-G/RCA SiO_2/Si(100)) as indicated by the C atomic percent trends displayed in Figure 4.13b, estimated from the C 1s XPS data. Not only is less carbon deposited on the surface silylated in the gas-phase throughout the process of TiO_2 film growth, but also a reduction in the overall carbon content is observed even prior to ALD: the carbon content decreases from 18% to 13% after gas-phase silylation whereas it evolves to 22% in the case of the liquid-phase method. The calculated film thickness as a function of TiO_2 ALD cycles for both gas- and liquid-phase silylated RCA-cleaned SiO_2/Si(100) surfaces are displayed in Figure 4.14.

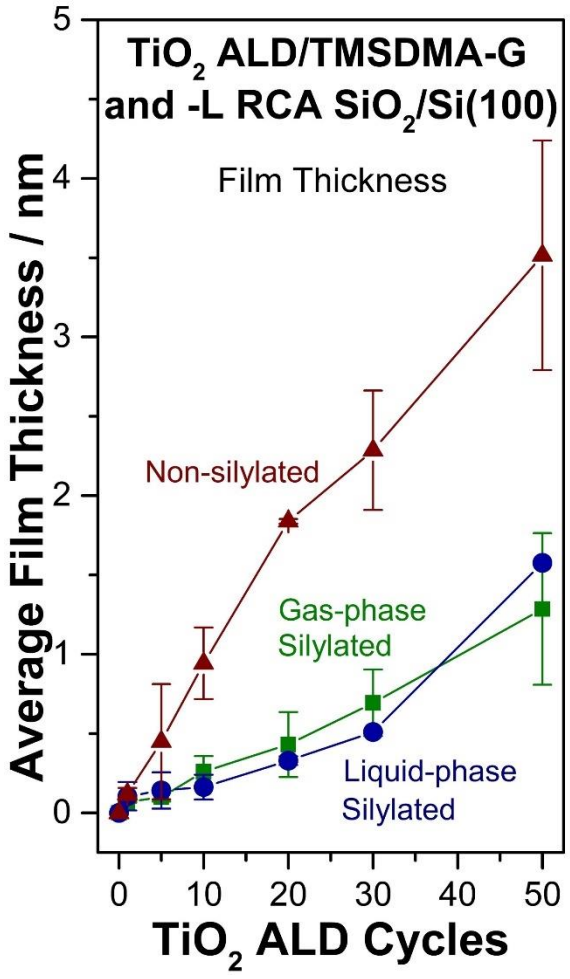


Figure 4.14 Average TiO_2 film thickness for TMSDMA-G and -L/RCA SiO_2/Si(100) compared to the non-silylated (RCA SiO_2/Si(100)) substrate, estimated using the SiO_2-Si 2p and SiO_2-O 1s XPS peak areas in combination with corresponding ASFs.

Similar to previous results, linear film growth is again observed after a nucleation delay of 5 TiO_2 ALD cycles (Figure 4.14). Unlike the film thickness measurements on the PE-CVD SiO_2/Si(100) substrates, the deposition rate on the RCA SiO_2/Si(100) surfaces is approximately the same for both the gas- and liquid-phase silylated substrates between 10 and 30 ALD cycles: 0.2 Å/ALD cycle. The similar growth behavior for both these surfaces diverges by 50 cycles where the film growth continues linearly for the gas-phase silylated

surface but grows at a faster rate for that of the liquid-phase to the point where a higher film thickness of approximately 1.6 nm is reached over that of approximately 1.3 nm on the former surface. This is intriguing, as the results observed here may reiterate the notion of potential defect propagation that may occur within the passivating monolayer generated in the liquid phase after reaching a certain threshold during the film deposition process, leading to larger film growth during the later stages of ALD. In comparison, the steady-state film growth observed again for the gas-phase silylated surface may suggest a lower degree of defects that exist within the network of trimethylsilyl groups that comprise the monolayer.

After thoroughly examining the passivation efficacy of silica surfaces, prepared using two different cleaning methods, using TiO_2 ALD as a reference system, subsequent experiments were conducted to understand how this passivation scheme would inhibit other metal oxide film growth using metalorganic precursors possessing higher reactivity.

4.6 Silylation Efficacy Against HfO_2 ALD on PE-CVD-Grown SiO_2/Si(100) – Gas vs. Liquid Phase

The passivation efficacy of the silylation process was next evaluated for the case of HfO_2 ALD using TDMAHf, which is known to be more reactive relative to TDMATi,[82] and H_2O in order to assess the limitations of the passivation scheme. PE-CVD-grown SiO_2/Si(100) substrates were selected as the starting surface of interest. It should be noted that from this point, all further experiments and data presented regarding SiO_2 surfaces refer to those grown using PE-CVD. Figure 4.15 displays the Hf 4f XPS data for both the

gas- (a) and liquid-phase (b) silylated (S) and non-silylated (NS) PE-CVD-grown SiO_2/Si(100) surfaces as a function of increasing number of HfO_2 ALD cycles performed.

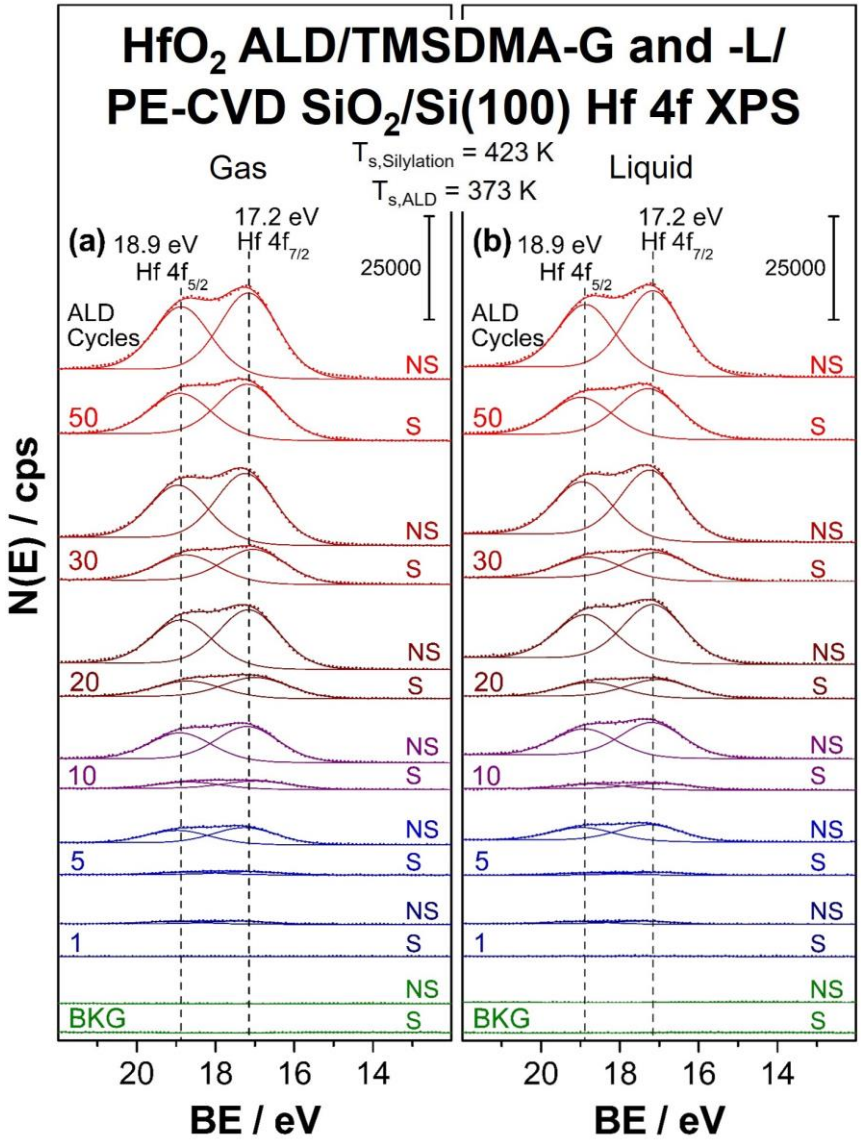


Figure 4.15 Hf 4f XPS data for the gas- (a) and liquid- (b) phase TMSDMA-silylated (TMSDMA-G or -L/PE-CVD SiO_2/Si(100); S) and non-silylated (PE-CVD SiO_2/Si(100); NS) substrates as a function of increasing number of HfO_2 ALD cycles. The raw data are shown as dots and the fitted peaks as lines.

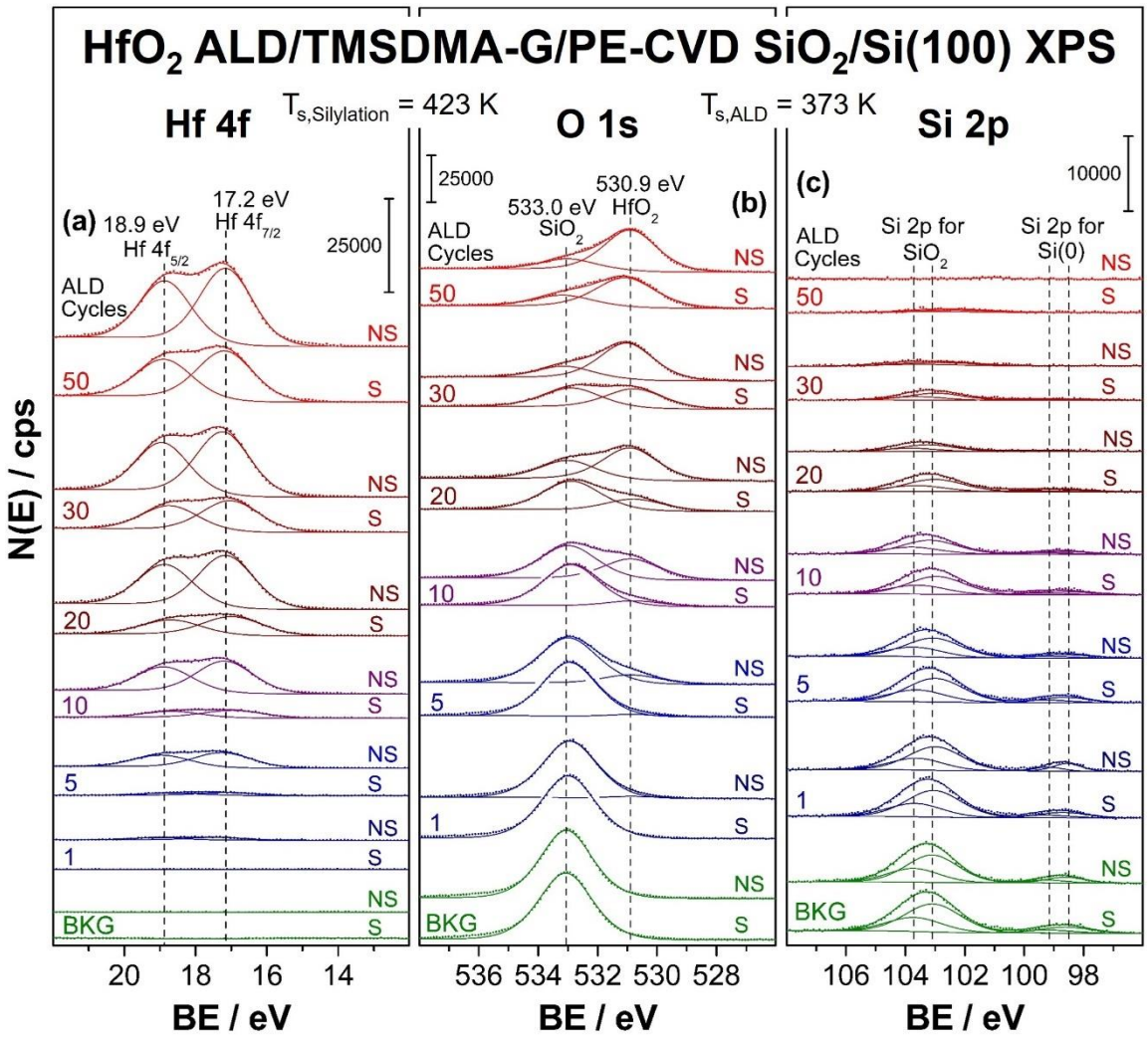


Figure 4.16 Hf 4f (a), O 1s (b), and Si 2p (c) XPS data for the gas-phase TMSDMA-silylated (TMSDMA-G/PE-CVD SiO_2/Si(100); S), and non-silylated (PE-CVD SiO_2/Si(100); NS) PE-CVD-grown SiO_2/Si(100) substrates as a function of increasing number of HfO_2 ALD cycles. The raw data are shown as dots and the fitted peaks as lines. The Hf 4f XPS data in Figure 4.16a is the same as that displayed in Figure 4.15a.

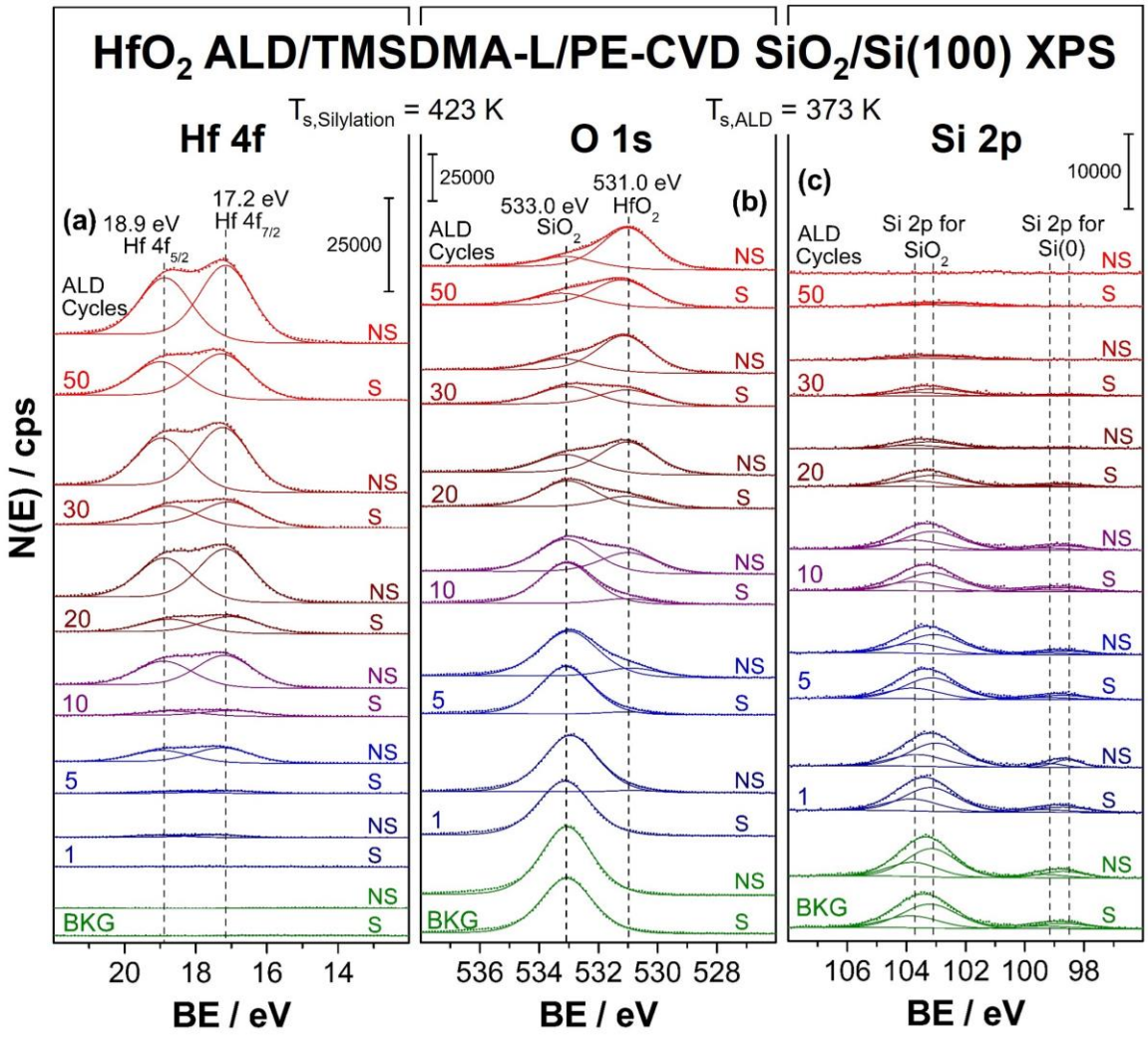


Figure 4.17 Hf 4f (a), O 1s (b), and Si 2p (c) XPS data for the liquid-phase TMSDMA-silylated (TMSDMA-L/PE-CVD SiO_2/Si(100); S), and non-silylated (PE-CVD SiO_2/Si(100); NS) PE-CVD-grown SiO_2/Si(100) substrates as a function of increasing number of HfO_2 ALD cycles. The raw data are shown as dots and the fitted peaks as lines. The Hf 4f XPS data in Figure 4.17a is the same as that displayed in Figure 4.15b.

Similar to the case of the TiO_2 ALD tests using TDMATi, an initial nucleation delay in the adsorption of TDMAHf and subsequent growth of HfO_2 was observed after functionalizing the SiO_2 surface with passivating trimethylsilyl groups, although to a lesser extent. Specifically, in the case of both gas- (Figure 4.15a) and liquid-phase (Figure 4.15b)

silylated surfaces the Hf 4f spin-orbit split XPS signals are absent after the first ALD cycle. In comparison, the appearance of these peaks at 18.9 and 17.2 eV corresponding to the Hf $4f_{5/2}$ and $4f_{7/2}$ photoelectrons, respectively, is already observed in the spectrum for the blank substrate. Both the gas- and liquid-phase silylated surfaces display a similar ability to inhibit HfO_2 ALD film growth when comparing the evolution of the spectra in panels (a) and (b), consistent with the results obtained previously when employing TiO_2 ALD. Concomitant to these observations are the changes in the O 1s XPS data, in which the appearance of a peak at 531.0 eV corresponding to a Hf-O bonding environment is already observed after the first ALD cycle on the blank surface, but does not appear until after 5 cycles for both the gas- and liquid-phase silylated substrates (Figure 4.16b and 4.17b, respectively). Finally, attenuation of both the PE-CVD-grown SiO_2 overlayer (SiO_2-Si 2p) and the Si(0) bulk (Si(0)-Si 2p) signals in the Si 2p XPS are observed after the one-cycle nucleation delay. The Si 2p signal for both SiO_2 and Si(0) completely attenuate to 0 CPS after 50 HfO_2 ALD cycles on the non-silylated PE-CVD SiO_2/Si(100) surface, suggestive of the overlayer completely burying the underlying silica substrate.

The processed XPS data for these experiments are summarized in the form of Si 2p and Hf 4f XPS peak areas and atomic compositions in Figure 4.18, the fraction of the O 1s XPS signal attributed to HfO_2 in Figure 4.19, and the average film thickness in Figure 4.20, all plotted as a function of increasing number of HfO_2 ALD cycles conducted.

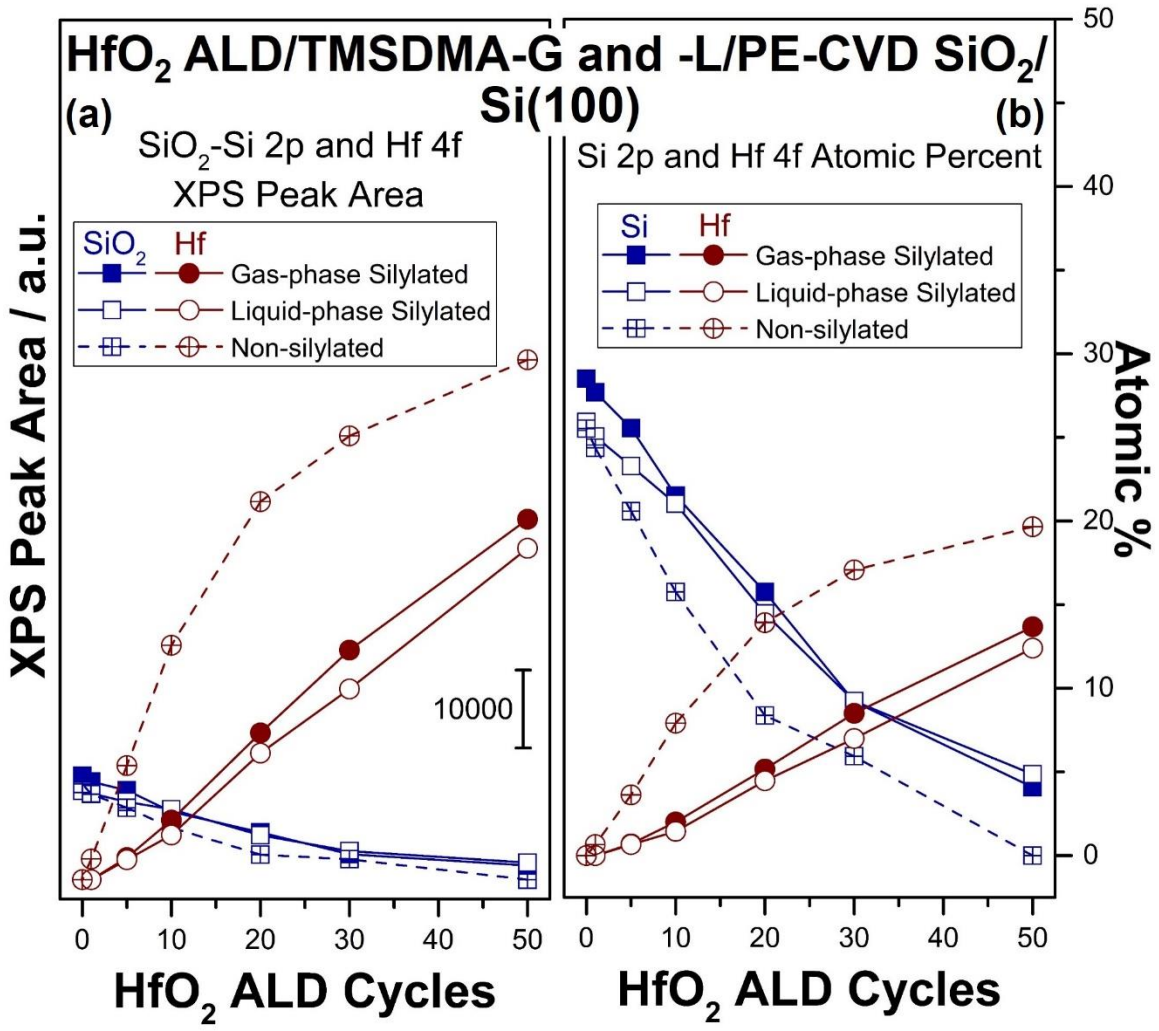


Figure 4.18 (a) Areas of the SiO_2-Si 2p and Hf 4f peaks derived from the XPS data presented in Figures 4.16 and 4.17 for both gas- and liquid-phase silylated PE-CVD-grown SiO_2/Si(100) compared to that of a non-silylated substrate as a function of increasing number of HfO_2 ALD cycles. (b) Si and Ti surface atomic-percent composition profiles calculated from the data in panel (a) in combination with corresponding ASFs.

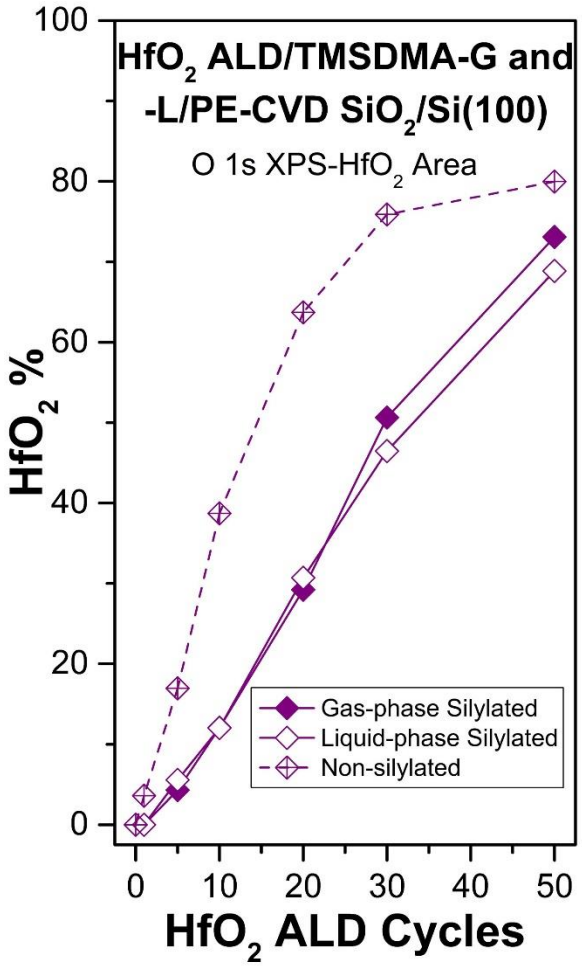


Figure 4.19 Peak areas of the HfO_2 component of the O 1s XPS signal (HfO_2-O 1s XPS) measured for gas- and liquid-phase silylated PE-CVD-grown SiO_2/Si(100) (denoted as HfO_2 ALD/TMSDMA-G/PE-CVD SiO_2/Si(100) and TiO_2 ALD/TMSDMA-L/PE-CVD SiO_2/Si(100), respectively) after depositing HfO_2 films via ALD. The HfO_2-O 1s data are compared to that of a non-silylated substrate (HfO_2 ALD/PE-CVD SiO_2/Si(100)) and are plotted as a percentage of the total O 1s XPS signal (obtained from Figures 4.16 and 4.17) versus the number of HfO_2 ALD cycles conducted.

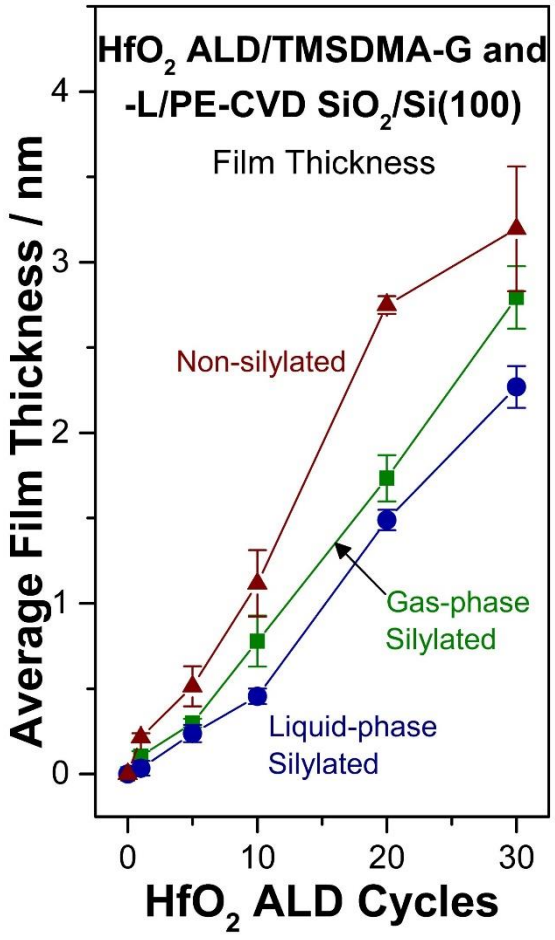


Figure 4.20 Average HfO_2 film thickness for TMSDMA-G and -L/PE-CVD SiO_2/Si(100) compared to the non-silylated (PE-CVD SiO_2/Si(100)) substrate, estimated using the SiO_2-Si 2p and SiO_2-O 1s XPS peak areas in combination with corresponding ASFs.

The experiments involving HfO_2 ALD on the silylated PE-CVD grown SiO_2/Si(100) (TMSDMA-G or -L/PE-CVD SiO_2/Si(100)) are interesting, as the trends observed here diverge significantly from those for the films deposited using TiO_2 ALD. While comparable efficacies between the gas- and liquid-phase silylated surfaces are observed with regards to their ability to inhibit the first HfO_2 ALD cycle, the amount of HfO_2 deposited after this nucleation delay, in terms of Hf 4f XPS peak area and Hf surface

atomic-percent (Figure 4.18), is always lower on the surface modified in the liquid-phase relative to that of the gas-phase as the number of HfO_2 ALD cycles used increases. The average film thickness derived from this data and displayed in Figure 4.20 is also reflective of this observation. Furthermore, an intriguing observation is made in the film deposition rate for both the gas- and liquid-phase silylated substrates: a constant GPC of approximately 0.10 Å/ALD cycle is observed in the former, while two distinct growth regimes exist between 1 to 10 and 10 and 30 cycles in the case of the liquid-phase.

These results suggest that, in the case of HfO_2 ALD, the liquid-phase organosilane monolayer may exhibit a slightly higher efficacy in keeping hydroxyl nucleation centers passivated and delaying precursor chemisorption at defect nucleation sites throughout the HfO_2 film deposition process, even after the initial nucleation delay is lost. A more comprehensive understanding of the quality of the passivation layer generated in both the gas- and liquid-phase can be derived based on the C 1s XPS data presented in Figures 4.21 and 4.22.

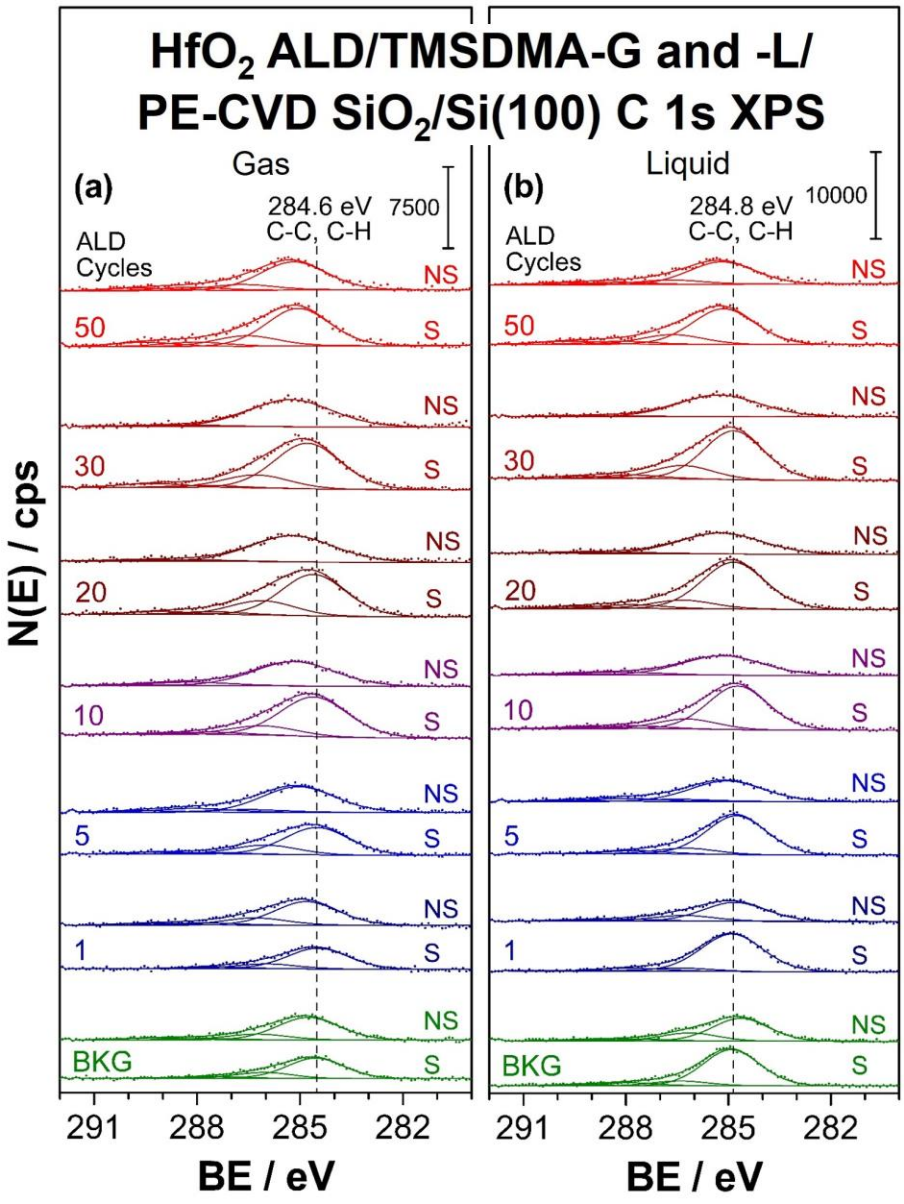


Figure 4.21 C 1s XPS data for the gas- (a) and liquid- (b) phase TMSDMA-silylated (TMSDMA-G or – L/PE-CVD SiO_2/Si(100); S) and non-silylated (PE-CVD SiO_2/Si(100); NS) substrates as a function of increasing number of HfO_2 ALD cycles. The raw data, shown as dots, were fitted to four peaks (from high to low BE: O-C=O, C=O, C-O-C/C-O-H, and C-C/C-H bonding environments), shown as lines.

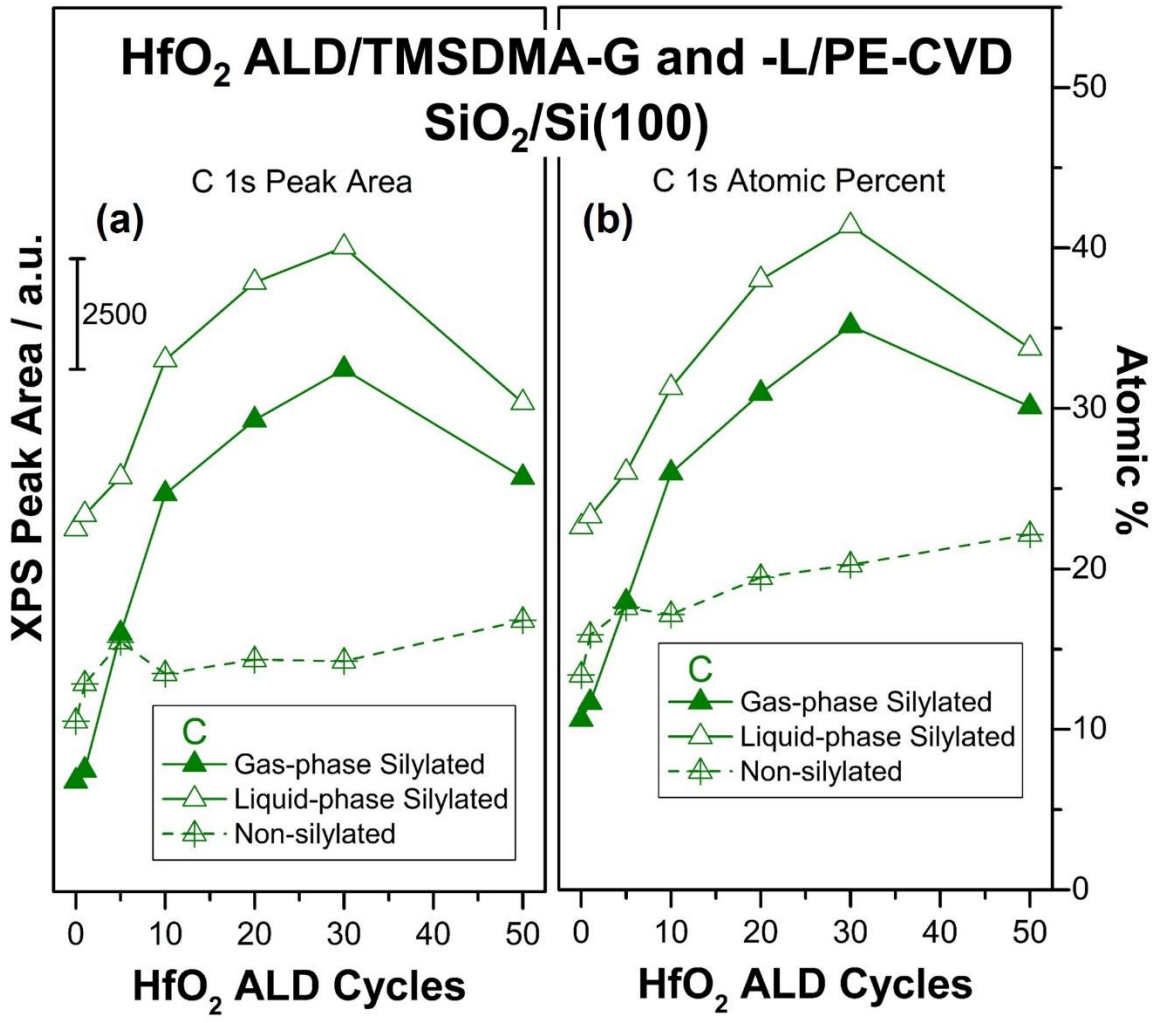


Figure 4.22 (a) C 1s XPS peak area and (b) C surface atomic-percent composition profiles for both gas- and liquid-phase silylated TMSDMA-G or -L/PE-CVD SiO_2/Si(100) surfaces as a function of increasing HfO_2 ALD cycles. The data is compared to the results from the non-silylated (PE-CVD SiO_2/Si(100)) substrate.

The plot of the total carbon surface atomic-percent composition, obtained from the data in Figure 4.21, is displayed in Figure 4.22. Similar to the previous results, the surface carbon content is observed to decrease immediately after gas-phase silylation but prior to HfO_2 ALD from approximately 13% to about 11%. In comparison, the carbon content for the liquid-phase method evolves from 13% to 23%. The carbon content exhibits a

consistent trend with increasing number of ALD cycles but is always lower on the gas-phase silylated surface. In addition to the carbon content observed for the experiments involving TiO_2 ALD on PE-CVD and RCA SiO_2/Si(100), the third example provided here demonstrates a higher degree of carbon within the monolayer formed using the liquid-phase method. This underscores an inherent difference that exists between the two passivating monolayers generated in different media: while both have similar inhibition efficacies, the gas-phase approach generates a monolayer with a lower carbon content compared to its liquid-phase counterpart. Certainly, the gas-phase method does not lead to an increase in the surface carbon content like that observed for the liquid-phase. The absence of any signals in the N 1s XPS data shown in Figure 4.23 confirmed that precursor decomposition in the form of dimethylamido moieties did not occur. The observations from the C 1s XPS data indicate differences in the quality of the monolayers generated in both the gas- and liquid-phase. It is speculated that this may imply fundamental differences in the structure, binding modes, and/or order of the trimethylsilyl functionalities that comprise the monolayer. Other studies would be needed to confirm this, which are beyond the scope of this current work.

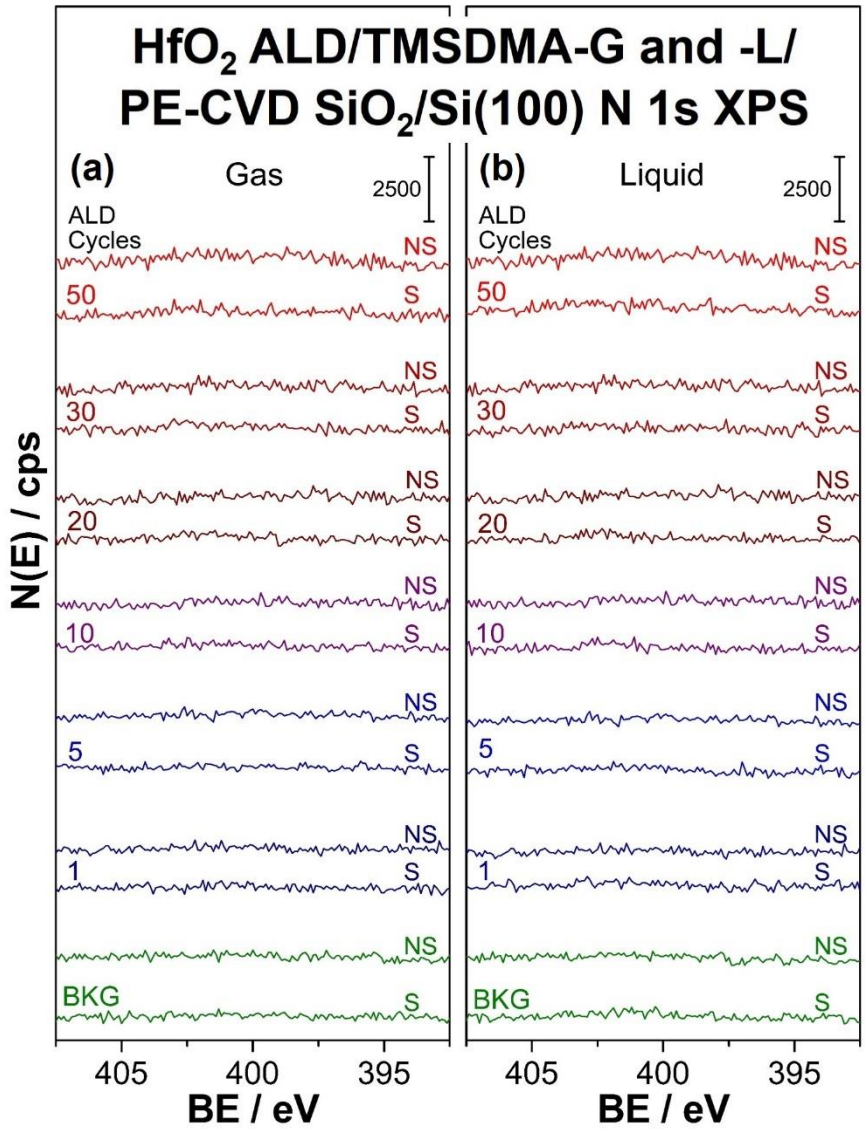


Figure 4.23 N 1s XPS data for the gas- (a) and liquid- (b) phase TMSDMA silylated (TMSDMA-G or -L/PE-CVD SiO_2/Si(100); S) and non-silylated (PE-CVD SiO_2/Si(100); NS) substrates as a function of increasing HfO_2 ALD cycles.

4.7 Discussion

Most silica surfaces exhibit a low density of silanol sites, typically ranging from approximately 1-2 Si-OH groups/nm^2.[83,84] This value may even be lower on flat substrates – fewer than 1 silanol site/nm^2. As a result, the initial silica surface is not ideal for the formation of a densely packed passivating monolayer capable of inhibiting chemical reactions such as those in ALD[26], thus allowing for more energetically favorable surface nucleation pathways during ALD. A SiO_2 PE-CVD step was therefore employed prior to surface modification with TMSDMA as it is well-established that high-quality clean silica films can be formed when using plasma, in addition to improving the surface hydroxyl density.[85,86] The SiO_2 overlayer deposited using PE-CVD on the Si(100) substrates was calculated to be approximately 4.5 nm in thickness (Figure 4.1). Additionally, an RCA cleaning protocol was conducted on different substrates prior to silylation as an alternative method for surface cleaning.

Following metal oxide ALD to assess the passivation efficacy of the silylated silica substrates, differences in the Ti 2p and Hf 4f XPS peak positions were observed during the early stages of TiO_2 or HfO_2 ALD, respectively. In the case of TiO_2 ALD on silica, a minor shift in the Ti 2p spin-orbit split XPS signals to lower binding energies in Figure 4.3a and Figure 4.6a (gas- vs. liquid-phase silylated PE-CVD SiO_2/Si(100), respectively) is observed as the number of TiO_2 ALD cycles used is increased, stabilizing at approximately 458.5 eV (or 459.1 eV for the TMSDMA-silylated RCA-cleaned SiO_2/Si(100) shown in Figure 4.11a and 4.12a) by 50 cycles. The binding energy of Ti atoms at the interface after the first TiO_2 ALD cycle appears at a higher position due to the formation of Si-O-Ti

bonds[54]; as Si is more electronegative than Ti, the photoelectrons from the Ti 2p orbital are ejected with lower kinetic energy and thus possess a higher binding energy. A decrease in the binding energy of approximately 0.5 eV is observed as the TiO_2 film becomes more bulklike with increasing ALD cycles forming a larger network of Ti-O-Ti bonds. This observation occurs to a lesser extent for the RCA-cleaned silica substrates (Figure 4.11a).

Following HfO_2 ALD on the PE-CVD-grown SiO_2 substrates, an inverse trend is observed in the Hf 4f XPS data (Figure 4.15) wherein a slight shift towards higher binding energies is exhibited for the silylated surfaces with increasing number of HfO_2 ALD cycles. However, the Hf 4f peak position remains stable for unmodified silica. This is interesting, as it may reflect a difference in the nucleation pathway of TDMAHf on the trimethylsilyl-terminated surface relative to the unmodified substrate. The Hf $4f_{7/2}$ binding energy increases to a constant value of 17.2 eV as the thickness of the deposited HfO_2 is increased. These distinct observations may suggest different passivation loss mechanisms between TiO_2 and HfO_2 ALD, relying on differences in the underlying surface chemistry of TDMAHf with silylated SiO_2 relative to that of TDMATi.

The XPS results from these studies showed that both the PE-CVD-grown and RCA-cleaned SiO_2/Si(100) surfaces remained passivated up to 5 TiO_2 ALD cycles and 1 HfO_2 ALD cycle (on the former surface) after silylation with TMSDMA in either the gas or liquid phase. After enough ALD cycles however, nucleation of the metalorganic precursor on the surface eventually occurs leading to propagating film growth of the metal oxide. While the exact nature of inhibition loss for these specific systems is complex and not yet fully understood, some speculations can be made into potential nucleation mechanisms of

precursor chemisorption onto the non-growth surface (NGS). For example, it has been reported that fixed nucleation sites may already be present on the NGS after silylation but prior to ALD.[87] Simulations have showed that the interaction of small-molecule inhibitors (SMIs) with the surface in the gas phase can limit the density of inhibitor moieties due to random surface adsorption, in combination with steric shielding effects that may arise leading to a few surface nucleation centers remaining active even after inhibitor saturation.[88,89] Consequently, precursor chemisorption with energetically favorable nucleation centers could be made possible through this mechanistic route. In relation to this work however, this is believed not to be the case for the systems discussed herein as precursor nucleation was inhibited for at least five TiO_2 ALD cycles and the first HfO_2 ALD cycle, indicating the hydroxyl nucleation sites where nucleation takes place on during ALD were already fully consumed and/or inaccessible for chemical reactions. Additionally, Xu et. al. has demonstrated alternative nucleation pathways that neither involve the loss of organosilane inhibitor molecules (dimethyl or trimethylsilyl moieties on SiO_2) from the passivation layer nor precursor chemisorption on hydroxyl nucleation sites after ZrO_2 ALD system using tetrakisethylmethylamido zirconium (TEMAZr) and H_2O.[90] In their in-situ FT-IR study, signal attenuations were observed for the Si-O-Si phonon modes at 1080 and 1250 cm^{-1} without any attenuation in the 2800-3000 cm^{-1} region corresponding to the methyl functional groups of adsorbed organosilane inhibitor species. This suggested a mechanism where the initial interaction of TEMAZr molecules with bridge-bonded oxygen sites induced a strain in siloxane ring structures of the passivated SiO_2/Si(100) surface without breaking the siloxane bonding network. The perturbation of

the Si-O-Si bonds persisted even after the 6th ALD cycle; this was attributed to repeated TEMAZr and H_2O exposures finally reacting with the strained Si-O-Si bonds allowing for the formation of nucleation sites in the silica network without initially compromising the passivating monolayer, as no increase in the isolated OH stretching modes was observed. Similarly, it has also been demonstrated that highly reactive molecules may become trapped in strongly bound physisorbed states on the passivated surface without generating defects within the passivating monolayer.[35,36] These molecules remain on the surface even after the purging step following the precursor pulse, becoming available for chemisorption during the next ALD cycle.[24,91] While these mechanisms may have been involved in our systems herein, it is difficult to distinguish between the individual nucleation sites that exist on these particular surfaces. However, it is believed that the loss of inhibition likely occurs through a ligand exchange mechanism on the initially fully passivated substrate, in which trimethylsilyl moieties are eventually randomly displaced on the NGS with repeated ALD cycles. The continued interaction of the precursor molecules with the surface may reduce the energy barrier for chemisorption until stable nuclei are able to initially bond to available active sites. Precursor chemisorption on these defects becomes facilitated after overcoming this initial induction period allowing for thicker films to grow as the number of ALD cycles used is increased.

As previously mentioned, it is difficult to distinguish between different types of nucleation centers present on our silica surfaces. However, it is suggested that differences in nucleation sites that exist on these silica surfaces play a critical role in determining the passivation efficacy that can be obtained when considering various ALD processes.

Distinct passivation efficacies were obtained between the TiO_2 and HfO_2 ALD conducted in this work, both of which employed metalorganic precursors possessing the same TDMA-framework. It has been reported that different precursors may react with various types of hydroxyl nucleation sites. For example, TMA is observed to adsorb on both isolated and vicinal hydroxyl groups whereas lower reactivity aluminum-based molecules such as dimethylaluminum isopropoxide and tris(dimethylamino)aluminum only have a high affinity for bonding to isolated hydroxyl sites.[91,92] This may be the case for TDMATi and TDMAHf, in which the higher reactivity of the TDMAHf molecule could be attributed to its ability to adsorb on multiple types of hydroxyl nucleation centers whereas TDMATi may have a higher tendency to only adsorb on a single type (Figure 4.24). However, this is only speculation and further experiments such as in-situ FT-IR measurements would be necessary to support this claim.

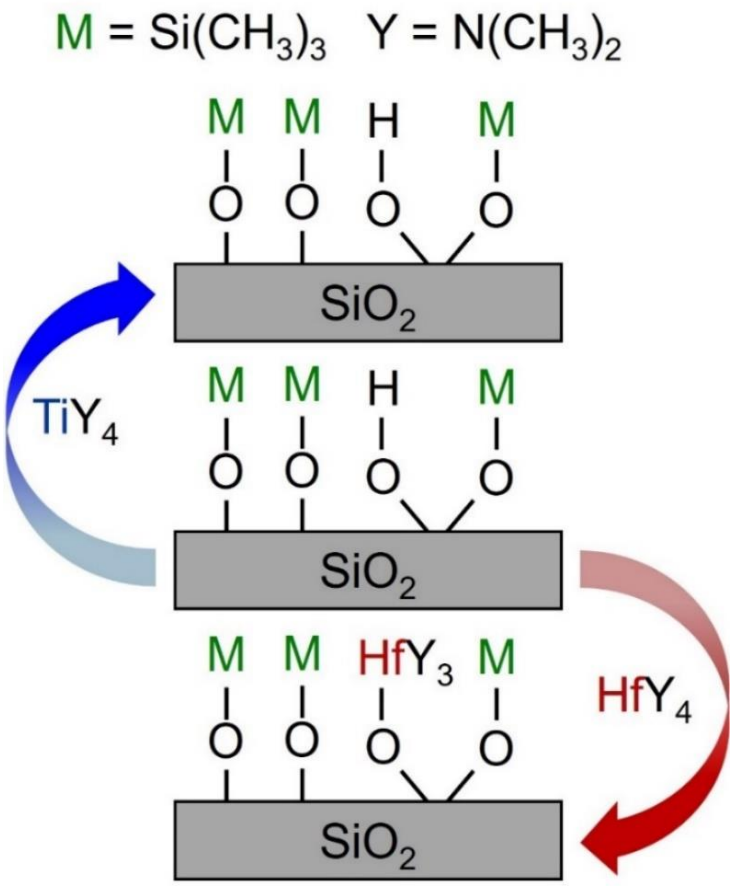


Figure 4.24 Schematic depicting possible chemisorption pathways that may exist between TDMATi and TDMAHf based on differences in the affinity to react with hydroxyl nucleation centers. The byproduct formed in either of these reactions is dimethylamine.

Density functional theory measurements have also shown that a relatively low energy barrier of 0.84 eV exists for the adsorption of TDMAHf on silica.[28] Thus, it is plausible that the higher reactivity of TDMAHf over TDMATi is in part due to an energetically favorable chemisorption process that can occur on multiple types of nucleation sites. It is also interesting to note that, to the best of our knowledge, only one other XPS study so far has directly assessed the impact of HfO_2 ALD, using TDMAHf as

the metalorganic precursor, on silica surfaces passivated with TMSDMA in the gas phase and found that precursor nucleation on the surface occurred by 1 ALD cycle.[64] Contrastingly, the results obtained here demonstrated that the silica surface remained passivated for at least the first HfO_2 ALD cycle.

It was determined that regardless of the parameters changed throughout the series of experiments conducted (SiO_2 cleaning procedure or metal oxide ALD system), both the gas- and liquid-phase silylation methods displayed similar abilities to inhibit thin-film deposition. Additionally, similar peak intensities and spectral trends throughout the process of deposition the metal oxide films were obtained indicative of comparable growth during the ALD process. Based on these observations, it can be concluded that an intrinsic limitation exists with regards to the degree of passivation that is achievable using this surface modification scheme. While the passivation efficacies for both the gas- and liquid-phase silylation method have been comparable, one critical difference observed was within the C 1s XPS data reflective of the distinct carbon contents of the silica surfaces passivated using these two methods. Immediately after liquid-phase silylation but prior to metal oxide ALD, an increase in the carbon signal by approximately a factor of two relative to the-phase method was observed on the PE-CVD-grown SiO_2/Si(100) surfaces. This may be attributed to a lack of controllability over the reaction that occurs with SiO_2 in the liquid phase. While comparable efficacy is achieved, the passivating monolayer is likely comprised of a number of defective sites containing multiple carbon-based agglomerates not associated with the layer leading to a reduction in its quality.[40] Contrastingly, the gas-phase method generated a passivating monolayer where the carbon composition is nearly

half that of the liquid-phase counterpart, indicative of a lower degree of defects that exist within the layer.

Based on these observations, it is proposed that the gas-phase modification scheme affords greater advantages over that of the liquid-phase, especially when put into the broader context of industrial applications such as integrability with microelectronics manufacturing steps and process design. This is promising, as Chapter 6 will later discuss how the gas-phase approach may also provide a way to control the density of available silanol nucleation centers on silica surfaces for the tunability of films grown by ALD.

4.8 Conclusion

Both PE-CVD-grown and RCA-cleaned SiO_2/Si(100) surfaces were passivated with TMSDMA in both the gas- and liquid-phase, and the silylation efficacy was assessed by evaluating the kinetics of TiO_2 ALD on both surfaces and HfO_2 on the former. Complete surface passivation was achieved during the early stages of ALD up to 5 TiO_2 and 1 HfO_2 ALD cycle(s) prior to film growth occurring on the modified surfaces. A nucleation delay of approximately 10 TiO_2 or 2 HfO_2 ALD cycles was achieved depending on the metal oxide ALD system employed. Inhibition loss on the NGS was eventually detected in the form of precursor chemisorption possibly through a ligand exchange mechanism; however, the surface remained partially passivated up to 50 ALD cycles. It was observed that the TDMAHf precursor displayed higher reactivity with the surface relative to TDMATi, which may be attributed to a higher affinity for multiple types of hydroxyl nucleation sites rather than only one type. After the onset of nucleation, similar film growth rates were

obtained between the gas- and liquid-phase silylated substrates for either metal oxide ALD process, reflective of comparable passivation efficacies. Furthermore, an intrinsic limitation may exist with regards to the degree of inhibition achievable.

While similar passivation efficacies were observed, one major difference that existed was the carbon content for each surface prior to ALD evidenced by the C 1s XPS data. In the case for the liquid-phase process, a C 1s signal intensity nearly twice that of the gas-phase method was observed indicative that a higher degree of carbon-based species unassociated with the monolayer was present. The lower C 1s signal in the gas-phase method demonstrated higher controllability of the silylation reaction, likely generating a more ordered monolayer possibly with fewer defects relative to the liquid-phase. The gas-phase silylation process is proposed here to be the better choice between the two, as it allows for higher controllability and easy integration with other microelectronics manufacturing steps or process design.

FIVE

TMSDMA Treatment of Copper Surfaces as a Way to Control Metal Oxide ALD

5.1 Introduction

Due to its low electrical resistivity and cost combined with affording high signal propagation, Cu has been the dominant material used for interconnects in microelectronics for nearly three decades (replacing Al) for transmitting electrical signal and power throughout the framework of transistors that are fabricated onto integrated circuits.[93–96] Intermetal dielectric layers such as SiO_2 insulators are also required between Cu interconnects in order to reduce signal interference and crosstalk between different layers. Early studies investigated the chemical deposition of Cu on SiO_2 substrates using methods such as ALD, a promising technique for depositing high-purity Cu films with excellent resistivity.[97–100] In recent years however, focus has shifted to using Cu/SiO_2 patterned substrates for the deposition of metal oxide films on a growth surface (GS) over a non-growth surface (NGS) in an area-selective fashion using ALD.[32,101–103]

Alkanethiol self-assembled monolayers (SAMs) are well known to spontaneously organize on metallic surfaces, with the primary driving force being the formation of a strong metal-sulfur bond to form a thiolate.[61,104–106] This chemistry has been greatly utilized to protect the metal during area-selective deposition processes.[101–103,107] On the other hand,

silane-based SAMs are known to adsorb on various metal oxide surfaces including binding to copper oxide in the form of stable Cu-O-Si$(R)_x$ groups.[108–110] Fewer studies however currently exist that have explored the impact of organosilane small-molecule inhibitors (SMIs) such as TMSDMA as a way to achieve AS-ALD, with limited investigations conducted specifically on the interaction of the inhibitor with the Cu surface. Furthermore, the nature of the initial Cu surface is typically left undefined in these ALD studies, information that is critical in understanding the surface chemistry that occurs during the subsequent ALD steps.[71,111] To address these issues, the gas-phase silylation scheme developed in Chapter 4 was applied to oxygen-free high-conductivity (OFHC) Cu substrates to explore the interaction of the inhibitor with the substrate. Thus, a better understanding of the role of copper in the context of AS-ALD could be developed.

The primary goal of the work presented in this chapter was to assess the interaction of TMSDMA with OFHC Cu substrates in comparison to PE-CVD-grown SiO_2/Si(100) substrates and evaluate the role of each surface as a potential GS and/or NGS for the AS-ALD of metal oxides such as TiO_2 and HfO_2.

5.2 Experimental

The experimental details regarding the acetic acid cleaning, treatment with TMSDMA, and TiO_2 and HfO_2 ALD on OFHC Cu substrates are all thoroughly described in Chapter's 2.2.2, 2.2.3, and 2.2.4, respectively. All treatments with TMSDMA in this chapter were conducted in the gas phase only.

The OFHC bulk Cu that was used in these experiments always displayed some degree of oxygen even after ex-situ acetic acid cleaning and in-situ Ar^+ sputtering, as evidenced by the O 1s XPS data (Figure 2.3). Two OFHC Cu surfaces with varying oxygen content were used in these studies following cleaning with acetic acid, differentiated by the information listed in Table 5.1: substrates that were Ar^+ sputtered for 20 min. (cleaning method 1) and those that were Ar^+ sputtered for 20 min. while rastering (cleaning method 2) are referred to as "CuO_x/Cu" and "cleaner CuO_x/Cu", respectively, as the latter method exhibited a lower O 1s and C 1s XPS signal after cleaning relative to the former. It is noted here that the identity of the residual O 1s XPS signal is believed to arise from CuO_x, but there may also be some contributions from atomic oxygen adsorbed on the Cu surface as well. In any case, these substrates are referred to as "CuO_x/Cu" throughout the rest of this work to indicate the surface oxygen present.

Table 5.1 Description of the two cleaning methods applied to the OFHC Cu surfaces used.

Method	Acetic acid-cleaned OFHC Cu	Treatment
1	CuO_x/Cu	20 min. Ar^+ sputtering
2	Cleaner CuO_x/Cu	20 min. Ar^+ sputtering while rastering

Other Cu surfaces were also prepared in a separate UHV chamber in the nanofabrication cleanroom facility by sputtering a Cu target onto PE-CVD-grown SiO_2/Si(100) to deposit high purity Cu films. The substrates were cleaned ex-situ in the same fashion as those of the bulk OFHC Cu following their removal from this separate UHV chamber. After ex-situ cleaning, these samples were immediately transferred to the lab UHV chamber (UC system) where they were applied with cleaning method 2 prior to

XPS analysis. The sputter-deposited Cu/PE-CVD SiO_2 surfaces were assessed only for their cleanliness and oxygen content; no further ALD experiments were ever conducted on them. The parameters used for their preparation are described in Table 5.2. The average thickness of the deposited Cu film was determined using ellipsometry.

Table 5.2 Parameters used for the sputter-deposition of Cu films on PE-CVD-grown SiO_2. The average thickness of the sputter-deposited Cu film was approximately 157 nm and the sputtering rate derived from this measurement was 0.05 Å/s. The average was calculated by measuring the thickness at 3 separate points on the substrate surface.

Material	Ar Flow (sccm)	Power (W)	Sample Rotation (%)	Sample Height (mm)	Process Pressure (mTorr)	Average Rate (Å/s)	Thickness (nm)
Cu	10	75 (DC, 10 %)	40	30	4.4	0.5	157

Finally, reapplications of the TMSDMA inhibitor were conducted on both substrates after every 5 TiO_2 or 2 HfO_2 ALD cycles using the same silylation protocol used for SiO_2 substrates to investigate the ability to restore passivation on the dielectric surface against metal oxide ALD to potentially extend the area-selectivity that was achievable.

5.3 Initial Studies on Cu Substrates

It was first crucial to ensure that an appropriate copper substrate had been selected prior to conducting ALD experiments. As such two different Cu materials were initially explored, each comprising of varying degrees of oxygen content.

5.3.1 Surface Cleaning and WCA Measurements

Cu cut from Cu foil and OFHC Cu cut from Cu sheets were investigated as potential substrates to be used for these ALD studies. It is well known that acetic acid can etch the surface of copper to remove its native oxide layer without damaging the underlying metal substrate.[112] Both types of substrates were first cleaned using ethanol and an acetic acid protocol followed by immediately measuring their water contact angles (WCA), reported as a function of etching time in Table 5.3. The impact of a 20 min. sputtering treatment in the case of the OFHC Cu substrate was also evaluated.

Table 5.3 WCA measurements for various Cu substrates after ex-situ cleaning with acetic acid to etch the native oxide layer.

Substrate	Treatment	Contact Angle /°
Cu Foil	N/A	76±1
	2 min. acetic acid etch	40±2
	5 min. acetic acid etch	35±2
	10 min. acetic acid etch	35±2
OFHC Cu Sheet (CuO_x/Cu)	N/A	55±1
	5 min. acetic acid etch	35±2
	Previous + 20 min. sputtering	36±2

The OFHC Cu sheet exhibited a lower initial WCA measurement compared to that of the Cu foil indicative of fewer organic impurities and a cleaner starting surface. As such, this substrate was selected as an appropriate copper surface to conduct further experiments with. A plateau of approximately 35° was reached after a 5 min. treatment with acetic acid indicating a limitation with regards to the cleanliness achievable ex-situ. Additional in-situ Ar^+ sputtering for 20 min. was also carried out after this. A WCA measurement on this

sputtered surface was taken within 2 min. of ex-situ transfer to ambient conditions. Interestingly, the measurement obtained after the Ar^+ sputtering treatment remained constant (Table 5.3). However, XPS measurements (shown later in Figure 5.1) confirmed further removal of oxygen following the sputtering treatment. This suggests that some oxygen species may form on the surface immediately after transferring the sample ex-situ following the sputtering procedure but prior to the WCA measurement, to an extent comparable post-acetic acid treatment. After completing these WCA studies, all acetic-acid cleaned OFHC Cu samples were only transferred ex-situ to carry out ALD.

5.3.2 OFHC Cu vs. Sputter-deposited Cu/PE-CVD SiO_2

Other means of establishing a clean oxygen-free Cu surface were also explored since the OFHC Cu (CuO_x/Cu) surfaces still exhibited residual oxygen following the original sputtering treatment. While a number of options were tested, continuous rastering of the sample during the 20 min. Ar^+ sputtering period was identified as a way to achieve a slightly more pristine OFHC Cu surface (cleaning method 2). As aforementioned, this new surface will be denoted as "cleaner CuO_x/Cu" to distinguish it from those of the OFHC Cu (CuO_x/Cu) surfaces sputtered without rastering (cleaning method 1).

Alternative methods in attempts to obtain fully metallic Cu(0) surfaces were concurrently investigated. Figure 5.1 compares the XPS data for the OFHC Cu (CuO_x/Cu) (two different samples treated with cleaning method 1 and 2, respectively) to Cu surfaces prepared via PVD on PE-CVD-grown SiO_2/Si(100). The same in-situ Ar^+ sputtering

treatment that was applied to the cleaner CuO_x/Cu bulk samples (method 2, sputtering while rastering) was also applied to those of the sputter-deposited Cu/PE-CVD SiO_2.

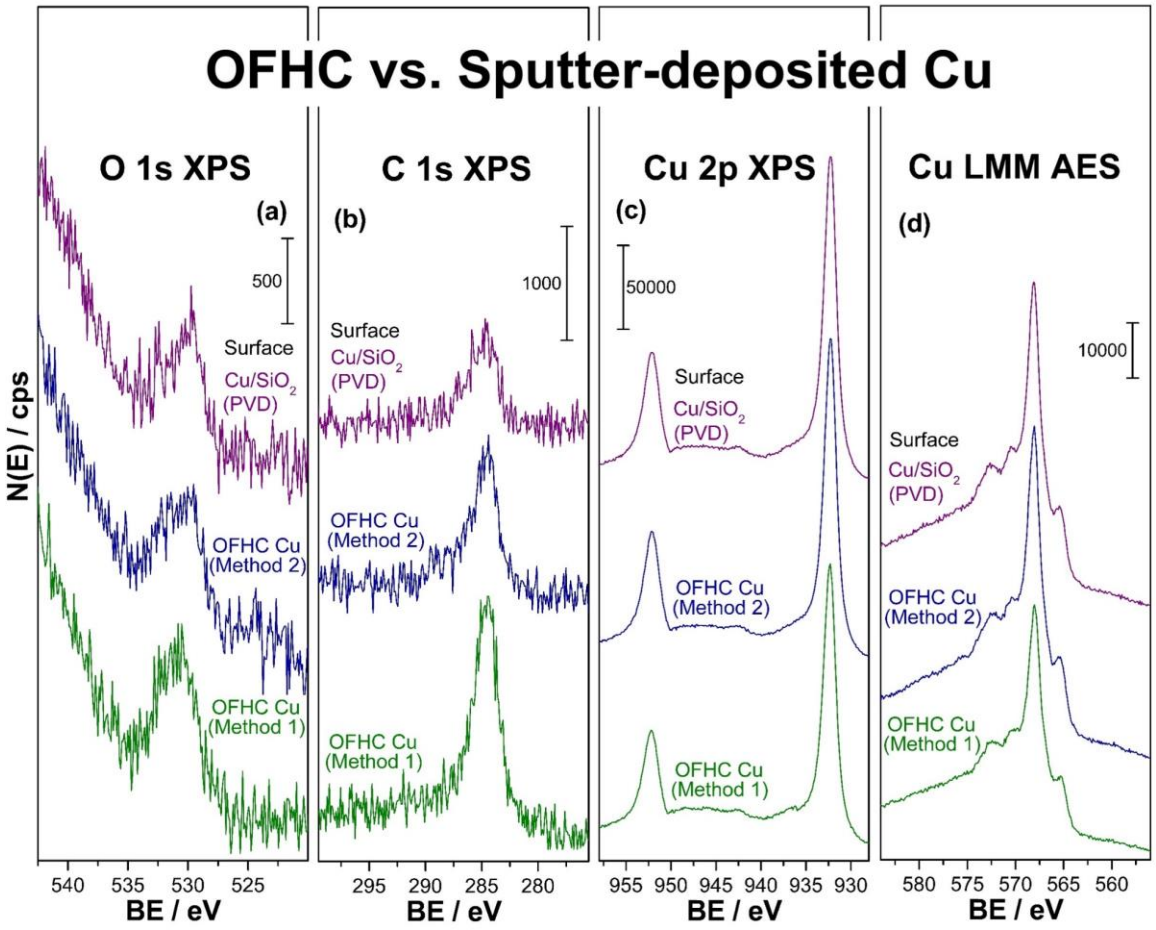


Figure 5.1 O 1s (a), C 1s (b), Cu 2p (c) XPS, and Cu LMM AES (d) for OFHC bulk Cu compared to sputter-deposited PVD Cu/PE-CVD-grown SiO_2/Si(100) surfaces (purple). OFHC Cu (CuO_x/Cu) treated with cleaning method 1 (Ar^+ sputtering only, green) is also compared to OFHC Cu (cleaner CuO_x/Cu) cleaned using method 2 (Ar^+ sputtering while rastering, blue). The information for the preparation of the OFHC bulk Cu and PVD Cu/PE-CVD-grown SiO_2/Si(100) samples are located in tables 5.1 and 5.2, respectively.

The comparison of the XPS data for CuO_x/Cu (cleaning method 1) and cleaner CuO_x/Cu (cleaning method 2) samples in Figure 5.1 demonstrates that sputtering while

rastering in the case of the latter led to further attenuation of the O 1s (slightly) and C 1s XPS signals accompanied by an evolution of the Cu 2p XPS and Cu LMM AES signals, respectively. Furthermore, the comparison of the O 1s XPS in Figure 5.1a for the OFHC bulk Cu (cleaner CuO_x/Cu) and PVD Cu/PE-CVD SiO_2/Si(100) revealed similar degrees of oxygen content present on both surfaces. The Cu 2p XPS in Figure 5.1c for these surfaces also exhibit comparable spectral features. Finally, the characteristic line shape and peak position at 566 eV, unique to Cu(0), in the Cu LMM AES data in Figure 5.1d suggest that the surface is predominantly metallic in nature after cleaning despite the persisting surface oxygen that remains.[113,114] Higher Cu LMM AES signal intensities are also observed for the cleaner OFHC Cu (cleaner CuO_x/Cu) and PVD Cu/PE-CVD SiO_2 substrates relative to the original CuO_x/Cu (cleaning method 1). As both the cleaner OFHC Cu (cleaner CuO_x/Cu) and PVD Cu/PE-CVD SiO_2/Si(100) samples exhibited similar degrees of oxygen post-cleaning, the former were chosen for subsequent ALD experiments to maintain both consistency in the series of experiments already conducted by this point, as well as having better control over their cleaning in the lab UHV chamber (UC System). In the future, it would be ideal to conduct the same set of experiments done in this work using the sputter-deposited copper samples reported here, since the C 1s XPS data in Figure 5.1b indicate that these surfaces contain fewer carbon impurities. Alternatively, Cu(0) may be thermally evaporated on silica by doing so in our own UHV chamber in the future (Chapter 7).

It should also be noted that cleaning method 2 was discovered later on and will be introduced at a later stage in a comparative study to cleaning method 1 using HfO_2 ALD.

5.3.3 Interaction of TMSDMA with Ar^+-Sputtered OFHC Cu (CuO_x/Cu)

Acetic acid-cleaned OFHC Cu substrates were cleaned in-situ under UHV by Ar^+ sputtering for 20 min. (cleaning method 1). The degree of oxygen sputtered off the surface and the subsequent impact of the TMSDMA exposure is displayed in Figure 5.2.

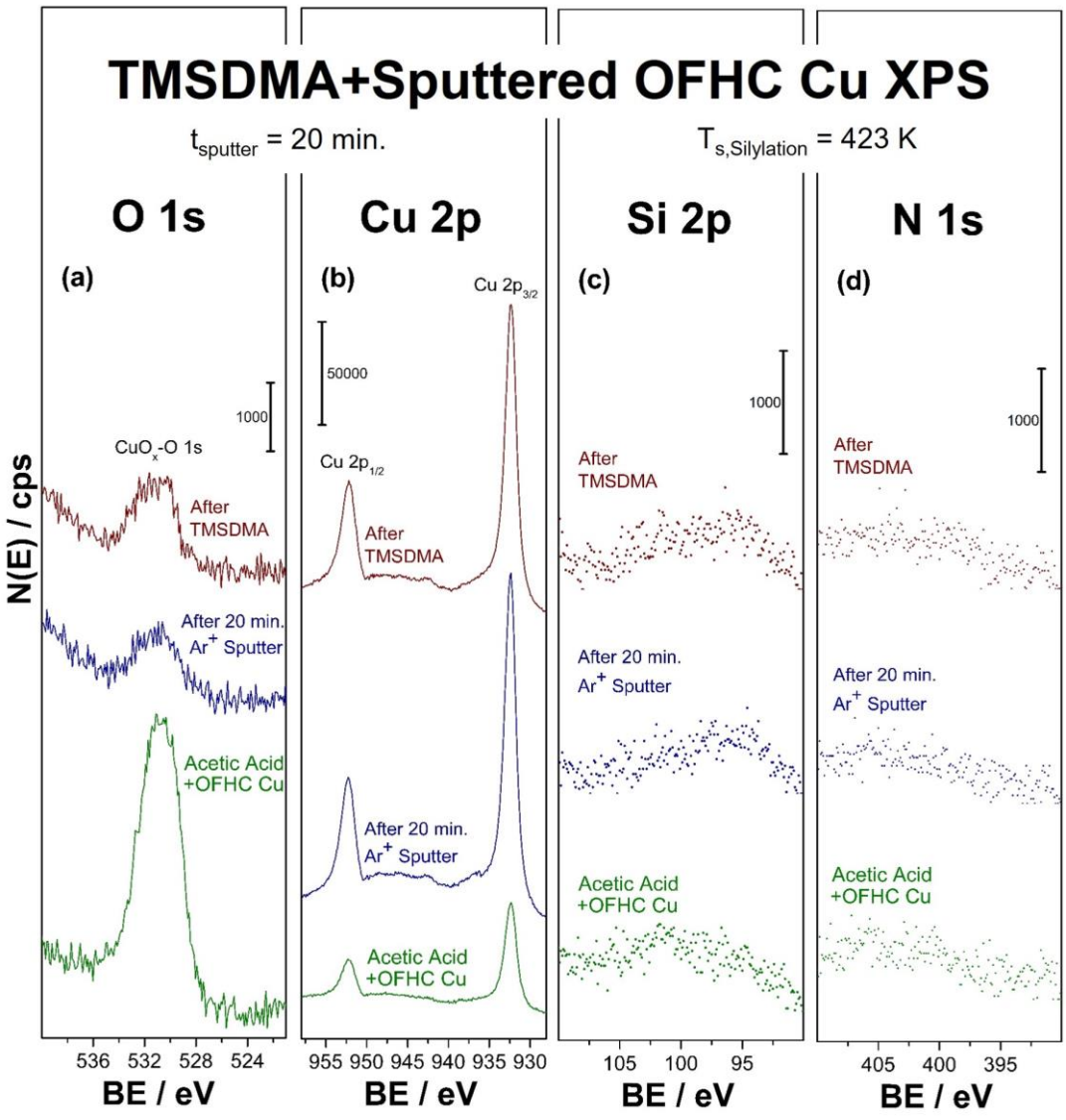


Figure 5.2 O 1s (a), Cu 2p (b), Si 2p (c), and N 1s (d) XPS data for an OFHC Cu (CuO_x/Cu) substrate after a 20 min. Ar^+ sputtering treatment followed by treatment with TMSDMA.

Attenuation of the O 1s XPS signal at 531 eV is observed following the Ar^+ sputtering treatment (Figure 5.2a). Concomitant to this is the evolution of the Cu $2p_{1/2}$ and $2p_{3/2}$ spin-orbit split features at 952.2 eV and 932.4 eV, respectively, associated with Cu(0) and/or Cu(I) species (Figure 5.2b). As Cu(0) and Cu(I) species exhibit nearly identical binding energies (932.4 and 932.6 eV, respectively), their peak components are unable to be properly distinguished and thus overlap, appearing as one individual set of spin-orbit split peaks.[113] This feature will be denoted as Cu(0)/Cu(I) in this work to convey this information (not to be confused with the ratio of the two signal intensities). While the Cu LMM AES data in Figure 5.1d demonstrates a characteristic peak position at 566 eV attributed to metallic Cu, this does not rule out the possibility of the presence of low coverages of CuO_x due to the signal that still persists in the O 1s XPS. The trends observed in the O 1s and Cu 2p XPS data taken together indicate that the copper surface becomes cleaner as some oxygen is removed after sputtering. The absence of a strong, broad satellite (shake-up) feature between 938-946 eV in the Cu 2p XPS data (Figure 5.2b), associated with Cu(II), indicates that that little CuO exists on the surface.[115] Therefore, the oxygen observed in the O 1s XPS data is suggested to mostly arise from to Cu_2O (although it is noted that some CuO is likely present here but not fitted in this particular data).[114] This is corroborated by other studies that have reported Cu_2O to persist on the surface even after similar sputtering timeframes, which may be the case here.[116]

After sputtering, the OFHC Cu (CuO_x/Cu) surfaces were exposed to TMSDMA at 423 K in the same manner as for the flat silica substrates discussed in Chapter 4. However, no new features appeared in either the Si 2p (Figure 5.2c) or N 1s (Figure 5.2d) XPS data

following the inhibitor exposure, confirming that new Si or N atoms were not added after this treatment. This indicated that no trimethylsilyl moieties adsorbed on the surface and that the decomposition of the dimethylamine group was not favorable at this process temperature. In other words, silylation did not occur on these OFHC Cu (CuO_x/Cu) surfaces using the exact same conditions that passivated SiO_2. It was therefore concluded that the OFHC Cu (CuO_x/Cu) substrates prepared here are expected to be an ideal GS in the context of AS-ALD. Metal oxide ALD was next conducted on Ar^+-sputtered OFHC Cu (CuO_x/Cu) substrates, both as is and treated with TMSDMA, to investigate potential changes in film growth resulting from the inhibitor treatment.

It should be mentioned that similar to ALD on silica substrates, no signal was ever detected in the N 1s XPS data for OFHC Cu (CuO_x/Cu) at any point after treatment with TMSDMA, or after TiO_2 or HfO_2 ALD, and are as such omitted from the figures in this chapter for the sake of brevity. It is also implied hereafter that all Cu substrates used were first cleaned ex-situ in acetic acid for at least 5 min. followed by Ar^+ sputtering for 20 min. unless otherwise specified (cleaning method 2 includes an additional rastering step).

5.4 TiO_2 ALD

5.4.1 CuO_x/Cu – With (W/) vs. Without (W/o) TMSDMA

TiO_2 ALD was used to test whether or not the silylation reaction with TMSDMA inhibited thin film growth on OFHC Cu (CuO_x/Cu) surfaces; the corresponding XPS data are shown in Figure 5.3.

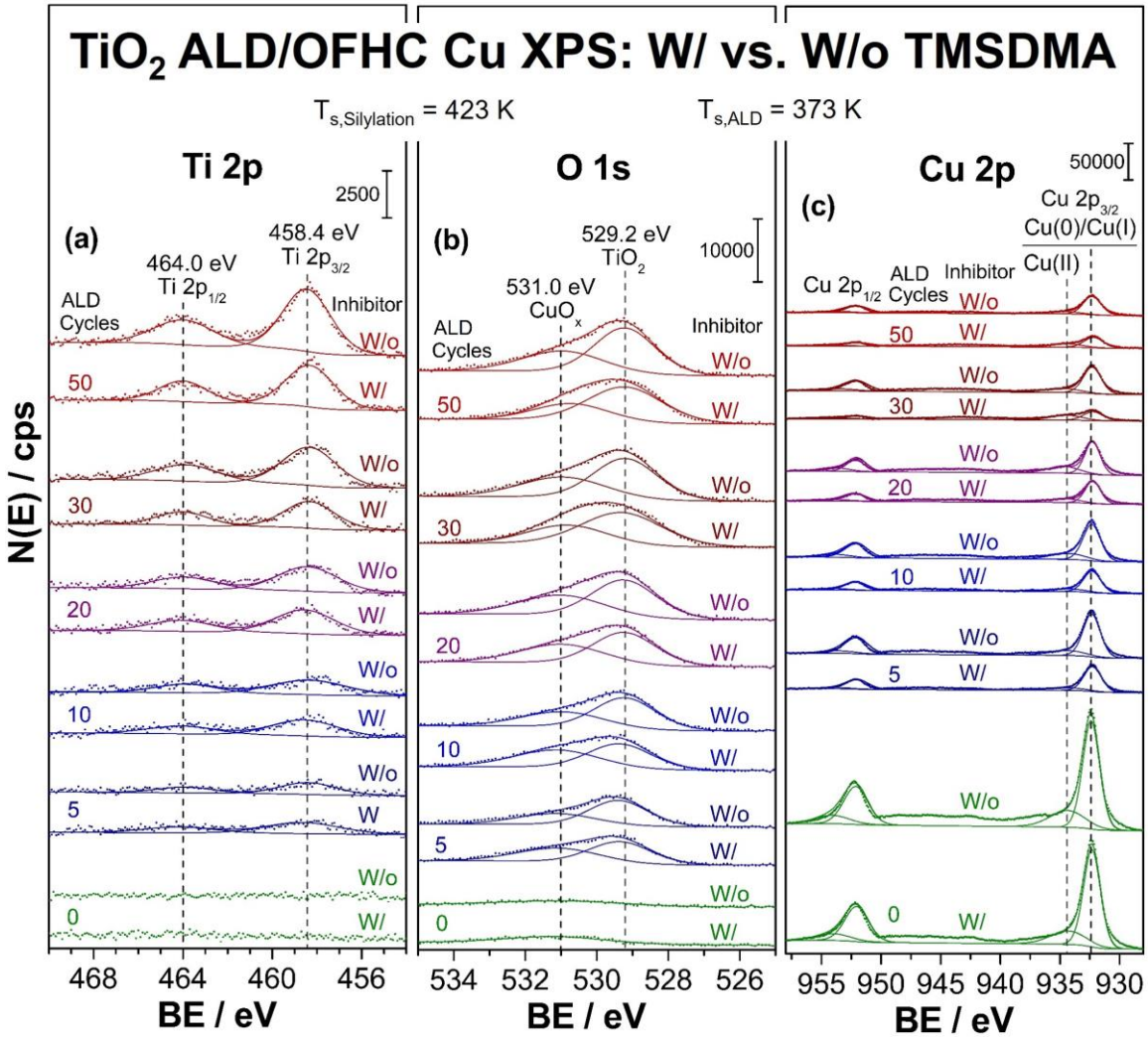


Figure 5.3 Ti 2p (a), O 1s (b), and Cu 2p (c) XPS data for OFHC Cu (CuO_x/Cu) substrates treated with (W/) and without (W/o) TMSDMA as a function of increasing number of TiO_2 ALD cycles.

The Ti $2p_{1/2}$ and Ti $2p_{3/2}$ spin-orbit split XPS peaks are observed at 464.0 eV and 458.4 eV, respectively, after 5 TiO_2 ALD cycles for both OFHC Cu (CuO_x/Cu) substrates, as is or after treatment with TMSDMA (Figure 5.3a), indicative of the presence of Ti atoms on the surface associated with TiO_2. These signals evolve slowly with increasing number of ALD cycles; however, the films appear to grow at the same rate on both OFHC Cu

substrates during the first 20 ALD cycles regardless of the inhibitor exposure. It is noted that the deviation in the Ti 2p signal evolution between the two surfaces after 30 and 50 ALD cycles is not yet fully understood but is correlated to the attenuation seen in the Cu(0)/Cu(I)-Cu 2p XPS in Figure 5.3c at these stages. It is speculated that this may be due to some sample contamination that occurred during ex-situ transfer. These experiments would need to be repeated in the future to rule this out. In any case, it is still understood that no inhibition of film growth occurred during the initial stages of ALD on the TMSDMA-treated substrate.

A single peak is initially observed at 531.0 eV in the O 1s XPS data in Figure 5.3b attributed to CuO_x species. Then, a new component at a lower binding energy of 529.2 eV appears after 5 ALD cycles associated with the Ti-O chemical environment in TiO_2. The evolution of the CuO_x signal observed following ALD occurred due to a combination of ex-situ sample transfer and surface oxidation that may occur during the reaction with H_2O in the second half-cycle.

Two sets of peak-fit spin-orbit split features are observed in the Cu 2p XPS shown in Figure 5.3c; these appear at 952.2 eV and 932.4 eV for the Cu $2p_{1/2}$ and $2p_{3/2}$ peaks of Cu(0)/Cu(I) species, and at 954.2 eV and 934.4 eV for the Cu $2p_{1/2}$ and $2p_{3/2}$ of Cu(II) species, respectively. The signals for the underlying substrate immediately attenuate following an ex-situ transfer and 5 TiO_2 ALD cycles; however, the signal for the OFHC Cu substrate treated with TMSDMA attenuates more relative to the blank OFHC Cu. The changes in these peak intensities are better illustrated by plotting the integrated peak area as a function of increasing TiO_2 ALD cycles, as displayed in Figure 5.4.

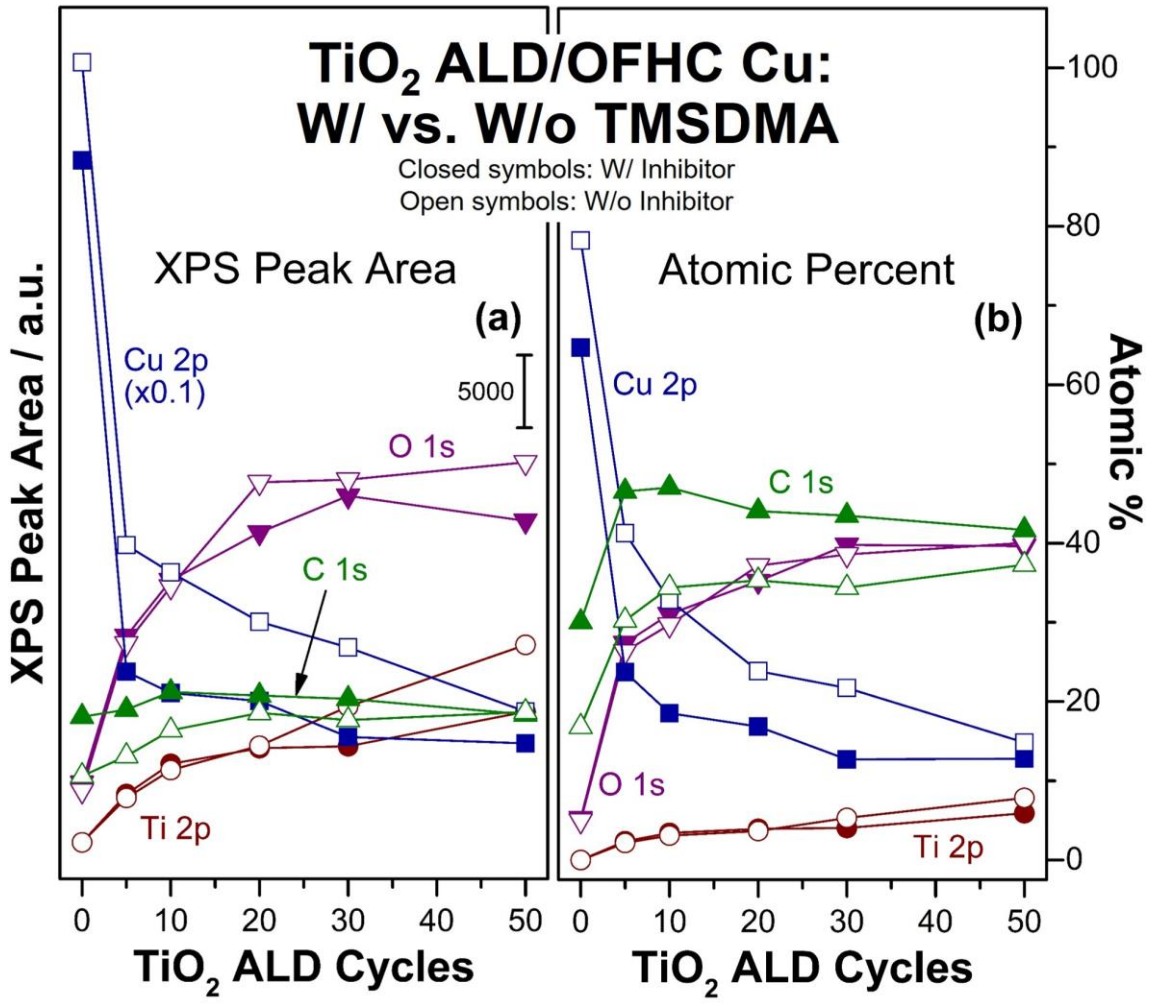


Figure 5.4 (a) Cu 2p, O 1s, C 1s, and Ti 2p XPS peak areas for OFHC Cu (CuO_x/Cu) substrates treated with (W/) and without (W/o) TMSDMA as a function the number of ALD cycles used to grow TiO_2 films. (b) Atomic-percent composition profiles estimated from the data in panel (a) in combination with corresponding ASFs.

Figure 5.4a displays the peak area profile for each XPS signal as a function of increasing number of ALD cycles for the OFHC Cu (CuO_x/Cu) substrates treated with and without TMSDMA. Despite undergoing identical sputtering treatments, a discrepancy exists between the initial Cu 2p and C 1s integrated XPS peak areas for both substrates. Although the Si 2p XPS in Figure 5.2c confirmed that silylation of OFHC Cu (CuO_x/Cu)

did not occur after exposure to TMSDMA, an evolution of the C 1s signal concomitant with the attenuation of the Cu 2p signal was observed for the TMSDMA-treated sample. It is unlikely that only methyl moieties were deposited on the surface at this low temperature without other nitrogen impurities being detected. One possible explanation for this observation is the adsorption of some form of adventitious carbon during the silylation exposure step post-sputtering, which was conducted under rough vacuum conditions at 300 mTorr, significantly higher than that of the UHV conditions established in the analysis chamber where the sample was originally cleaned. Alternatively, it may be that the TMSDMA exposure introduced some form of carbon to the surface; however, did not result in the surface being passivated regardless of whatever form it may exist in. Despite this, it is clear from the Ti 2p peak areas and the corresponding Ti surface atomic-percent composition in Figure 5.4b that the quantity of TiO_2 present on both surfaces is comparable and initially evolves at a similar rate as the number of ALD cycles used increases. This confirmed that the exposure of the sample to TMSDMA did not inhibit the growth of TiO_2 films on the surface. Next, we set ourselves to test how effective these surfaces would be in an area-selective deposition scheme against PE-CVD-grown SiO_2.

5.4.2 TMSDMA-treated: PE-CVD SiO_2 vs. CuO_x/Cu

Deposition of TiO_2 on TMSDMA-silylated PE-CVD-grown SiO_2 (SiO_2/Si(100), NGS) was compared to that on TMSDMA-treated OFHC Cu (CuO_x/Cu, GS) as a function of increasing number of ALD cycles, as displayed in Figure 5.5.

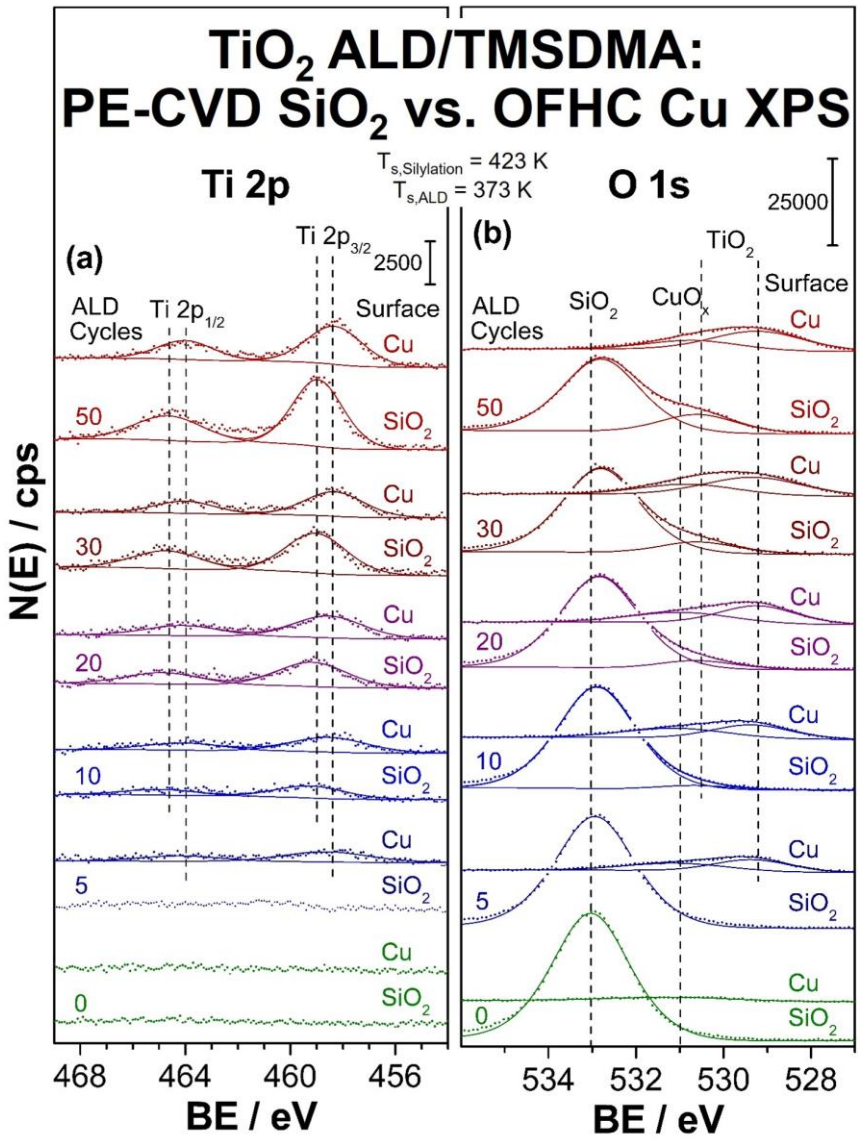


Figure 5.5 Ti 2p (a) and O 1s (b) XPS data for TMSDMA-silylated PE-CVD-grown SiO_2/Si(100) and TMSDMA-treated OFHC Cu (CuO_x/Cu) substrates as a function of increasing number of TiO_2 ALD cycles.

From the comparison of the Ti 2p XPS data between TMSDMA-silylated PE-CVD SiO_2 and TMSDMA-treated OFHC Cu (CuO_x/Cu) in Figure 5.5a, it is evident that area-selective deposition of TiO_2 is achieved on the TMSDMA-treated OFHC Cu GS over the

TMSDMA-silylated PE-CVD SiO_2 NGS after 5 TiO_2 ALD cycles. However, this selectivity is quickly lost after 10 cycles as film growth is detected on the PE-CVD SiO_2, resulting in comparable Ti 2p XPS signals for both substrates afterwards. Film growth predominantly occurs on the silylated PE-CVD SiO_2 surface by 20 cycles while little signal evolution is observed for that of the TMSDMA-treated OFHC Cu. Similar trends are reflected in the evolution of the TiO_2-O 1s XPS component in Figure 5.5b of both substrates: the rate of signal evolution is initially faster on the copper substrate over the silica substrate but is reversed after a higher number of ALD cycles.

While some degree of area-selectivity is maintained up to the first few ALD cycles, the nucleation delay on the NGS is quickly lost as Ti nuclei begin to chemisorb on the TMSDMA-silylated PE-CVD SiO_2. It has been reported that some form of inherent selectivity of TiO_2 ALD using TDMATi as the metalorganic precursor exists between Cu and SiO_2 surfaces due to differences in the local surface free energy.[117] In order to evaluate this on the OFHC Cu (CuO_x/Cu) and PE-CVD SiO_2 surfaces here, the blank profiles for both substrates without exposure to any TMSDMA were compared next.

5.4.3 Unmodified: PE-CVD SiO_2 vs. CuO_x/Cu

The XPS data for the unmodified PE-CVD-grown SiO_2/Si(100) sample presented in Chapter 4 was compared to that reported here for untreated OFHC Cu (CuO_x/Cu) as a function of increasing number of TiO_2 ALD cycles, displayed in Figure 5.6.

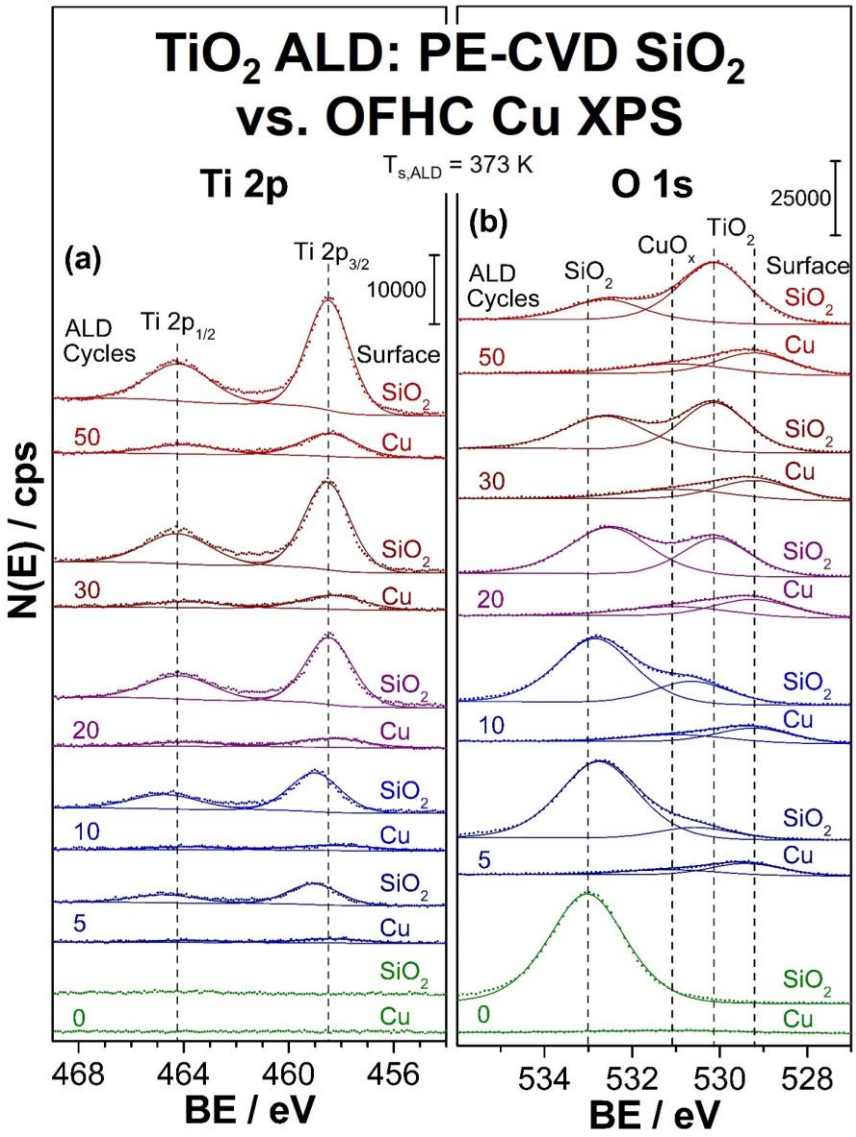


Figure 5.6 Ti 2p (a) and O 1s (b) XPS data for unmodified PE-CVD-grown SiO_2/Si(100) and untreated OFHC Cu (CuO_x/Cu) substrates as a function of increasing number of TiO_2 ALD cycles.

In contrast to the XPS data shown in Figure 5.5, a shift in the GS and NGS for the area-selective deposition of TiO_2 is observed between untreated OFHC Cu (CuO_x/Cu) and unmodified PE-CVD-grown SiO_2. Here, the selectivity is reversed: SiO_2 becomes the new GS while Cu becomes the new NGS when TMSDMA is not used to passivate the dielectric

surface. The dielectric surface is more reactive than that of the copper in this case due to the free Si-OH nucleation centers available for precursor chemisorption. This scheme reveals an inherently selective process for depositing TiO_2 films on SiO_2 over Cu, demonstrated as early as 5 ALD cycles with minimal growth on the CuO_x/Cu surface (Figure 5.6a). While some film growth is observed on the untreated CuO_x/Cu surface with increasing number of cycles, higher Ti 2p XPS peak intensities are consistently observed for the unmodified PE-CVD SiO_2 sample up to 50 TiO_2 ALD cycles. This trend is also supported by those observed in Figure 5.6b for the TiO_2-O 1s XPS signal. This difference in reactivity is believed to arise due to the variation in nucleation centers between the two substrates: highly reactive Si-OH sites exist on the dielectric surface that facilitate the chemisorption of ALD precursor molecules while the same advantages do not apply to the copper surface, on which defect sites are likely primarily used to initiate ALD reactions and subsequent film growth.

5.5 HfO_2 ALD

A more reactive metal oxide system was used next in order to better understand the limitations of using this passivation approach for area-selective deposition processes.

5.5.1 CuO_x/Cu – With (W/) vs. Without (W/o) TMSDMA

Similar to the series of experiments using TiO_2 ALD, HfO_2 ALD was used to determine if film growth would be impeded on OFHC Cu (CuO_x/Cu) after exposure to TMSDMA as displayed in Figure 5.7.

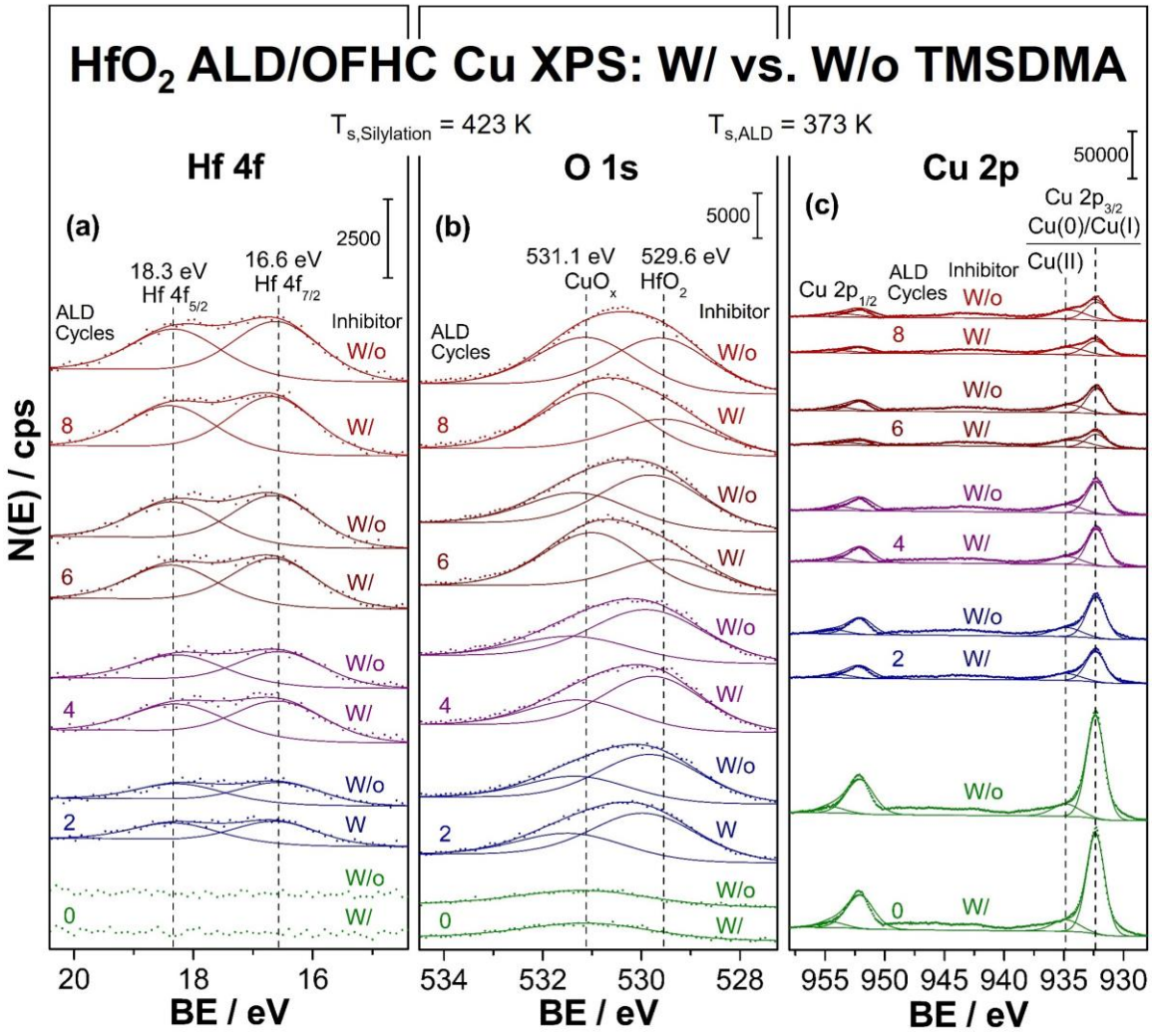


Figure 5.7 Hf 4f (a), O 1s (b), and Cu 2p (c) XPS data for OFHC Cu (CuO_x/Cu) substrates treated with (W/) and without (W/o) TMSDMA as a function of increasing number of HfO_2 ALD cycles.

Hf nuclei chemisorb onto both surfaces by 2 HfO_2 ALD cycles evidenced by the appearance of comparable Hf $4f_{5/2}$ and $4f_{7/2}$ XPS peak intensities at 18.3 eV and 16.6 eV, respectively, in the Hf 4f XPS for both the TMSDMA-treated and blank substrates (Figure 5.7a). These signals continue to evolve nearly identically as the number of ALD cycles

used is increased, suggesting that the degree of HfO_2 present on both surfaces is similar. It is noted here that an unexpected increase in the CuO_x-O 1s XPS component signal (Figure 5.7b) for the TMSDMA-treated OFHC Cu (CuO_x/Cu) substrate is observed after 6 HfO_2 ALD cycles reflected by the sudden attenuation of the Cu(0)/Cu(I)-Cu 2p XPS signal (Figure 5.7c). The source of this oxidation resulting in these sudden spikes is not yet fully understood, however; it is likely not due to the ALD process itself. Further experiments would need to be repeated to confirm this. In a similar manner to the XPS data presented in Figure 5.3 when using TiO_2 ALD, the XPS data in Figure 5.7 demonstrates that exposure of TMSDMA to OFHC Cu (CuO_x/Cu) surfaces does not inhibit HfO_2 ALD. The results here can be compared to the those obtained on PE-CVD-grown SiO_2 in order to assess the ability to deposit HfO_2 in an area-selective fashion.

5.5.2 TMSDMA-treated: PE-CVD SiO_2 vs. CuO_x/Cu

TMSDMA-silylated PE-CVD-grown SiO_2 (NGS) was compared to TMSDMA-treated OFHC Cu (CuO_x/Cu, GS) as a function of increasing number of HfO_2 ALD cycles, presented in Figure 5.8. Additionally, XPS was acquired for both samples after every 2 ALD cycles instead of every 5 (the case for TiO_2 ALD) due to the higher reactivity of TDMAHf compared that of TDMATi.

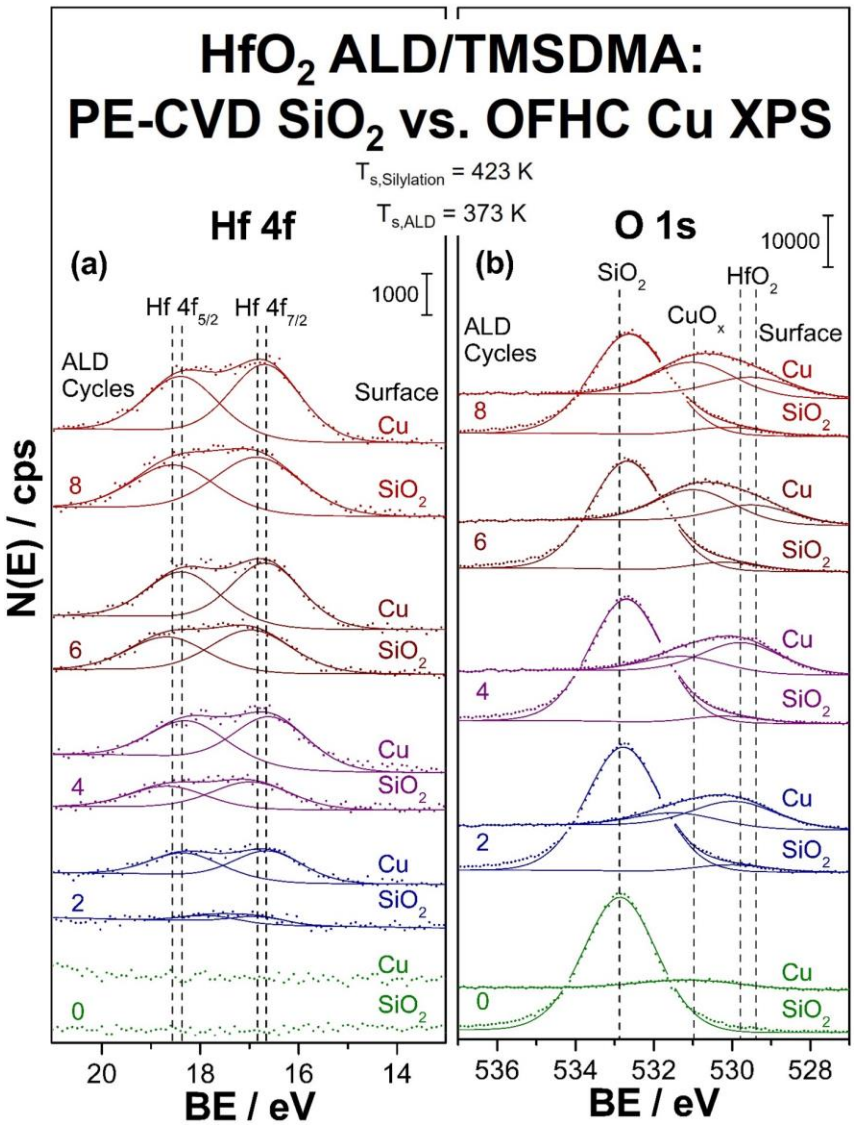


Figure 5.8 Hf 4f (a) and O 1s (b) XPS data for TMSDMA-silylated PE-CVD-grown SiO_2/Si(100) and TMSDMA-treated OFHC Cu (CuO_x/Cu) substrates as a function of increasing number of HfO_2 ALD cycles.

The presence of Hf atoms is detected as early as 2 HfO_2 ALD cycles on both surfaces, displayed in Figure 5.8a. While distinct Hf $4f_{5/2}$ and $4f_{7/2}$ features appear by the second ALD cycle on the OFHC Cu (CuO_x/Cu) substrate, their development is less pronounced for the PE-CVD-grown SiO_2 surface. Previous results (Chapter 4) indicated

that the TMSDMA-silylated PE-CVD-grown SiO_2 surface remained passivated during the initial HfO_2 ALD cycle with passivation loss occurring between the second and fifth ALD cycle. Here, passivation loss is confirmed after the second ALD cycle due to the presence of a small degree of Hf on the surface. This observation is reflected by the appearance of weak Hf 4f and HfO_2-O 1s XPS features by this point, associated with HfO_2. The Hf 4f peak intensities for both substrates increase with further ALD cycles, becoming comparable by 6 and 8 cycles. This suggests that while the initial silylated PE-CVD SiO_2 surface remained unreactive relative to the OFHC Cu (CuO_x/Cu) surface, the chemisorption of TDMAHf molecules on defect sites (free hydroxyl groups) quickly reversed this. However, the Hf XPS signal for the silylated dielectric sample is always lower than that of the copper. Since no area-selectivity was achieved using the TMSDMA-treated substrates, the inhibitor exposure step was removed and the ALD profiles on both blank surfaces compared to investigate if another inherently selective process existed here similar to that of when using TiO_2 ALD.

5.5.3 Unmodified: PE-CVD SiO_2 vs. CuO_x/Cu

HfO_2 ALD was carried out on unmodified PE-CVD SiO_2 and OFHC Cu (CuO_x/Cu) substrates without any prior treatment to TMSDMA. The results for these experiments are displayed in Figure 5.9.

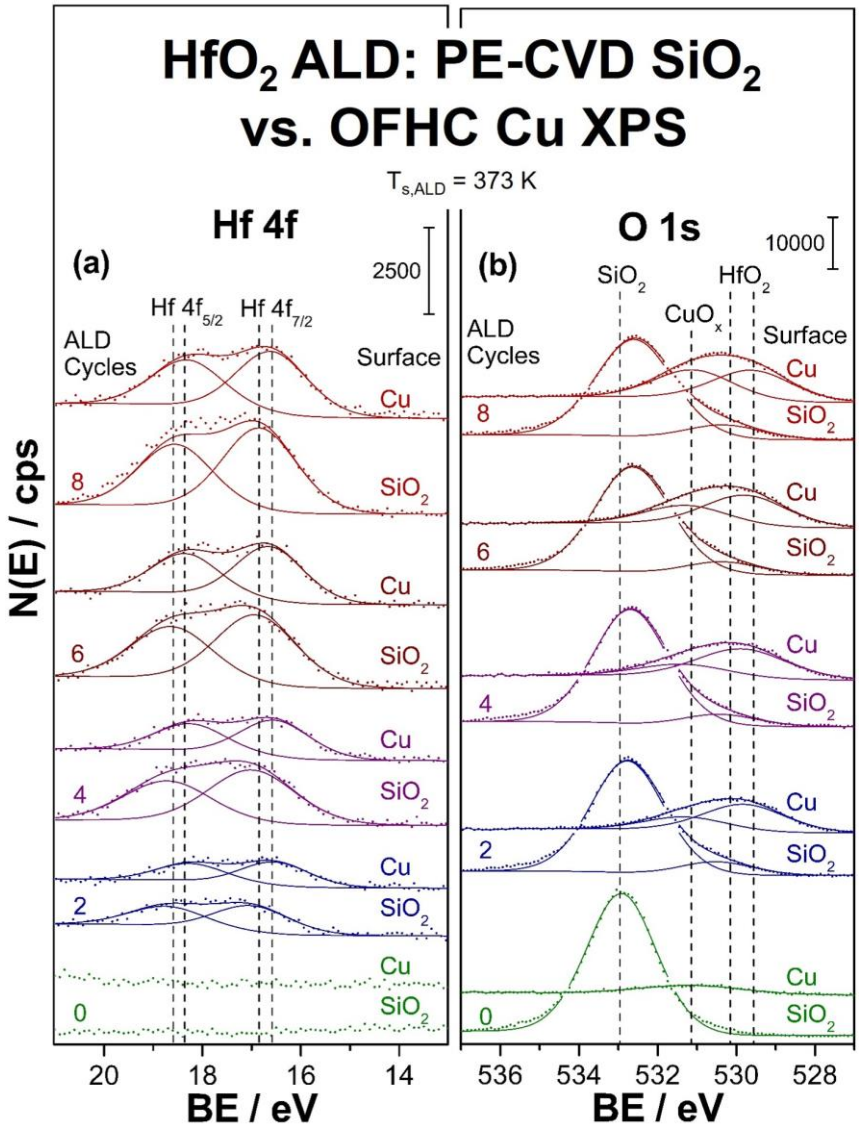


Figure 5.9 Hf 4f (a) and O 1s (b) XPS data for unmodified PE-CVD-grown SiO_2/Si(100) and untreated OFHC Cu (CuO_x/Cu) substrates as a function of increasing number of HfO_2 ALD cycles.

In contrast to the inherent area-selective deposition observed using TiO_2 ALD on unmodified PE-CVD-grown SiO_2 vs. OFHC Cu (CuO_x/Cu), HfO_2 is deposited indiscriminately on both unmodified surfaces here as early as 2 ALD cycles evidenced from the appearance of Hf 4f spin-orbit split XPS signals on both substrates in Figure 5.9a.

In addition, film growth progresses at a higher rate on PE-CVD SiO_2 compared to OFHC Cu, likely due to the availability of more nucleation centers on the starting surface prior to ALD.

The differences observed in the Ti 2p and Hf 4f XPS for the data discussed in Chapters 5.4 and 5.5 following TiO_2 or HfO_2 ALD, respectively, on both PE-CVD SiO_2 and OFHC Cu (CuO_x/Cu) substrates, as is or treated with TMSDMA, are summarized in Figure 5.10 in the form of the XPS peak area profile as a function of increasing ALD cycles.

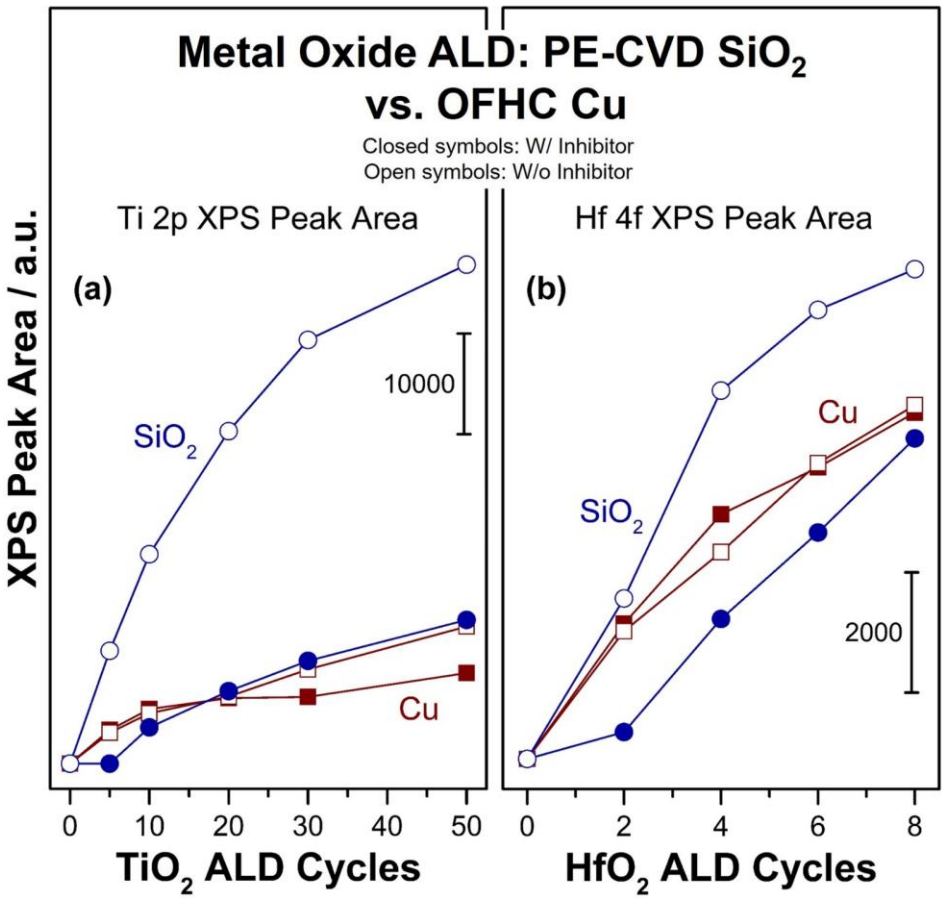


Figure 5.10 Ti 2p (a) and Hf 4f (b) XPS peak area profiles on PE-CVD-grown SiO_2 and OFHC Cu (CuO_x/Cu) substrates treated with and without TMSDMA as a function of the increasing number of ALD cycles used to deposit the respective TiO_2 or HfO_2 films.

In Figure 5.10a, inherent AS-ALD of TiO_2 on unmodified PE-CVD SiO_2 over OFHC Cu (CuO_x/Cu) occurs by 5 TiO_2 ALD cycles evidenced by the difference in the Ti 2p XPS peak area, likely due to the energy of TDMATi adsorption on the surface hydroxyl nucleation sites of the dielectric surface being more favorable. However, it is evident that this process is not fully selective as undesirable precursor nucleation and subsequent film growth still occurs the copper substrate. A difference in the growth rates of the Ti 2p XPS signal is also seen, with that of the OFHC Cu (CuO_x/Cu) curiously reaching an asymptote by 20 cycles. Then, a linear growth regime is observed between 20 to 50 cycles. This may suggest that TiO_2 deposition on the OFHC Cu (CuO_x/Cu) surface is initially a slow process, likely occurring through the formation of dispersed 3-D islands. As the number of cycles used is increased, these islands coalesce together to form a more contiguous layer of TiO_2 to a point where the induction period ends and nucleation becomes favorable on the hydroxyl groups of the deposited metal oxide, facilitating the kinetics of the overall reaction. While this type of induction period is typically unfavorable in many instances, it may be useful here as it provides a window to implement a way to mitigate and remove defects from the copper surface as they form thereby maintaining it as a viable NGS should growth be desired on PE-CVD SiO_2. Conversely, uninhibited evolution of the Ti 2p XPS signal for PE-CVD SiO_2 is observed, although the rate of evolution decreases as the number of TiO_2 ALD cycles used increases, possibly due to the self-termination of available hydroxyl groups on the deposited metal oxide throughout the ALD process.

When TMSDMA is applied to both surfaces, trimethylsilyl moieties preferentially adsorb on and chemically remove the hydroxyl nucleation centers of silica and do not

adsorb in the same manner on the copper substrate. This results in a shift in the area-selectivity achieved, as the deposition of TiO_2 now occurs on OFHC Cu (CuO_x/Cu) over the silylated PE-CVD SiO_2 surface for up to 5 TiO_2 ALD cycles, due to the energy barrier of TDMATi adsorption on the latter surface essentially being increased. However, selectivity is quickly lost after 10 TiO_2 ALD cycles as the Ti 2p XPS peak area of PE-CVD SiO_2 and OFHC Cu (CuO_x/Cu) become nearly identical; the area of the former becomes larger than that of the latter at a higher number of cycles, suggestive of film growth on defect sites. Similar to the previous case, a window exists during the first 5 ALD cycles to remove defect-nuclei and/or the defective passivating monolayer from the NGS (discussed later). These results are promising, as they indicate that selective deposition may be controlled (in some instances) by preferentially tuning the surface free energy using SMIs such as TMSDMA to invert the GS and NGS.

In Figure 5.10b, inherent area-selective deposition of HfO_2 is not achieved as indiscriminate film growth occurs on both surfaces, evidenced by the evolution of the Hf XPS peak areas by 2 HfO_2 ALD cycles. After applying TMSDMA to both substrates, the nucleation of TDMAHf by 2 cycles still occurs on the silylated dielectric surface, although to a lesser extent. Due to this, a more stringent means of control to periodically remove defect-nuclei from the PE-CVD SiO_2 NGS will be necessary in the future.

The cleaner OFHC Cu (cleaner CuO_x/Cu) samples prepared using cleaning method 2 were next evaluated with HfO_2 ALD and compared to those using method 1 to determine if the cleanliness of the substrate, with regards to the oxygen present on the starting surface in particular, had any impact on subsequent film growth.

5.5.4 TMSDMA-treated CuO_x/Cu: Cleaning method 1 vs. 2

The XPS data for TMSDMA-treated OFHC Cu cleaned using method 1 vs. method 2 was compared as a function of increasing number of HfO_2 ALD cycles, presented in Figure 5.11.

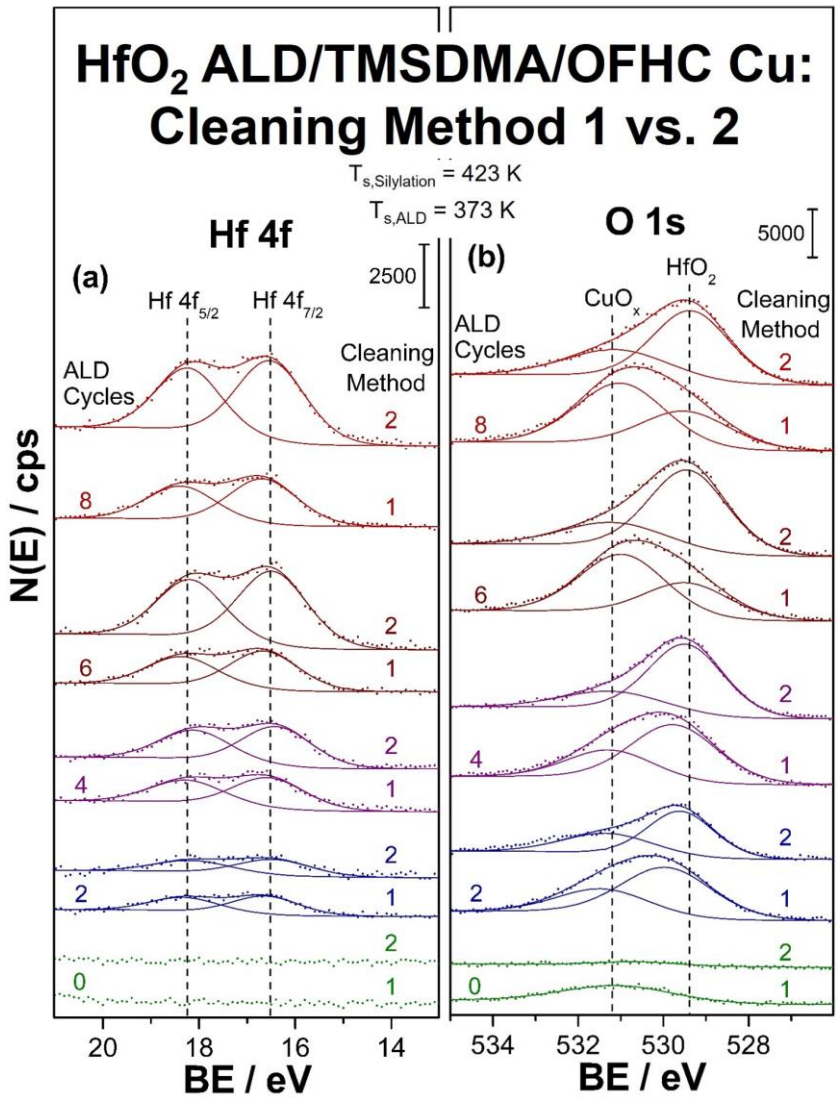


Figure 5.11 Hf 4f (a) and O 1s (b) XPS data for TMSDMA-treated OFHC Cu comparing cleaning method 1 vs. 2 as a function of increasing number of HfO_2 ALD cycles.

Compared to the Hf 4f XPS data (Figure 5.8a) for the previous TMSDMA-treated OFHC Cu (CuO_x/Cu) surfaces (cleaning method 1) after HfO_2 ALD, Figure 5.11a indicates that a thicker HfO_2 film is deposited on the TMSDMA-treated cleaner OFHC Cu (cleaner CuO_x/Cu) (cleaning method 2) surface by 8 ALD cycles evidenced by higher Hf $4f_{5/2}$ and $4f_{7/2}$ XPS peak intensities. However, the Hf 4f peak intensities after the first two ALD cycles are comparable when using either method. This suggests that additional cleaning using method 2 did not enhance deposition on the starting substrate during the early stages of ALD. It should be reiterated at this point that the unexpected oxidation of the OFHC Cu (CuO_x/Cu) cleaned using method 1 after 6 ALD cycles (Figure 5.11b) likely partially deactivates the surface from further chemical reactions, thereby slightly hindering the comparison of these two datasets.

Further insight can be derived from the analysis of the O 1s XPS (Figure 5.11b), which demonstrates that a slightly lower CuO_x-O 1s XPS signal is initially achieved using cleaning method 2 prior to any ALD. The appearance of a new peak component at lower binding energies is observed as HfO_2 is deposited after 2 ALD cycles attributed to HfO_2-O 1s. The component intensities continue to evolve on both surfaces following 4 ALD cycles. While the HfO_2 ALD experiments after 6 and 8 cycles using cleaning method 1 would need to be repeated, the data up to 4 ALD cycles demonstrates that the removal of additional oxide using cleaning method 2 (relative to method 1) does not significantly impact the initial nucleation of TDMAHf and growth of HfO_2. Experiments using cleaning method 2 on OFHC Cu (CuO_x/Cu) substrates followed by HfO_2 ALD without treatment with TMSDMA should be carried out in the future.

The integrated XPS peak area profile for the OFHC Cu substrates, treated with both cleaning methods 1 and 2, compared to that of the silylated PE-CVD SiO_2 substrate as a function of increasing HfO_2 ALD cycles is shown in Figure 5.12.

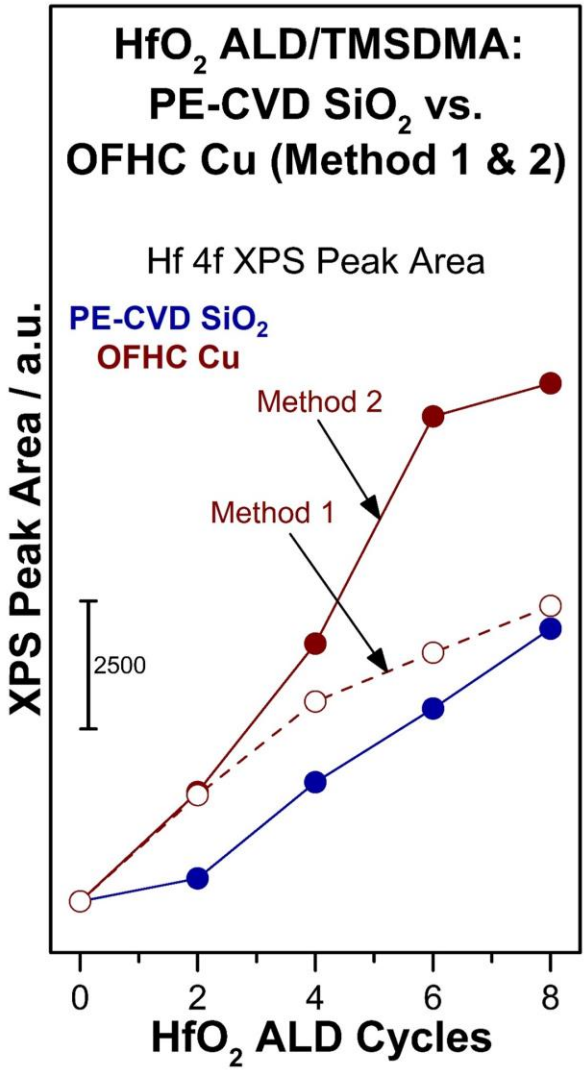


Figure 5.12 Hf 4f XPS peak area profiles for TMSDMA-silylated PE-CVD-grown SiO_2/Si(100) and TMSDMA-treated OFHC Cu (CuO_x/Cu) substrates, comparing those that were treated with cleaning methods 1 and 2, as a function of increasing number of HfO_2 ALD cycles. The data presented here was derived from Figure 5.11.

The comparison of the Hf 4f XPS peak areas between the two OFHC Cu (CuO_x/Cu) substrates treated with cleaning methods 1 and 2, respectively, in Figure 5.12 indicate that a similar degree of HfO_2 is deposited after 2 ALD cycles regardless of the method used. This confirms that the additional surface cleaning did not promote film growth on the starting copper surface. However, a deviation in the growth rate is observed by 4 cycles that exhibits a higher rate of deposition on the substrate cleaned using method 2. These experiments should be repeated in the future to check for reproducibility and rule out the possibility of oxidation of the copper substrate during the experiments using method 1.

The comparison of either of the TMSDMA-treated OFHC Cu (CuO_x/Cu) substrates and the TMSDMA-silylated PE-CVD SiO_2 samples indicate that area-selectivity was not achieved, evidenced by the nucleation of TDMAHf on the dielectric surface as early as 2 ALD cycles. This was of course expected as no changes were induced to the dielectric sample. However, the amount of HfO_2 deposited on the PE-CVD SiO_2 surface is consistently lower than that of the OFHC Cu. This is promising as it suggests that a defect mitigation step could be implemented in the future to remove unwanted Hf nuclei and the defective organosilane monolayer from the silica surface, which would then be followed by re-silylation of the original silica substrate. This same treatment should also be applied to the copper substate, but it is expected that a positive trend in film growth may still be observed as more HfO_2 would be deposited during the subsequent ALD steps than removed during the mitigation steps.

The results shown here indicate that the degree of Hf nuclei adsorbed on the PE-CVD SiO_2 surface after 2 ALD cycles is small relative to that deposited during later cycles.

This is encouraging, as it demonstrates that passivation scheme may still be used for more reactive ALD processes when assisted by additional defect mitigation steps immediately as they form. The Cu 2p XPS and Cu LMM AES data for the cleaner OFHC Cu (cleaner CuO_x/Cu) substrate treated using method 2 are provided in Figure 5.13.

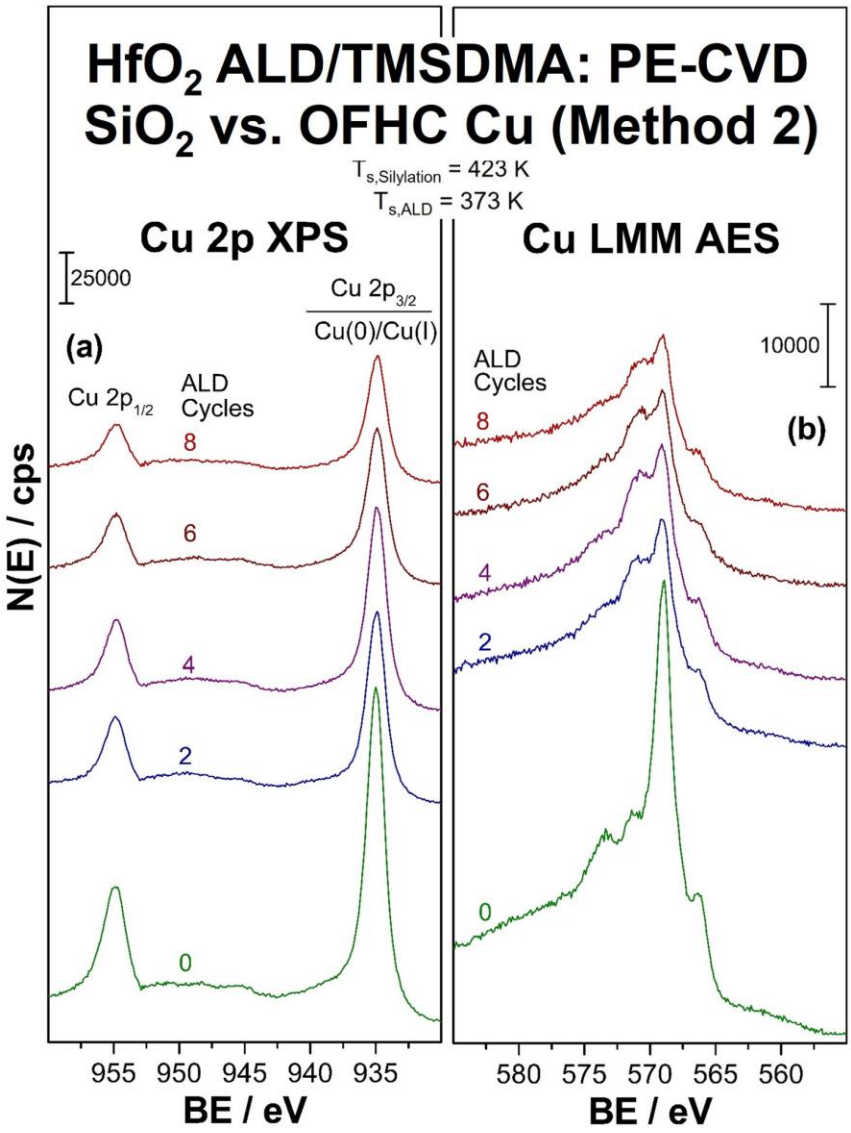


Figure 5.13 Cu 2p XPS (a) and Cu LMM AES (b) for the TMSDMA-treated cleaner OFHC Cu (cleaner CuO_x/Cu, method 2) substrate used in the data in Figure 5.11**.**

Although the Cu 2p XPS and Cu LMM AES signals in Figure 5.13a and 5.13b, respectively, for OFHC Cu (cleaner CuO_x/Cu) attenuate with the number of HfO_2 ALD cycles used, the latter data suggests that the surface retains some of its metallic character even after 8 HfO_2 ALD cycles. This is indicated by the appearance and position of the persisting peak at approximately 566 eV that is characteristic of Cu(0).[113]

Periodic reapplications of the inhibitor were investigated next given the lack of any area-selective deposition on either surface with or without the initial TMSMDA inhibitor exposure. These studies aimed to extend the passivation on the dielectric surface to a higher number of TiO_2 or HfO_2 ALD cycles prior to inhibition loss with the hopes of improving area-selectivity.

5.6 TMSDMA Inhibitor Reapplications: PE-CVD SiO_2 vs. CuO_x/Cu

The surface passivation efficacy of silylated PE-CVD-grown SiO_2 is eventually lost after a certain number of TiO_2 or HfO_2 ALD cycles; in other words, after a certain number of repeated exposures to the TDMATi or TDMAHf metalorganic precursors (and H_2O). The impact of periodic inhibitor reapplications using TMSDMA (using the same conditions as prior) was therefore investigated to potentially restore the initial passivation of the dielectric sample by healing any defects that may form within the organosilane monolayer after a sufficient number of ALD cycles. In doing so the selectivity window could theoretically be extended to a higher number of ALD cycles. In contrast, since the initial TMSDMA exposure did not inhibit thin film deposition on OFHC Cu (CuO_x/Cu), it was expected that further reapplications would also have the same effect.

5.6.1 TiO_2 ALD

In addition to the initial TMSDMA treatment, inhibitor reapplications were conducted every 5 TiO_2 ALD cycles on both substrates up to the 10th cycle, as displayed in Figure 5.14.

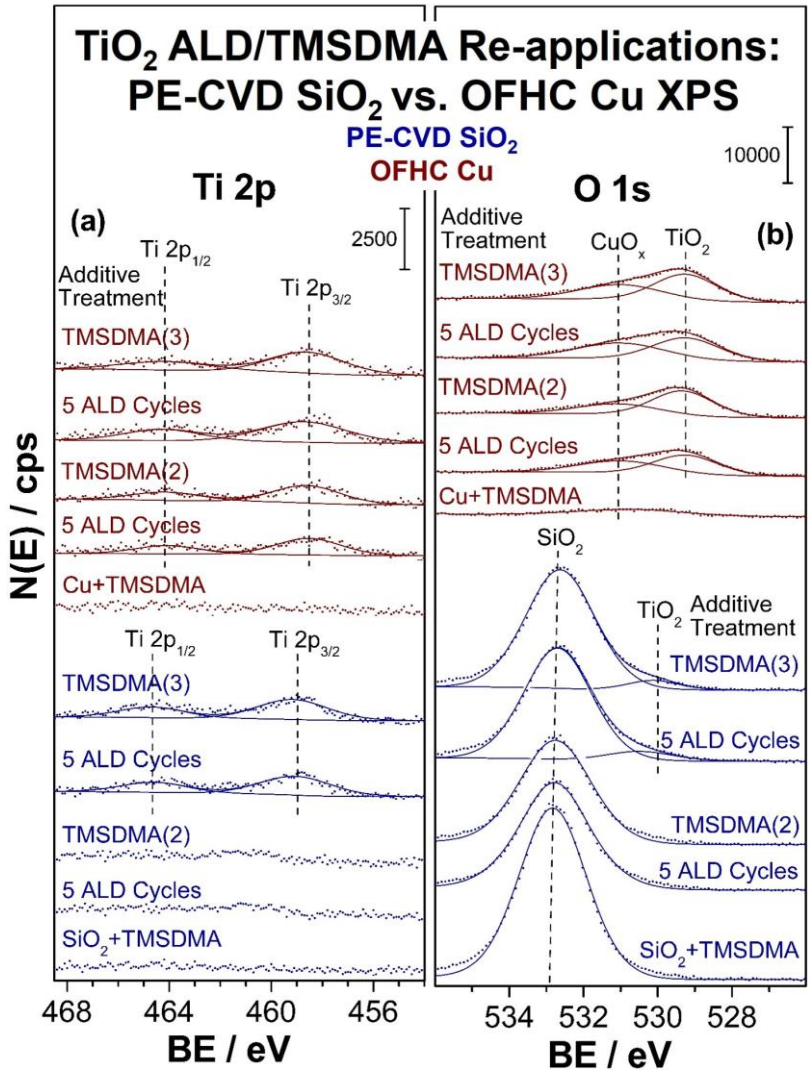


Figure 5.14 Ti 2p (a) and O 1s (b) XPS for TMSDMA-silylated PE-CVD-grown SiO_2/Si(100) and TMSDMA-treated OFHC Cu (CuO_x/Cu) substrates as a function of increasing number of TiO_2 ALD cycles. TMSDMA was reapplied on each surface after every 5 TiO_2 ALD cycles until after the 10th cycle.

For the PE-CVD-grown SiO_2 substrate, the absence of the characteristic Ti 2p XPS signals after 5 TiO_2 ALD cycles in Figure 5.14a indicated that complete surface passivation was achieved up to this point. In contrast, these signals appear in the Ti 2p XPS for OFHC Cu (CuO_x/Cu) by this stage indicating the presence of Ti atoms on the surface. These observations are consistent with those reported earlier. No changes in the XPS data for either surface was discerned following the first TMSDMA reapplication (the second overall exposure, denoted as TMSDMA(2)). Two peaks appear in the Ti 2p XPS for the PE-CVD SiO_2 substrate after the first TMSDMA reapplication (TMSDMA(2)), which is carried out after another 5 ALD cycles (10 total). This is corroborated in the O 1s XPS in Figure 5.14b by the appearance of the TiO_2-O 1s peak component. Despite a second TMSDMA exposure, TiO_2 was still deposited on the PE-CVD SiO_2 surface after 10 ALD cycles indicative that the inhibitor reapplication did not heal any defects in the organosilane monolayer to extend the passivation. As a result, the selectivity window remained unchanged compared to the data where only an initial TMSDMA exposure was used. Furthermore, a second inhibitor reapplication (TMSDMA(3)) had no effect on inhibiting TiO_2 growth on the dielectric. Similarly, neither reapplication of TMSDMA inhibited film deposition on OFHC Cu (CuO_x/Cu).

The TMSDMA reapplications did not result in any significant changes to the spectral features of the Ti 2p or O 1s XPS data and thus do not impact the deposition of TiO_2 ALD on either sample. Analysis of the Cu 2p and Si 2p XPS data in Figure 5.15 provides further insight into the changes that occur with the underlying OFHC Cu (CuO_x/Cu) surface.

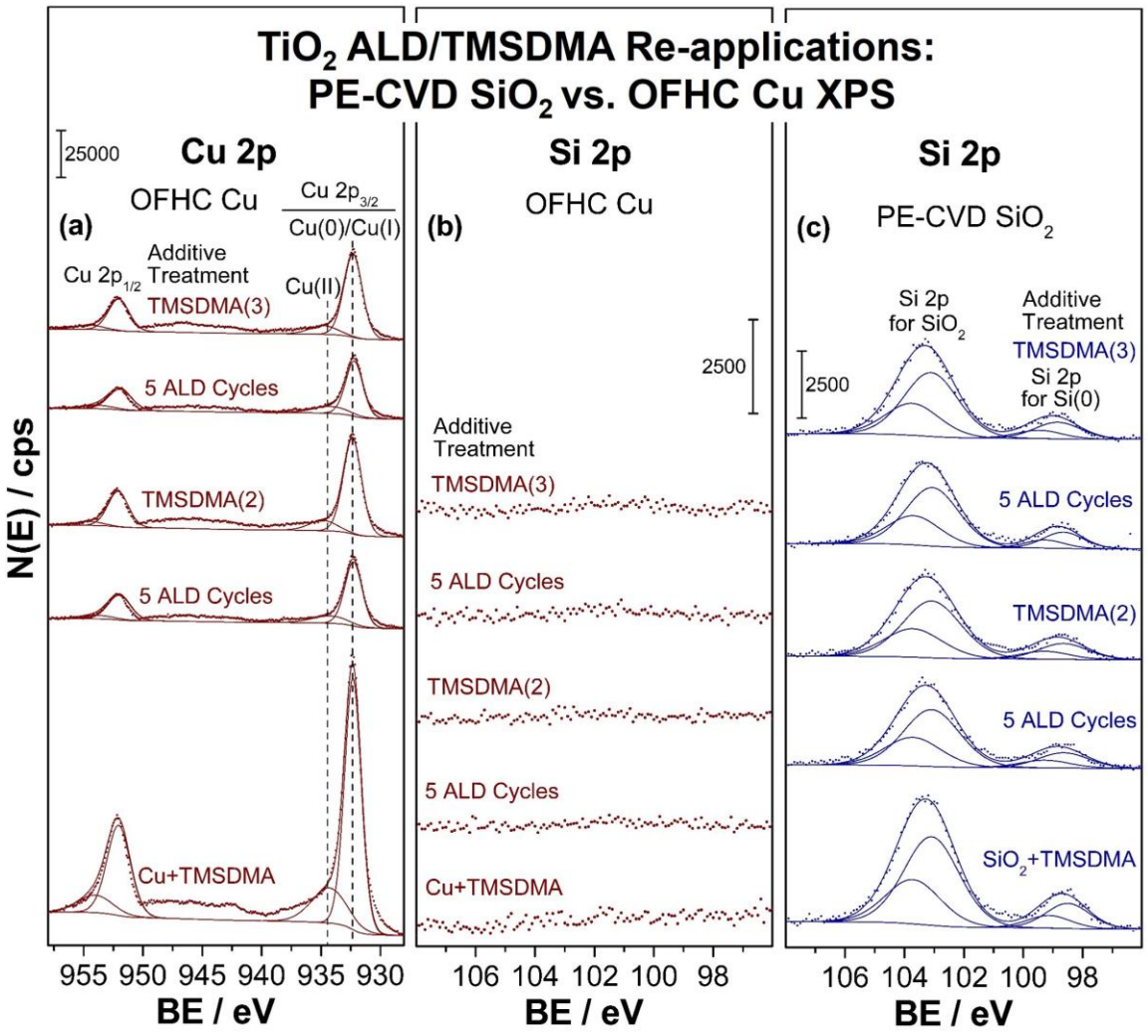


Figure 5.15 Cu 2p XPS (a) and Si 2p XPS (b) for the TMSDMA-treated OFHC Cu (CuO_x/Cu) substrate, and Si 2p XPS (c) for the TMSDMA-silylated PE-CVD-grown SiO_2/Si(100) substrate used for the data displayed in Figure 5.10, as a function of increasing number of TiO_2 ALD cycles. TMSDMA was reapplied on each surface after every 5 TiO_2 ALD cycles until after the 10^{th} cycle.

The Cu 2p and Si 2p XPS data for the OFHC Cu (CuO_x/Cu) and the Si 2p XPS data for the PE-CVD-grown SiO_2 substrates, used in Figure 5.14, are displayed in Figure 5.15a and 5.15b, and 5.15c, respectively. The attenuation of both the Cu(0)/Cu(I)-Cu 2p and Cu(II)-Cu 2p spin-orbit split XPS signals after 5 TiO_2 ALD cycles is observed in Figure

5.15a. The former pair of features, however, unexpectedly evolved following the first TMSDMA reapplication (TMSDMA(2)). A similar trend is observed after the next 5 TiO_2 ALD cycles and second TMSDMA reapplication (TMSDMA(3)), in which attenuation of the Cu(0)/Cu(I)-Cu 2p XPS peaks are observed followed by an evolution in these signals. Conversely for the PE-CVD SiO_2 substrate (Figure 5.15c), only attenuation of the SiO_2-Si 2p XPS signal is observed after 5 TiO_2 ALD cycles. Unlike the observations in the Cu 2p XPS data for the OFHC Cu (CuO_x/Cu) substrate, no continuous fluctuating trends (attenuation during ALD followed by evolution during inhibitor reapplications) in the Si 2p XPS signals pertaining to the PE-CVD SiO_2/Si(100) sample were observed. Moreover, no Si 2p XPS signals were ever detected for the OFHC Cu (CuO_x/Cu) sample (Figure 5.15b) throughout the entire process, indicating that no Si atoms were present on these surfaces and that silylation does not occur during any of the TMSDMA (initial or subsequent) exposures.

To better understand the changes in the Cu 2p XPS peak intensities due to the inhibitor reapplications, the integrated XPS peak areas for the OFHC Cu substrate were plotted as a function of increasing TiO_2 ALD cycles and TMSDMA reapplications, as depicted in Figure 5.16.

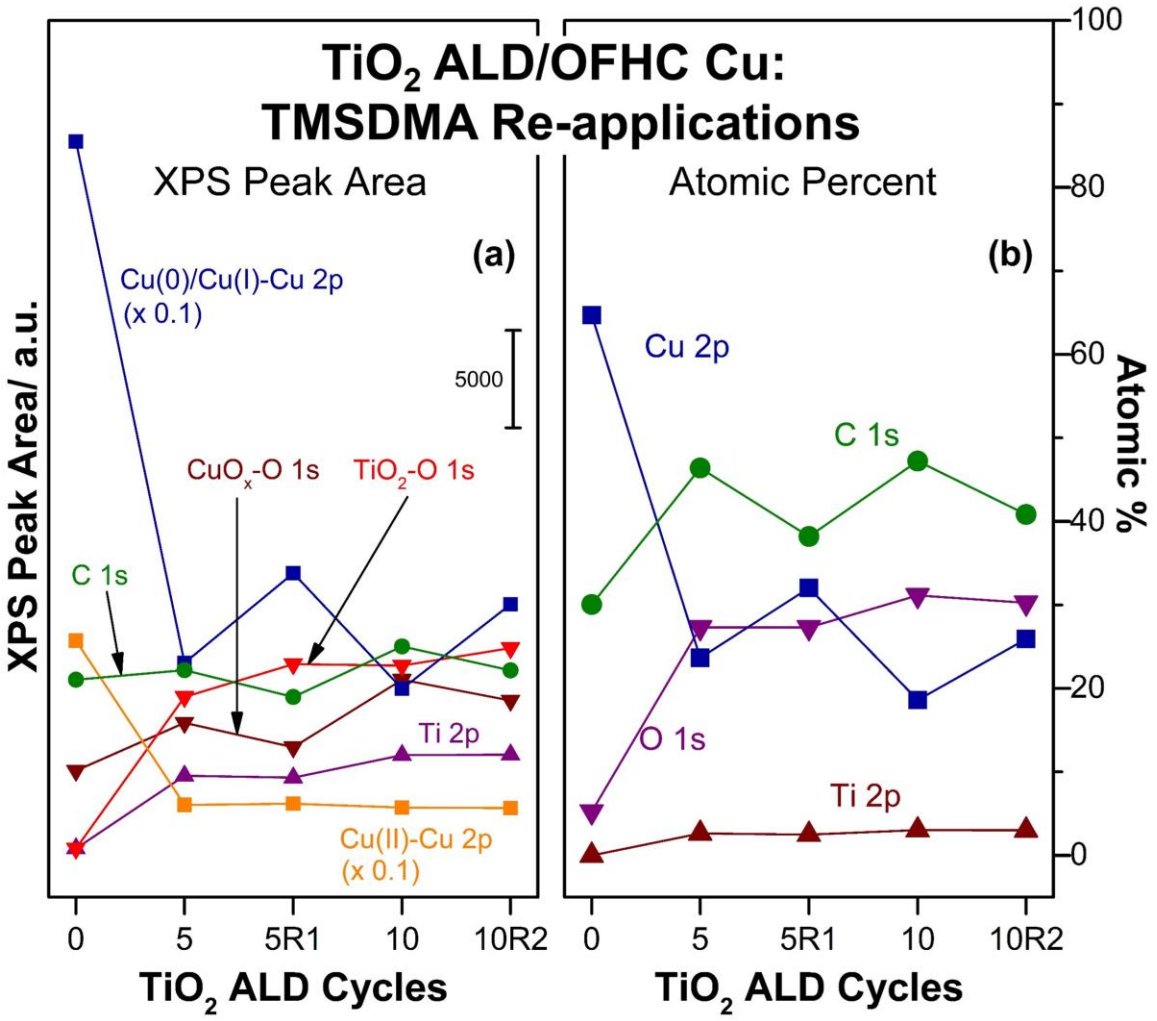


Figure 5.16 (a) Cu(0)/Cu(I)-Cu 2p, Cu(II)-Cu 2p, CuO_x-O 1s, TiO_2-O 1s, C 1s, and Ti 2p XPS peak areas derived from the XPS data for TMSDMA-treated OFHC Cu (CuO_x/Cu) substrate displayed in Figure 5.14 and 5.15a, as a function of increasing TiO_2 ALD cycles and TMSDMA inhibitor exposures. TMSDMA was reapplied on each surface after every 5 TiO_2 ALD cycles until after the 10th cycle, where "5R1" and "10R2" denote the first and second inhibitor reapplication after the 5th and 10th ALD cycle, respectively. (b) Atomic-percent composition profiles estimated from the data in panel (a) in combination with corresponding ASFs.

The integrated XPS peak area profiles for all elements present on the TMSDMA-treated OFHC Cu (CuO_x/Cu) surface are displayed in Figure 5.16a as a function of increasing ALD cycles and TMSDMA exposures, where "5R1" and "10R2" denote the

first (TMSDMA(2)) and second (TMSDMA(3)) inhibitor reapplications, respectively. A decrease in the Cu(0)/Cu(I)-Cu 2p and Cu(II)-Cu 2p peak areas is observed after 5 ALD cycles accompanied by the evolution of both the CuO_x-O 1s and TiO_2-O 1s component peak areas. Furthermore, the C 1s peak area also evolves due to the ex-situ transfer of the sample that is required to conduct subsequent ALD. Following the first TMSDMA reapplication (5R1), the Cu(0)/Cu(I)-Cu 2p signal unexpectedly increased concomitant to a decrease in the CuO_x-O 1s component area. The Cu(II)-Cu 2p component area remained constant throughout this process while a decrease in the C 1s peak area is observed after 5R1 and 10R2. Some adventitious carbon that is adsorbed on the surface after ex-situ transfer is expected to be removed after annealing the substrate to 423 K during the TMSMDA reapplications. Due to this, an increase in the Cu(0)/Cu(I)-Cu 2p peak area is observed as the surface becomes cleaner and uncovers the underlying Cu(0) and Cu_2O.

The observations with regards to the alternating Cu 2p and C 1s XPS peak areas are further highlighted in Figure 5.16b from the plot of the surface atomic-percent composition profiles. A clear conclusion can be made in that the decrease in the total carbon coverage following each inhibitor application results in the exposure of more underlying copper atoms. It is also seen here that the degree of Ti from TiO_2 present on the surface is quite small relative to the chemical concentrations of other species, remaining below 5% even after 10 TiO_2 ALD cycles. Furthermore, the Ti 2p XPS signal (Figure 5.16a) remains constant after the removal of adventitious carbon following each reapplication. Taken together, these observations suggest that adventitious carbon may not form over the Ti atoms and that sub-monolayer coverages of TiO_2 exist by 10 cycles.

5.6.2 HfO_2 ALD

The same series of experiments were repeated using HfO_2 ALD with more periodic inhibitor reapplications conducted between every 2 ALD cycles on both the OFHC Cu (CuO_x/Cu) and PE-CVD-grown SiO_2 substrate up to the 8th cycle, shown in Figure 5.17.

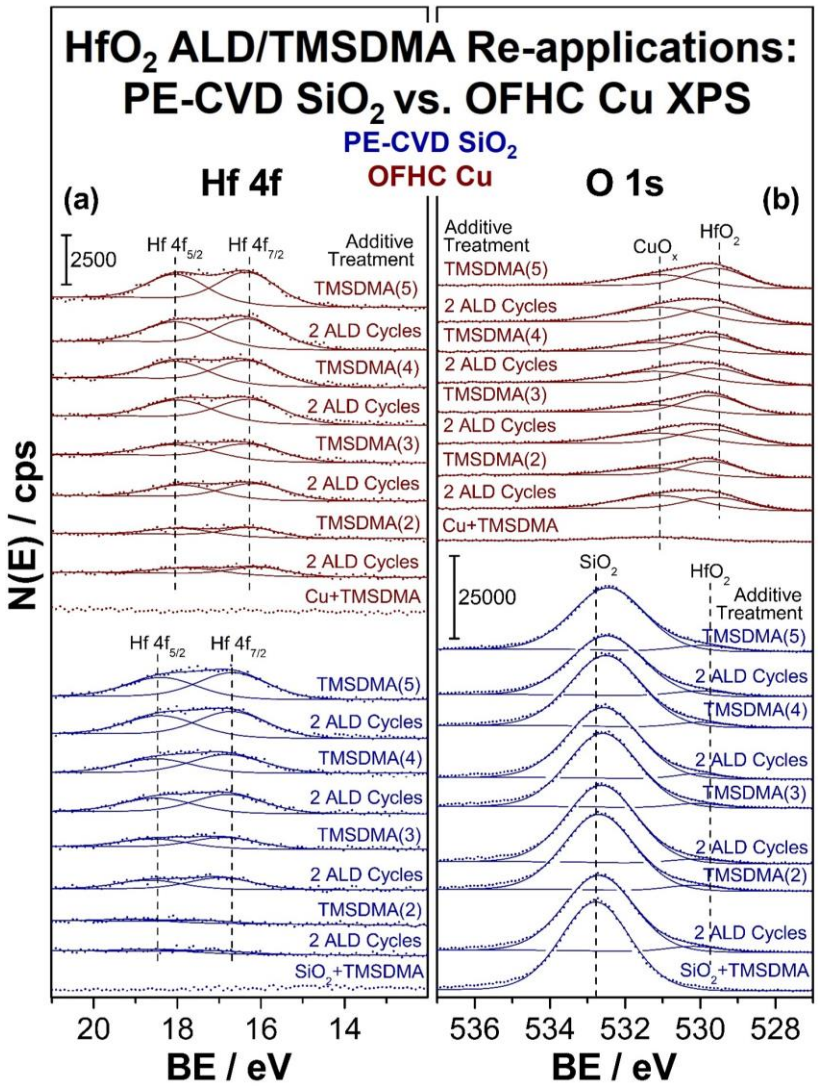


Figure 5.17 Hf 4f (a) and O 1s (b) XPS for TMSDMA-silylated PE-CVD-grown SiO_2/Si(100) and TMSDMA-treated OFHC Cu (CuO_x/Cu) substrates as a function of increasing number of HfO_2 ALD cycles. TMSDMA was reapplied on each surface after every 2 HfO_2 ALD cycles until after the 8thth cycle.

In Figure 5.17a, the Hf 4f XPS spectra exhibit characteristic $4f_{5/2}$ and $4f_{7/2}$ spin-orbit split signals for both the TMSDMA-treated OFHC Cu (CuO_x/Cu) and TMSDMA-silylated PE-CVD-grown SiO_2 samples; however, lower peak intensities are observed for the latter (as expected). Similar to the trends observed when using TiO_2 ALD in Figure 5.14, the organosilane monolayer becomes irreversibly damaged despite multiple TMSDMA reapplications as evidenced by the inability to prevent HfO_2 deposition after a higher number of ALD cycles. This reiterates the notion that the defects that form within the organosilane monolayer are unable to be healed to restore the surface passivation to a point comparable to the initially silylated surface. Inhibitor reapplications also do not block subsequent film deposition on the OFHC Cu (CuOx/Cu) substrate. No changes to the HfO_2-O 1s component area (Figure 5.13b) on either surface is discernible throughout the entire process.

The Cu 2p and Si 2p XPS data were plotted in Figure 5.18 to assess if changes between the underlying OFHC Cu (CuO_x/Cu) surface and adsorbed adventitious carbon would occur here similar to the data shown prior.

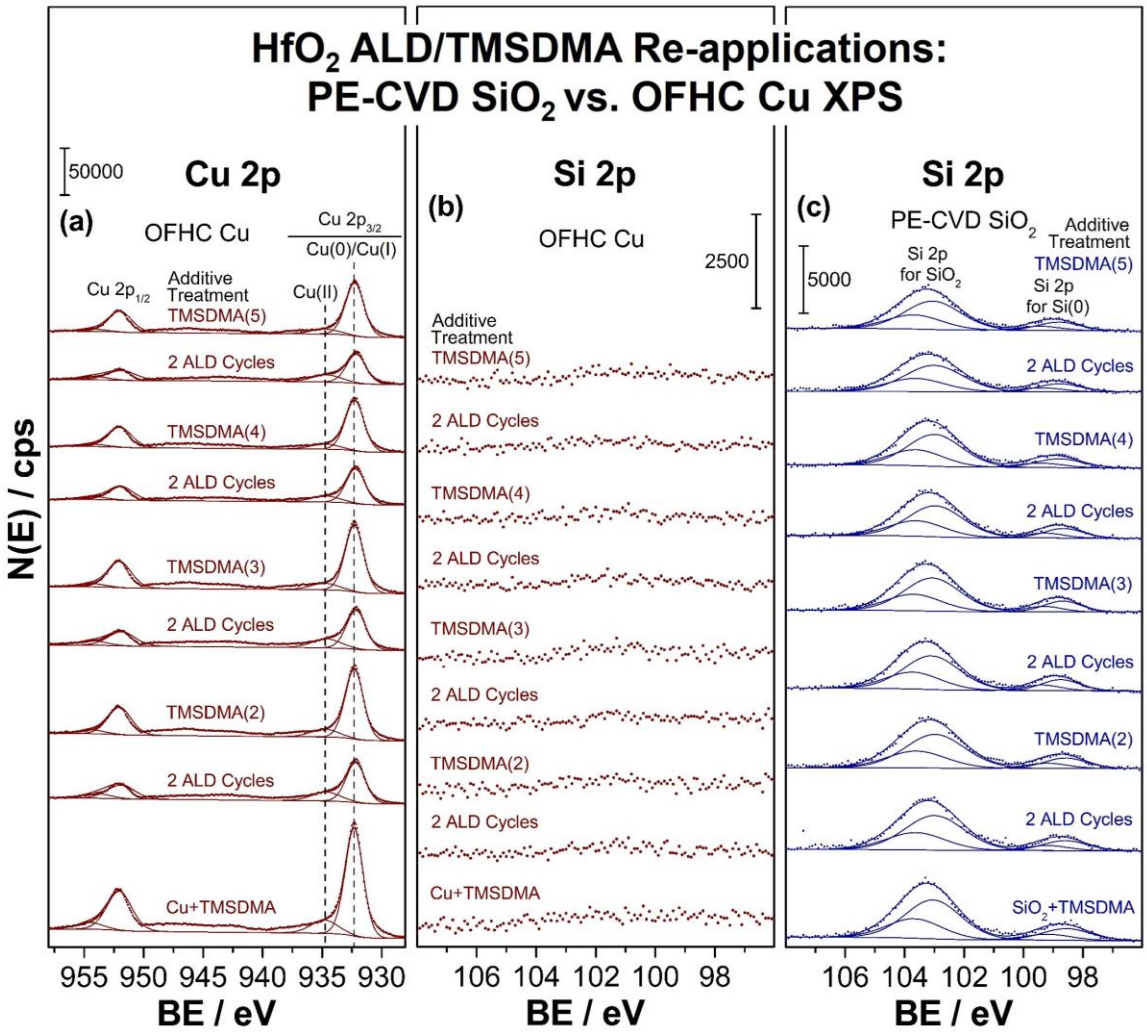


Figure 5.18 Cu 2p XPS (a) and Si 2p XPS (b) for the TMSDMA-treated OFHC Cu (CuO_x/Cu) substrate, and Si 2p XPS (c) for the TMSDMA-silylated PE-CVD-grown SiO_2/Si(100) substrate used for the data displayed in Figure 5.13, as a function of increasing number of HfO_2 ALD cycles. TMSDMA was reapplied on each surface after every 2 HfO_2 ALD cycles until after the 8thth cycle.

The Cu 2p and Si 2p XPS data for the OFHC Cu (CuO_x/Cu) and Si 2p XPS data for PE-CVD-grown SiO_2 samples used in Figure 5.17, are displayed in Figure 5.18a and 5.18b, and 5.18c, respectively. The number of reapplications performed here were increased (from two to four) in order to further investigate the trend in the evolution of the

Cu(0)/Cu(I)-Cu 2p and attenuation of the CuO_x-O 1s and C 1s XPS signals during the later inhibitor reapplications. It is evident from Figure 5.18a that an enhancement in the Cu(0)/Cu(I)-Cu 2p signal intensity is also observed following each TMSDMA reapplication, as frequently as after every 2 HfO_2 ALD cycles. The extent of evolution decreases during later reapplications (TMSDMA(4) and (5)). In contrast, the SiO_2-Si 2p signal in the Si 2p XPS data (Figure 5.18c) for the silylated PE-CVD-grown SiO_2 surface does not exhibit this same fluctuating trend after treatment with HfO_2 ALD followed by reapplication of TMSDMA, similar to the observations in Figure 5.15c. Only attenuation of this signal is observed throughout the entire process. Moreover, the reapplications did not extend the selectivity window as indicated by the consistent attenuation of the SiO_2-Si 2p signal after every 2 ALD cycles. Similar to Figure 5.15b, the Si 2p XPS data in Figure 5.18b show that silylation does not occur on the OFHC Cu (CuO_x/Cu) surface during any of the TMSDMA exposures.

To further analyze these trends, the integrated XPS peak areas for the OFHC Cu substrate were plotted as a function of increasing HfO_2 ALD cycles and TMSDMA reapplications shown in Figure 5.19.

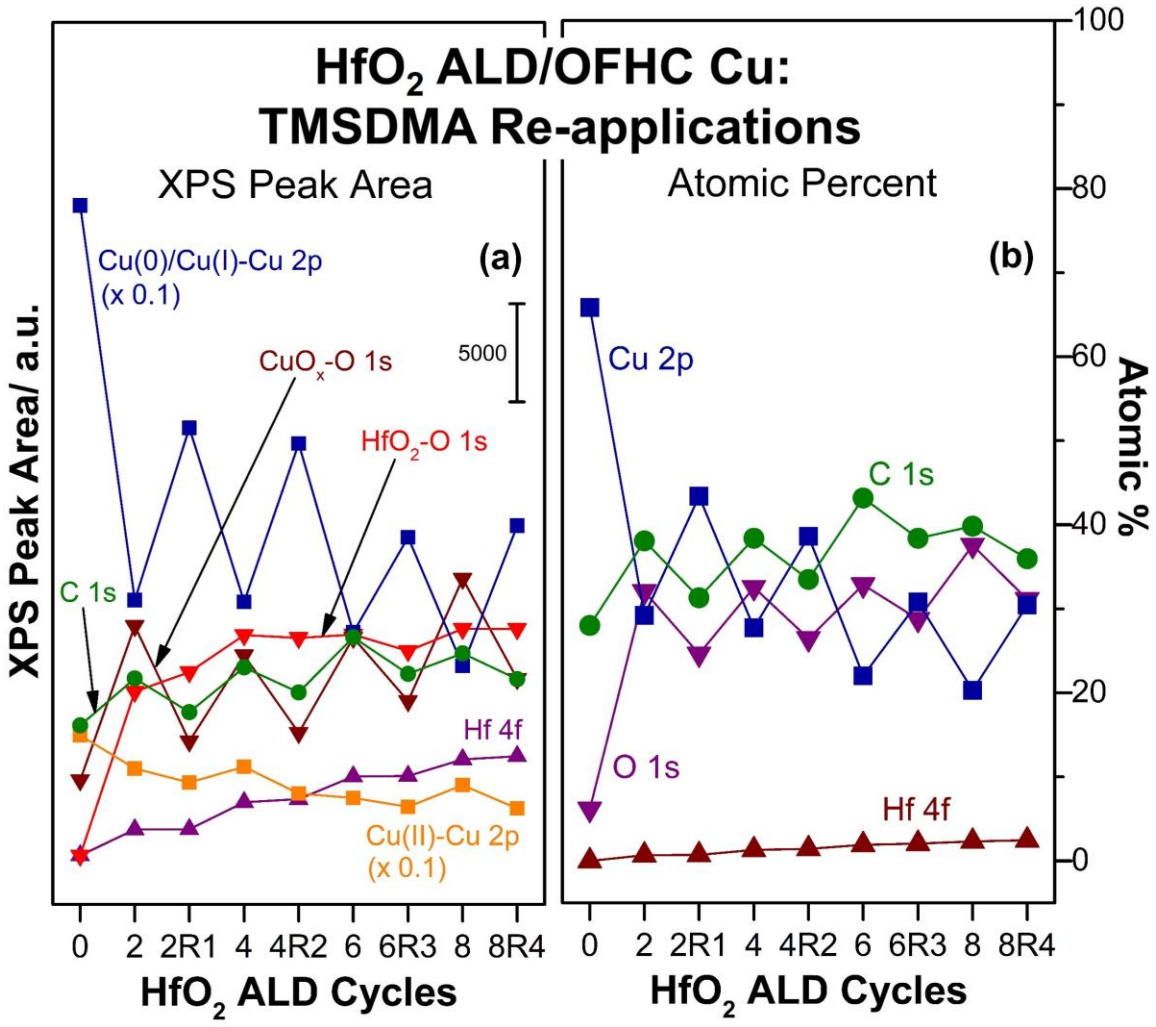


Figure 5.19 (a) Cu(0)/Cu(I)-Cu 2p, Cu(II)-Cu 2p, CuO_x-O 1s, HfO_2-O 1s, C 1s, and Hf 4f XPS peak areas derived from the XPS data for the TMSDMA-treated OFHC Cu (CuO_x/Cu) substrate, displayed in Figure 5.17 and 5.18a, as a function of increasing HfO_2 ALD cycles. TMSDMA was reapplied on each surface after every 2 HfO_2 ALD cycles until after the 8th cycle, where "2R1", "4R2", "6R3", and "8R4" denote the first, second, third, and fourth inhibitor reapplication after the 2nd, 4th, 6th, and 8th ALD cycle, respectively. (b) Atomic-percent composition profiles estimated from the data in panel (a) in combination with corresponding ASFs.

Figure 5.19a provides the XPS peak areas for all elements present on the TMSDMA-treated OFHC Cu (CuO_x/Cu) substrate where "2R1", "4R2", "6R3", and "8R4" denote the first (TMSDMA(2)), second (TMSDMA(3)), third (TMSDMA(4)), and fourth

(TMSDMA(5)) inhibitor reapplications, respectively, after every two HfO_2 ALD cycles. The Cu(0)/Cu(I)-Cu 2p, Cu(II)-Cu 2p, and CuO_x-O 1s peak area decreased while those for C 1s, HfO_2-O 1s, and Hf 4f increased after 2 HfO_2 ALD cycles. Following the first TMSDMA reapplication (2R1) however, the Cu(0)/Cu(I)-Cu 2p component area increases accompanied by the decrease in the Cu(II)-Cu 2p, CuO_x-O 1s and C 1s peak areas. Similar to before, the C 1s XPS peak area attenuates after each inhibitor reapplication since the removal of some adventitious carbon is expected when heating the sample to 423 K, thereby exposing the copper surface in the process. A unique observation here is that the Cu(II)-Cu 2p peak area decreases after each inhibitor reapplication, whereas it remained constant in the data shown previously in Figure 5.16a. It is speculated here that this may indicate some degree of partial reduction of CuO to Cu_2O, although further studies are required to unequivocally confirm this. While fluctuating trends in the Cu(0)/Cu(I)-Cu 2p, Cu(II)-Cu 2p, and CuO_x-O 1s peak areas are periodically observed, this behavior markedly occurs to a greater extent here as opposed to the data shown in 5.16a even though the inhibitor treatments were applied in the exact same manner in both cases.

The surface atomic-percent composition data in Figure 5.19b indicates that the degree of Hf atoms present on the surface is minimal (<5%) even after 8 ALD cycles. Sub-monolayer coverages of HfO_2 likely exist similar to the case in Figure 5.16b after conducting 10 TiO_2 ALD cycles.

The evolution of the XPS peak areas for the PE-CVD SiO_2 surface, similar to those plotted for the OFHC Cu (CuO_x/Cu) surface following TiO_2 (Figure 5.16a) or HfO_2 (Figure 5.19a), was assessed and is displayed in Figures 5.20a and 5.20b, respectively.

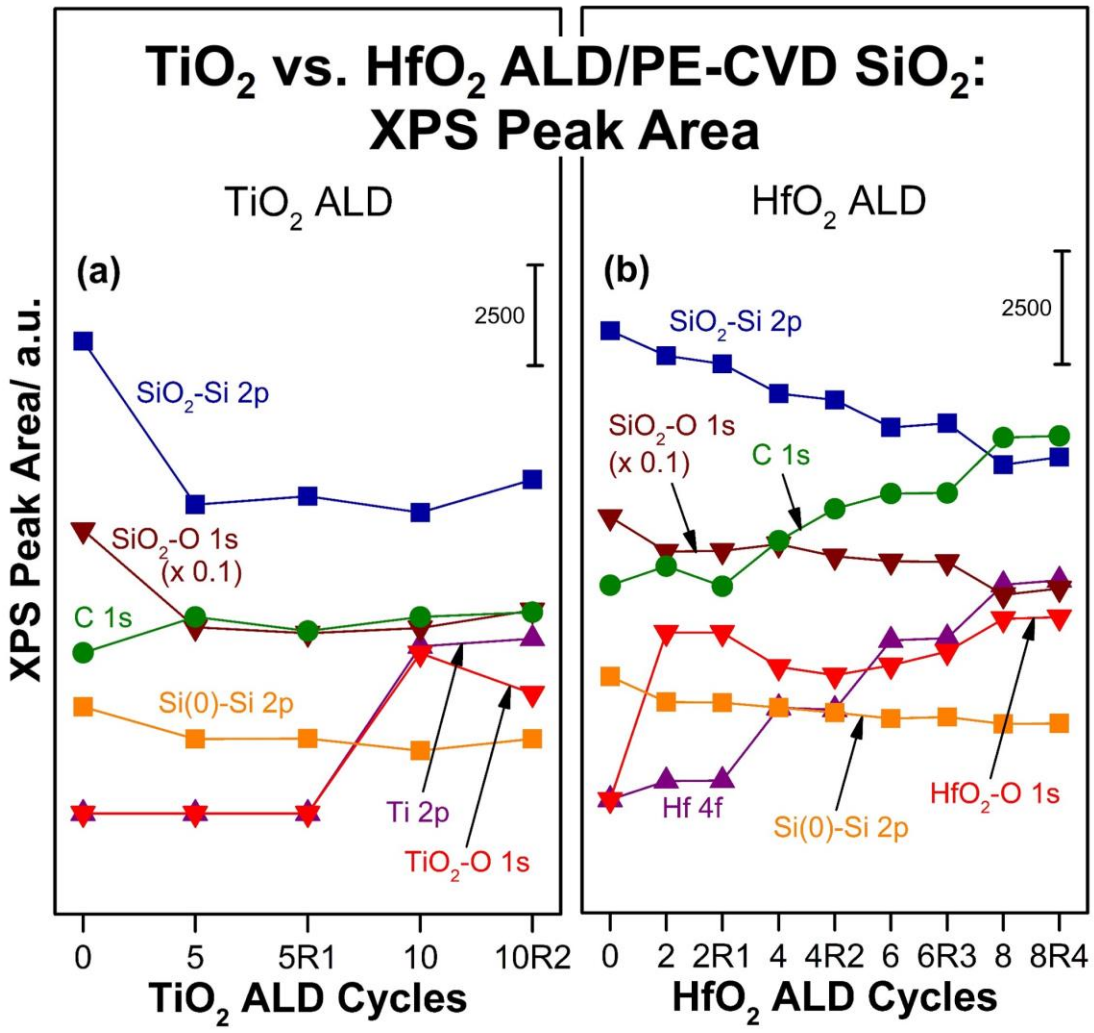


Figure 5.20 (a) SiO_2-Si 2p, Si(0)-Si 2p, SiO_2-O 1s, TiO_2-O 1s, C 1s, and Ti 2p XPS peak areas for the TMSDMA-silylated PE-CVD-grown SiO_2/Si(100) substrate (from Figure 5.15c), as a function of increasing TiO_2 ALD cycles. (b) SiO_2-Si 2p, Si(0)-Si 2p, SiO_2-O 1s, HfO_2-O 1s, C 1s, and Hf 4f XPS peak areas for the TMSDMA-silylated PE-CVD-grown SiO_2/Si(100) substrate (from Figure 5.18c), as a function of increasing HfO_2 ALD cycles. In both cases, the TMSDMA reapplication label, "R", denotes the same information as previously described.

As aforementioned, no fluctuating trends in the SiO_2-Si 2p, C 1s, or SiO_2-O 1s XPS signals, similar to those observed for the OFHC Cu (CuO_x/Cu) substrate, were seen here for the PE-CVD SiO_2 substrates following TiO_2 or HfO_2 ALD. In the case of TiO_2 ALD (Figure 5.20a), no significant changes in the XPS peak area are observed until 10 cycles

when an evolution in the Ti 2p and TiO_2-O 1s signal are observed indicative of the formation of TiO_2. Unexpectedly, the SiO_2-Si 2p signal does not attenuate following this. While the C 1s peak area initially increases after transferring the sample ex-situ, it remains relatively constant after TiO_2 ALD and the subsequent inhibitor reapplications unlike in the case for the copper substrate. In comparison, the Hf 4f XPS peak area slightly evolves by 2 HfO_2 ALD cycles (Figure 5.20b). The periodic evolution of this signal every 2 cycles is accompanied by the attenuation of the SiO_2-Si 2p peak area. A distinguishable difference here as opposed to Figure 5.20a is the trends observed in the C 1s peak areas. In the case of HfO_2 ALD, the area begins to increase after both ALD and subsequent inhibitor reapplications starting from the second TMSDMA reapplication and reaches an asymptote by the third TMSDMA reapplication. Then, the area suddenly increases after the 8^{th} cycle and remains constant following the final reapplication. What is clear from the XPS peak area profiles is that periodic treatment with TMSDMA did not heal the defective organosilane monolayer.

As the inhibitor reapplications were not successful in extending the passivation on the dielectric surfaces after every 2 HfO_2 ALD cycles, the frequency of the reapplications was increased next. It was previously confirmed that the initially silylated PE-CVD-grown SiO_2/Si(100) surface blocked TDMAHf nucleation during the first HfO_2 ALD cycle (Chapter 4). With this information in mind, the inhibitor was therefore next reapplied in an alternating sequence between each cycle prior to any passivation loss observed in the Hf 4f XPS data. This approach aimed to potentially heal any defects within the organosilane monolayer before any undesirable Hf nuclei could chemisorb onto the surface during ALD.

5.6.2.1 Reapplications on PE-CVD-grown SiO_2/ALD Cycle

XPS data for PE-CVD SiO_2/Si(100) as a function of alternating TMSDMA exposures and single HfO_2 ALD cycles (as opposed to applying the silylation treatment every two ALD cycles) for the first 2 ALD cycles is displayed in Figure 5.21.

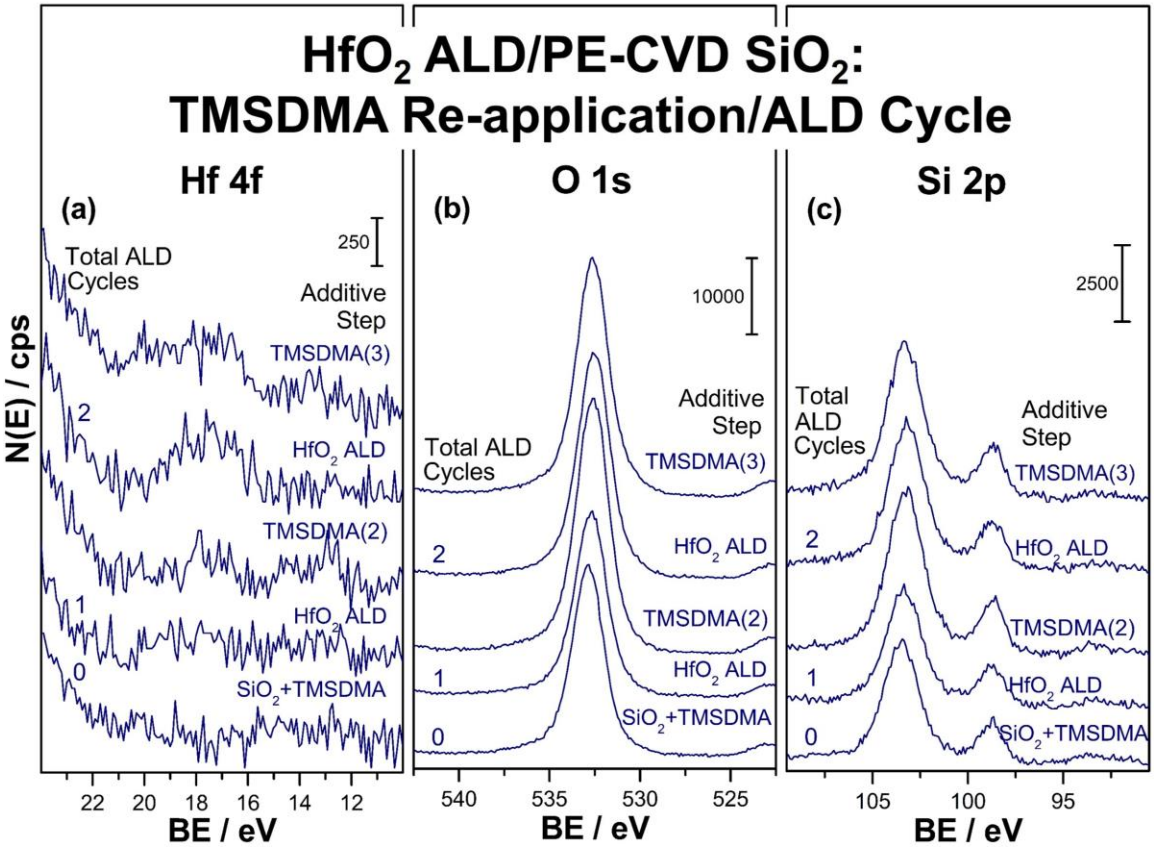


Figure 5.21 (a) Hf 4f, (b) O 1s, and (c) Si 2p XPS for TMSDMA-silylated PE-CVD-grown SiO_2/Si(100) after each HfO_2 ALD cycle up to the first two cycles. TMSDMA was reapplied between each ALD cycle.

No characteristic Hf 4f XPS signals appear after the first HfO_2 ALD cycle in the Hf 4f XPS shown in Figure 5.21a, confirming that TDMAHf does not chemisorb onto the

surface. Then, the O 1s (Figure 5.21b), SiO_2-Si 2p, and Si(0)-Si 2p (Figure 5.21c) XPS signals unexpected increase after the first TMSDMA reapplication (TMSDMA(2)). This is not yet fully understood but may be due to some experimental error during the data acquisition process and is likely not due to any chemical changes that occur. The appearance of Hf 4f XPS signals is in any case evident after 2 ALD cycles, indicating that the inhibitor reapplication did not facilitate blocking further chemical reactions against the metalorganic precursor even when used in between each ALD cycle. This is concomitant to the shift observed in the O 1s XPS (Figure 5.20b) of the SiO_2-O 1s signal towards slightly lower binding energies after 2 cycles indicating the formation of HfO_2. These results demonstrate that the inhibitor reapplications alone would be insufficient in healing any defects within the organosilane monolayer that may arise during ALD. Other treatments will be ultimately necessary in the future to remove the defective monolayer and form a new one to allow film growth to proceed in an area-selective fashion.

5.7 Discussion

Due to the formation of a native oxide layer on metallic surfaces upon exposure to air, acetic acid was used to etch the oxide on the OFHC Cu substrates used in these studies.[112] While vapor phase chemical treatments have been shown to reduce copper oxide, they are typically complex, require the use of temperatures higher than 473 K, and may result in the addition of other undesirable impurities to the surface.[118–120] The as-received untreated OFHC Cu substrate exhibited a WCA measurement of approximately 55°, in contrast to the value of 76° obtained for the untreated Cu foil sample. The lower

measurement observed in the case of the OFHC Cu may be attributed to the lower degree of oxygen content present on those surfaces. A lower contact angle for the OFHC Cu sheet relative to the Cu foil is possible since surface wettability increases as a surface becomes more metallic.[121] The angle decreases significantly after a 2 min. treatment in acetic acid, indicative of the removal of the native oxide as more of the metallic surface is exposed. However, a limitation with regards to the removal of oxygen is reached by 5 min. on both surfaces, as the contact angle is not reduced below approximately 35°. This value is approximately within experimental error to that obtained for Cu surfaces prepared via PVD, in which clean 100 nm thick Cu films were deposited onto flat SiO_2 substrates under high vacuum conditions resulting in a WCA measurement of approximately 38°.[122] It is likely that this WCA measurement range reflects the minimum degree of oxidation that occurs on the Cu surface after transferring it ex-situ from UHV to take the measurement, or after cleaning in acetic acid.

The broad Cu(II) satellite feature between 938-946 eV in the Cu 2p XPS data (Figure 5.2b) nearly vanishes following the acetic acid treatment indicating the removal of most of the oxide that exists in the form of CuO; however, a weak signal still persisted. Furthermore, some copper oxide is confirmed based on the O 1s XPS signal (Figure 5.2a). Due to the very weak Cu(II) satellite feature in the Cu 2p XPS and residual oxygen observed in the O 1s XPS, the oxide content observed here is likely comprised of a mixture of mostly Cu_2O with some degree of CuO. It should be mentioned however that some contribution to the O 1s XPS peak area may be attributed to atomic oxygen adsorbed on the surface; as such, this surface oxygen is referred to as CuO_x. This suggests that the

prominent Cu $2p_{3/2}$ and $2p_{1/2}$ peaks in the Cu 2p XPS data may be due to both Cu(0) and Cu(I) species.[114,120]

Only one other work, by Mandal et. al., so far has, to the best of our knowledge, investigated the interaction of Cu with TMSDMA, in which it was claimed that the surface is not passivated by TMSDMA and remained fully reactive for subsequent Ru CVD.[122] However, the inhibitor-substrate interaction was only qualitatively demonstrated in the form of WCA measurements that did not increase after treatment with TMSDMA, suggestive of the absence of trimethylsilyl groups on the Cu surface (the nature of which was left undefined) in an indirect manner. Furthermore, no comparison was made to Cu substrates not treated with TMSDMA during the film deposition measurements. Conversely, the results here provide in-situ evidence for these result using spectroscopy. To the best of our knowledge, the work in this dissertation is the first study to directly investigate the interaction of TMSDMA with OFHC Cu (CuO_x/Cu) using XPS. The principal finding from the results reported here was that TMSDMA does not passivate the OFHC Cu (CuO_x/Cu) surface: trimethylsilyl moieties did not adsorb on the surface as no Si atoms were ever detected in the Si 2p XPS data (Figure 5.2c). The adsorption of $Si(CH_3)_3$ functional groups is typically characterized by the appearance of a peak at approximately 101 eV in the Si 2p XPS,[123] a feature that is absent in the Si 2p XPS data belonging to the copper surfaces shown in this work. This was further corroborated by the Ti 2p (Figure 5.3a) and Hf 4f (Figure 5.7a) XPS data, which demonstrated that the evolution of the Ti 2p or Hf 4f signals after TiO_2 or HfO_2 ALD, respectively, is not impeded for copper substrates

treated with TMSDMA (in whatever form it may exist). This is useful, as it establishes OFHC Cu (CuO_x/Cu) as a viable GS when film deposition on the metal substrate is desired.

Inherent selectivity was observed between the OFHC Cu (CuO_x/Cu) and PE-CVD SiO_2/Si(100) blank substrates as demonstrated by the XPS data in Figure 5.6a, favoring TiO_2 ALD film growth on the hydroxyl-rich dielectric surface over the metal substrate. TDMATi chemisorption preferentially occurs on silica to the presence of acidic silanol nucleation centers, allowing for a thicker film to be deposited on PE-CVD SiO_2 relative to OFHC Cu (CuO_x/Cu).[117] The results from Chapter 4 already confirmed that silylation of PE-CVD SiO_2 dielectric substrates with TMSDMA occurs using the same conditions as applied on OFHC Cu (CuO_x/Cu) here, with the surface fully passivated for at least 5 TiO_2 ALD cycles. By capping the hydroxyl nucleation centers of silica and removing them from being available for subsequent chemical reactions the activation energy for TDMATi to chemisorb onto the surface of SiO_2 is essentially increased, spatially directing the film growth onto the OFHC Cu (CuO_x/Cu) surface (Figure 5.5) during the initial stages of ALD. This one-step silylation process provides control over the selective deposition of TiO_2 between the two surfaces, providing a way to tune their function as a GS or NGS. Using TMSDMA in this case, the differences in surface chemistry between the two substrates can be exploited to shift the selectivity to favor film growth on the metal surface over the dielectric surface.

However, this direction is still in its nascent stages as a few drawbacks exist in the area-selectivity achievable using this scheme. In the inherent (as is, without using TMSDMA) area-selective system for example, while film deposition predominantly

occurred on SiO_2 some undesired growth is still observed on copper as early as 5 TiO_2 ALD cycles (Figure 5.10a). Furthermore, in the inverted (using TMSDMA) area-selective system preferential film deposition was only maintained up to 5 TiO_2 ALD cycles. In any case the findings reported here are encouraging, as they demonstrate a proof of concept for the prospect of controllable area-selectivity where the original functionality of the GS and NGS between the unmodified OFHC Cu (CuO_x/Cu) and PE-CVD SiO_2/Si(100) substrates may be inverted using a SMI such as TMSDMA when depositing certain metal oxides such as TiO_2. The case of HfO_2 ALD (Figure 5.10b) is less effective as indiscriminate film deposition occurs on both the OFHC Cu (CuO_x/Cu) and PE-CVD SiO_2/Si(100) surfaces without any inherent area-selectivity, likely due to the higher reactivity of TDMAHf with surface nucleation sites (discussed in Chapter 4). Even after applying TMSDMA to both surfaces, no form of area-selectivity was achieved as nucleation begins to occur on the dielectric substrate as early as 2 ALD cycles. Due to these reasons, periodic inhibitor reapplications to both substrates were investigated as a way to maintain selectivity for a higher number of metal oxide ALD cycles by attempting to re-silylate the dielectric sample.

Attempts to restore surface passivation on PE-CVD SiO_2/Si(100) using TMSDMA reapplications were ultimately unsuccessful at neither extending the delay in nucleation of the metalorganic precursor (TDMATi or TDMAHf) on the surface, nor reducing the amount of TiO_2 (Figure 5.14) or HfO_2 (Figure 5.17) that is deposited. This indicated that the original passivation layer becomes defective and irreversibly damaged after repeated exposures to the metalorganic precursor and H_2O, even prior to the nucleation of the metalorganic precursor. Consequently, it may become energetically and/or sterically

unfavorable for trimethylsilyl groups to react with surface hydroxyl nucleation centers (that may become liberated during the process of ALD and act as defect sites), preventing their removal chemically prior to the chemisorption of the metalorganic precursor on these sites. Moreover, the inhibitor reapplications did not passivate hydroxyl sites that may exist on the HfO_2 or TiO_2 grown by ALD. Chemisorption of Hf nuclei continued to occur on both OFHC Cu (CuO_x/Cu) and PE-CVD SiO_2/Si(100) surfaces, and Ti nuclei on at least the former (since growth was evident by 5 cycles in this case). It cannot be definitively claimed that trimethylsilyl moieties did not passivate TiO_2 deposited on the PE-CVD SiO_2 surface used in this example because an additional 5 ALD cycles following the second TMSDMA reapplication (TMSDMA(3)) was never performed (Figure 5.14a). Nevertheless, it is speculated that this may still be the case here as well. These observations are in good agreement with studies assessing the interaction of TMSDMA with various metal oxides that conclude that HfO_2 remains reactive after exposure to TMSDMA using conditions that otherwise passivate SiO_2,[56] and that less than 5% of hydroxyl groups on TiO_2 are consumed by trimethylsilyl groups.[56,123]

Fluctuations in the XPS peak areas for Cu 2p, C 1s, and O 1s were observed during each of the TMSDMA reapplication treatments on OFHC Cu (CuO_x/Cu) surfaces following TiO_2 (Figure 5.16) or HfO_2 (Figure 5.19) ALD; this was not observed for the case of the PE-CVD SiO_2 samples as only the attenuation of the Si 2p XPS signals was observed. It was evident that the removal of adventitious carbon following the 423 K annealing treatment during the TMSDMA reapplications of both ALD processes cleaned

the surface, thereby increasing the Cu(0)/Cu(I) signal from copper atoms that were buried beneath.

In the case after TiO_2 ALD (Figure 5.16a), the unexpected attenuation of the CuO_x-O 1s XPS signal accompanied by the evolution of that of the TiO_2-O 1s following each inhibitor reapplication is unexpected. While some studies report that reduction of CuO to Cu_2O in both film and bulk form occurs upon vacuum annealing to 800 K,[124,125] others have reported that reduction of partially oxidized CuO films can begin at approximately 380 K.[126] While it could be speculated that the results from the latter study may explain the attenuation of the CuO_x-O 1s signal observed here, it is unlikely that sub-monolayer coverages of copper oxide exist following ex-situ sample transfer and subsequent metal oxide ALD using H_2O as the co-reagent. Moreover, no attenuation of the O 1s XPS signal accompanied by an evolution of that of the Cu 2p was ever observed after annealing the sample to 423 K during the initial TMSDMA treatment of the in-situ cleaned sample (Figure 5.2a). One possible explanation for the attenuation of the CuO_x-O 1s component observed here is that contaminant oxygen species may adsorb on the topmost layer after ex-situ transfer following the inhibitor reapplication and periodic ALD treatments. This oxygen may desorb as the sample is annealed to 423 K during the next inhibitor reapplication step, which would account for the concomitant evolution of the TiO_2-O 1s component peak area as more TiO_2 is exposed when the surface is cleaned of these oxygen species. However, the Ti 2p XPS peak area (Figure 5.16a) and the total surface oxygen content (Figure 5.16b) remains constant after each inhibitor reapplication, which does not support this idea. Taken together, these observations suggest that there is a redistribution

of oxygen atoms between surface species to the deposited TiO_2 with no loss in the total surface oxygen content. This could be possible, since oxygen vacancies in the TiO_2 lattice may form when annealing the copper substrate under vacuum during the inhibitor reapplications.[127] These reactive vacancies can capture nearby oxygen atoms incorporating them into the film and resulting in their diffusion or the removal of these vacancies altogether.[127,128] If the oxygen species following ex-situ transfer is atomic oxygen adsorbed on top of copper, it can be speculated that some of these oxygen atoms migrate to the neighboring TiO_2 upon vacuum annealing. The standard Gibbs free energy of formation for CuO and Cu_2O is approximately -129.7 kJ/mol and -146.0 kJ/mol, respectively, while that of TiO_2 is approximately -884.5 kJ/mol and -889.5 kJ/mol for the anatase and brookite polymorphs, respectively.[129] Furthermore, the bond dissociation energy (BDE) for Cu-O is much lower and thus weaker than that for Ti-O: approximately 343 kJ/mol vs. 662 kJ/mol, respectively.[130] Based on this information, it would be expected that the deposited TiO_2 is thermodynamically more stable and possesses a lower chemical potential than that of CuO_x. These conditions may be favorable to drive the diffusion of oxygen adsorbed on copper towards the vacancy sites of neighboring TiO_2. To confirm these speculations, these experiments should be repeated in the same manner without conducting TiO_2 ALD. It may also be speculated that TMSDMA may facilitate this process; however, these experiments must similarly be repeated in the future in the absence of the inhibitor exposures to definitively confirm this.

The case of HfO_2 ALD (Figure 5.19a) is more complex. While the same attenuating trend for the CuO_x-O 1s component as in Figure 5.16a is observed following every

TMSDMA reapplication, the HfO_2-O 1s component area only evolves after the first inhibitor reapplication and remains constant after that of the second and fourth. Furthermore, the total oxygen content decreases following each inhibitor reapplication rather than remaining constant (Figure 5.19b). While this result is not yet fully understood, some speculations can still be made to attempt to explain these discrepancies. The standard Gibbs free energy of formation for HfO_2 is approximately -1088.2 kJ/mol and the Hf-O BDE is approximately 791 kJ/mol.[129,130] This indicates that the HfO_2 is the more thermodynamically stable than TiO_2 and should possess a lower chemical potential. This suggests that the evolution of the HfO_2-O 1s after 2 cycles may in part be due to the migration of some oxygen atoms to the deposited HfO_2. However, this does not explain the decrease in the total oxygen content that is also observed. It has been reported that the presence of excess oxygen species on HfO_2 grown by ALD may result in enhanced hydrogen bonding with interfacial water molecules.[131] As the periodicity of the number of cycles used between inhibitor reapplications for HfO_2 ALD was lower than that of TiO_2 (2 vs. 5), it may be speculated that a higher density of surface hydroxyl groups still exists on the deposited HfO_2 during these first few cycles. If that were the case, this may result in the abstraction of more oxygen contaminants, likely water, through strong hydrogen bonding interactions with surface hydroxyl groups during the ex-situ transfer of the sample after HfO_2 ALD. These species can be desorbed following the annealing treatment to 423 K, which would account for the loss in total oxygen content observed here. To fully assess and compare the impact of the periodicity of TiO_2 vs. HfO_2 ALD, the same set of experiments should be repeated using intervals of 2 TiO_2 and 5 HfO_2 ALD cycles,

respectively. Taken altogether, these observations suggest that additional oxygen contaminants, such as water, were present on the OFHC Cu (CuO_x/Cu) surfaces involved for the HfO_2 ALD studies (Figure 5.19) following ex-situ transfer of the sample. Along with adventitious carbon, these oxygen contaminants desorb from the surface upon annealing to 423 K (Figure 5.19b) resulting in an increase of the Cu(0)/Cu(I) XPS peak area to a higher extent following each inhibitor reapplication step relative to the inhibitor reapplication study involving TiO_2 ALD (Figure 5.16a).

What is clear from both Figures 5.16 and Figure 5.19 is that annealing the ex-situ exposed OFHC Cu (CuO_x/Cu) surface partially removes these carbon and/or oxygen contaminant overlayers that enveloped the underlying substrate, resulting in the increase of the XPS signals corresponding to the surface. As aforementioned, these experiments must be repeated in the exact same manner without the use of the inhibitor in order to evaluate the impact of TMSDMA in these processes, if any. This will also confirm if the attenuation of the Cu(II)-Cu 2p XPS signal unique to the case of HfO_2 ALD that is observed following the inhibitor reapplications is in fact real.

One study (out of a few handful that currently exist in the literature) by Soethoudt et. al. reported a positive result in the form of XPS data between the interaction of TMSDMA with a surface other than SiO_2, but in that case SiCO islands had form on a RuO_x/Ru surface[123] rather than trimethylsilyl groups that typically adsorb on SiO_2; in contrast, neither of these interactions with copper occurred in this work. This is also the only study to report an interaction involving TMSDMA (besides silylation) where surface defluoridation occurs as trimethylsilyl moieties partially abstract fluoride impurities from

a post-CF_4/CHF_3 plasma-etched TiO_2/TiN substrate, resulting in a surface cleaning mechanism (however, it is noted that the omission of the C 1s XPS data from these results leaves room for questioning).[123] While it could be speculated that TMSDMA may be involved in a analogous surface cleaning mechanism for the data displayed in Figure 5.16 and 5.19, these experiments must be repeated in the absence of the inhibitor to unquestionably confirm this.

The case of the peak area profiles following TiO_2 ALD or HfO_2 ALD and TMSDMA reapplications on PE-CVD SiO_2 surfaces (Figure 5.20) is not yet fully understood. Although the C 1s peak area initially evolves after ex-situ sample transfer for TiO_2 ALD, it remains constant during subsequent ALD and inhibitor reapplication steps indicating that little adventitious carbon gets adsorbed again on those surfaces even after passivation is lost and the organosilane monolayer becomes defective. Conversely, the C 1s peak area in the case of HfO_2 ALD begins to increase after 4 cycles, reaches an asymptote after 6 cycles, and then jumps to a higher value after 8 cycles. Opposite trends are seen in the HfO_2-O 1s peak area, which decreases to an asymptote after the second inhibitor reapplication nearly mirroring the trend observed for the C 1s evolution. However, no attenuation of the Hf 4f XPS peak area accompanies this. The SiO_2-O 1s signal also remains relatively constant. Based on these observations, it is speculated that the nucleation of TDMAHf and the resulting passivation loss that ensues after 2 HfO_2 ALD cycles may lead to the organosilane monolayer becoming defective in an alternative manner than that of TiO_2 ALD, which facilitates the adsorption of carbonaceous species. This may primarily occur on top of oxygen atoms of HfO_2, burying them and resulting in

the attenuation of the HfO_2-O 1s XPS signal. The amount of carbon may initially reach saturation; however, carbon adsorption appears to become favorable after a sufficient threshold has been reached. Ultimately, it is noted that the evolution of carbon here is difficult to interpret due to the nature of adventitious carbon that gets deposited during ex-situ handling. These experiments must be repeated in-situ in the future to improve the analysis of this data.

Much work is still needed in this early direction since selectivity is not maintained for a high number of ALD cycles to allow for the deposition of a thick film on the GS. It was already discussed that alternating inhibitor reapplications between each HfO_2 ALD cycle were not successful (Figure 5.21). As previously alluded to throughout this chapter, the next step forward is to incorporate this silylation scheme into an ALD "supercycle" that includes a way to mitigate undesirable defects on the NGS. Many defect mitigation strategies exist, with one of the most common being atomic layer etching (ALE).[132,133] This etch-back corrective process is typically seen as the "opposite" of ALD, as it is a highly controllable etch process that uses alternating and self-limiting surface reactions for the removal of thin layers. Two types of ALE exist: thermal ALE[134] (described before), which leads to conformal isotropic etching, and plasma ALE[135], which utilizes ions/neutrals to remove the surface layer resulting in directional anisotropic etching. For the sake of simplicity however, a mild Ar^+ sputtering treatment is proposed as an alternative to ALE in order to remove defect nuclei from the NGS in-situ prior to the inhibitor reapplication step. This way, the sample would not need to be transferred ex-situ for this step since the lab UHV chamber (UC System) used to conduct the silylation experiments is already

equipped with a sputter ion gun. Thus, these two steps may be conducted in the same apparatus in tandem such that no ex-situ contaminants adsorb prior to the re-silylation step.

This etch-back corrective measure should be periodically applied to both surfaces and must be frequent enough such that selectivity can still be maintained. To fit these criteria using the example of TiO_2 ALD, both surfaces should be sputtered every 5 ALD cycles in both the inherent and inverted selectivity pathways. This hypothetical idea is illustrated in the ALD supercycle schematic shown in Figure 5.22.

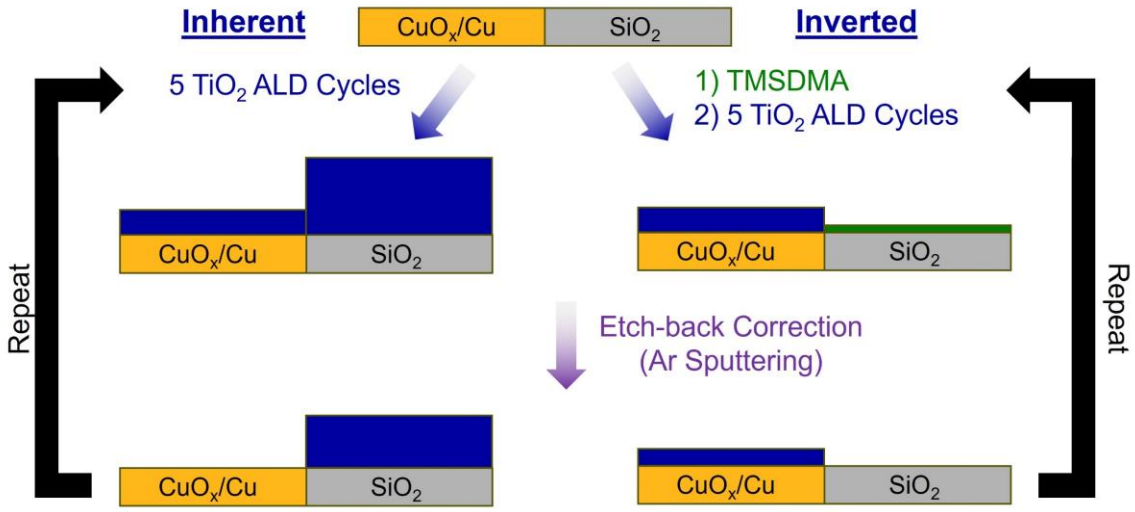


Figure 5.22 Schematic depicting an ideal TiO_2 ALD "supercycle" where an etch-back corrective measure can be utilized to remove defect nuclei from the GS. The amount of material removed should be less than the amount to be deposited during the ALD sequence. In the case of film deposition on the dielectric surface, the defective organosilane monolayer should also be removed so that new trimethylsilyl moieties can adsorb in the following supercycle prior to ALD.

An ALD supercycle typically consists of a surface modification step (such as with TMSDMA) the sequential half-reaction steps that make up the ALD process, and a defect mitigation step. Instead of the typical "AB" sequence for a normal ALD cycle, a supercycle

would follow an "ABCD" sequence where the surface modification step is ascribed as "A", followed by the ALD half-reactions as "B" and "C", and finally the etch-back step as "D" (the case of an inherently selective system is an "ABC" process without a surface modification step). However, this strategy of etching defects may only be applied if the amount of undesirable film grown on the NGS is smaller than the film deposited on the GS during the periodic ALD reactions.[136] For the inherently selective pathway without using TMSDMA, the quantity of TiO_2 etched from the OFHC Cu (CuO_x/Cu) NGS must be less than that deposited on the PE-CVD SiO_2 GS during the 5-ALD-cycle period. For the inverted selective pathway in comparison, the defective organosilane monolayer that results following 5 TiO_2 ALD cycles should be sputtered off the PE-CVD SiO_2 NGS so that the surface can be functionalized with new trimethylsilyl groups during the next inhibitor reapplication. The same sputtering treatment should be applied to the OFHC Cu (CuO_x/Cu) GS, however the material etched off here is expected to be minimal as the thickness of the trimethylsilyl monolayer is quite small. In the case of the more reactive deposition process of HfO_2 ALD using TDMAHf and H_2O, the etch-back and inhibitor reapplication steps for this supercycle would need to be carried out between each HfO_2 ALD cycle. Despite this strict requirement, this may still be promising as there have been no previous reports of completely passivating the initial HfO_2 ALD cycle specifically using TMSDMA outside of this work (to the best of our knowledge). The results reported here thus establish an encouraging path towards utilizing SMIs such as TMSDMA for the AS-ALD of metal oxides, implementing ALD supercycles in the future to extend area-selectivity.

5.8 Conclusion

The exposure of TMSDMA to the copper substrates studied in this work did not result in the functionalization of the surface with trimethylsilyl moieties, evidenced by the absence of any Si 2p XPS signals that indicated no Si atoms were ever present on the surface. This was further corroborated by the comparable peak intensities of the Hf 4f or Ti 2p XPS signals for the OFHC Cu (CuO_x/Cu) surface treated with the inhibitor compared to the blank profiles, as no significant difference was discerned indicating that the inhibitor exposure to the substrate did not impede film growth. This result established these copper substrates as viable GS for film deposition.

While passivation using TMSDMA did not yield favorable area-selectivity even when the inhibitor was reapplied to both substrates, a promising path to extend AS-ALD in the future was proposed. While other work have explored the impact of inhibitor reapplications using different types of SMIs that demonstrated that the ability to extend the selectivity window[88,137–139] this is the first study to investigate the reapplication of TMSDMA on both OFHC Cu (CuO_x/Cu) and PE-CVD SiO_2 substrates, which may undergo an alternative passivation mechanism on the latter surface that prevents easy healing of defects that are formed within the organosilane monolayer after ALD. Future work should be conducted to integrate this inhibitor into a supercycle process that includes the use of etch-back correction steps prior to inhibitor reapplications to restore the passivation efficacy of the monolayer to its original state.

SIX

Controlling ALD Nucleation Site (Silanol) Density in Mesoporous Silica (SBA-15) via Chemical Treatments

6.1 Introduction

As aforementioned in previous chapters, ALD is one of the most promising techniques to generate conformal thin films due to its atomic scale precision, which plays a significant role in the design of microelectronics and device fabrication owing to its ability to deposit a wide range of materials (such as metal oxides like TiO_2 or HfO_2) with exquisite control at sub-nanometer dimensions. Film growth using ALD has also garnered significant interest in the field of catalysis for the deposition of noble metals such as Pt and Pd.[140–144] However, the uniform deposition of these metal films can be challenging due to long induction periods that exist prior to precursor nucleation. Contrastingly, ALD may also be used to facilitate the deposition of metal nanoparticles (NPs); however, these tend to aggregate and sinter, typically through Ostwald ripening and/or dynamic coalescence, when exposed to high processing temperatures resulting in a loss in catalytic performance.[142,145] The ability to control these deposition processes on silicon oxide surfaces requires stringent control over the surface nucleation centers where these reactions occur on. As the density of the films deposited by ALD are directly reliant upon this,

preliminary surface modification steps may be employed to alter the density of surface hydroxyl groups and with that, the properties of the deposited film.

In the context of semiconductor manufacturing, deposition on certain substrates (such as metals) can be challenging due to the limited availability of chemisorption sites during the initial stages of ALD, leading to an undesirable nucleation delay.[146] The necessity for creating noble metal films quickly and efficiently requires enhanced precursor nucleation during the onset of ALD. This in turn demands that some form of surface modification be used to control the nucleation centers for these ALD reactions such that subsequent metal film growth on oxides may be accelerated during the initial stages of ALD, possibly with near-monolayer growth/cycle. It has been established that pre-functionalizing the surface with small molecules, such as common ALD precursors like TMA or diethylzinc, can result in enhanced nucleation by acting as a seed layer.[147–149] However, these molecules remain trapped between the metal/metal oxide interface after film deposition without being removed, and may act as impurities that detrimentally impact device performance during semiconductor manufacturing. Alternative methods have involved using SiO_2 ALD to hydroxylate the surface; however, TMA was once again involved in this process and remained between the substrate-film interface.[150] It is thus imperative to determine other surface modification methods to enhance nucleation that do not require the addition of new atoms not associated with the thin film to be deposited on the surface. One method proposed in this work is using a NaOH etching step to directly modify the silica surface and increase the density of surface hydroxyl nucleation centers as a way to tune metal film growth.

In contrast to increasing the film density, the ability to deposit metal NPs using ALD has also garnered significant interest in the framework of heterogenous catalysis due to the unique chemical, optical, and catalytic properties that can be obtained.[151–153] Controlling the nucleation and growth during ALD to deposit highly dispersed and immobilized NPs may improve catalytic performance as well as prevent undesirable effects that occur at elevated temperatures such as NP aggregation and sintering.[145,154–157] However, as ALD leads to isotropic coverage without providing control over the arrangement of atoms across the surface, some form of surface modification prior to growth is once again required. In this sense the number of nucleation centers must be reduced in a controlled fashion, which can be achieved using partial silylation to block Si-OH groups. Previous studies have explored this in the liquid phase using self-assembled monolayers (SAMs), in which unknown solvent effects may hinder the overall reaction kinetics and provide little to no control with regards to the ability to remove available hydroxyl nucleation centers for ALD reactions.[154] Furthermore, these studies employed flat silicon oxide surfaces that initially possess too few hydroxyl groups. In this work, an all gas-phase silylation process involving small-molecule inhibitors (SMIs) such as TMSDMA was used to acquire better control over the extent of the reaction on mesoporous supports.

Mesoporous materials are widely considered to be excellent catalytic supports owing to their favorable properties that include high surface area, thermal and chemical stability, and well-ordered pore structures.[158] Due to this, SBA-15 was chosen over flat SiO_2 substrates for these experiments due to its high surface area, well-defined and narrow pore size distribution, and higher hydroxyl density of approximately 1-2 OH

groups/nm^2.[84,159] The results discussed in this chapter underscore the significance of controlling hydroxyl nucleation centers, where chemisorption of ALD precursors occurs on, using two different surface modification processes in order to potentially tune the density of the resulting film that is deposited (Figure 6.1). Based on our findings, it is proposed that a partial silylation process can diminish the number of nucleation sites and act as steric shields such that subsequent ALD reactions may form immobilized NPs that do not aggregate and sinter at high temperatures due to limited diffusion. Conversely, a NaOH etching pretreatment capable of enhancing the density of these silanol groups is proposed as a way to facilitate the deposition of films with high densities during the initial stages of ALD with near-monolayer growth/cycle. It should be noted here that the proposed ALD experiments will be conducted in the future, as emphasis for the work in this chapter was placed on initially identifying the correct surface modification steps required.

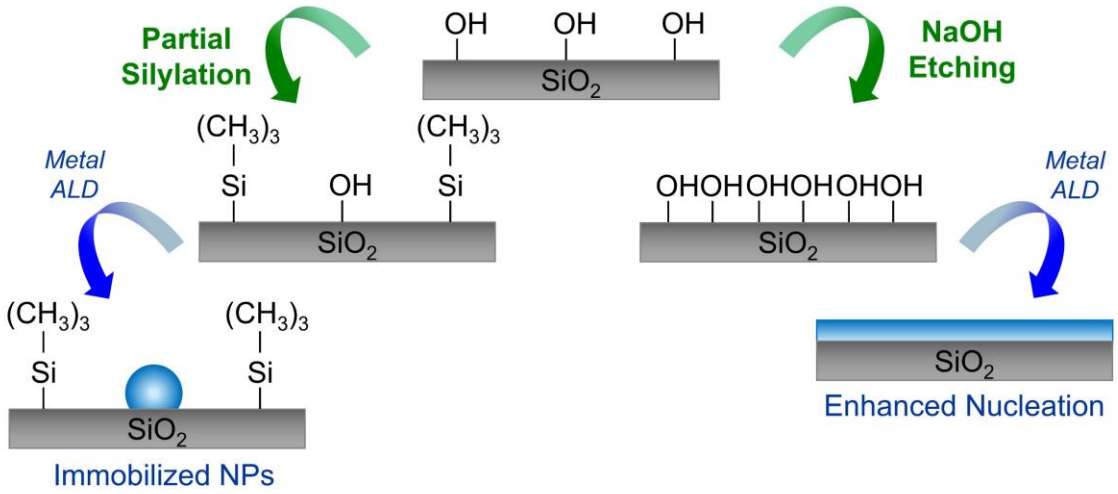


Figure 6.1 Schematic depicting two different surface modification steps to alter the density of silanol nucleation centers present on the silica surface. Partial silylation may be employed to reduce the number of Si-OH sites while NaOH etching may be used to enhance them.

6.2 Experimental

The general experimental details for the surface modification procedures, silylation reactor, and primary characterization tools used to conduct the studies in this chapter are previously described in Chapter 2.3. The specific details are as follows:

Silanol Density Reduction via Partial Silylation

1. Heat approximately 50 mg of SBA-15 for 2 hrs. to remove adventitious carbon inside a batch reactor, which is heated to 373 K.
2. Set the sample and reactor temperature to 423 K and 373 K, respectively, while keeping the TMSDMA inhibitor at room temperature.
3. Throttle both sets of precision valves and the bottom Swagelok valve to reduce the molecular flux of TMSDMA. Slightly open the TMSDMA Swagelok valve to dose the inhibitor for the desired time period. The pressure should increase by approximately 5 mTorr.
4. Close the TMSDMA Swagelok valve. Fully open all throttled valves. Purge with Ar for 5 min.
5. Shut off all the heating. Slowly cool the sample back down to room temperature prior to collecting it.

Silanol Density Enhancement via NaOH Etching

1. Disperse 200 mg of SBA-15 in 15 mL of DI H_2O. Add 15 mL of NaOH solution to obtain 30 mL of desired etching concentration.
2. Allow the etching reaction to continue for 5 min.
3. Centrifuge the sample (7 min. at 9000 rpm) to remove the solvent by washing with DI H_2O three times and ethanol twice, centrifuging in between each washing step.
4. Dry the powder overnight at approximately 423 K to remove residual water.

It is noted here that additional etching continued after the 5 min. NaOH treatment as the sample remains in the etching solution during the first 7 min. centrifugation step.

^{29}Si and 13C CP/MAS ssNMR were employed to quantify the changes in the density and distribution of silanol nucleation groups as well as assess how the chemical environment evolved throughout the reaction. The chemical structures associated with each peak component are depicted in Figure 6.2.[160]

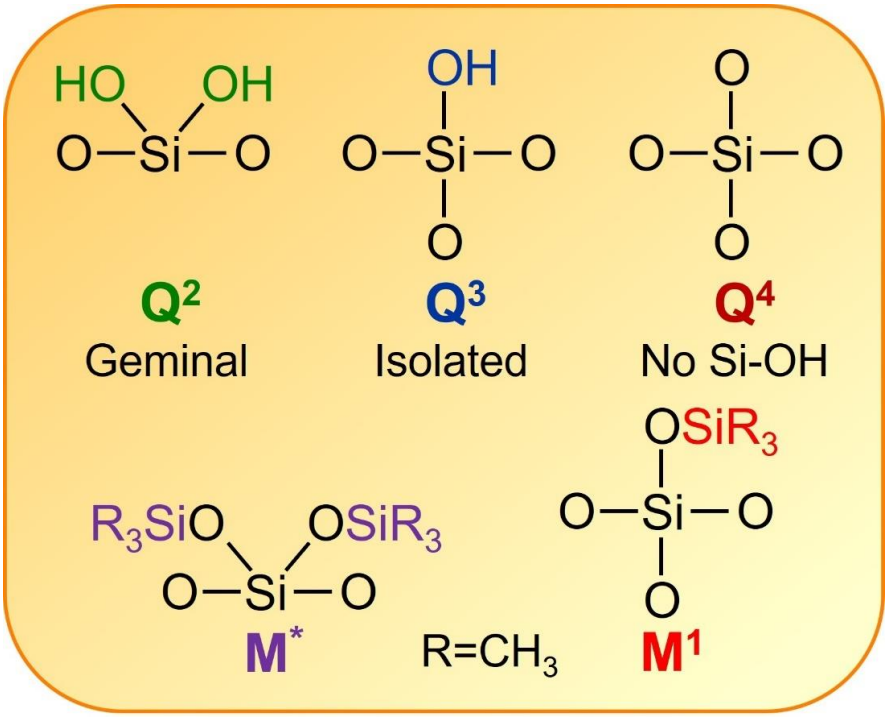


Figure 6.2 Chemical structures corresponding to each of the labels used to assign peak components in the ^{29}Si and ^{13}C CP/MAS ssNMR data.

Geminal silanols (Q^2) possess two hydroxyl groups, providing a higher number of nucleation sites for reactions to occur on. If only one silanol becomes occupied however, these may be converted to isolated silanol groups (Q^3). As trimethylsilyl moieties chemisorb on Q^2 and Q^3 sites during silylation and chemically remove them from further reactions, they are converted to M^* and M^1, respectively. On the other hand, the enhancement of the silanol density during the NaOH etching treatment was expected to convert Si bulk atoms (Q^4) not bonded to any hydroxyl groups to Q^2 and Q^3 nucleation centers. The use of ssNMR was therefore critical due to its capability to distinguish the subtle differences between these chemical environments as they evolve following chemical

treatments. The abundance, density, and distribution of these silanol sites are expected to have significant implications on subsequent metal (oxide) ALD processes.

6.3 Partial Silylation to Reduce the Silanol Density

Previous silylation experiments on flat silica samples involved completely blocking all types of silanol nucleation centers, with a focus on forming a densely packed passivating monolayer quickly and efficiently. For the experiments on SBA-15 in this chapter, emphasis was placed on evaluating how the quantity and distribution of the different types of silanol groups evolved as a function of silylation time.

Partial silylation was performed using TMSDMA in order to control the density of surface hydroxyl groups. It was expected that by gradually removing the available nucleation centers of SBA-15, a partially passivated surface conducive for the preparation of uniformly dispersed and immobilized NPs via ALD could be achieved in the future. To assess the controllability of the gas-phase silylation process in passivating the hydroxyl nucleation sites of SBA-15, the changes in the distribution of silanol groups as a function of TMSDMA dosing time were monitored using ssNMR (Figure 6.3).

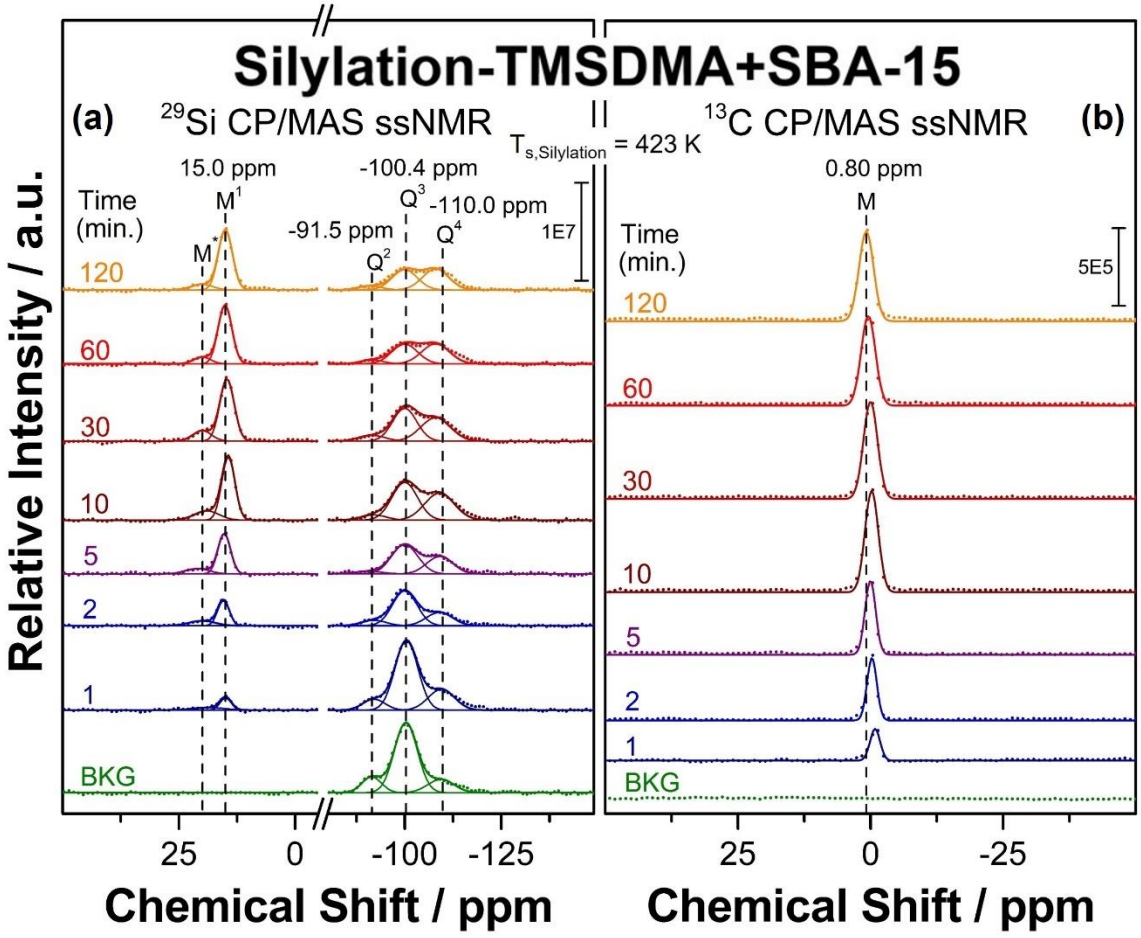


Figure 6.3 ^{29}Si (a) and ^{13}C (b) CP/MAS ssNMR spectra for gas-phase TMSDMA-silylated SBA-15 as a function of increasing inhibitor exposure time. The raw data are shown as dots and the fitted peaks as lines.

Prior to silylation, three peaks are initially observed in the ^{29}Si CP/MAS ssNMR spectra in Figure 6.1a at -91.5 ppm, -100.4 ppm, and -110.0 ppm that correspond to (O_2Si)-$(OH)_2$ (geminal silanol, Q^2), (O_3Si)-OH (isolated silanol, Q^3), and SiO_4 (no silanol, Q^4), respectively.[160,161] The initial SBA-15 surface is dominated by isolated groups evidenced by the prominent Q^3 peak. The appearance of a peak at 15.0 ppm is observed after a 1 min. TMSDMA exposure, attributed to $Si(CH_3)_3$ groups adsorbed on Si-OH nucleation sites

((O_3Si)-$Si(CH_3)_3$, M^1).[162,163] This feature evolves with increasing inhibitor dosing time indicative that a higher number of nucleation sites are capped by trimethylsilyl moieties. This is corroborated by the concomitant attenuation of the Q^2 and Q^3 signals and evolution of the Q^4 signal. Moreover, the ^{13}C CP/MAS ssNMR exhibits only a single peak at 0.80 ppm (M) indicative of a $Si(CH_3)_3$ chemical environment. The fact that the appearance of only a single peak is observed in the carbon spectra is indicative of surface functionalization with only trimethylsilyl moieties without the presence of any other decomposed species. Additionally, a second small shoulder is observed by 1 min. of TMSDMA exposure in the ^{29}Si CP/MAS ssNMR spectra, which becomes more pronounced after 10 min. This feature is associated with trimethylsilyl groups adsorbed on geminal hydroxyl nucleation centers ((O_2Si)-$((CH_3)_3)_2$, M^*).[162] A shifting towards a slightly higher chemical shift is also observed in the ^{13}C CP/MAS ssNMR spectra as the inhibitor dosing time is increased, suggestive of the formation of a complete organosilane monolayer as the chemical environment stabilizes around the carbon atoms. Additional information pertaining to the evolution of the silanol density distribution over silylation dosing time can be derived from the relative area fractions displayed in Figure 6.4.

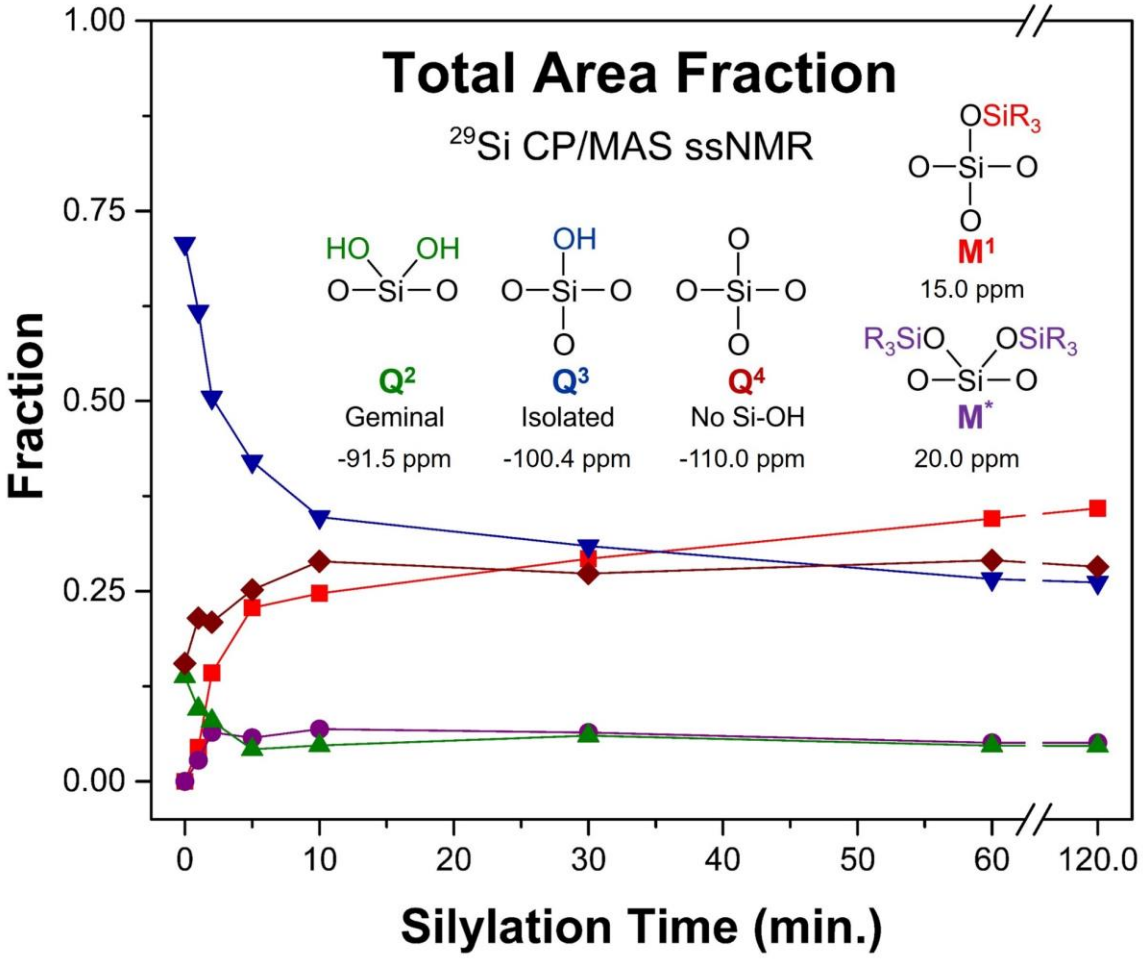


Figure 6.4 Relative peak area fractions for the main components of the ^{29}Si CP/MAS ssNMR spectra displayed in Figure 6.4a. Features from two types of Si chemical environments exist, with those associated with hydroxyl groups labeled as Q and those associated with trimethylsilyl groups labeled as M. The former are designated as Q^2 (green, -91.5 ppm), Q^3 (blue, -100.4 ppm), and Q^4 (dark red, -110.0) corresponding to geminal silanol groups, isolated silanol groups, and Si atoms from the SiO_2 bulk, respectively. The latter are designated as M^1 (light red, 15.0 ppm) and M^* (purple, 20.0 ppm) corresponding to Si atoms from trimethylsilyl groups after reacting with isolated silanol sites and those after reacting with geminal sites, respectively.

After integrating the peak areas of the ssNMR spectra in Figure 6.3, the relative peak area fractions in Figure 6.4 demonstrated that three distinct silylation regimes are observed. By only 1 min., initial rapid chemisorption of the trimethylsilyl functionalities

occurs on both isolated and geminal hydroxyl sites evidenced by the sharp attenuation of the Q^3 and Q^2 fractions and evolution of the M^1 and M^* fractions, respectively. Then, the rate of the silylation reaction begins to decline after 10 min., by which point only the isolated nucleation centers are consumed whereas the geminal groups are no longer utilized; to a similar extent, the inverse is reflected by the evolution of the M^1 signal. Finally, the silylation reaction with the mesoporous silica surface reaches saturation after 60 min. where an approximately 50:50 distribution between the free (Q^3) vs. capped (Q^4) Si-OH groups exists, demonstrating the controllability of this gas-phase silylation scheme over the surface hydroxyl nucleation centers of SBA-15. However, it is noted that no further reaction with TMSDMA was observed even after doubling the silylation process time. As such, it is speculated that the remaining Si-OH species are unavailable for further reaction with TMSDMA to chemisorb more trimethylsilyl groups by this point.

6.4 NaOH Etching to Enhance the Silanol Density

In addition to suppressing the available hydroxyl nucleation sites using silylation, other surface modification processes were explored in order to increase the density of silanol nucleation centers. The goal of this direction was to prepare surfaces conducive for rapid film deposition during the initial stages of ALD, especially in cases where long induction periods exist such as those for noble metals. To this end, ex-situ treatment with NaOH was determined as an appropriate method for the surface modification of SBA-15. It is well-known that NaOH is a powerful etching agent commonly used in the preparation of core-shell nanostructured catalysts via selective etching of the inner core to produce a

porous structure.[164–166] Therefore, the effects of NaOH etching on surface silanol groups were investigated. Prior to this however, it was important to develop an understanding of the impact of NaOH concentration on the amount of SBA-15 etched away after the reaction was complete. The mass loss of SBA-15 after treatment with varying NaOH concentration, [NaOH], is illustrated in Table 6.1.

Table 6.1 Evolution of SBA-15 mass loss after 5 min. of etching with increasing [NaOH].

Top: Photos of SBA-15 samples after NaOH etching. From left to right – SBA-15 blank (no NaOH etching), 0.5 M, 1 M, 2 M, 3 M, and 4 M (5 M is omitted due to losing a majority of the sample). Post-etched samples lost their fine quality and instead began to clump up together, becoming light and flakey in appearance.

Bottom: 200 mg of SBA-15 were initially used in all experiments. Overall, a reduction in the quantity of SBA-15 remaining is observed at higher [NaOH]. Approximately 3 mg of SBA-15 remained in the case of using 5 M NaOH (not shown); as such, the etch time was reduced from 5 min. to 30 s for this trial.

		[NaOH]/ M					
		0	0.5	1	2	3	4
-							
Mass/ mg	Initial	~200.0	~200.0	~200.0	~200.0	~200.0	~200.0
	Final	~200.0	154.4	122.2	82.8	85.5	31.2
	Δ	0	45.6	77.8	117.2	114.5	168.8

Approximately 200 mg SBA-15 were initially used prior to etching. The mass loss was measured using a balance following the etching treatment; however, it is noted that some sample loss (a few mg) occurs during sample transferring/handling. It should also be mentioned that some degree of water absorption into the pores may interfere with the analysis of this data by contributing to the final mass measured. Nevertheless, the results

here still demonstrate that a trend in sample mass loss exists as the [NaOH] is increased. Approximately 25% reduction in mass is evident after treatment with 0.5 M NaOH. An increase in the quantity of SBA-15 etched away is observed reflective of the increase in [NaOH]. By 4 M only 31.2 g of SBA-15 remains, approximately 15.6% of the original quantity. Testing with 5 M NaOH (not shown) demonstrated a significant decrease in sample mass as only approximately 3 mg of SBA-15 remained, indicating that this concentration was too high. The corresponding photos for each sample are also provided. The blank SBA-15 (far left) is a fine powder prior to any treatment; however, as the etching concentration is increased up to 4 M the sample transitions to a more flakey texture and begins to agglomerate in addition to a visible reduction in the remaining sample quantity, indicating that a distinct change to the sample had occurred.

Next, ATR-IR was used to probe the changes to the vibrational modes of -OH functional groups on SBA-15, listed in Table 6.2,[66,167–169] after the NaOH etching treatments, displayed in Figure 6.5.

Table 6.2 Assignment of the vibrational modes that appear in the ATR-IR data in Figure 6.5 for SBA-15 after treatment with increasing [NaOH]. The relative intensity of each peak is provided next to its wavenumber.

Mode Assignment	Peak Position / cm^{-1}
δ(Si-O-Si)	805 (s)
ν(Si-OH)	965 (m, sh)
ν(Si-O-Si)	1057 (vs)
δ(O-H)	1633 (w)
ν(O-H)	3360 (w)

Vibrational mode: stretching (ν), bending (δ)
Relative intensity: weak (w), medium (m), strong (s), very strong (vs), shoulder (sh)

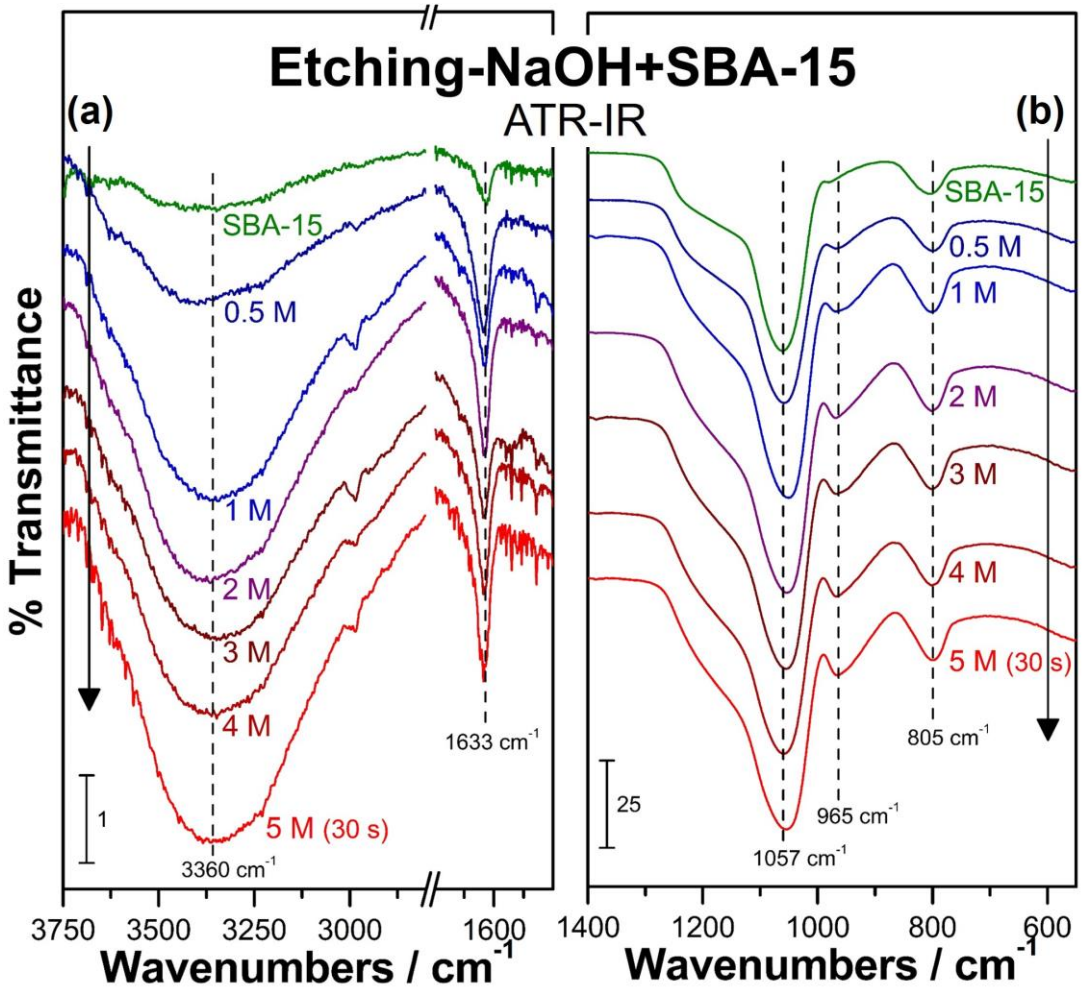


Figure 6.5 ATR-IR spectra for SBA-15 before and after etching with NaOH for 5 min. as a function of increasing [NaOH]. The O-H vibration region between 3750-1400 cm^{-1} is displayed in (a) while that of the Si-O-Si and Si-OH between 1400-550 cm^{-1} is displayed in (b). It should be noted that the scale in panel (a) is approximately 25x smaller than that shown in panel (b). The data was acquired after drying the samples overnight at 423 K.

Two vibrational modes characteristic of SiO_2 are observed in the ATR-IR spectra of pristine SBA-15 at 1057 cm^{-1} and 805 cm^{-1} (Figure 6.5b) correspond to the Si-O-Si stretching and bending modes, respectively.[167] In addition, an initially minor shoulder off the prominent 1057 cm^{-1} peak is observed at 965 cm^{-1} attributed to the Si-OH stretching mode.[168] A weak broad and weak sharp feature at 3360 cm^{-1} and 1633 cm^{-1},[66,169] typically

associated with the stretching and scissoring modes of H_2O, respectively, are present for the starting SBA-15 prior to etching (Figure 6.5a). This indicates that some water content was already present in the sample even after drying or was physisorbed afterwards prior to ATR-IR analysis. However, it should be noted that the scale used in Figure 6.5a is 25x smaller than that used in Figure 6.6b, suggesting a minor contribution from the presence of adsorbed water. A slight evolution in both the O-H stretching and bending, and Si-OH stretching modes was observed after etching with 0.5 M NaOH for 5 min.; these features continue to evolve with increasing etching concentration. By 3 M, the Si-OH mode at 965 cm^{-1} transitions to a separate individual peak. While the O-H bending mode of H_2O at 1633 cm^{-1} grows as the etching concentration is increased, suggesting that part of the O-H stretching mode at 3360 cm^{-1} arises due to the increase in water content, a clear evolution in the Si-OH vibrational mode is also observed. In addition, samples etched with 5 M NaOH for 30 s still exhibited consistent observations with the appearance of a strong Si-OH peak at 965 cm^{-1}, reflective of the rapid kinetics of surface etching using this high concentration. It is also noted that a weak vibrational mode at 2987 cm^{-1} is also observed. Considering its peak position and the fact that it does not appear in the background SBA-15 spectra, this assignment is speculated to be due to the CH_3 asymmetric stretching mode of some contamination, possibly from ethanol washing during the centrifugation step.

These initial results suggested that treatment with NaOH successfully induced a chemical change in the surface of SBA-15 resulting in an increase in the degree of silanol groups. BET was used next to better understand how the properties of the mesopores changed as the etching concentration was increased, as shown in Figure 6.6.

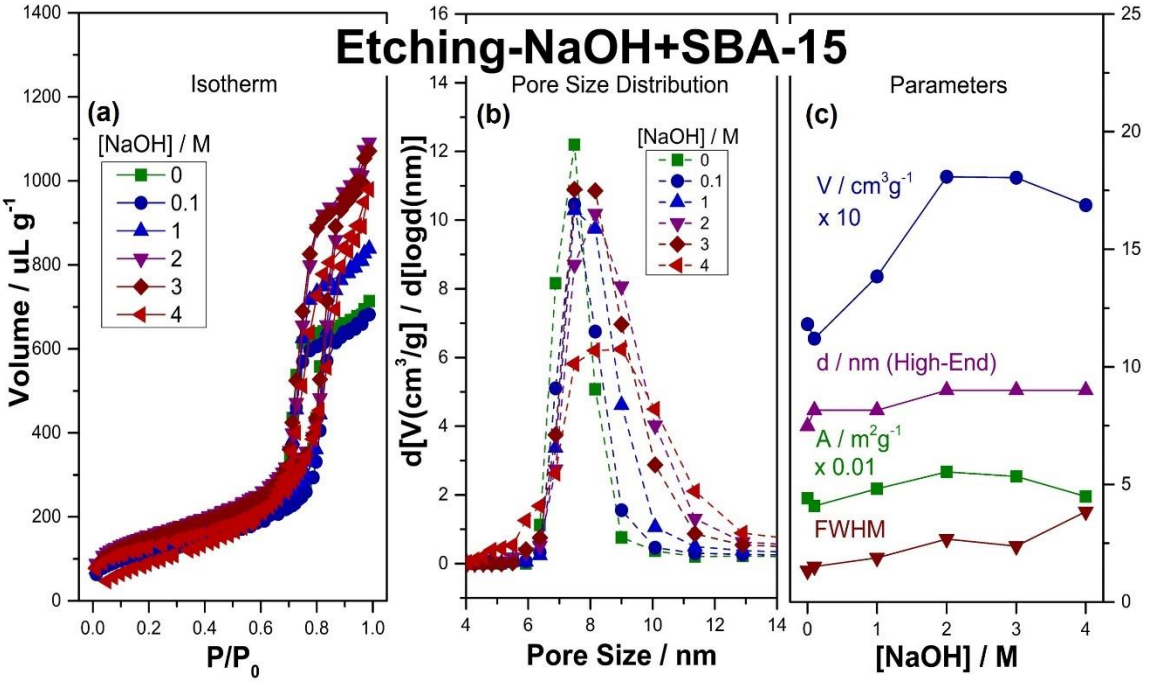


Figure 6.6 (a) Isotherm trend, (b) BET pore size distribution, and (c) various parameters for SBA-15 before and after etching with NaOH for 5 min. as a function of increasing [NaOH].

BET analysis was used to investigate the impact of increasing [NaOH] on the physical properties of SBA-15. A well-developed hysteresis loop between P/P_0 = 0.67-0.85 is observed in Figure 6.6a for the unmodified SBA-15, characteristic for mesoporous materials. A slight decrease in the pore volume is observed by 0.1 M. However, the pores are observed to substantially widen and the pore volume increased following a 1 M etching treatment. This suggested that the etching process modified the surface uniformly, gradually enlarging the pores in both diameter and volume. In Figure 6.6b, a distinct sharp peak at 7.5 nm for the unmodified SBA-15 is observed reflective of a narrow uniform pore size distribution (calculated from the desorption branch). After 2 M, a slight increase in the high-end pore diameter (Figure 6.6c) is observed and remains constant with increasing

etching concentration. A wide broadening of the SBA-15 pore size distribution is evident by 4 M NaOH in Figure 6.6b as the pores are no longer narrow and uniform in size, an observation that is reflected by the increase in the full-width half-maximum (FWHM) parameter in Figure 6.6c. The results from this BET analysis confirmed that the etching treatment with NaOH effectively modified SBA-15.

Next, ^{29}Si CP/MAS ssNMR was used to directly investigate the changes in the chemical environment of Si atoms in the samples as a function of etching concentration.

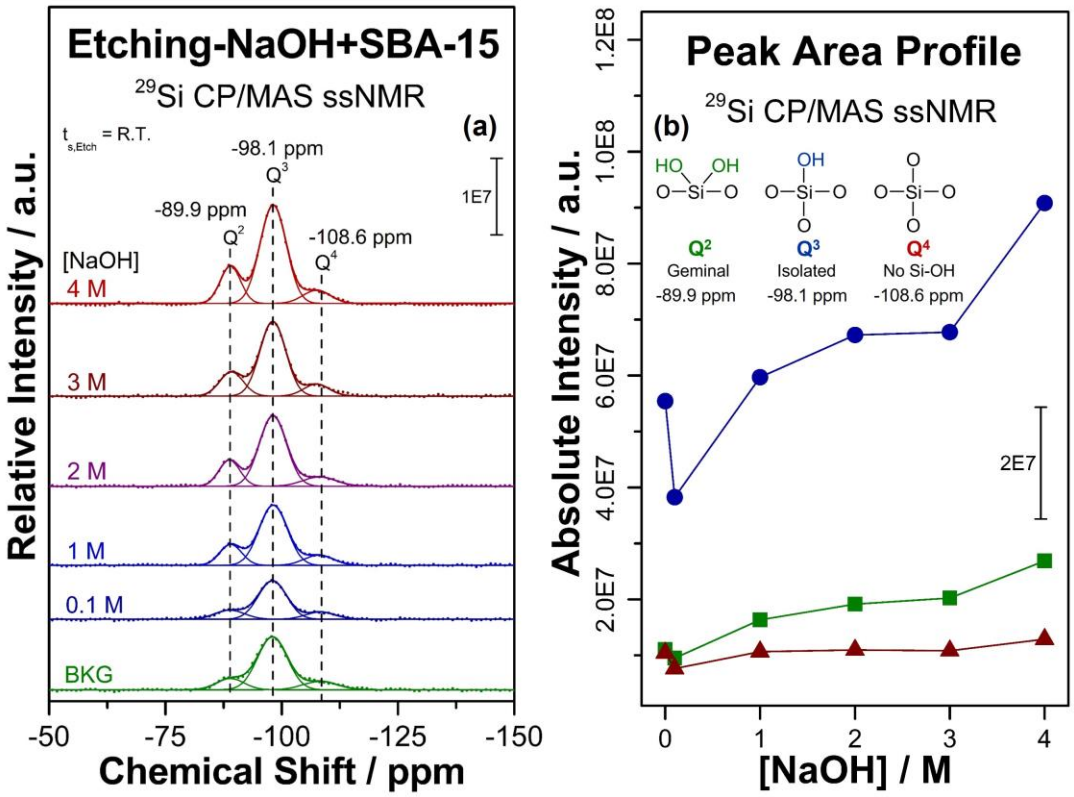


Figure 6.7 (a) ^{29}Si CP/MAS ssNMR spectra for SBA-15 before and after etching with NaOH for 5 min. as a function of increasing [NaOH]. The raw data are shown as dots and the fitted peaks as lines. (b) Absolute peak areas integrated from the main components of the ^{29}Si CP/MAS ssNMR spectra displayed in panel (a), labeled as Q^2 (green, -89.9 ppm), Q^3 (blue, -98.1 ppm), and Q^4 (red, -108.6) corresponding to geminal silanol groups, isolated silanol groups, and Si atoms from the SiO_2 bulk, respectively.

Three peaks are initially observed in the ^{29}Si CP/MAS ssNMR spectra in Figure 6.7a for pristine SBA-15 at -89.9 ppm, -98.1 ppm, and -108.6 ppm that correspond to Q^2, Q^3, and Q^4, respectively. With the exception of 0.1 M, an increase in the peak intensities is observed as the Q^2 and Q^3 signals evolve with increasing [NaOH]. To better quantify this, the absolute peak areas for the data are plotted in Figure 6.7b. an asymptote in the Q^2 and Q^3 peak area value is reached by 3 M; then, a sudden increase is observed after 4 M. However, this observation may likely be due to the sample acquisition process as Q^4 is also seen to unexpectedly increase. To better understand how the distribution of the silanol groups changed with increasing [NaOH], the absolute peak area for each component in Figure 6.7b was plotted as a fraction of the total area, which is displayed in Figure 6.8.

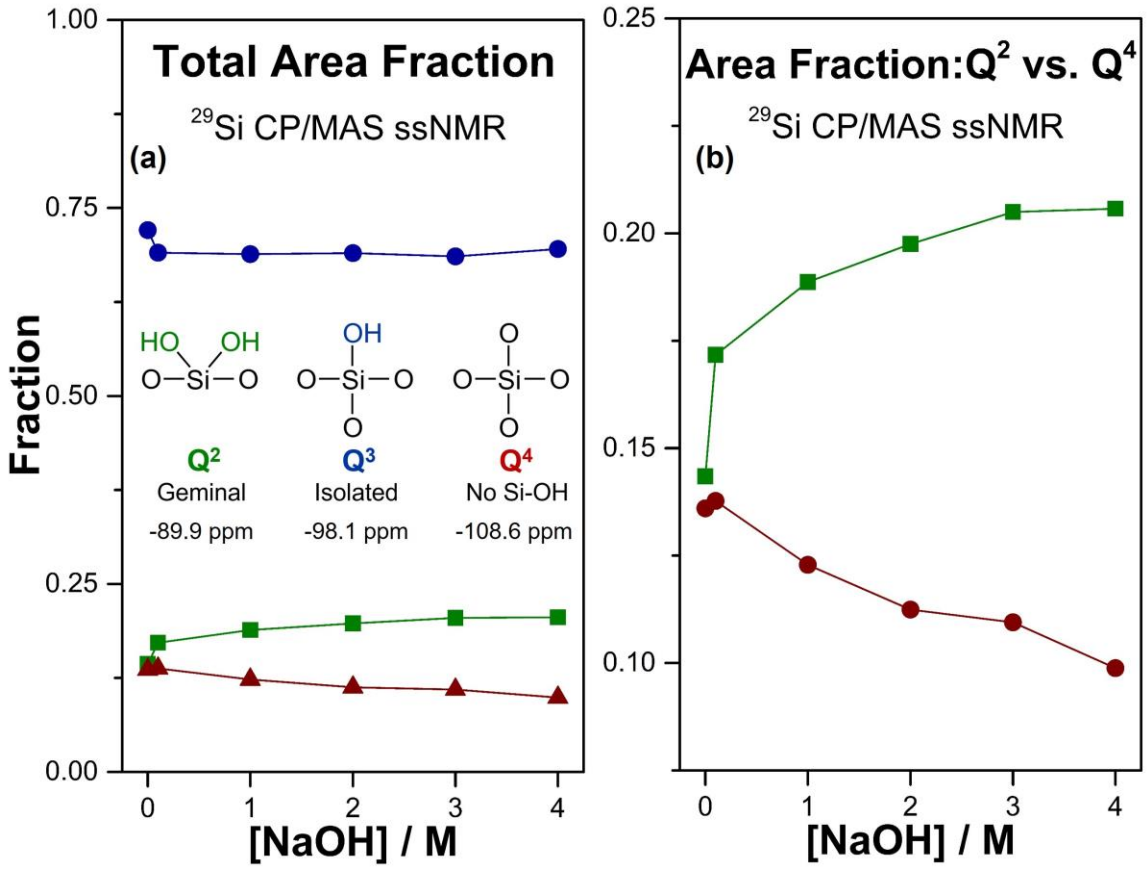


Figure 6.8 (a) Relative peak area fractions for the main components of the ^{29}Si CP/MAS ssNMR spectra displayed in Figure 6.8b, labeled as Q^2 (green, -89.9 ppm), Q^3 (blue, -98.1 ppm), and Q^4 (red, -108.6) corresponding to geminal silanol groups, isolated silanol groups, and Si atoms from the SiO_2 bulk, respectively. To better understand how the density of specific silanol groups changes as a function of increasing [NaOH], a plot focusing on Q^2 vs. Q^4 is displayed in (b).

In the total area fraction profile displayed in Figure 6.8a, a change in the distribution of different types of silanol sites is already evident by 0.1 M as a small, unexpected reduction in the fraction of isolated silanol groups is observed. The Q^3 fraction then remains constant at approximately 0.70 as the [NaOH] is increased. To clearly examine how the other Si chemical environments are impacted, an enhanced graph displaying only the Q^2 vs. the Q^4 area fraction is plotted in Figure 6.8b. The Q^4 signal remained relatively constant

after a 5 min. 0.1 M etching treatment. Contrastingly, the Q^2 signal evolved concomitant to the reduction in the Q^3 fraction shown in Figure 6.8a. The Q^4 area fraction decreased after 1 M while that of Q^2 continued to grow, although at a slightly lower rate compared to the initial jump observed at 0.1 M. The Q^2 signal continues to evolve until reaching a plateau after 3 M. An approximate 43% enhancement in Q^2 and a 23% reduction in Q^4 from the original unmodified SBA-15 sample is observed following a 4 M etching treatment. To reiterate, the Q^3 signal remained constant throughout the entire process following the treatment with 0.1 M NaOH.

6.5 Discussion

Mesoporous SBA-15 was selected as an ideal silica material for these investigations not only due to the aforementioned benefits it possesses as a catalytic support, but also for its capacity to provide a larger number of silanol nucleation centers and existing in the form of a powder. The latter affords the advantage of being able to conduct ssNMR studies in order to directly probe changes in the chemical environment of Si atoms, and thus the evolution of silanol nucleation centers as well.

Chapter 4 of this work originally discussed the impact of the media used to conduct silylation of flat silica substrates on the passivation efficacy, demonstrating that the gas-phase method was more favorable due to the providing the unique advantage of greater controllability over both the surface reaction and quality of the resulting passivating monolayer. Due to this, it was desirable to evaluate the gas-phase silylation method as a way to directly control the number of hydroxyl nucleation centers on silica in a powder

form. The reaction was observed to occur immediately within the first minute of TMSDMA exposure without any induction period as evidenced by the appearance of M^1 and M^* peaks in the ^{29}Si CP/MAS ssNMR spectra presented in Figure 6.3a. Although the greater peak intensity of M^1 compared to M^* may initially imply preferential adsorption of trimethylsilyl moieties on isolated hydroxyl groups over those of geminal, it has been demonstrated that TMSDMA efficiently reacts with and is capable of removing all types of available hydroxyl chemisorption sites.[61] Furthermore, the number of geminal groups relative to isolated groups on the starting surface is much lower. The subsequent evolution of both M signals at the expense of the attenuation of the Q signals was observed until after 60 min., by which point no further changes in the peak intensities were observed. The changes in the ^{13}C CP/MAS ssNMR reflected this in the form of a single peak, ascribed to a $Si(CH_3)_3$ chemical environment, which continued to evolve with increasing inhibitor dosing time. This is encouraging, as it demonstrates that the degree of silylation can be controlled over time such that a partially passivated monolayer comprised of different coverages dependent only on the inhibitor dosing time may be achieved.

This silylation scheme is promising as it is expected that subsequent chemical reactions with ALD precursors would occur at only the remaining hydroxyl nucleation centers; as such, a complete monolayer would not form initially so long as the passivated sites remain inactive. This is especially true during the initial stages of ALD, during which only a small number of nuclei would be expected to chemisorb forming NPs of varying size. Due to some degree of steric hindrance and repulsion, it is expected that these SMI molecules would adsorb in a dispersed fashion to minimize the overall surface free

energy.[88] These trimethylsilyl groups may also assist in spatially directing ALD precursors to chemisorb onto neighboring nucleation centers that are energetically favorable, facilitating their dispersion and keeping them immobilized once bonded to the surface.

By plotting the distributions of the different existing silanol groups as area fractions in Figure 6.4, it is evident that the silylation reaction with Q^3 sites followed a non-linear rate with increasing TMSDMA dosing time. It is noted that the fast reaction rates during the initial inhibitor exposures may provide some difficulty in controlling the size and shape of NPs grown during subsequent ALD in the future. However, it is suggested that the reaction kinetics may be slowed down during the initial stages of silylation by lowering the temperature and vapor pressure of TMSDMA using a cold bath, which may provide better control over the silylation rate and thus trimethylsilyl density. Finally, by 60 min. a 50:50 split was observed with regards to the number of available vs. unavailable Si-OH nucleation sites (Q^3 vs. Q^4). This observation indicated that all accessible sites for the adsorption of trimethylsilyl groups had been consumed by this point. This is still promising however, as smaller NPs may still be able to access the Si-OH sites that have not yet been removed by $Si(CH_3)_3$ groups. Ideally, the NPs to be deposited during ALD at this stage should possess a smaller diameter than that of the trimethylsilyl moieties such that they remain immobilized between the inhibitor groups without diffusing across the surface, maximizing their dispersion in the process. A lower silylation time may be required to reduce the steric hindrance around available nucleation sites so that ALD precursor molecules may physically reach them.

The ATR-IR and BET studies presented in Figures 6.5 and 6.6, respectively, demonstrated the successful modification of SBA-15 using an NaOH etching treatment. The ssNMR spectra in Figure 6.7 confirmed that the distribution of silanol groups changed over increasing [NaOH], resulting in a higher number of geminal sites compared to that of unmodified SBA-15. This is evidenced by the plot of the area fraction in Figure 6.8, as a transition of the Si atoms associated with bulk SiO_2 to Si-OH groups is observed. The incremental enhancement in the silanol density is beneficial, as it demonstrates a method to control the hydroxyl density through the etching concentration. While ALD is known for its ability to generate conformal thin films, this is typically achieved after multiple deposition cycles in an island-type growth behavior. In some instances, severe induction periods may exist during the initial stages of ALD, especially in the cases of noble metals such as Pt and Pd. Through the introduction of this NaOH etching scheme as a preliminary surface modification step, an improvement to the overall film density reflective of ideal layer-by-layer growth during the initial ALD cycles is expected in the future.

6.6 Conclusion

Partial silylation using TMSDMA demonstrated that the adsorption kinetics of trimethylsilyl moieties on SBA-15 vary over inhibitor dosing time, as three distinct silylation regimes were observed evidenced by the changes in the distributions of silanol nucleation centers in the ssNMR spectra. The peak area fraction data showed that the consumption of both Q^2 and Q^3 silanol sites occurs rapidly, even by 1 min. The silylation rate remains constant until approximately 10 minutes, when the trimethylsilyl adsorption

rate slows down and only the Q^3 sites are consumed. Finally, saturation is achieved after 60 min. as no further reduction of the silanol area fractions is observed even with extended dosing time, indicative that all the accessible silanol sites have become occupied by $Si(CH_3)_3$ groups. An approximate 50:50 distribution of free vs. capped nucleation centers is achieved, which may show promise in the future for the deposition of highly dispersed and immobilized NPs between these inhibitor groups.

With regards to the evolution of Si-OH nucleation sites through NaOH etching, an enhancement in the geminal nucleation centers, Q^2, at the expense of Q^4 sites was observed, indicative of a transition to a more reactive surface conducive for ALD film growth. Initially, a few isolated hydroxyl sites, Q^3, were converted to Q^2 by 0.1 M. With higher concentrations however, the Si atoms of SiO_2 (Q^4) were converted to that of (O_2Si)-$(OH)_2$ (Q^2).

Future work should include systematic metal (oxide) ALD studies on partially silylated SBA-15 to develop an understanding of how NPs will grow on these surfaces, and to determine whether or not they will do so ideally as described in this work. Using elemental analysis coupled with imaging tools, further insight into the spatial distribution may be derived for not only the NPs deposited on the surface, but also for the trimethylsilyl moieties. Moreover, after conducting the same series of ALD experiments on the NaOH-etched samples, BET analysis should provide insight into the density and thickness of the films grown on these modified surfaces relative to that of a blank.

The results obtained from these studies are promising as they suggest that the controllable gas-phase silylation process can be used to spatially direct film growth after

ALD by promoting the formation of immobilized 3-D NPs. Further studies should be conducted to investigate the characteristics of NP formation and the efficacy of this silylation scheme to prevent NP sintering and aggregation under high processing temperatures. In addition, surface modification using NaOH etching suggested that the enhanced hydroxyl density of SBA-15 would be suitable for growing dense 2-D films during the initial stages of ALD, ideally with near-monolayer/cycle control. This can also assist with mitigating (or ideally completely removing) the undesirable induction period that exists for certain deposition processes, such as in the case of noble metal ALD.

SEVEN

Conclusions and Future Directions

7.1 Overall Conclusions

The primary work presented in this dissertation elucidated the passivation efficacy of gas- vs. liquid-phase silylation of silica surfaces using the small-molecule inhibitor (SMI) TMSDMA. These XPS-focused studies were carried out employing two metal oxide ALD systems, TiO_2 and HfO_2, which revealed limitations with respect to the degree of passivation achievable using this silylation agent. In both media, complete surface passivation was achieved up to 5 ALD cycles in the case of TiO_2 film deposition, whereas this was possible up to the first ALD cycle in the case of HfO_2. The comparable efficacy using both procedures demonstrated the advantage of using the in-situ gas-phase silylation scheme, as this approach would allow for its use in microelectronics manufacturing due to its ease of integration with other gas-phase steps. Furthermore, a lower carbon content was observed when using this approach as opposed to the liquid-phase, indicating that a higher quality passivating monolayer was generated. The higher carbon content in the organosilane monolayer formed using the liquid phase method is suggestive of the formation of carbon-based agglomerates that may result in defect sites within the monolayer. Finally, the comparison of TiO_2 vs. HfO_2 ALD highlighted the differences in reactivities between the two metalorganic precursors used to grow these respective films, as TDMAHf exhibited a higher affinity to nucleate on trimethylsilyl-passivated silica

surfaces compared to TDMATi. It is speculated here that the difference in nucleation behavior between the two precursors lies in the affinity to consume various surface hydroxyl nucleation centers, as TDMAHf may tend to react with multiple types relative to TDMATi. Further studies such as in-situ ATR-IR experiments would be required in order to fully confirm this in the future.

The XPS results in this dissertation also revealed that TMSDMA does not interact with OFHC Cu (CuO_x/Cu) substrates; no Si atoms were ever detected in the Si 2p XPS for these samples indicative that trimethylsilyl moieties did not chemisorb on those surfaces. Furthermore, film growth was not inhibited on these TMSDMA-exposed surfaces as evidenced from the comparison to untreated OFHC Cu (CuO_x/Cu) substrates as a function of increasing TiO_2 or HfO_2 ALD cycles. This is promising, as it indicates that the TMSDMA-treated OFHC Cu substrates can be used as a suitable growth surface (GS) for AS-ALD. After exposure of the inhibitor to both silica and copper surfaces, the dielectric surface is selectively passivated such that preferential film growth occurs on the metal. Based on the results on blanket substrates, area-selective deposition on the copper substrate could be maintained for up to 5 TiO_2 ALD cycles and the first HfO_2 ALD cycle. Inherent selectivity existed for preferential TiO_2 film growth on the dielectric surface over the metal when TMSDMA was not used as a surface modification step; although, it is noted that some undesirable growth still occurred on OFHC Cu (CuO_x/Cu) in this case after ALD.

Attempts to re-silylate the dielectric substrate using periodic TMSDMA reapplications to extend the selectivity window to a higher number of TiO_2 or HfO_2 ALD cycles were ultimately unsuccessful. When applying the same treatments to the OFHC Cu

(CuO_x/Cu) substrates, fluctuating trends in the XPS signals were observed as contaminants in the form of carbon or oxygen species would adsorb during ex-situ transfer of the sample and desorb upon annealing the substrates to 423 K in-situ during the inhibitor reapplication steps at recurring intervals thereby cleaning the surfaces and partially restoring the signal from the underlying surface.

The results from these studies are still encouraging, as they indicate that SMIs such as TMSDMA may be implemented in an all gas-phase process to shift the role of the GS and non-growth surface (NGS) when the deposition of certain materials, such as TiO_2, is required in a versatile manner. In the broader context of AS-ALD, it is suggested that this passivation scheme may still be viable when using more reactive systems such as HfO_2 ALD, albeit without control over the area-selectivity and with a lower selectivity window. Inhibitor reapplications were periodically applied prior to the nucleation of TDMATi or TDMAHf as a possible way to extend the ALD window and overcome these challenges; however, this did not assist with healing the passivation loss that occurred on the SiO_2 substrate indicative of irreversible damage to the monolayer after a sufficient number of repeated ALD cycles. Nevertheless, these results are still encouraging as the next step in the future direction of this project will be to carry out ALD supercycles in an "ABCD" fashion that include a defect mitigation step to periodically remove the defective organosilane passivating monolayer in this inverted AS-ALD scheme. It is speculated that this may establish a way to frequently re-silylate the silica NGS in between ALD cycles while allowing for film growth to continue on the copper GS thereby extending the

selectivity window. The same etch-back corrective measure should also be applied to the GS, in which the amount of material etched off is less than that deposited during ALD.

Transitioning from flat substrates to mesoporous silica, ssNMR results demonstrated that surface modification steps may be used to alter the density of hydroxyl nucleation groups of SBA-15 in a controllable fashion. In the case of reducing the silanol density, partial silylation was employed to control the silylation kinetics as a function of inhibitor exposure time. This revealed three distinct inhibition regimes with rapid silylation occurring immediately, followed by an intermediate rate of consumption of Si-OH sites, until finally achieving saturation after a 60 min dose. In the case of enhancing the silanol density, NaOH etching served as a way to functionalize the surface with additional hydroxyl groups. As the concentration of NaOH was increased the distribution of different types of hydroxyl sites was changed, favoring the formation of geminal sites at the expense of Si atoms associated with the bulk. These results demonstrated two paths to control the reactivity of the initial surface, which may be a promising to tune the density of ALD films in the future.

7.2 Prospective Work

7.2.1 Studies on Cu(0) Surfaces

The studies on the OFHC Cu (CuO_x/Cu) substrates discussed in this work are part of an ongoing effort to extend the AS-ALD process to fully metallic Cu surfaces. The presence of some oxygen on the starting Cu substrates here partially hampered the analysis of how the silylation agent may react with only Cu(0). Furthermore, the need to transfer

the sample ex-situ for subsequent film deposition during the ALD step led to the adsorption of carbon and oxygen contaminants further reducing the surface reactivity. Experiments with a higher degree of control should be performed to remove these issues in the future that include implementing additional cleaning measures to remove the residual surface oxygen prior to treatment with TMSDMA. For example, repeated cycles of Ar^+ sputtering (2 kV ions) followed by high temperature annealing has been demonstrated to completely attenuate the O 1s XPS signal below the detection limit,[170] which may be implemented here for these copper substrates prior to the inhibitor exposure. Alternatively, a more desirable approach may be to physically evaporate or sputter a Cu target in-situ in the lab UHV chamber (UC System) to deposit clean Cu(0) films on PE-CVD SiO_2/Si(100) surfaces instead of using bulk OFHC Cu substrates. It is expected that these metallic Cu films would contain fewer impurities since they are deposited in a clean UHV environment without being exposed to ambient conditions. The cleaning of these surfaces should also be facilitated as it is expected that few bulk impurities such as carbon would be exfoliated when annealing the sample. The subsequent ALD of TiO_2 and HfO_2 films should also be conducted in-situ without ever exposing the sample to ambient conditions, allowing for a fundamental understanding of the surface chemistry involved following each precursor half-cycle reaction. The in-situ experiments proposed here will establish a more controlled reaction environment to better elucidate the interaction between TMSDMA and Cu(0).

7.2.2 Expanding Supercycle Process to Include an Etch-back Step

Periodic inhibitor reapplications were unsuccessful in restoring the passivation efficacy of the organosilane monolayer on the dielectric surface; as such, a loss in selectivity was observed after only a few metal oxide ALD cycles. An etch-back step was proposed to remove both unwanted nuclei adsorbed to the NGS as well as the defective organosilane monolayer prior to reapplying TMSDMA. The implementation of this defect mitigation measure has been displayed using an "ABCD" supercycle sequence to extend the selectivity window to a higher number of ALD cycles, allowing for the deposition of thicker films on the GS prior to a loss in area-selectivity.[23,138,171–174] Ar^+ sputtering is proposed here as a viable method to remove defect nuclei from the NGS after every few ALD cycles (or between each cycle for more reactive ALD processes) prior to the inhibitor reapplication. It should be reiterated that this strategy can only be applied if the total thickness removed on the NGS is less than that of the film deposited on the GS during the periodic ALD cycles.

7.2.3 Studies on Other Potential Growth Surfaces

Cu continues to be used as the primary material during back-end-of-line processing to connect transistors, capacitors, and resistors together in devices. However, as critical dimensions continue to shrink and transistor densities continue to scale up the use of Cu leads to various problems in devices including electromigration, delayed signal propagation, and interference between neighboring lines. It is therefore important to also evaluate alternative interconnect metals as potential growth surfaces, such as Co or Ru,

which show great promise as next-generation replacements for Cu.[175–177] However, many studies up to now have primarily focused on evaluating other materials such as TiN as a potential GS in the context of AS-ALD[122,174,178] due to its technological relevance as a diffusion barrier. Co and Ru have yet to be as extensively studied as a possible GS. In particular, Co has demonstrated a lower resistance and reduced electromigration at much smaller critical dimensions compared to that of Cu, leading to higher current densities. In the context of AS-ALD studies however, Co has only been employed as a NGS passivated using alkylthiol self-assembled monolayers (SAMs) to allow film deposition on a SiO_2 GS.[179,180] Moreover, the nature of these Co surfaces was left undefined with no substantial indication that the starting substrates were truly metallic. We propose here to extend our studies to use Co(0) as a potential GS while SiO_2 is preferentially passivated by TMSDMA to allow film deposition on the metal over the dielectric surface.

7.2.4 Metal Oxide ALD on Surface-modified SBA-15

Two surface modification procedures were established from this work as ways to control the silanol density of mesoporous silica by either reducing or enhancing the number of Si-OH nucleation sites. The next direction in this project will be to conduct TiO_2 ALD on these modified surfaces and evaluate the growth modality primarily using imaging techniques coupled with elemental analysis, such as transmission electron microscopy and energy-dispersive X-ray spectroscopy. The spatially resolved information obtained from these experiments is expected to be useful in providing insight into the growth characteristics of the deposited films.[71]

In the case of partially silylated SBA-15, well-dispersed 3-D NPs are expected to form that should decrease in size as the silylation time is increased due to limiting the number of available nucleation centers. These samples should ideally undergo post-treatment under catalytically relevant temperatures to assess the degree of NP aggregation and sintering. Conversely, 2-D films are expected to be deposited from the onset of ALD in the case of NaOH-etched SBA-15, instead of the coalescence of small islands that typically occurs over a number of cycles to form the first layer. The deposition of these films using these modified surfaces should ideally proceed with a monolayer/cycle growth rate. In addition, a reduction in the induction period that exists during the initial stages of metal ALD, as is the case for the deposition of Pt and Pd films, is expected. These metal ALD systems should also be evaluated using these modified surfaces in the future. Finally, these experiments will then be extended to flat SiO_2/Si(100) substrates to serve as a point of comparison to those conducted on modified SBA-15 powders.

References

1. Moore, G. E. *Lithography and the Future of Moore's Law*.

2. Leskelä, M. & Ritala, M. Atomic Layer Deposition Chemistry: Recent Developments and Future Challenges. *Angewandte Chemie - International Edition* vol. 42 5548–5554 Preprint at https://doi.org/10.1002/anie.200301652 (2003).

3. Johnson, R. W., Hultqvist, A. & Bent, S. F. A brief review of atomic layer deposition: From fundamentals to applications. *Materials Today* vol. 17 236–246 Preprint at https://doi.org/10.1016/j.mattod.2014.04.026 (2014).

4. Marichy, C., Bechelany, M. & Pinna, N. Atomic layer deposition of nanostructured materials for energy and environmental applications. *Advanced Materials* **24**, 1017–1032 (2012).

5. Wen, L., Zhou, M., Wang, C., Mi, Y. & Lei, Y. Nanoengineering Energy Conversion and Storage Devices via Atomic Layer Deposition. *Advanced Energy Materials* vol. 6 Preprint at https://doi.org/10.1002/aenm.201600468 (2016).

6. Kim, H., Lee, H. B. R. & Maeng, W. J. Applications of atomic layer deposition to nanofabrication and emerging nanodevices. *Thin Solid Films* vol. 517 2563–2580 Preprint at https://doi.org/10.1016/j.tsf.2008.09.007 (2009).

7. Meng, X. *et al.* Atomic layer deposition for nanomaterial synthesis and functionalization in energy technology. *Materials Horizons* vol. 4 133–154 Preprint at https://doi.org/10.1039/c6mh00521g (2017).

8. Knez, M., Nielsch, K. & Niinistö, L. Synthesis and surface engineering of complex nanostructures by atomic layer deposition. *Advanced Materials* vol. 19 3425–3438 Preprint at https://doi.org/10.1002/adma.200700079 (2007).

9. Oneill, B. J. *et al.* Catalyst design with atomic layer deposition. *ACS Catal* **5**, 1804–1825 (2015).

10. Sun, S. *et al.* Single-atom catalysis using Pt/graphene achieved through atomic layer deposition. *Sci Rep* **3**, (2013).

11. Leskela, M. & Ritalä, M. R. *Atomic Layer Deposition (ALD): From Precursors to Thin Film Structures*. *Thin Solid Films* vol. 409 (2002).

12. Zaera, F. The surface chemistry of thin film atomic layer deposition (ALD) processes for electronic device manufacturing. *J Mater Chem* **18**, 3521–3526 (2008).

13. Zaera, F. The surface chemistry of atomic layer depositions of solid thin films. *Journal of Physical Chemistry Letters* vol. 3 1301–1309 Preprint at https://doi.org/10.1021/jz300125f (2012).

14. Guo, L. J. Nanoimprint lithography: Methods and material requirements. *Advanced Materials* **19**, 495–513 (2007).

15. Mackus, A. J. M., Bol, A. A. & Kessels, W. M. M. The use of atomic layer deposition in advanced nanopatterning. *Nanoscale* vol. 6 10941–10960 Preprint at https://doi.org/10.1039/c4nr01954g (2014).

16. Oviroh, P. O., Akbarzadeh, R., Pan, D., Coetzee, R. A. M. & Jen, T. C. New development of atomic layer deposition: processes, methods and applications. *Science and Technology of Advanced Materials* vol. 20 465–496 Preprint at https://doi.org/10.1080/14686996.2019.1599694 (2019).

17. Puurunen, R. L. A short history of atomic layer deposition: Tuomo Suntola's atomic layer epitaxy. *Chemical Vapor Deposition* vol. 20 332–344 Preprint at https://doi.org/10.1002/cvde.201402012 (2014).

18. George, S. M. Atomic layer deposition: An overview. *Chem Rev* **110**, 111–131 (2010).

19. George, S. M., Ott, A. W. & Klaus, J. W. *Surface Chemistry for Atomic Layer Growth*. https://pubs.acs.org/sharingguidelines (1996).

20. Groner, M. D., Fabreguette, F. H., Elam, J. W. & George, S. M. Low-Temperature Al2O3 Atomic Layer Deposition. *Chemistry of Materials* **16**, 639–645 (2004).

21. Ye, P. D. *et al.* GaN metal-oxide-semiconductor high-electron-mobility-transistor with atomic layer deposited Al2 O3 as gate dielectric. *Appl Phys Lett* **86**, 1–3 (2005).

22. Minton, T. K. *et al.* Protecting polymers in space with atomic layer deposition coatings. *ACS Appl Mater Interfaces* **2**, 2515–2520 (2010).

23. Mackus, A. J. M., Merkx, M. J. M. & Kessels, W. M. M. From the Bottom-Up: Toward Area-Selective Atomic Layer Deposition with High Selectivity †. *Chemistry of Materials* **31**, 2–12 (2019).

24. Parsons, G. N. & Clark, R. D. Area-Selective Deposition: Fundamentals, Applications, and Future Outlook. *Chemistry of Materials* vol. 32 4920–4953 Preprint at https://doi.org/10.1021/acs.chemmater.0c00722 (2020).

25. Biswas, A. *et al.* Advances in top-down and bottom-up surface nanofabrication: Techniques, applications & future prospects. *Advances in Colloid and Interface Science* vol. 170 2–27 Preprint at https://doi.org/10.1016/j.cis.2011.11.001 (2012).

26. Chen, R., Kim, H., McIntyre, P. C. & Bent, S. F. Investigation of self-assembled monolayer resists for hafnium dioxide atomic layer deposition. *Chemistry of Materials* **17**, 536–544 (2005).

27. Atanasov, S. E., Kalanyan, B. & Parsons, G. N. Inherent substrate-dependent growth initiation and selective-area atomic layer deposition of TiO2 using "water-free" metal-halide/metal alkoxide reactants. *Journal of Vacuum Science & Technology A: Vacuum, Surfaces, and Films* **34**, (2016).

28. Longo, R. C. *et al.* Selectivity of metal oxide atomic layer deposition on hydrogen terminated and oxidized Si(001)-(2×1) surface. *Journal of Vacuum Science & Technology B, Nanotechnology and Microelectronics: Materials, Processing, Measurement, and Phenomena* **32**, 03D112 (2014).

29. Cao, K., Cai, J. & Chen, R. Inherently Selective Atomic Layer Deposition and Applications. *Chemistry of Materials* **32**, 2195–2207 (2020).

30. Jiang, X., Chen, R. & Bent, S. F. Spatial control over atomic layer deposition using microcontact-printed resists. *Surf Coat Technol* **201**, 8799–8807 (2007).

31. Chen, R., Kim, H., McIntyre, P. C., Porter, D. W. & Bent, S. F. Achieving area-selective atomic layer deposition on patterned substrates by selective surface modification. *Appl Phys Lett* **86**, 1–3 (2005).

32. Bobb-Semple, D., Nardi, K. L., Draeger, N., Hausmann, D. M. & Bent, S. F. Area-Selective Atomic Layer Deposition Assisted by Self-Assembled Monolayers: A Comparison of Cu, Co, W, and Ru. *Chemistry of Materials* **31**, 1635–1645 (2019).

33. Jiang, X. & Bent, S. F. Area-selective ALD with soft lithographic methods: Using self-assembled monolayers to direct film deposition. *Journal of Physical Chemistry C* **113**, 17613–17625 (2009).

34. Merkx, M. J. M. *et al.* Insight into the removal and reapplication of small inhibitor molecules during area-selective atomic layer deposition of SiO2. *Journal of Vacuum Science & Technology A: Vacuum, Surfaces, and Films* **39**, (2021).

35. Xu, W. *et al.* Functionalization of the SiO2Surface with Aminosilanes to Enable Area-Selective Atomic Layer Deposition of Al2O3. *Langmuir* **38**, 652–660 (2022).

36. Xu, W., Lemaire, P. C., Sharma, K., Hausmann, D. M. & Agarwal, S. Extending growth inhibition during area-selective atomic layer deposition of Al2O3 on aminosilane-functionalized SiO2. *Chemical Communications* **58**, 6650–6652 (2022).

37. Junsic, H., Porter, D. W., Sreenivasan, R., McIntyre, P. C. & Bent, S. F. ALD resist formed by vapor-deposited self-assembled monolayers. *Langmuir* **23**, 1160–1165 (2007).

38. Sugimura, H., Hozumi, A., Kameyama, T. & Takai, O. Organosilane self-assembled monolayers formed at the vapour/solid interface. in *Surface and Interface Analysis* vol. 34 550–554 (2002).

39. Bunker, B. C. *et al.* Impact of solution agglomeration on the deposition of self-assembled monolayers. *Langmuir* **16**, 7742–7751 (2000).

40. Hinckley, A. P. & Muscat, A. J. Detecting and Removing Defects in Organosilane Self-Assembled Monolayers. *Langmuir* **36**, 2563–2573 (2020).

41. Gates, H. J. B. D. Monitoring and mapping imperfections in silane-Based self-Assembled monolayers by chemical amplification. *Langmuir* **25**, 9078–9084 (2009).

42. Tiznado, H. & Zaera, F. Surface chemistry in the atomic layer deposition of TiN films from TiCl4 and ammonia. *Journal of Physical Chemistry B* **110**, 13491–13498 (2006).

43. Sun, H. & Zaera, F. Chemical vapor deposition of manganese metallic films on silicon oxide substrates. *Journal of Physical Chemistry C* **116**, 23585–23595 (2012).

44. John C. Vickerman. *Surface Analysis - The Principal Techniques*. (John Wiley & Sons, Manchester, UK, 1997).

45. Ulgut, B. & Suzer, S. XPS studies of SiO2/Si system under external bias. *Journal of Physical Chemistry B* **107**, 2939–2943 (2003).

46. Major, G. H. *et al.* Practical guide for curve fitting in x-ray photoelectron spectroscopy. *Journal of Vacuum Science & Technology A* **38**, 061203 (2020).

47. Motin, M. A. & Zaera, F. Thermal Chemistry of Nickel Diketonate Atomic Layer Deposition (ALD) Precursors on Tantalum and Silicon Oxide Surfaces. *Journal of Physical Chemistry C* **125**, 22006–22022 (2021).

48. Moulder, F. J., Stickle, F. W., Sobol, E. P. & Bomben, D. K. *Handbook of X-Ray Photoelectron Spectroscopy*. (Perkin-Elmer Corporation, Eden-Prairie, 1993).

49. *XPS Atomic Sensitivity Factors* versus Atomic Number*.

50. Tanuma, S., Powell, C. J. & Penn, D. R. *Calculations of Electron Inelastic Mean Free Paths. V. Data for 14 Organic Compounds over the 50-2000 EV Range*. *SURFACE AND INTERFACE ANALYSIS* vol. 21 (1993).

51. Alexander, M. R., Thompson, G. E., Zhou, X., Beamson, G. & Fairley, N. Quantification of oxide film thickness at the surface of aluminium using XPS. in *Surface and Interface Analysis* vol. 34 485–489 (2002).

52. Guo, L. & Zaera, F. Spatial resolution in thin film deposition on silicon surfaces by combining silylation and UV/ozonolysis. *Nanotechnology* **25**, (2014).

53. Kern, W. *The Evolution of Silicon Wafer Cleaning Technology*.

54. Methaapanon, R. & Bent, S. F. Comparative study of titanium dioxide atomic layer deposition on silicon dioxide and hydrogen-terminated silicon. *Journal of Physical Chemistry C* **114**, 10498–10504 (2010).

55. Chopra, S. N., Zhang, Z., Kaihlanen, C. & Ekerdt, J. G. Selective Growth of Titanium Nitride on HfO2 across Nanolines and Nanopillars. *Chemistry of Materials* **28**, 4928–4934 (2016).

56. Van Dongen, K. *et al.* Aminosilane small molecule inhibitors for area-selective deposition: Study of substrate-inhibitor interfacial interactions. *Journal of Vacuum Science & Technology A* **41**, 032404 (2023).

57. Baik, K.-H. Gas phase silylation in the diffusion enhanced silylated resist process for application to sub-0.5 μm optical lithography. *Journal of Vacuum Science & Technology B: Microelectronics and Nanometer Structures* **8**, 1481 (1990).

58. Mirji, S. A. *et al.* Adsorption of octadecyltrichlorosilane on mesoporous SBA-15. *Appl Surf Sci* **252**, 4097–4103 (2006).

59. Deyhimi, F. & Coles, J. A. Rapid Silylation of a Glass Surface: Choice of Reagent and Effect of Experimental Parameters on Hydrophobicity. *Helv Chim Acta* **65**, 1752–1759 (1982).

60. Ahn, S., Kim, Y., Kang, S., Im, K. & Lim, H. Low-temperature-atomic-layer-deposition of SiO2 using various organic precursors. *Journal of Vacuum Science & Technology A: Vacuum, Surfaces, and Films* **35**, (2017).

61. Mameli, A. & Teplyakov, A. V. Selection Criteria for Small-Molecule Inhibitors in Area-Selective Atomic Layer Deposition: Fundamental Surface Chemistry Considerations. *Acc Chem Res* **56**, 2084–2095 (2023).

62. Guo, L., Lee, I. & Zaera, F. Patterning of Solid Films via Selective Atomic Layer Deposition Based on Silylation and UV/Ozonolysis. *ACS Appl Mater Interfaces* **8**, 19836–19841 (2016).

63. Guo, L., Qin, X. & Zaera, F. Chemical Treatment of Low-k Dielectric Surfaces for Patterning of Thin Solid Films in Microelectronic Applications. *ACS Appl Mater Interfaces* **8**, 6293–6300 (2016).

64. Khan, R. *et al.* Area-Selective Atomic Layer Deposition Using Si Precursors as Inhibitors. *Chemistry of Materials* **30**, 7603–7610 (2018).

65. Morrow, B. A. & Mcfarlan, A. J. *61 North-Holland CHEMICAL REACTIONS AT SILICA SURFACES*. *Journal of Non-Crystalline Solids* vol. 120 (1990).

66. Hair, M. L. *HYDROXYL GROUPS ON SILICA SURFACE*. *Journal of Non-Crystalline Solids* vol. 19 (1975).

67. Sneh, O. & George, S. M. *Thermal Stability of Hydroxyl Groups on a Well-Defined Silica Surface*. *J. Phys. Chem* vol. 99 https://pubs.acs.org/sharingguidelines (1995).

68. Färm, E., Kemell, M., Ritala, M. & Leskelä, M. Self-assembled octadecyltrimethoxysilane monolayers enabling selective-area atomic layer deposition of iridium. *Chemical Vapor Deposition* **12**, 415–417 (2006).

69. Barry, S. T., Teplyakov, A. V. & Zaera, F. The Chemistry of Inorganic Precursors during the Chemical Deposition of Films on Solid Surfaces. *Acc Chem Res* **51**, 800–809 (2018).

70. Rozlosnik, N., Gerstenberg, M. C. & Larsen, N. B. Effect of solvents and concentration on the formation of a self-assembled monolayer of octadecylsiloxane on silicon (001). *Langmuir* **19**, 1182–1188 (2003).

71. Zaera, F. The surface chemistry of the atomic layer deposition of metal thin films. *Nanotechnology* **35**, 362001 (2024).

72. Bobb-Semple, D. *et al.* Substrate-dependent study of chain orientation and order in alkylphosphonic acid self-assembled monolayers for ALD blocking. *Langmuir* **36**, 12849–12857 (2020).

73. Abendroth, B. *et al.* Atomic layer deposition of TiO2 from tetrakis(dimethylamino) titanium and H2O. *Thin Solid Films* **545**, 176–182 (2013).

74. Xie, Q. *et al.* Atomic layer deposition of Ti O2 from tetrakis-dimethyl-amido titanium or Ti isopropoxide precursors and H2 O. *J Appl Phys* **102**, (2007).

75. Jin, C., Liu, B., Lei, Z. & Sun, J. Structure and photoluminescence of the TiO2 films grown by atomic layer deposition using tetrakis-dimethylamino titanium and ozone. *Nanoscale Res Lett* **10**, (2015).

76. Zhuiykov, S. *et al.* Wafer-scale fabrication of conformal atomic-layered TiO2 by atomic layer deposition using tetrakis (dimethylamino) titanium and H2O precursors. *Mater Des* **120**, 99–108 (2017).

77. Kim, J. C., Cho, Y. S. & Moon, S. H. Atomic layer deposition of HfO2 onto Si using Hf(NMe 2)4. *Jpn J Appl Phys* **48**, (2009).

78. Blaschke, D. *et al.* A correlation study of layer growth rate, thickness uniformity, stoichiometry, and hydrogen impurity level in HfO2 thin films grown by ALD between 100°C and 350°C. *Appl Surf Sci* **506**, (2020).

79. Gusev, E. P., Cabral, C., Copel, M., D'Emic, C. & Gribelyuk, M. Ultrathin HfO2 films grown on silicon by atomic layer deposition for advanced gate dielectrics applications. in *Microelectronic Engineering* vol. 69 145–151 (2003).

80. CATALOG NO. 26 STREM. vols 2017–2019.

81. Kan, B. C., Boo, J. H., Lee, I. & Zaera, F. Thermal chemistry of tetrakis(ethylmethylamido)titanium on Si(100) surfaces. *Journal of Physical Chemistry A* **113**, 3946–3954 (2009).

82. Cortez-Valadez, M. *et al.* Comparison of HfCl4, HfI4, TEMA-Hf, and TDMA-Hf as precursors in early growing stages of HfO2 films deposited by ALD: A DFT study. *Chem Phys* **472**, 81–88 (2016).

83. Ide, M. *et al.* Quantification of silanol sites for the most common mesoporous ordered silicas and organosilicas: Total versus accessible silanols. *Physical Chemistry Chemical Physics* **15**, 642–650 (2013).

84. Ke, W. *et al.* Nucleation and Initial Stages of Growth during the Atomic Layer Deposition of Titanium Oxide on Mesoporous Silica. *Nano Lett* **20**, 6884–6890 (2020).

85. Deshmukh, S. C. Investigation of low temperature SiO2 plasma enhanced chemical vapor deposition. *Journal of Vacuum Science & Technology B: Microelectronics and Nanometer Structures* **14**, 738 (1996).

86. Han, S. M. & Aydil, E. S. Study of surface reactions during plasma enhanced chemical vapor deposition of SiO 2 from SiH 4 , O 2 , and Ar plasma . *Journal of Vacuum Science & Technology A: Vacuum, Surfaces, and Films* **14**, 2062–2070 (1996).

87. Nye, R. A., Song, S. K., Van Dongen, K., Delabie, A. & Parsons, G. N. Mechanisms for undesired nucleation on H-terminated Si and dimethylamino-trimethylsilane passivated SiO2during TiO2area-selective atomic layer deposition. *Appl Phys Lett* **121**, (2022).

88. Li, J. *et al.* Packing of inhibitor molecules during area-selective atomic layer deposition studied using random sequential adsorption simulations. *Journal of Vacuum Science & Technology A* **40**, 062409 (2022).

89. Tezsevin, I. *et al.* Computational Investigation of Precursor Blocking during Area-Selective Atomic Layer Deposition Using Aniline as a Small-Molecule Inhibitor. *Langmuir* **39**, 4265–4273 (2023).

90. Xu, W. *et al.* Mechanism for growth initiation on aminosilane-functionalized SiO 2 during area-selective atomic layer deposition of ZrO 2 . *Journal of Vacuum Science & Technology A* **39**, 032402 (2021).

91. Oh, I. K., Sandoval, T. E., Liu, T. L., Richey, N. E. & Bent, S. F. Role of Precursor Choice on Area-Selective Atomic Layer Deposition. *Chemistry of Materials* **33**, 3926–3935 (2021).

92. Merkx, M. J. M. *et al.* Relation between Reactive Surface Sites and Precursor Choice for Area-Selective Atomic Layer Deposition Using Small Molecule Inhibitors. *Journal of Physical Chemistry C* **126**, 4845–4853 (2022).

93. Murarka, S. P., Gutmann, R. J., Kaloyeros, A. E. & Lanford, W. A. *Advanced Multilayer Metallization Schemes with Copper as Interconnection Metal*. *Thin Solid Films* vol. 236 (1993).

94. Hu, C.-K. *et al. Copper Interconnection Integration and Reliability*. *Thin Solid Films* vol. 262 (1995).

95. Rosenberg, R., Edelstein, D. C., Hu, C.-K. & Rodbell, K. P. *COPPER METALLIZATION FOR HIGH PERFORMANCE SILICON TECHNOLOGY*. (2000).

96. Wang, Y.-L. *et al. Electroplating Copper onto Resistive Barrier Films You May Also like Kinetics of Polishing Friction for Copper Pits Formation during Copper Chemical Mechanical Polishing Light Assisted Electrodeposition and Silicidation of Ni for Silicon Photovoltaic Cell Metallization*. *J. Electrochem. Soc* vol. 147 (2000).

97. Dai, M., Kwon, J., Halls, M. D., Gordon, R. G. & Chabal, Y. J. Surface and interface processes during atomic layer deposition of copper on silicon oxide. *Langmuir* **26**, 3911–3917 (2010).

98. Yao, Y., Chen, B. & Zaera, F. On the Mechanism of the Atomic Layer Deposition of Cu Films on Silicon Oxide Surfaces: Activation Using Atomic Hydrogen and Three-Dimensional Growth. *Chemistry of Materials* **35**, 2155–2164 (2023).

99. Huo, J., Solanki, R. & McAndrew, J. Characteristics of copper films produced via atomic layer deposition. *J Mater Res* **17**, 2394–2398 (2002).

100. Li, Z. & Gordon, R. G. Thin, continuous, and conformal copper films by reduction of atomic layer deposited copper nitride. *Chemical Vapor Deposition* **12**, 435–441 (2006).

101. Liu, T. L., Harake, M. & Bent, S. F. Sequential Use of Orthogonal Self-Assembled Monolayers for Area-Selective Atomic Layer Deposition of Dielectric on Metal. *Adv Mater Interfaces* **10**, (2023).

102. Bergsman, D. S. *et al.* Formation and Ripening of Self-Assembled Multilayers from the Vapor-Phase Deposition of Dodecanethiol on Copper Oxide. *Chemistry of Materials* **30**, 5694–5703 (2018).

103. Liu, T. L., Nardi, K. L., Draeger, N., Hausmann, D. M. & Bent, S. F. Effect of Multilayer versus Monolayer Dodecanethiol on Selectivity and Pattern Integrity in Area-Selective Atomic Layer Deposition. *ACS Appl Mater Interfaces* **12**, 42226–42235 (2020).

104. Hutt, D. A. & Liu, C. Oxidation protection of copper surfaces using self-assembled monolayers of octadecanethiol. *Appl Surf Sci* **252**, 400–411 (2005).

105. Love, J. C., Estroff, L. A., Kriebel, J. K., Nuzzo, R. G. & Whitesides, G. M. Self-assembled monolayers of thiolates on metals as a form of nanotechnology. *Chemical Reviews* vol. 105 1103–1169 Preprint at https://doi.org/10.1021/cr0300789 (2005).

106. Petrovykh, D. Y. *et al.* Alkanethiols on platinum: Multicomponent self-assembled monolayers. *Langmuir* **22**, 2578–2587 (2006).

107. Färm, E., Vehkamäki, M., Ritala, M. & Leskelä, M. Passivation of copper surfaces for selective-area ALD using a thiol self-assembled monolayer. *Semicond Sci Technol* **27**, (2012).

108. Kelkar, S. S., Chiavetta, D. & Wolden, C. A. Formation of octadecyltrichlorosilane (OTS) self-assembled monolayers on amorphous alumina. *Appl Surf Sci* **282**, 291–296 (2013).

109. Lee, J. P. *et al.* Photocatalytic decomposition of alkylsiloxane self-assembled monolayers on titanium oxide surfaces. *Journal of Physical Chemistry B* **107**, 8997–9002 (2003).

110. Hoque, E., Derose, J. A., Houriet, R., Hoffmann, P. & Mathieu, H. J. Stable perfluorosilane self-assembled monolayers on copper oxide surfaces: Evidence of siloxy-copper bond formation. *Chemistry of Materials* **19**, 798–804 (2007).

111. Yao, Y., Coyle, J. P., Barry, S. T. & Zaera, F. Effect of the nature of the substrate on the surface chemistry of atomic layer deposition precursors. *Journal of Chemical Physics* **146**, (2017).

112. Chavez, K. L. & Hess, D. W. A Novel Method of Etching Copper Oxide Using Acetic Acid. *J Electrochem Soc* **148**, G640 (2001).

113. Martin, L. *et al.* Comprehensive X-ray photoelectron spectroscopy study of the conversion reaction mechanism of CuO in lithiated thin film electrodes. *Journal of Physical Chemistry C* **117**, 4421–4430 (2013).

114. Biesinger, M. C. Advanced analysis of copper X-ray photoelectron spectra. *Surface and Interface Analysis* **49**, 1325–1334 (2017).

115. Brisk, M. A. & Baker, A. D. *Review Shake-up Satellites in X-Ray Photoelectron Spectroscopy*. *Journal of Efecfron Spectroscopy and Related Phenomena* vol. 7 (1975).

116. Panzner, G., Egert, B. & Schmidt, H. P. *THE STABILITY OF CuO AND Cu,O SURFACES DURING ARGON SPUTTERING STUDIED BY XPS AND AES*.

117. Tao, Q., Overhage, K., Jursich, G. & Takoudis, C. On the initial growth of atomic layer deposited TiO 2 films on silicon and copper surfaces. *Thin Solid Films* **520**, 6752–6756 (2012).

118. Pena, L. F., Veyan, J. F., Todd, M. A., Derecskei-Kovacs, A. & Chabal, Y. J. Vapor-Phase Cleaning and Corrosion Inhibition of Copper Films by Ethanol and Heterocyclic Amines. *ACS Appl Mater Interfaces* **10**, 38610–38620 (2018).

119. Anderson, N., Saha, S., Jursich, G. & Takoudis, C. G. Optimization of substrate-selective atomic layer deposition of zirconia on electroplated copper using ethanol as both precursor reactant and surface pre-deposition treatment. *Journal of Materials Science: Materials in Electronics* **32**, 5442–5456 (2021).

120. Li, Y. *et al.* Self-aligned patterning of tantalum oxide on Cu/SiO2 through redox-coupled inherently selective atomic layer deposition. *Nat Commun* **14**, (2023).

121. Taylor, D. *Wettability of Clean Metal Surfaces*. (1984).

122. Mandal, A. K. *et al.* Selectivity and Growth Rate Modulations for Ruthenium Area-selective Deposition by Co-Reagent and Nanopattern Design. *Adv Mater Technol* **9**, (2024).

123. Soethoudt, J., Tomczak, Y., Meynaerts, B., Chan, B. T. & Delabie, A. Insight into Selective Surface Reactions of Dimethylamino-trimethylsilane for Area-Selective Deposition of Metal, Nitride, and Oxide. *Journal of Physical Chemistry C* **124**, 7163–7173 (2020).

124. Kirsch, P. D. & Ekerdt, J. G. Chemical and thermal reduction of thin films of copper (II) oxide and copper (I) oxide. *J Appl Phys* **90**, 4256–4264 (2001).

125. Poulston, S., Parlett, P. M., Stone, P. & Bowker, M. Surface oxidation and reduction of CuO and Cu2O studied using XPS and XAES. *Surface and Interface Analysis* **24**, 811–820 (1996).

126. Lee, S. Y., Mettlach, N., Nguyen, N., Sun, Y. M. & White, J. M. *Copper Oxide Reduction through Vacuum Annealing*.

127. Schaub, R.; Wahlström, E.; Rønnau, A.; Lægsgaard, E.; Stensgaard, I.; Besenbacher, F. Oxygen-Mediated Diffusion of Oxygen Vacancies on the TiO 2 (110) Surface. Science (1979) 2003, 299 (5605), 377–379.

128. Lu, Q. *et al.* Metal–insulator transition tuned by oxygen vacancy migration across TiO2/VO2 interface. *Sci Rep* **10**, (2020).

129. Wagman D. Donald *et al.* The NBS Table of Chemical Thermodynamic Properties.

130. Properties of Atoms, Radicals, and Bonds.

131. Lee, S., Yoon, H., Lee, S., Chung, S. min & Kim, H. Investigation of the hydrophilic nature and surface energy changes of HfO2 thin films prepared by atomic layer deposition. *Vacuum* **219**, (2024).

132. Kanarik, K. J. *et al.* Overview of atomic layer etching in the semiconductor industry. *Journal of Vacuum Science & Technology A: Vacuum, Surfaces, and Films* **33**, 020802 (2015).

133. T. Carver, C. *et al.* Atomic Layer Etching: An Industry Perspective. *ECS Journal of Solid State Science and Technology* **4**, N5005–N5009 (2015).

134. Fischer, A., Routzahn, A., George, S. M. & Lill, T. Thermal atomic layer etching: A review. *Journal of Vacuum Science & Technology A* **39**, 030801 (2021).

135. Agarwal, A. & Kushner, M. J. Plasma atomic layer etching using conventional plasma equipment. *Journal of Vacuum Science & Technology A: Vacuum, Surfaces, and Films* **27**, 37–50 (2009).

136. Soethoudt, J. *et al.* Defect Mitigation in Area-Selective Atomic Layer Deposition of Ruthenium on Titanium Nitride/Dielectric Nanopatterns. *Adv Mater Interfaces* **6**, (2019).

137. Mameli, A. *et al.* Area-Selective Atomic Layer Deposition of SiO2 Using Acetylacetone as a Chemoselective Inhibitor in an ABC-Type Cycle. *ACS Nano* **11**, 9303–9311 (2017).

138. Merkx, M. J. M. *et al.* Area-Selective Atomic Layer Deposition of TiN Using Aromatic Inhibitor Molecules for Metal/Dielectric Selectivity. *Chemistry of Materials* **32**, 7788–7795 (2020).

139. Karasulu, B., Roozeboom, F. & Mameli, A. High-Throughput Area-Selective Spatial Atomic Layer Deposition of SiO2 with Interleaved Small Molecule Inhibitors and Integrated Back-Etch Correction for Low Defectivity. *Advanced Materials* **35**, (2023).

140. Mackus, A. J. M. *et al.* Atomic layer deposition of Pd and Pt nanoparticles for catalysis: On the mechanisms of nanoparticle formation. *Nanotechnology* **27**, (2015).

141. Li, J., Liang, X., King, D. M., Jiang, Y. B. & Weimer, A. W. Highly dispersed Pt nanoparticle catalyst prepared by atomic layer deposition. *Appl Catal B* **97**, 220–226 (2010).

142. Grillo, F., Moulijn, J. A., Kreutzer, M. T. & van Ommen, J. R. Nanoparticle sintering in atomic layer deposition of supported catalysts: Kinetic modeling of the size distribution. *Catal Today* **316**, 51–61 (2018).

143. Lu, J. *et al.* Toward atomically-precise synthesis of supported bimetallic nanoparticles using atomic layer deposition. *Nat Commun* **5**, (2014).

144. Weber, M. J., MacKus, A. J. M., Verheijen, M. A., Van Der Marel, C. & Kessels, W. M. M. Supported core/shell bimetallic nanoparticles synthesis by atomic layer deposition. *Chemistry of Materials* **24**, 2973–2977 (2012).

145. Grillo, F., Van Bui, H., Moulijn, J. A., Kreutzer, M. T. & Van Ommen, J. R. Understanding and Controlling the Aggregative Growth of Platinum Nanoparticles in Atomic Layer Deposition: An Avenue to Size Selection. *Journal of Physical Chemistry Letters* **8**, 975–983 (2017).

146. Soethoudt, J. *et al.* Diffusion-Mediated Growth and Size-Dependent Nanoparticle Reactivity during Ruthenium Atomic Layer Deposition on Dielectric Substrates. *Adv Mater Interfaces* **5**, (2018).

147. Raiford, J. A. *et al.* Enhanced Nucleation of Atomic Layer Deposited Contacts Improves Operational Stability of Perovskite Solar Cells in Air. *Adv Energy Mater* **9**, (2019).

148. Rothman, A., Werbrouck, A. & Bent, S. F. Enhanced Growth in Atomic Layer Deposition of Ruthenium Metal: The Role of Surface Diffusion and Nucleation Sites. *Chemistry of Materials* **36**, 541–550 (2024).

149. Goldstein, D. N. & George, S. M. Enhancing the nucleation of palladium atomic layer deposition on Al2 O 3 using trimethylaluminum to prevent surface poisoning by reaction products. *Appl Phys Lett* **95**, (2009).

150. Cho, J., Kim, T., Seegmiller, T. & Chang, J. P. Mechanistic study of atomic layer deposition of AlxSiyO thin film via in-situ FTIR spectroscopy . *Journal of Vacuum Science & Technology A: Vacuum, Surfaces, and Films* **33**, (2015).

151. Kamat, P. V. Photophysical, photochemical and photocatalytic aspects of metal nanoparticles. *Journal of Physical Chemistry B* **106**, 7729–7744 (2002).

152. Kelly, K. L., Coronado, E., Zhao, L. L. & Schatz, G. C. The optical properties of metal nanoparticles: The influence of size, shape, and dielectric environment. *Journal of Physical Chemistry B* **107**, 668–677 (2003).

153. Cuenya, B. R. Synthesis and catalytic properties of metal nanoparticles: Size, shape, support, composition, and oxidation state effects. *Thin Solid Films* vol. 518 3127–3150 Preprint at https://doi.org/10.1016/j.tsf.2010.01.018 (2010).

154. Lee, H. B. R., Mullings, M. N., Jiang, X., Clemens, B. M. & Bent, S. F. Nucleation-controlled growth of nanoparticles by atomic layer deposition. *Chemistry of Materials* **24**, 4051–4059 (2012).

155. Weber, M. J., Verheijen, M. A., Bol, A. A. & Kessels, W. M. M. Sub-nanometer dimensions control of core/shell nanoparticles prepared by atomic layer deposition. *Nanotechnology* **26**, (2015).

156. Cao, K., Zhu, Q., Shan, B. & Chen, R. Controlled synthesis of Pd/Pt core shell nanoparticles using area-selective atomic layer deposition. *Sci Rep* **5**, (2014).

157. Xie, T., Shi, L., Zhang, J. & Zhang, D. Immobilizing Ni nanoparticles to mesoporous silica with size and location control via a polyol-assisted route for coking- and sintering-resistant dry reforming of methane. *Chemical Communications* **50**, 7250–7253 (2014).

158. Verma, P., Kuwahara, Y., Mori, K., Raja, R. & Yamashita, H. Functionalized mesoporous SBA-15 silica: Recent trends and catalytic applications. *Nanoscale* vol. 12 11333–11363 Preprint at https://doi.org/10.1039/d0nr00732c (2020).

159. Weng, Z., Chen, Z. H., Qin, X. & Zaera, F. Sub-monolayer control of the growth of oxide films on mesoporous materials. *J Mater Chem A Mater* **6**, 17548–17558 (2018).

160. Ke, W. *et al.* Redox Properties of TiO2 Thin Films Grown on Mesoporous Silica by Atomic Layer Deposition. *J Phys Chem Lett* **14**, 4696–4703 (2023).

161. Yu, T. & Zaera, F. Synthesis of Enantioselective Solid Tandem Catalysts with Tethered Molecular Functionalities. *Journal of Physical Chemistry C* **127**, 2349–2359 (2023).

162. Dm, D. B. & Dm, M. H. *A 29Si NMR Study of the Silanol Population at the Surface of Derivatized Silica*. *NMR Study of Silanol on Silica Langmuir* vol. 6 (1990).

163. Zhao, H. & Han, H. Synthesis and characterization of functionalized SBA-15 silica through template removal. *J Solid State Chem* **282**, (2020).

164. Joo, J. B., Dahl, M., Li, N., Zaera, F. & Yin, Y. Tailored synthesis of mesoporous TiO2 hollow nanostructures for catalytic applications. *Energy and Environmental Science* vol. 6 2082–2092 Preprint at https://doi.org/10.1039/c3ee41155a (2013).

165. Zhang, Q., Lee, I., Joo, J. B., Zaera, F. & Yin, Y. Core-shell nanostructured catalysts. *Acc Chem Res* **46**, 1816–1824 (2013).

166. Lee, I., Joo, J. B., Yin, Y. & Zaera, F. A Yolk@Shell Nanoarchitecture for Au/TiO 2 Catalysts . *Angewandte Chemie* **123**, 10390–10393 (2011).

167. Pérez, H. *et al.* Green and facile sol-gel synthesis of the mesoporous SiO2-TiO2catalyst by four different activation modes. *RSC Adv* **10**, 39580–39588 (2020).

168. Kim, Y. S., Lee, J. H., Lim, J. T., Park, J. B. & Yeom, G. Y. Atmospheric pressure PECVD of SiO2 thin film at a low temperature using HMDS/O2/He/Ar. *Thin Solid Films* **517**, 4065–4069 (2009).

169. Tripp, C. P. & Hair, M. L. *An Infrared Study of the Reaction of Octadecyltrichlorosilane with Silica*. *Langmuir* vol. 8 https://pubs.acs.org/sharingguidelines (1992).

170. Ma, Q. & Zaera, F. Thermal chemistry of the Cu-KI5 atomic layer deposition precursor on a copper surface. *Journal of Vacuum Science & Technology A: Vacuum, Surfaces, and Films* **33**, (2015).

171. Vos, M. F. J. *et al.* Area-Selective Deposition of Ruthenium by Combining Atomic Layer Deposition and Selective Etching. *Chemistry of Materials* **31**, 3878–3882 (2019).

172. Song, S. K., Saare, H. & Parsons, G. N. Integrated Isothermal Atomic Layer Deposition/Atomic Layer Etching Supercycles for Area-Selective Deposition of TiO2. *Chemistry of Materials* **31**, 4793–4804 (2019).

173. Bonvalot, M. *et al.* Area selective deposition using alternate deposition and etch super-cycle strategies. *Dalton Transactions* **51**, 442–450 (2022).

174. Soethoudt, J. *et al.* Defect Mitigation in Area-Selective Atomic Layer Deposition of Ruthenium on Titanium Nitride/Dielectric Nanopatterns. *Adv Mater Interfaces* **6**, (2019).

175. Mont, F. W. *et al. Cobalt Interconnect on Same Copper Barrier Process Integration at the 7nm Node*.

176. Wen, L. G. *et al.* Atomic Layer Deposition of Ruthenium with TiN Interface for Sub-10 nm Advanced Interconnects beyond Copper. *ACS Appl Mater Interfaces* **8**, 26119–26125 (2016).

177. IEEE International Reliability Physics Symposium 55. 2017 Monterey, C. *et al. 2017 IEEE International Reliability Physics Symposium (IRPS) 2-6 April 2017*.

178. Lee, J. M., Lee, S. H., Oh, J. & Kim, W. H. Area-selective atomic layer deposition of high-quality Ru thin films by chemo-selective adsorption of short alkylating agents. *Mater Lett* **333**, (2023).

179. Chang, C. W., Hsu, H. H., Hsu, C. S. & Chen, J. T. Achieving area-selective atomic layer deposition with fluorinated self-assembled monolayers. *J Mater Chem C Mater* **9**, 14589–14595 (2021).

180. Chang, C. W., Tseng, Y. H., Hsu, C. S. & Chen, J. T. Area-Selective Atomic Layer Deposition on Metal/Dielectric Patterns: Amphiphobic Coating, Vaporizable Inhibitors, and Regenerative Processing. *ACS Appl Mater Interfaces* **15**, 28817–28824 (2023).